ABSTRACT

Title of Document: A WAVE-CHAOTIC APPROACH TO PREDICTING AND MEASURING ELECTROMAGNETIC FIELD QUANTITIES IN COMPLICATED ENCLOSURES

Sameer D. Hemmady, Doctor of Philosophy, 2006

Directed By: Dr. Steven M. Anlage
Professor- Dept. of Physics
Affiliate Faculty- Dept. of Electrical Engineering

The coupling of short-wavelength electromagnetic waves into large complicated enclosures is of great interest in the field of electromagnetic compatibility engineering. The intent is to protect sensitive electronic devices housed within these enclosures from the detrimental effects of high-intensity external electromagnetic radiation penetrating into the enclosure (which acts as a resonant cavity) through various coupling channels (or ports). The Random Coupling Model introduced by Zheng, Antonsen and Ott is a stochastic model where the mechanism of the coupling process is quantified by the non-statistical "radiation impedance" of the coupling-port, and the field variations within the cavity are conjectured to be explained in a statistical sense through Random Matrix Theory- by assuming that the waves possess chaotic ray-dynamics within the cavity.

The Random Coupling Model in conjunction with Random Matrix Theory thus makes explicit predictions for the statistical aspect (Probability Density

Functions-PDFs) of the impedance, admittance and scattering fluctuations of waves within such wave-chaotic cavities. More importantly, these fluctuations are expected to be universal in that their statistical description depends only upon the value of a single dimensionless cavity loss-parameter. This universality in the impedance, admittance and scattering properties is not restricted to electromagnetic systems, but is equally applicable to analogous quantities in quantum-mechanical or acoustic systems, which also comprise of short-wavelength waves confined within complicated-shaped potential wells or acoustic-resonators.

In this dissertation, I will experimentally show the validity of the "radiation impedance" to accurately quantify the port-coupling characteristics. I will experimentally prove the existence of these universal fluctuations in the impedance, admittance and scattering properties of quasi-two-dimensional and three-dimensional wave-chaotic systems driven by one-port or two-ports, and validate that their statistical nature is described through Random Matrix Theory. Finally, I will utilize the Random Coupling Model to formulate a prediction-algorithm to determine the shape and scales of induced voltages PDFs at specific points within complicated enclosures, such as computer boxes, when irradiated by high-intensity, short-wavelength electromagnetic energy. The insight gained from the experimental validation of the Random Coupling Model allows one to conceive of certain design-guidelines for cavity-enclosures that are more resistant to attack from an external short-wavelength electromagnetic source.

A WAVE-CHAOTIC APPROACH TO PREDICTING AND MEASURING ELECTROMAGNETIC FIELD QUANTITIES IN COMPLICATED ENCLOSURES

By

Sameer D. Hemmady

Dissertation submitted to the Faculty of the Graduate School of the
University of Maryland, College Park, in partial fulfillment
of the requirements for the degree of
Doctor of Philosophy
2006

Advisory Committee:
Professor Steven M. Anlage, Chair
Professor Thomas M. Antonsen Jr.
Professor Edward Ott
Professor Victor Granatstein
Professor Daniel P. Lathrop

Dedication

"To my dearest Mom and Dad, my adorable sister Karishma, and my cherished soul-mate Caroline, for their love, encouragement and unwavering support through all these years…"

Acknowledgements

It seems my surreal journey through graduate-school is finally coming to an end. Looking back over the years, it was one filled with moments of elation, depression, frustration and bouts of sheer terror especially during the onset of the mid-terms and final examinations. But through it all, I have been truly blessed with the unconditional love of my family, the continual encouragement and advice of my faculty-advisors, and the unfaltering support of my colleagues and friends that has gotten me this far.

I am truly at a loss for words to express my gratitude towards my research-advisor, Prof. Anlage- but I will try my best. I sincerely thank Prof. Anlage for all the time and effort he has dedicated these past four years to instill in me an appreciation for wave-chaos physics and the experimental aspects of microwave and RF engineering. Through his jovial nature, patient guidance and unabated enthusiasm, he created a highly dynamic environment in the lab which pushed me to challenge myself and strive harder to fulfill my research pursuits. His steadfast commitment to provide me with the best technical advice and state-of-the-art measurement devices and equipment has been one of the major contributory factors that have made my research-project a success. I strongly believe that my interaction with him has given me the confidence to face tomorrow's challenges in my professional career with a positive outlook. Thank You, Prof. Anlage for everything you've done for me!

On equal footing, I would also like to thank Prof. Antonsen and Prof. Ott for their invaluable advice and teachings which have cultivated in me a deeper understanding of the aspects of theoretical wave-physics and electromagnetism. Our

weekly lunch-meetings at the Stamp Union are one of the things I will miss most once I leave graduate school. I thank Dr. Gaudet, Dr. Harrison, and Prof. Schamiloglu for their useful suggestions, feedbacks and opportunities to present my work in New Mexico. I would also like to thank Henry (Xing Zheng), James Hart, Chris Bertand and Michael Johnson for their valued help and support during all phases of my research-project. Thanks guys!

My gratitude also goes out to Prof. Granatstein, Prof. Lathrop, Prof. Goldsman, Prof. Dagenais, John Rodgers, Prof. Melngailis, Prof. Newcomb and Prof. Dellomo, for all the knowledge I have gained through their courses and through casual discussions in the A. V. Williams and IREAP hallways. I would also like to thank my fellow "lab-rats"- John Lee, Atif, Mike, Dragos, Hua, Xu, Yi Qi, Nathan, Sudeep, Josh, Hanhee, Gus, Dyan and Todd for all their help and fascinating discussions on a wide spectrum of topics ranging from non-linear pulses in optical fibers to creating bottle-rockets using Coca-Cola and Mentos!

On a more personal note, I would like to thank my Mom and Dad for their tender affection, moral support, and the countless personal-sacrifices they have willingly endured so that I could procure my doctorate degree today. I also thank my cuddly sister Karishma and my "sweet Caroline" for their loving-care, encouragement and for standing by me through thick and thin, these past years. All that I have achieved today would just not have been possible without the backing of my family. Last but not least, I would like to thank all my dear friends from undergrad and grad school for being there for me. I consider myself really fortunate to have friends like you!

Table of Contents

List of Figures

Chapter 1: Introduction

With the external environment becoming ever more polluted with electromagnetic radiation from numerous sources such as wireless data services, radar and the rising threat of electromagnetic weapons, there is an urgent need to study the effects of this radiation on key electronic and electrical systems, and the means by which to protect them. Interest in this field arose in the 1970s when scientists studied the nature of electromagnetic pulses (EMP) generated by the low-altitude detonation of a nuclear device **[1]**. A nuclear-EMP is a very intense but short (hundreds of nano-seconds) electromagnetic field transient which has the potential to produce high electromagnetic power densities that can be lethal to electronic and electrical systems in its proximity. The proliferation of High-Power Microwave (HPM) weapons such as Flux Compressed Generators (FCGs), High-Intensity Radiated Field (HIRF) guns and Electromagnetic Pulse Transformer (EMPT) bombs pose an even more serious threat **[2]**. These devices can produce narrow-band or ultra-wide-band electromagnetic pulses on the order of tens to hundreds of microseconds with transient power-levels of up to tens of Terawatts **[3]**. Such high power densities can induce voltages on the order of Kilovolts on exposed electronic components thereby severely damaging military and civilian electrical or electronic systems at ranges of hundreds of meters.

Civilian systems are particularly vulnerable to nuclear-EMP and HPM effects. High density metal-oxide semiconductor devices, which are ubiquitous in all these systems, are very sensitive to even moderate level voltage transients. Any voltage transient in excess of tens of volts can lead to a dielectric breakdown of the gate-

oxide layer in these devices thereby giving rise to a large gate-drain current which effectively destroys the device **[4]**. This irreversible effect is known as "gate breakdown". Such devices may still function, but their reliability is severely impaired. Electromagnetic Shielding **[5]** of such systems by enclosing it within a metallic casing can provide only limited protection. Unlike nuclear-EMP which has frequency-spectra in the Megahertz range, HPM weapons can produce narrow-band or ultra-wideband electromagnetic pulses with frequency-spectrums in the 500 MHz to 10 GHz range. On account of the short-wavelength, this HPM-EMP can induce large voltage transients on exposed wiring or cables that run in and out of these enclosures. These exposed components act as antennas, guiding the transient energy into the enclosure and inducing large voltage swings on the electronics within the enclosure. This makes the EMP generated by HPM weapons potentially more destructive as it can couple electromagnetic energy into a target system contained within an enclosure.

Two principle modes of coupling have been recognized:

(i) Front Door Coupling typically occurs when electromagnetic energy enters the system through dedicated antennas associated with radar or telecommunications equipment housed within the enclosure (Fig. 1.1(a)).

(ii) Back Door Coupling occurs when electromagnetic energy induces large voltage transients on exposed wiring or power cables which, in turn, guide the transient energy into the enclosure (Fig. 1.1(b)).

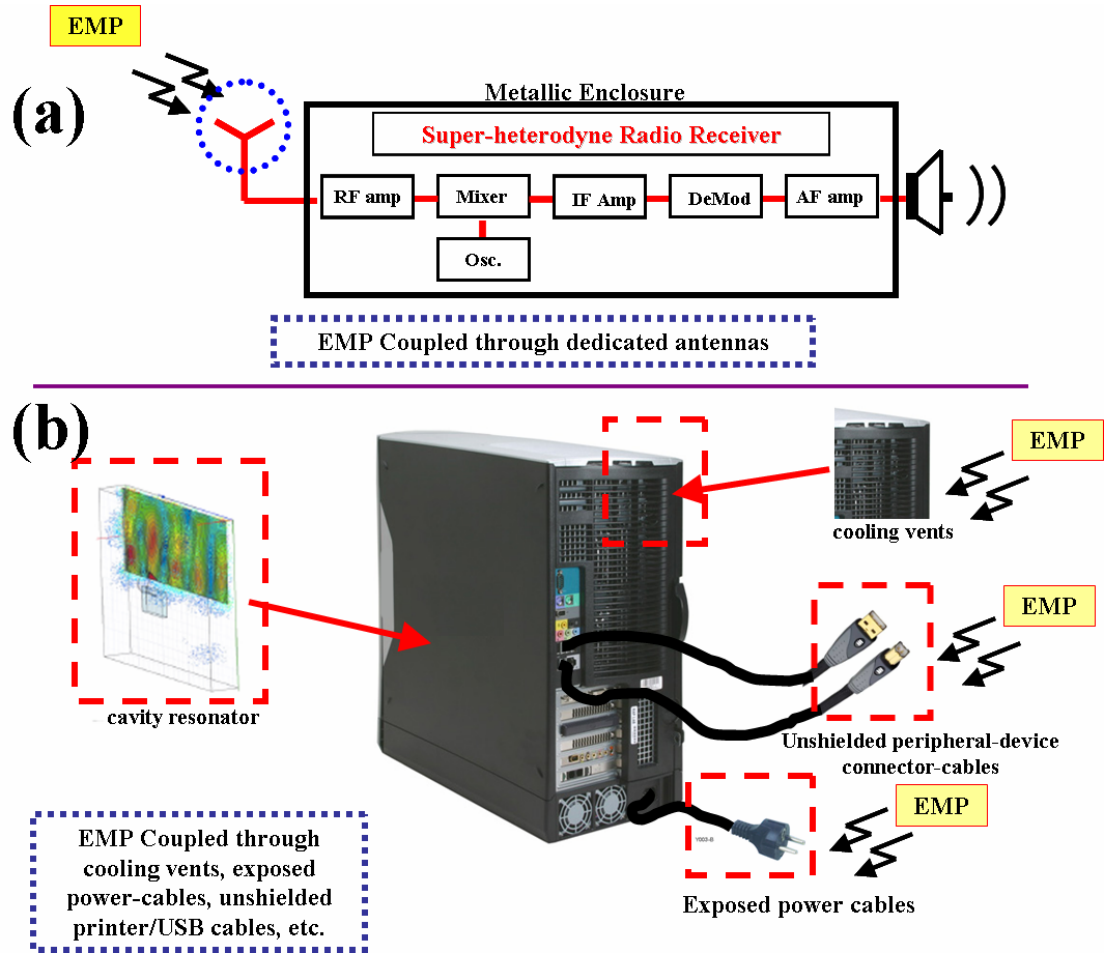

Fig. 1.1: (a) Schematic representation of a "Front Door" coupling attack for a super-heterodyne radio receiver where the EMP is coupled into the system through dedicated antennas. (b) Schematic representation of a "Back Door" coupling attack in a desktop-computer where the EMP is coupled into the system through exposed wiring, power cables, cavity resonance modes, etc.

Generally, nuclear-EMP (in the MHz range), couples well to wiring and cabling. HPM weapons that generate centimeter or millimeter wave-length radiation can produce a more elusive type of Back-Door Coupling attack. The small wavelength radiation can couple efficiently through small apertures, gaps between

panels and cooling vents which are commonly found on the metallic enclosures of most electronic systems. Under these conditions, the apertures on the enclosure act as slot-antennas allowing the electromagnetic energy to enter and directly excite resonances within the metallic enclosure which now acts like a microwave cavity. These resonances are high-order cavity-modes and have complicated standing wave patterns. Sensitive components situated near the anti-nodes of these modal patterns (commonly referred to as "hot spots") are then exposed to high and potentially lethal electromagnetic fields.

1.1 Need for Statistical Electromagnetism

On account of the wave (short-wavelength) nature of this radiation, coupling properties of the enclosure depend in great detail on its size and shape, the structure of the apertures that act as ingress or egress routes for the electromagnetic energy, and the frequency of the radiation. Moreover, the nature of the modal patterns within the enclosure is extremely sensitive to small changes in frequency, shape of the enclosure and orientation of the internal components. This is shown in Fig. 1.2(a) for a computer-box where the different components-connectors, cables, PC board, etc.- all of which interact with the incoming electromagnetic energy and produce a highly dynamic electromagnetic environment within the computer-box, as indicated by the frequency-dependent trend of the induced voltage (black squares in Fig. 1.2(b)) on the IC-pin lead (port 2). Minute changes in the shape of the enclosure, such as contractions or expansions due to ambient thermal fluctuations or the reorientation of an internal component, can result in totally different internal field patterns. This is

shown in Fig. 1.2, where the bending of the an internal power-cable shown as the dotted red line in Fig. 1.2(a), results in a drastic change in the nature of the induced voltage at port 2 (shown as the red circles in Fig. 1.2(b)). Thus, intimate knowledge of the electromagnetic response of the enclosure for one configuration will provide no information in predicting that of another nearly identical configuration.

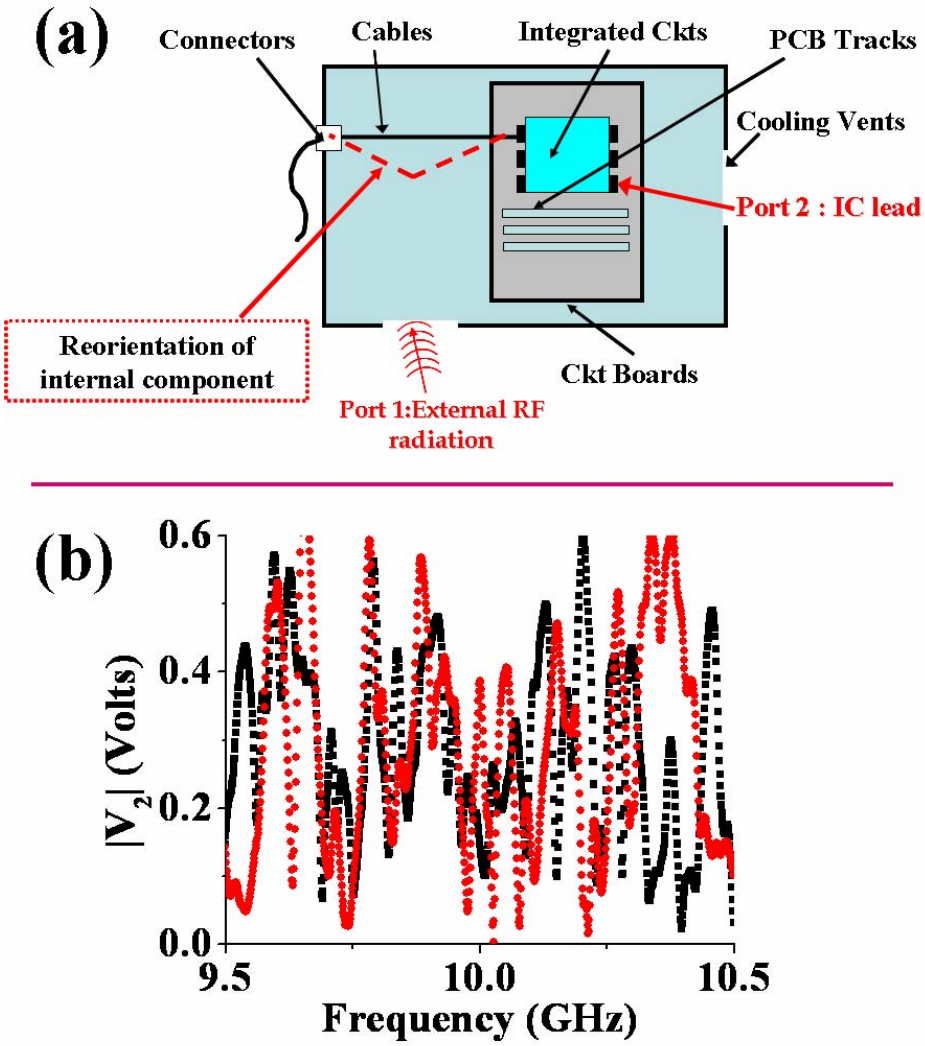

Fig.1.2: (a) Schematic of a computer box showing the inherent complexity associated with determining the induced voltage on an IC lead (port 2) for external electromagnetic radiation penetrating from a cooling vent (port 1). The different

components- connectors, cables, PC board, etc.- all interact with the incoming electromagnetic energy producing highly frequency-dependent voltage swings at port 2. (b) Measured induced voltage data on port 2 for a real computer-box with a set-up similar to that in (a). Note the drastic change in the induced voltage values for two slightly different orientations of an internal component (shown schematically as the black and dashed-red line in (a)).

Today, even with the availability of extremely fast and computationally powerful computers that utilize highly efficient 3-D electromagnetic-analysis algorithms, tackling a detailed problem as the one described above is still a challenge. Two major technical issues arise. Firstly is the problem of large "aspect-ratio"- which is defined as the ratio of the largest dimension to the smallest dimension in the problem. Most of these analysis-codes apply Maxwell's equations after meshing the entire geometry of the problem. For low frequencies (about 100 MHz), these codes have proven to be reliable for calculating internal electromagnetic radiated fields for large scale systems such as the fuselage of an airplane **[6]**. However, for attempting to solve the fields generated within the fuselage at higher frequencies (in the Giga-Hertz range), the entire geometry of the fuselage would have to be meshed at scales much smaller than the wavelength. Due to the large aspect-ratio (ratio of the typical length of the fuselage to the wavelength) associated with this problem, an impractically large number of mesh-points would be required thereby making such an approach infeasible.

The second difficulty arises from the extreme sensitivity of the internal field structure to the frequency, shape of the enclosure and orientation of the internal components, as previously explained. Thus, even if it were possible to obtain a deterministic assessment of the internal fields for one possible configuration (say for an airplane fuselage with the bomb-bay doors open), it is of limited use for assessing a slightly different configuration (when the bomb-bay doors are closed). One would thus have to resort to averaging over a large ensemble of such configurations in order to derive any meaningful assessment of the internal field structure. This would be outrageously expensive both in terms of time and computational resources. All these reasons call out for a statistical description to the problem of electromagnetic coupling and scattering in large, complicated enclosures.

Researchers in the field of "statistical electromagnetism" attempt to answer the fundamental question, "Given an electromagnetic environment and an electronic system, what is the probability that the system's performance will be unacceptably degraded?" **[7]**. Researchers then construct stochastic models based on certain fundamental assumptions for the fields within such complicated enclosures. They then validate the analytic predictions derived from their models with real-world measurements on systems enclosed within controlled, complicated enclosures known as "mode-stirred chambers" (Fig.1.3).

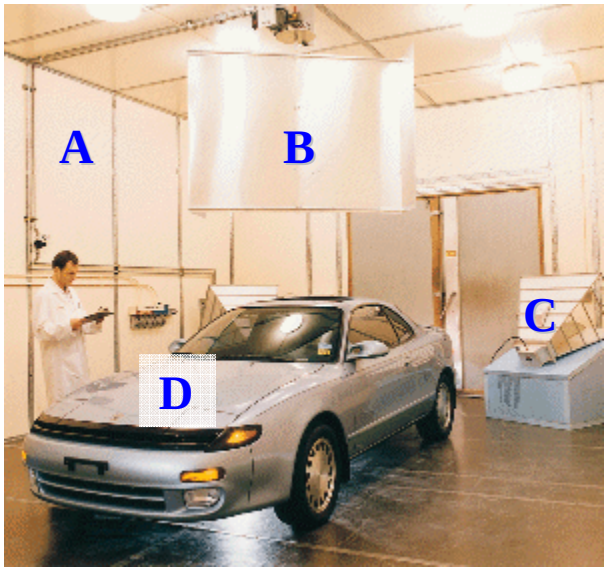

Fig. 1.3: Mode-Stirred Chamber (MSC) at Southwest Research Institute, San Antonio Texas, used for electromagnetic compatibility studies of automobile electronics. [A] Metallic side-walls of the MSC to create an over-moded, high Q environment. [B] Mode-Stirrer with large metallic panels which is rotated to create a statistically homogenous field intensity within the MSC.[C] Horn Antenna used to excite the MSC. [D] Device under test- (an automobile). Courtesy: www.swri.org.

Some of the main issues addressed so far in the field of statistical electromagnetism are: the probability distribution of fields at a point inside a highly over-moded mode-stirred chamber, the correlation function of fields at two points near each other, the statistics of the excitation of currents in cables and in small devices within the enclosure, and the quality factor (Q) of the chamber **[7, 8, 9, 10, 11, 12]**. In all of these studies, the antennas (ports) that drive the enclosure are assumed to be "perfectly coupled" (or "ideally coupled") to the enclosure. "Perfect coupling" refers to the situation in which an incoming wave on a driving port is

entirely transmitted into the enclosure (with no prompt reflection at the interface of the port and the enclosure). Any reflection that is then measured on this port is on account of the transmitted wave entering the enclosure, bouncing around, and subsequently returning to the same port. In Chapter 2, a more precise definition for "perfect coupling" will be given. Perfect coupling, however, is practically impossible to achieve experimentally for arbitrary port geometries and over arbitrarily large frequency ranges. Thus, there is a need for a statistical model that incorporates the effects of non-ideal coupling. One such model, called the "Random Coupling Model," will be elucidated in Chapter 2. The experimental validation of this model is the crux of my dissertation.

1.2 Wave Chaos

The coupling of high-frequency electromagnetic energy into complicated metallic enclosures falls within a larger class of similar problems previously encountered by physicists in the field of acoustics, mesoscopic transport and nuclear physics. All these systems comprise of short-wavelength waves (electromagnetic, acoustic or quantum mechanical) which are trapped within an irregularly-shaped enclosure or cavity, in the limit where the perimeter of the cavity is much larger than the wavelength. This limit is typically referred to "Ray Limit". In this limit, on account of the small wavelength, the waves within the enclosure can be approximated as rays which undergo specular reflections (i.e., angle of incidence equals the angle of reflection) off the walls of the enclosure, much like the trajectory of a Newtonian point-particle elastically bouncing inside a similar-shaped enclosure. Hence, such systems are also referred to as "Billiards".

It is thus intuitive that the dynamics of the rays within the enclosure depend on the shape of the enclosing boundaries. Typically, two types of ray-motion dynamics are possible, integrable or chaotic. A third type called "mixed dynamics" shows properties which are a combination of integrable and chaotic systems. Figure 1.4 shows two common billiard shapes (black outlines in Fig. 1.4). The square in Fig. 1.4(a) is known to be classically integrable - a point-particle elastically bouncing within the square will separately conserve the kinetic energies associated with its motion in the x and y direction. Figure 1.4 (b) shows a quarter-Sinai billiard, which is a symmetry-reduced version of a circle placed at the center of a square, and is known to be classically chaotic.

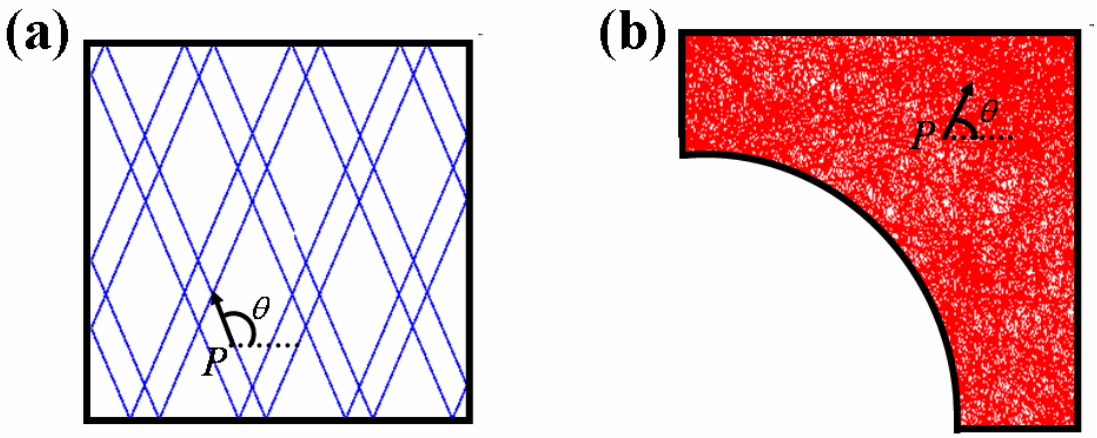

Fig. 1.4: (a) Trajectory (shown in blue) of a point-particle elastically bouncing inside a two-dimensional square billiard cavity. (b) Trajectory (shown in red) of a point-particle elastically bouncing inside a two-dimensional quarter-Sinai billiard cavity.

To observe a qualitative difference between the dynamics of these two systems, consider a particle initially placed at point P within the two enclosures. The points are picked at random with uniform probability density per unit area. Let v be the speed with which the particle is launched and θ be the angular orientation of the velocity vector with respect to the horizontal. The angle θ is chosen at random from a uniform distribution between 0 and 2π.

As the Mathematica simulation in Fig. 1.4 shows, the evolution of the trajectories of the two particles over the same duration in time, look very different. For the chaotic cavity (Fig. 1.4(b)), the velocity vector of the particle seems to sample all values of θ equally. It can be rigorously proved, that with probability one, the resulting chaotic trajectory will fill the cavity uniformly and isotropically. This is not the case for the square cavity in Fig. 1.4(a).

Another fundamental difference is that if two particles are launched with slightly different initial conditions (same or slightly different initial location, or slightly different angular orientations of their velocity vectors) but with the same speed v, the subsequent evolutions of the trajectories in the integrable and chaotic case are different. In both cases the trajectories separate from each other, but the separation is, on average, linear in time for the integrable case and exponential in time for the chaotic case for short time-scales. However, due to the finite system size constraint of the cavity, the trajectories may eventually come arbitrarily close or intersect each other as time progresses.

As suggested by Fig. 1.4, it is instructive to note that even very simple-shaped cavities can produce chaotic ray dynamics. This is of key significance for the problem

of short-wavelength electromagnetic coupling into enclosures. The inherent complexities associated with the boundary shape of the enclosure, say the inside of an airplane fuselage or the inside of a computer box, create a scenario which is highly conducive to the formation of chaotic dynamics for the rays within the enclosure. In fact, it does not take much to make a ray-chaotic enclosure. For instance, even a monopole antenna of diameter (d) radiating inside a perfectly cuboidal chamber (classically integrable system) will lead to ray-chaos if the wavelength of the radiation (λ) is of the order of the diameter of the antenna (i.e., $\lambda \approx d$) (see **[13]** for a 2-D version of this example**)**.

The study of such wave-systems, in the ray-limit or short-wavelength limit, that exhibit chaotic ray dynamics is widely known as "Wave Chaos" or, equivalently, "Quantum Chaos," when referring to quantum-mechanical wave systems such as atomic nuclei or mesoscopic condensed-matter systems.

1.3 Universal Aspects of Wave-Chaotic Systems

Figure 1.5 (a) shows a typical reflection spectrum for a wave-chaotic microwave cavity in the shape of a quarter bow-tie (inset). In Fig. 1.5(b), the typical reflection spectrum for an integrable microwave cavity in the shape of a rectangle (inset) is shown. Each minimum in the reflected microwave power corresponds to a resonator eigenfrequency. At first glance, the two spectra look totally haphazard and seemingly convey no relevant information about the two cavities.

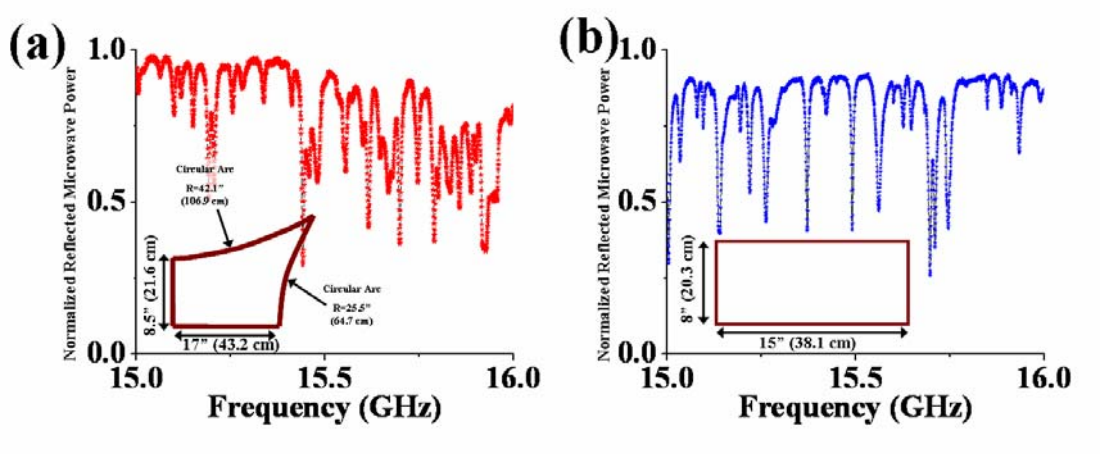

Fig. 1.5: (a) Normalized reflected power spectra for a quarter bow-tie cavity. The shape of the wave-chaotic cavity is shown in inset. (b) Normalized reflected power spectra for a rectangular cavity. The shape of the integrable cavity is shown in inset.

In the 1950s, Eugene Wigner **[14]** was confronted with a similar problem when studying the energy levels of large complicated nuclei. Just as in Fig. 1.5, the energy level density for a nucleus at high energies is rather dense. Wigner thus proposed a statistical formalism to extract information from these complicated looking spectra. He defined a normalized nearest neighbor eigenfrequency spacing (ε) which was expressed as $\varepsilon = (k_{n+1}^2 - k_n^2)/(\Delta k_n^2)$, where k_n is the wavenumber corresponding to the n^{th} eigenfrequency and Δk_n^2 represents the mean-spacing between the eigenlevels (i.e., $\Delta k_n^2 = \langle k_{n+1}^2 - k_n^2 \rangle$). In the limit that the wavelength is small compared to the perimeter of the cavity and n is large ($n >> 1$), the mean-spacing Δk_n^2, as given by the Weyl formula **[15]**, depends upon the physical dimensions of the cavity. For a quasi-two-dimensional cavity such as the ones shown in Fig. 1.5, $\Delta k_n^2 \cong 4\pi / A$, where A is the enclosed area of the cavity. For a three-

dimensional electromagnetic cavity, $\Delta k_n^2 \cong 2\pi^2/(kV)$, where V is the enclosed volume of the cavity. There are higher-order corrections terms to Δk_n^2 that depend upon the perimeter (2D) or surface area (3D) of the cavity **[16]**, but their contribution can be neglected in the limit where the wavelength is much smaller than the typical size of the enclosure.

Wigner discovered that the probability density function (PDF) of the normalized nearest neighbor eigenfrequency spacing (ε) for different atomic nuclei followed certain universal curves depending only upon whether the quantum-mechanical wave-dynamics within the nuclei was integrable or chaotic (Fig.1.6). i.e.,

$$P(\varepsilon) \quad \begin{cases} = & Exp[-\varepsilon] & (Poisson)-Integrable \\ \cong & \frac{\pi}{2}\varepsilon Exp[-\frac{\pi\varepsilon^2}{4}] & (TRS)-Chaotic \\ \cong & \frac{32}{\pi^2}\varepsilon^2 Exp[-\frac{4\varepsilon^2}{\pi}] & (BTRS)-Chaotic \end{cases}, \qquad (1.1)$$

where TRS corresponds to systems with Time Reversal Symmetry and BTRS corresponds to systems with Broken Time Reversal Symmetry, and will be explained in the following section.

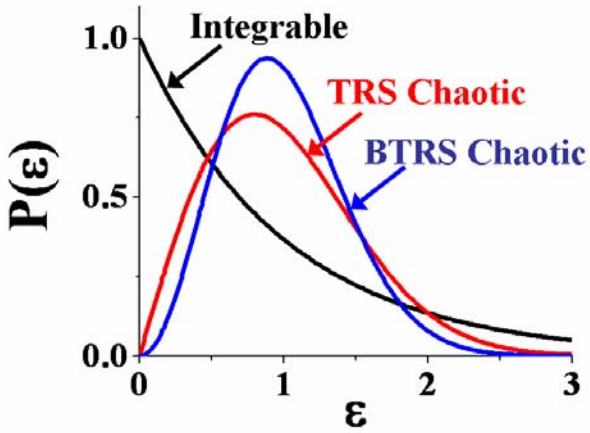

Fig. 1.6: Wigner distributions for the normalized eigenlevel spacing for three classes of systems (Integrable: black, TRS chaotic: red, BTRS chaotic: blue). The mean-spacing is normalized to 1. Note that for integrable systems $P(\varepsilon)$ peaks at $\varepsilon = 0$, implying a large number of degenerate energy states in such systems. For TRS-chaotic systems, $P(\varepsilon)$ is linear in ε for small ε; while for BTRS-chaotic systems, $P(\varepsilon)$ is quadratic in ε for small ε. In both TRS and BTRS cases, $P(\varepsilon) = 0$ at $\varepsilon = 0$, implying the absence of degenerate energy states in such chaotic systems.

In order to derive these results, Wigner formulated a novel statistical theory known as "Random Matrix Theory." Later, in the 1980s, Bohigas **[17]** and MacDonald **[18]** conjectured that Random Matrix Theory should be applicable to generic wave-chaotic systems (electromagnetic, acoustic, mesoscopic, etc.) in addition to complicated nuclei. The distributions shown in Fig. 1.6 are known as "Wigner Distributions" and have now been validated with experimental results for electromagnetic systems (as in Fig. 1.5) **[13]**, acoustic systems **[19, 20]** and quantum-

mechanical metal-cluster systems **[21]**, thereby bolstering the conjecture that Random Matrix Theory is applicable to all generic wave-chaotic systems.

1.4 Random Matrix Theory

A truly remarkable aspect of wave-chaotic systems is that despite their apparent complexity, they all possess certain universal statistical properties (such as the normalized nearest neighbor eigenfrequency spacing distributions described in Section 1.3). This seems to suggest that the dynamics of the system are governed, in a qualitative way, by the symmetry of the system and not by the details of the interactions within the cavity. Depending upon the symmetry of the system, Wigner uncovered three types of wave-chaotic systems: (i) systems with Time Reversal Symmetry (TRS), (ii) systems with Broken Time Reversal Symmetry (BTRS) and, (iii) TRS systems with spin-1/2 interactions.

In the case of electromagnetic wave-chaotic systems, only TRS and BTRS wave-chaotic systems are of interest. TRS systems comprise of electromagnetic-wave systems in which the medium within the cavity is characterized by real, symmetric permittivity and permeability tensors. Under these conditions the properties of an electromagnetic-ray, bouncing around inside the wave-chaotic cavity, are unaffected by the reversal of time (or equivalently, by reversing its direction of propagation). For such systems, the time-domain dynamical equations of the wave-system are invariant under $t \to -t$. BTRS systems, on the other hand, are those in which the medium within the cavity possesses asymmetric permittivity and permeability tensors with complex off-diagonal elements. Under these conditions, the presence of the off-diagonal terms leads to a phase-difference (possibly also a different ray-trajectory)

between the time-forward and time-reversed paths for a bouncing ray that are not equal and opposite, and results in the time-domain dynamical wave-equation becoming complex. BTRS systems can be realized by the introduction of a magnetized ferrite **[22]**.

Wigner hypothesized that the eigenvalue spectrum of these complicated wave-chaotic systems would be statistically similar to the spectra of ensembles of random matrices. Denoting one such random matrix as $\vec{\vec{H}}$, Wigner further hypothesized that two statistical conditions on the probability distribution of these random matrices ($P(\vec{\vec{H}})$) must be satisfied,

(i) the elements of the random matrices (H_{ij}) should be independent random variables, and

(ii) for random matrices describing TRS systems, the probability distribution of the ensemble of random matrices ($P(\vec{\vec{H}})$) should be invariant under orthogonal transformations, i.e, $P(\vec{\vec{H}}') = P(\vec{\vec{O}}\vec{\vec{H}}\vec{\vec{O}}^T)$, where $\vec{\vec{O}}$ is any orthogonal matrix with $\vec{\vec{O}}\vec{\vec{O}}^T = \vec{\vec{1}}$ ($\vec{\vec{O}}^T$ is the transpose of $\vec{\vec{O}}$).

For random matrices describing BTRS systems, $\vec{\vec{H}}$ is a complex Hermitian matrix and the probability distribution of the ensemble of random matrices ($P(\vec{\vec{H}})$) should be invariant under unitary transformations, i.e, $P(\vec{\vec{H}}') = P(\vec{\vec{U}}\vec{\vec{H}}\vec{\vec{U}}^{\dagger})$, where $\vec{\vec{U}}^{\dagger}$ is any unitary matrix with $\vec{\vec{U}}\vec{\vec{U}}^{\dagger} = \vec{\vec{1}}$ ($\vec{\vec{U}}^{\dagger} = \vec{\vec{U}}^{-1}$).

These two conditions imply that for TRS systems the distribution of the elements of the random matrix ($\ddot{H}$) are all independent-identically-distributed (i.i.d) real Gaussian random variables. The variance of the on-diagonal elements are equal and twice the variance of the off-diagonal elements. This specifies the Gaussian Orthogonal Ensemble (GOE) of random matrices for TRS wave-chaotic systems. For BTRS systems, each real on-diagonal element of the random matrix ($\ddot{H}$) is an i.i.d Gaussian random variable. The upper-diagonal elements are complex with real and imaginary parts being i.i.d Gaussian distributed each with a variance equal to that of the on-diagonal elements. The lower-diagonal elements are complex-conjugates of the corresponding upper-diagonal elements. This specifies the Gaussian Unitary Ensemble (GUE) of random matrices for BTRS wave-chaotic systems. There is a third Gaussian ensemble (Gaussian Symplectic Ensemble) which specifies TRS systems with spin-1/2 interactions, but it will not be discussed in this dissertation.

Using these Gaussian ensembles, several analytic predictions for the statistical properties of wave-chaotic systems have been derived **[23, 24]**. The "Random Coupling Model" of Chapter 2 is one such model that makes several statistical predictions for the scattering of short-wavelength waves inside wave-chaotic cavities based upon Random Matrix Theory and the assumption that it applies to real-world complicated electromagnetic enclosures.

1.5 Outline of the Dissertation

The objective of my research is to experimentally validate a statistical model called the "Random Coupling Model" (RCM), which will be introduced in Chapter 2.

This model makes use of certain aspects from Random Matrix Theory and the description of the eigenvalues and eigenfunctions of wave-chaotic systems to build up a statistical theory for the universal impedance, admittance and scattering fluctuations in wave-chaotic systems. The model has the potency to incorporate the non-ideal coupling between the ports and the cavity for arbitrary port geometries and over arbitrarily large frequency ranges. Most of my experiments will be performed on a quasi-two-dimensional quarter bow-tie shaped microwave cavity, which is known to be wave-chaotic and the experimental setup will be introduced in Chapter 3. The motivation to use a quasi-two-dimensional microwave cavity follows from the mathematical equivalence of the Helmholtz wave-equation for the electric field inside the quasi-two-dimensional microwave cavity, and the time-independent Schrödinger equation for the wave-function of a quantum-mechanical particle within a potential well, subject to the same boundary conditions. This equivalence broadens the applicability of my experimental results to include the scattering fluctuations in quantum-chaotic systems (atomic nuclei, quantum dots, quantum corrals, etc.) as well.

My dissertation can be broadly divided into two parts. In the first part (comprising of Chapters 4, 5, 6 and 7), my objective is to validate the statistical predictions of the Random Coupling Model for a time-reversal symmetric, quasi-two-dimensional wave-chaotic cavity driven by one or two ports (Fig. 1.7(a)). Here, I will show conclusively the efficacy of the model that allows one to take measurements on a driven wave-chaotic cavity, filter out the effects of non-ideal coupling between the driving ports and the cavity by means of a simple "radiation impedance"

normalization process (to be introduced in Chapter 2), and thereby uncover the universal fluctuating aspects of the impedance, admittance and scattering properties of these systems. These universal fluctuations will then be compared with theoretical predictions from Random Matrix Theory.

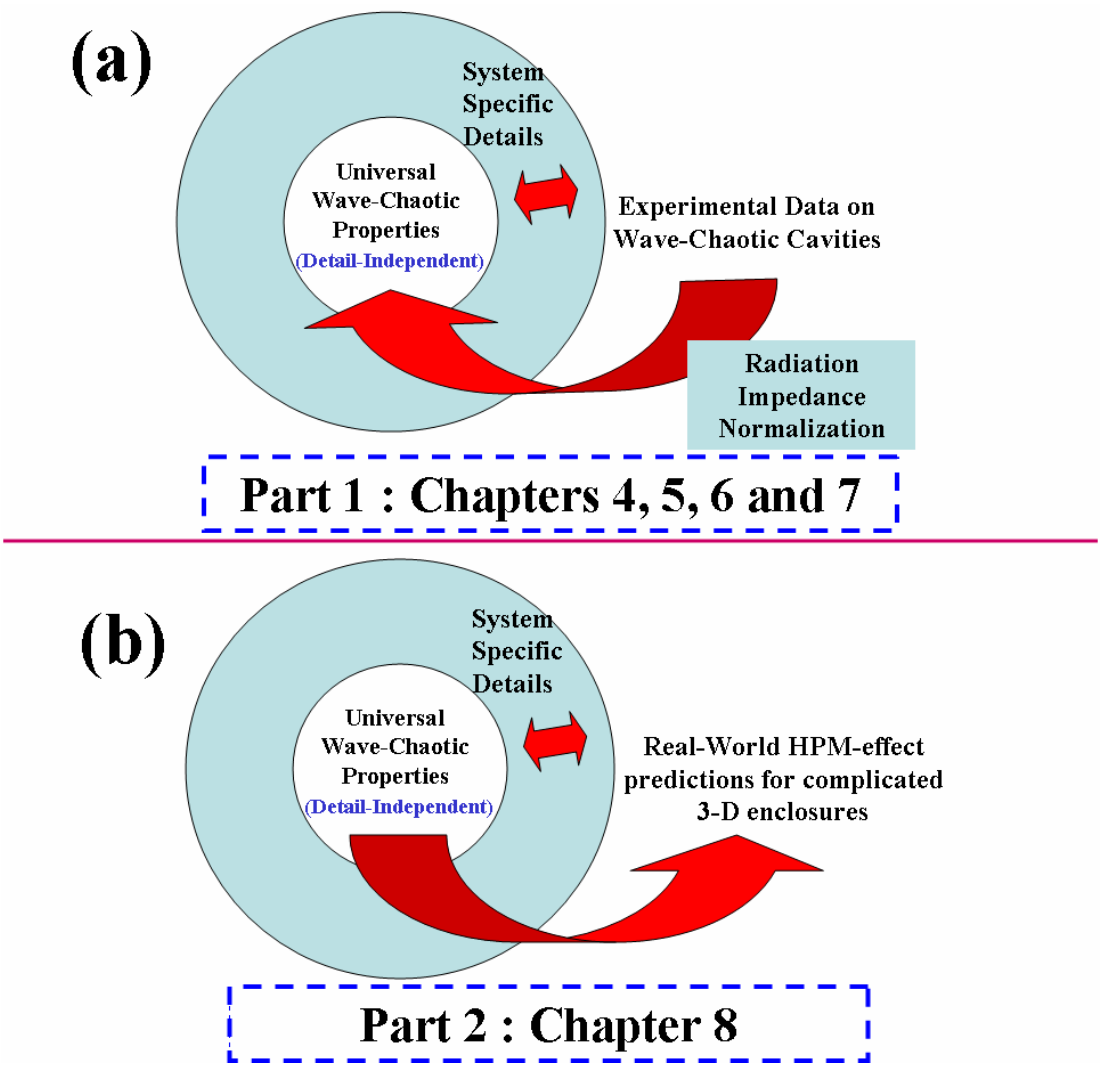

Fig.1.7: Schematic depicting my dissertation outline.

The second part of my dissertation mainly comprises of Chapter 8. Here, I will experimentally prove that real-world complicated enclosures such as computer-

boxes do indeed exhibit chaotic scattering ray-dynamics. In doing so, I will also show the applicability of the Random Coupling Model to three-dimensional cavities and mode-stirred chambers. My objective in that chapter will be to use the Random Coupling Model to make explicit *a priori* predictions for the Probability Density Functions (PDF) of induced-voltages at specific target points within the computer box for arbitrary types of excitation at a source port (corresponding to different back-door coupling attack scenarios) (Fig. 1.7(b)).

More specifically, my dissertation is outlined as follows:

- Chapter 2: The "Random Coupling Model," put forward by Zheng, Antonsen and Ott **[25, 26],** will be introduced and its salient features and predictions discussed. The Random Coupling Model introduces a novel "radiation impedance" normalization process. This allows one to separate the system-specific and detail dependent aspects of the scattering (brought about due to the non-ideal coupling between the port and the cavity) from the measured experimental data, and uncover the universal fluctuations in the impedance, admittance and scattering properties of wave-chaotic systems.
- Chapter 3: The experimental setup for the quasi-two-dimensional quarter-bow-tie shaped wave-chaotic microwave cavity drive by one or two ports is introduced, and the procedure of data-acquisition and analysis is explained.
- Chapter 4: The practicality of the "radiation impedance" normalization process will be experimentally tested for different wave-chaotic cavities

driven by different port-coupling geometries. Experimental validation of the predictions of the "Random Coupling Model" for the universal impedance and scattering fluctuations in a quasi-two-dimensional, quarter-bow-tie shaped wave-chaotic cavity driven by a single port will be discussed.

- Chapter 5: Experimental validation of the predictions of the "Random Coupling Model" for the universal impedance, admittance and scattering fluctuations in the eigenvalues of a quasi-two-dimensional, quarter-bow-tie shaped wave-chaotic cavity driven by two ports will be discussed.
- Chapter 6: The Schrödinger-Helmholtz analogy is used to treat the quarter-bow-tie shaped wave-chaotic microwave cavity as a surrogate for ballistic quantum-dots and thereby explore the universal fluctuations in the conductance of these mesoscopic condensed-matter systems in the presence of quantum-decoherence. An empirical linear relationship will be derived that relates the ohmic loss-parameter within a microwave cavity to the degree of incoherent electron-transport through a ballistic quantum-dot.
- Chapter 7: Statistical aspects concerning certain key universal relationships, known as Hauser-Feshbach relations, between the elements of the impedance and scattering matrices of wave-chaotic systems will be experimentally studied.
- Chapter 8: Experimental validation of the applicability of the "Random Coupling Model" for a real-world, three-dimensional complicated

enclosure (a computer box) will be discussed. Based upon the universal wave-chaotic scattering and impedance fluctuations derived from the Random Coupling Model, a prediction algorithm for the probability density function of induced-voltages within such enclosures for a given electromagnetic stimulus will be formulated and experimentally validated. A series of "bottom-line" lessons deduced from the Random Coupling Model which is applicable to the design of real-world systems (such as a computer box) which are more resistant to HPM attack is also discussed.

- Chapter 9: A summary of the results discussed in this dissertation and a discussion of the possible future work is included.

Chapter 2: The Random Coupling Model

The scattering of short-wavelength waves inside enclosures manifests itself in several fields of physics and engineering such as quantum dots **[27]**, atomic nuclei **[28]**, acoustic resonators **[19, 20]**, electromagnetic compatibility **[7],** etc. Of particular interest is the case when the ray trajectories within the enclosure show chaotic ray-dynamics. This interest has spawned the field of "wave chaos" (or "quantum chaos"), and has attracted much theoretical and experimental work **[23, 24]** to understand its nature. On account of the small wavelength of the scattered waves, as compared to the characteristic length-scale of the enclosure, the response of these systems exhibit extreme sensitivity to small changes in configuration, driving frequency, nature of driving ports, ambient conditions such as temperature, etc. Thus, an intimate knowledge of the response of any such system for a given well-defined stimulus or system configuration will not provide any foresight in predicting the response of a similar system when the stimulus or system configuration is slightly altered. This calls for a statistical approach to quantify the nature of such wave-chaotic systems.

In this regard, Random Matrix Theory **[23]** has proved to be an integral tool in predicting universal statistical aspects of wave chaotic systems. It has been conjectured that in the short-wavelength regime, Random Matrix Theory can be used to model wave-chaotic systems **[14, 17, 18]**. In particular, the statistics of systems that show Time-Reversal Symmetry (TRS) are conjectured to be described by the Gaussian Orthogonal Ensemble (GOE) of random matrices, while the statistics of systems showing Broken Time-Reversal Symmetry (BTRS) are conjectured to be described by the Gaussian Unitary Ensemble (GUE) of random matrices. There is

also a third random matrix ensemble corresponding to certain systems with spin-interactions (Gaussian Symplectic Ensemble). Random Matrix Theory provides a potential framework for uncovering universal statistical properties of short-wavelength wave-chaotic systems (e.g. Ericson fluctuations in nuclear scattering **[13, 29]** and universal conductance fluctuations (UCF) in quantum-transport systems **[30]**- see Chapter 5 **)**.

Since the applicability of Random Matrix Theory and the concomitant universal statistics is conjectural rather than rigorous, and since this conjectured applicability is said to be asymptotic in the limit of wavelength small compared to the system size, it is important to test the Random Matrix Theory conjecture against results obtained for specific real situations.

2.1 Motivation for the "Random Coupling Model"

Experimentally, however, validating the applicability of Random Matrix Theory has always proved challenging. One of the most common problems encountered by experimentalists is the presence of non-universal, system-specific artifacts introduced into the measured data by the experimental apparatus. These are generally referred to as the "direct processes", as opposed to the "equilibrated processes" which describe the chaotic scattering within the system **[31]**. A typical example presents itself while measuring the statistical fluctuations in the scattering of microwaves through cavities with chaotic ray dynamics. These fluctuations are studied by exciting the cavity through coupled ports (coaxial transmission lines or waveguides) and observing the response (reflection and transmission) for a given

excitation. Generally, it is not possible to perfectly couple (ideally match) the ports to the cavity at all frequencies. Thus, there is generally a deviation from perfect coupling, which I refer to as "mismatch". This mismatch, which is strongly determined by the geometry of the port, manifests itself as systematic fluctuations in the measured data. The result is that the measured data depends on the non-universal, direct processes of the ports, as well as the underlying universal, equilibrated processes of the chaotic scattering system.

Figure 2.1 (a) is a schematic diagram of a waveguide coupled to a wave-chaotic cavity and is used to demonstrate the mechanism of non-ideal port-coupling. The solid blue arrow represents a wave propagating along the waveguide and entering the cavity. On account of the impedance (potential) mismatch at the interface of the cavity and the coupled waveguide, a prompt reflection of the incoming wave is observed (indicated as the solid red arrow). This constitutes the "direct process" and is dependent upon the geometry of the waveguide, the frequency of the incoming wave and the structure of the cavity side-walls near the interface of the waveguide and the cavity. Thus only a fraction of the incident energy of the incoming-wave is transmitted into the cavity, wherein it experiences chaotic-scattering ray-dynamics ("equilibrated scattering process") before returning to the waveguide. The measured response of the cavity as seen through the open-end of the waveguide is thus a complicated function of the direct-process as well as the equilibrated-process.

In Fig. 2.1(b), the effects of non-ideal port coupling are shown on actual measured data for the wave-scattering in a wave-chaotic cavity coupled to a single port. The cavity is in the shape of a quasi-two-dimensional quarter-bow-tie (inset (ii))

excited by a single port which is a section of a coaxial transmission line with the inner conductor (of diameter 2a) extending from the top-plate of the cavity and making contact with the bottom-plate (inset (i)). Two metallic perturbations shown as the gray rectangles in inset (ii) (roughly the size of the wavelength at 5GHz) are systematically scanned and rotated through one-hundred positions within the volume of the cavity. For each position of the perturbations, the cavity reflection coefficient ($|S|^2$) is measured as a function of frequency from 6 to 11.85 GHz. The stars in Fig. 2.1(b) represents the Probability Density Function (PDF) of the measured ensemble of the cavity reflection coefficient ($|S|^2$) for a driving port with $2a = 1.27mm$. The circles represents the PDF of the measured ensemble of the cavity reflection coefficient ($|S|^2$) for a driving port with $2a = 0.635mm$. Although the measurements are performed on the same wave-chaotic cavity, note the significant disparity in the two measured PDFs due to the difference in the port-coupling geometry.

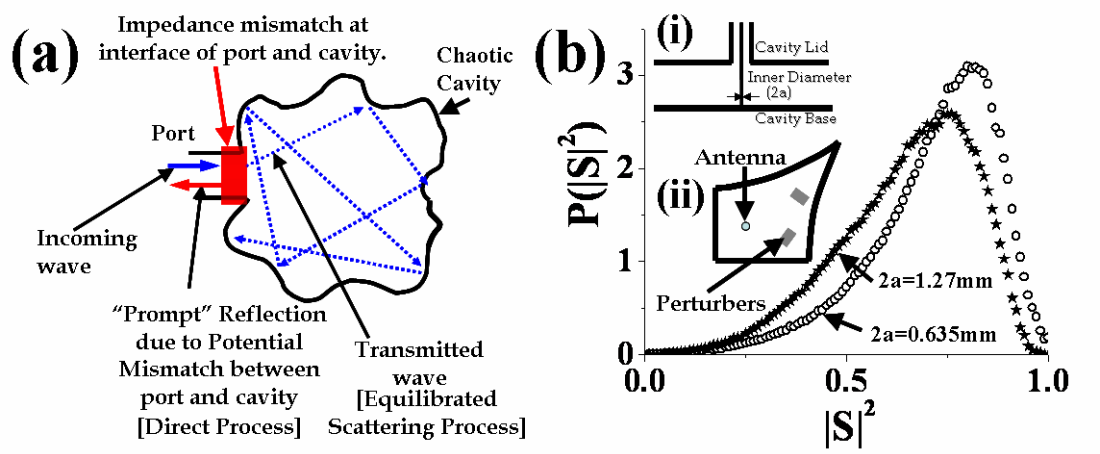

Fig. 2.1: (a) The mechanism of non-ideal coupling between the driving port and wave-chaotic cavity. (b) Probability Density Function (PDF) of the measured ensemble of the cavity reflection coefficient ($|S|^2$) for a wave-chaotic cavity (inset (ii)) which is driven by a single port (inset (i)) with inner-conductor diameter of 2a=1.27mm (stars) and 2a=0.635mm (circles). Note the difference in the measured PDFs for the same wave-chaotic cavity when only the inner-diameter (2a) of the driving port has been changed.

Several approaches have been formulated to account for these direct processes **[32, 33, 34]** of which the "Poisson Kernel" approach introduced by Mello, Pereyra and Seligman is of special mention. Based on an information-theoretic model, the "Poisson Kernel" characterizes the direct processes between the ports and the cavity by the ensemble-averaged scattering matrix $<< \vec{\vec{S}} >>$. In order to apply this theory to a specific real situation, it is thus necessary to obtain a quantity that plays the role of the ensemble average $<< \vec{\vec{S}} >>$ appropriate to that specific system. For example, one scheme proposed for determining such a surrogate for $<< \vec{\vec{S}} >>$ for a specific system

used system configuration averaging. I denote this surrogate for $<<\vec{S}>>$ as $<\vec{S}>$. Averaging over configurations, however, may suffer from excessive statistical error if the number of configurations averaged over is insufficiently large. Thus, to improve the estimate of the scattering coefficient statistics, Refs. **[35, 36]**, which treat one port (scalar S) scatterers, make use of an ergodic hypothesis **[37, 38]** to include an additional running average over frequency ranges that include many resonances, but are sufficiently small that the scattering coefficient statistics can be assumed to be nearly constant (i.e., a frequency range where the port coupling strengths are nearly constant). Using this approach, Refs.**[35, 36]** have investigated the universal fluctuations in the reflection coefficient of 1-port wave-chaotic microwave cavities. This was shown to produce favorable results for 1-port systems when compared with Random Matrix Theory predictions. We note, however, that the analysis is highly dependent on the accuracy of the experimentally-obtained $<S>$, which is prone to statistical errors.

The situation can become even more complicated when dealing with N ports. In the recent 2-port paper by H. Schanze *et.al.* Ref. **[39]**, the authors circumvent such problems by taking careful steps to ensure that the driving ports are nearly perfectly-coupled to the cavity in the frequency range where the data is analyzed. In doing so, Ref. **[39]** achieves good agreement between the experimental results for the fluctuations in the transmission coefficient, and the Random Matrix Theory predictions for time-reversal-symmetric and for broken-time-reversal-symmetric cavities. Note, however, that Ref. **[39]** is for the case of perfectly coupled ports and that it is desirable to also deal with arbitrary port couplings.

2.2 Formulating the "Random Coupling Model"

In Ref. **[25, 26]** a novel method to characterize the direct processes between the cavity and the driving ports was introduced. This method, which is motivated by electromagnetic-wave propagation inside complex enclosures, makes use of impedances to characterize the direct-processes rather than the ensemble-averaged scattering matrix as in Ref. **[32]**. For a N-port scattering system, the Scattering Matrix $\vec{\vec{S}}$ models the scattering region of interest in terms of a NxN complex-valued matrix. Specifically, it expresses the amplitudes of the N outgoing scattered waves ($\widetilde{b}$) in terms of the N incoming waves ($\widetilde{a}$) at the location of each port (i.e., $\widetilde{b} = \vec{\vec{S}}\widetilde{a}$). The impedance matrix $\vec{\vec{Z}}$, on the other hand, is a quantity which relates the complex voltages ($\widetilde{V}$) at the N driving ports to the complex currents ($\widetilde{I}$) in the N ports (i.e. $\widetilde{V} = \vec{\vec{Z}}\widetilde{I}$). The matrices $\vec{\vec{S}}$ and $\vec{\vec{Z}}$ are related through the bilinear transformation, $\vec{\vec{S}} = \vec{\vec{Z}}_o^{\,1/2}(\vec{\vec{Z}} + \vec{\vec{Z}}_o)^{-1}(\vec{\vec{Z}} - \vec{\vec{Z}}_o)\vec{\vec{Z}}_o^{\,-1/2}$ where $\vec{\vec{Z}}_o$ is the NxN real, diagonal matrix whose elements are the characteristic impedances of the waveguide (or transmission line) input channels at the N driving ports. Like $\vec{\vec{S}}$, $\vec{\vec{Z}}$ is also a well-established physical quantity in quantum mechanics. Just as the elements of $\vec{\vec{S}}$ represent the transition probabilities from one state to the other in a quantum scattering system, $\vec{\vec{Z}}$ is an electromagnetic analog to Wigner's Reaction Matrix **[40]**, which linearly relates the wave function to its normal derivative at the boundary separating the scattering region from the outside world.

For a cavity driven by a single port, **[25]** has shown that the frequency-dependent, complex-scalar cavity impedance (Z) can be written as an expansion over the M modes of the cavity as,

$$Z(k) = -\frac{j}{\pi}\sum_{n=1}^{M}\Delta k_n^2 \frac{R_R(k_n)w_n^2}{k^2(1-j/Q_{ul})-k_n^2} \ . \tag{2.1}$$

Here, $k = 2\pi f / c$ is the wavenumber for the incoming frequency f and Δk_n^2 is the mean-spacing of the adjacent eigenvalues of the Helmholtz operator, $\nabla^2 + k^2$. The quantity Q_{ul} represents the unloaded quality-factor of the cavity, and accounts for the losses within the cavity (dielectric losses, ohmic losses, etc.) excluding the dissipation through the port. The term, w_n represents the coupling between the port and the n^{th} eigenmode of the cavity, and is modeled as a Gaussian random number of zero mean and unit variance. This implicitly assumes two fundamental aspects of the wave-scattering process within the cavity,

(i) The cavity is over-moded ($M >> 1$). This means that there are many modes with k_n in the narrow interval δk centered at k (where $\Delta k_n^2 << (\delta k)^2 << k^2$), and if one of these modes is chosen at random, then its properties can be described by a statistical ensemble.

(ii) The eigenfunctions of the cavity satisfy the "Random Plane Wave Hypothesis".

Both these assumptions are generally applicable for wave-chaotic systems, where the wavelength is much smaller than the typical size of the cavity.

The "Random Plane Wave" hypothesis essentially states that the fields within a wave-chaotic cavity, in a statistical sense, behave like a random superposition of

isotropically propagating plane waves. The underlying basis for this hypothesis follows from the observation that ray trajectories in such chaotic systems, like the quarter-Sinai billiard of Fig. 1.4(b), are uniform in space and isotropic in direction. This has been well established numerically **[18]** as well as experimentally for quasi-two-dimensional microwave resonators **[41]** and for 3-D mode-stirred chambers **[10,11]**. This same hypothesis has also been used for plasma waves **[42]** and for quantum-chaotic systems **[43]**.

The term $R_R(k_n)$ incorporates the non-ideal coupling between the port and the cavity, and deserves special mention. If the cavity in Eq. (2.1) is driven by the same port (having the same coupling geometry) as before, but has the distant side-walls moved out to infinity (or coated with a material that perfectly absorbs the incident waves), then the port behaves as a free-space radiator. The boundary conditions corresponding to the outgoing waves, introduce a complex scalar impedance (Z_{rad}) known as the "radiation impedance" (or "terminal impedance") at the plane of measurement for the driving-port. For this radiation-boundary condition, the cavity-eigenvalues (k_n) now form a continuum with the impedance of the driven cavity being written as,

$$Z_{rad}(k) = \frac{-j}{\pi} \int_0^\infty \frac{dk_n^2}{k^2 - k_n^2} R_R(k_n) \,. \tag{2.2}$$

The evaluation of the contour-integral in Eq.(2.2) results in $R_R(k) = \mathrm{Re}[Z_{rad}(k)]$, which is known as the "radiation resistance" of the driving port and quantifies the energy dissipated in the far-field of the radiating port. The "radiation reactance," which arises from the energy stored in the near-field of the

radiating port, is determined by a Kramers-Kronig relation **[44]** for $R_R(k)$, and yields $X_R(k) = \mathrm{Im}[Z_{rad}(k)]$. The near-field structure of the port is determined by the geometry of the coupling port. The radiation impedance, Z_{rad}, is thus a non-statistical, smoothly-varying frequency-dependent quantity which accurately incorporates the detail-specific aspects of the coupling between the port and the cavity for any port geometry.

The final step in building up a statistical model for the cavity impedance assumes the applicability of Random Matrix Theory to such wave-systems. Rather than determining the exact values corresponding to the eigenvalues (k_n^2) of the wave-chaotic cavity, it can be described in a statistical sense with random numbers drawn from an appropriate Gaussian ensemble (GOE or GUE), depending upon the symmetry of the system (TRS or BTRS, respectively). This results in a robust framework, called the "Random Coupling Model" for the impedance and scattering properties of driven wave-chaotic cavities, wherein the system-specific aspects ("direct processes") of the scattering are accurately quantified by the radiation impedance of the driving port and the universal aspects ("equilibrated processes") are described in a statistical fashion by Random Matrix Theory.

2.3 The "Radiation Impedance" normalization process

Terms in the summation of Eq. (2.1) for which k^2 is close to k_n^2, either due to the choice of k^2 or the different realizations of the random numbers representing k_n^2, give rise to large fluctuations in the cavity impedance Z. The terms for which k^2 is

far from k_n^2 will contribute to the mean value of Z. Thus, the cavity impedance can be written as,

$$Z = \langle Z \rangle + Z_{fluc}, \tag{2.3}$$

where $\langle Z \rangle$ represents the mean value of the cavity impedance Z; and Z_{fluc} represents the fluctuating parts of the cavity impedance Z.

Reference **[25]** has shown that, for a cavity driven by a single port, the mean part of the cavity impedance($\langle Z \rangle$) is given by the radiation reactance of the driving port, and the fluctuating part(Z_{fluc}) comprises of a universal fluctuating quantity (called z) which is scaled by the radiation resistance of the driving ports. Thus,

$$Z = j\,\mathrm{Im}[Z_{rad}] + z\,\mathrm{Re}[Z_{rad}]\ . \tag{2.4}$$

The universal fluctuating quantity (z), is theorized to be described by Random Matrix Theory, and describes the scalar cavity impedance of a cavity which is perfectly coupled to its driving port (i.e., $Z_{rad} = Z_0$, where Z_0 is the characteristic impedance of the transmission line connected to the port). The real part of z is well known in solid state physics as the local density of states (LDOS) and its statistics have been studied **[45, 46]**. The imaginary part of z determines fluctuations in the cavity reactance. Equation (2.4) thus suggests a simple normalization process to uncover the universal fluctuations (Probability Density Functions of z) in the measured cavity impedance of wave-chaotic cavities (as explained in Fig. 2.2). The quantity z will henceforth also be referred to as the "normalized impedance."

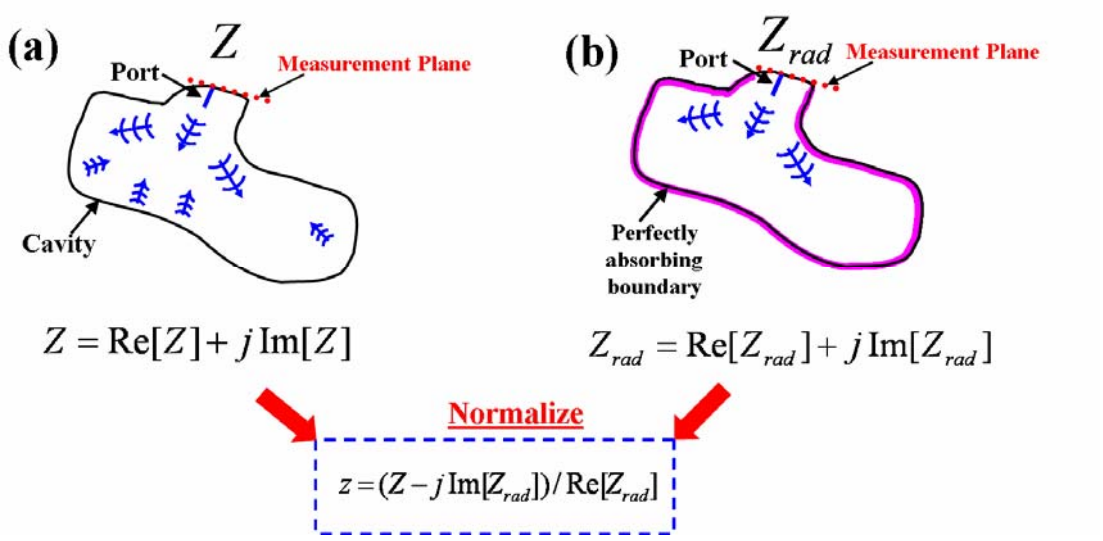

Fig. 2.2: Schematic representation of the "radiation impedance" normalization process for a cavity driven by a single port. The normalization process requires two measurement steps. (a) The first step referred to as the "Cavity Case" involves measuring the complex scalar impedance ($Z = \mathrm{Re}[Z] + j\,\mathrm{Im}[Z]$) of the cavity. For a low-loss chaotic-cavity, the quantity Z wildly oscillates with frequency due to waves returning to the port after reflecting off the cavity side-walls. (b) The second step referred to as the "Radiation Case" involves measuring the complex scalar radiation-impedance ($Z_{rad} = \mathrm{Re}[Z_{rad}] + j\,\mathrm{Im}[Z_{rad}]$) of the driving port which retains its coupling geometry as in the Cavity case, but has the cavity side-walls moved out to infinity or coated with a perfectly absorbing material. The radiation-impedance (Z_{rad}) is a smoothly varying function of frequency and is devoid of any wild fluctuations as seen in Z. The normalized impedance (z) is then defined as $z = (Z - j\,\mathrm{Im}[Z_{rad}]) / \mathrm{Re}[Z_{rad}]$.

According to the Random Coupling Model, the only parameter that determines the statistics of the normalized impedance z, is the dimensionless cavity loss-parameter called "α". For an electromagnetic cavity, $\alpha = k^2/(\Delta k_n^2 Q_{ul})$, where, $k = 2\pi f/c$ is the wavenumber for the incoming frequency f and Δk_n^2 is the mean-spacing of the adjacent eigenvalues of the Helmholtz operator, $\nabla^2 + k^2$, as predicted by the Weyl Formula **[15]** for the closed system. The use of the Weyl formula here is conventionally accepted for lack of a more complete treatment which is applicable to open systems or to systems with high absorption. The quantity Q_{ul} represents the unloaded quality-factor of the cavity and is defined as the ratio of the electromagnetic energy stored to the electromagnetic energy dissipated (due to ohmic and dielectric cavity losses) per cycle. The quantity Q_{ul} does not include dissipation through the coupled ports. The loss-parameter α can range from 0 to ∞, corresponding to a loss-less cavity ($Q_{ul} = \infty$) or an extremely lossy ($Q_{ul} \to 0$) cavity respectively. For the experimental results that follow in Chapters 4-8, it has been deduced that the dissipation through the ports amount to an α value contribution on the order of 0.03 to 0.12 [**45**], which is much less than the typical value of α due to ohmic and dielectric losses from the interior of the cavity (α ranging from about 1 to 300). Thus for all experimental results, I use the value of the loaded-quality factor (Q) when determining the value of α, i.e., $\alpha = k^2/(\Delta k_n^2 Q)$. The loaded-quality factor of the cavity (Q) is defined as the ratio of the electromagnetic energy stored to the electromagnetic energy dissipated (due to ohmic and dielectric cavity losses as well as dissipation through the coupled ports) per cycle. The explicit expressions for α

taking into account the Weyl expressions for Δk_n^2 (which are dependent upon the dimensions of the cavity- see chapter 1) yields, $\alpha = k^2 A/(4\pi Q)$ for 2-D cavities and $\alpha = k^3 V/(2\pi^2 Q)$ for 3-D cavities, where A and V represent the 2-D surface-area (not the full 3-D surface area including side-walls) and 3-D internal volume of the 2-D and 3-D cavity, respectively.

In the loss-less case, $Q = \infty$ with $\alpha = 0$, and the cavity impedance Z is thus a purely imaginary quantity. In this limit, **[25]** has shown that z is also purely imaginary and Lorentzian distributed with zero mean and unit full width at half maximum. The Probability Density Function (PDF) of the real part of z is a one-sided delta function at $\mathrm{Re}[z] = 0$ which has a mean value of 1. As losses increases ($\alpha > 0$), z develops a non-zero real part for which the PDF of $\mathrm{Re}[z]$ evolves from being peaked between $\mathrm{Re}[z] = 0$ and $\mathrm{Re}[z] = 1$, into a Gaussian-type distribution that peaks at $\mathrm{Re}[z] = 1$ for large α (Fig. 2.3(a)). At the same time, the PDF of the imaginary part of the normalized impedance loses its long tails and begins to sharpen up, developing a Gaussian appearance (Fig. 2.3(b)). At all values of α, the mean value of the real part of z (i.e., $\langle \mathrm{Re}[z] \rangle$) is equal to 1, while the mean value of the imaginary part of z (i.e., $\langle \mathrm{Im}[z] \rangle$) is equal to 0. For values of $\alpha > 0$, **[25]** predicts that the variance of the PDF of $\mathrm{Re}[z]$ (i.e., $\sigma^2_{\mathrm{Re}[z]}$) is approximately equal to the variance of the PDF of $\mathrm{Im}[z]$ (i.e., $\sigma^2_{\mathrm{Im}[z]}$). The magnitude of these variances depend only upon the value of the cavity loss-parameter α and the symmetry of the system,

$$\sigma^2_{\mathrm{Re}[z]} \approx \sigma^2_{\mathrm{Im}[z]} \cong \frac{1}{2\pi\alpha} \qquad \text{(BTRS)} \qquad \text{for } \alpha >> 1, \tag{2.5}$$

$$\sigma^2_{\mathrm{Re}[z]} \approx \sigma^2_{\mathrm{Im}[z]} \cong \frac{1}{\pi\alpha} \qquad \text{(TRS)} \qquad \text{for } \alpha >> 1. \tag{2.6}$$

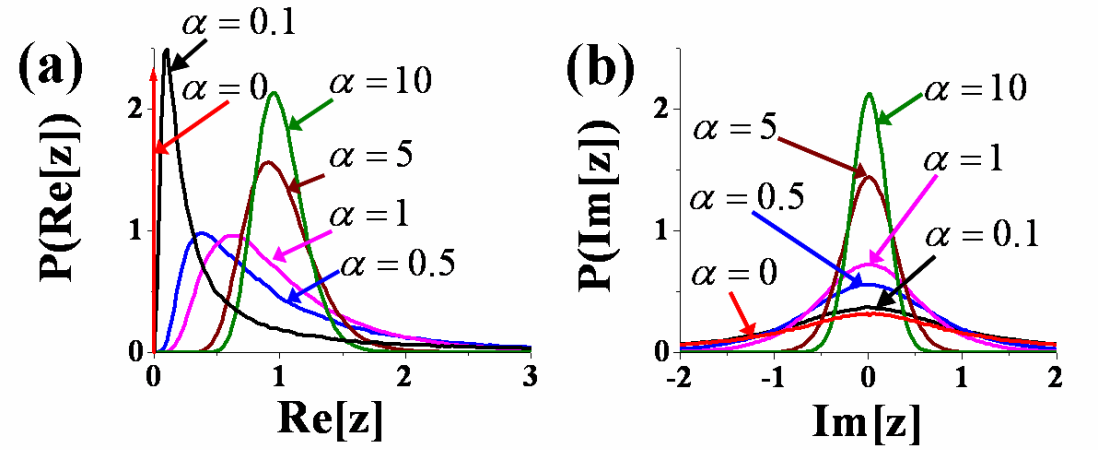

Fig. 2.3: Random Matrix Theory predictions for the Probability Density Functions of (a) Re[z] and (b) Im[z] as a function of increasing α, for a time-reversal symmetric wave-chaotic cavity.

Once the normalized impedance z has been obtained, it can be easily converted to the normalized admittance (y) or the normalized scattering coefficient (s) through,

$$y = 1/z \tag{2.7}$$

$$s = (z-1)/(z+1). \tag{2.8}$$

These universally-fluctuating, normalized quantities- z, y and s represent the electromagnetic scattering properties of a wave-chaotic cavity when the driving port is perfectly coupled to the cavity. Their PDFs are dependent only upon the value of

the cavity loss-parameter α, and are theorized to be described by Random Matrix Theory.

A similar stochastic electromagnetic-wave model for the complex scalar impedance fluctuations in a mode-stirred chamber as measured through a single antenna is presented by Warne *et.al.* from Sandia National Laboratories in Ref. **[49(a)]** (and later updated in Ref. **[49(b)]** to include the correlations between the eigenvalues of the complicated enclosure). Like the Random Coupling Model, the Sandia group also characterizes the non-ideal coupling between the enclosure and the driving antenna through the analytically determined "terminal impedance" (or free-space radiation-impedance) of the antenna. In doing so, Warne *et.al.* derive an expression similar to Eq.(2.4) for the measured cavity impedance in terms of the terminal impedance of the antenna and a universal fluctuating cavity impedance, whose statistics depends only upon the value of the loss-parameter within the enclosure. The cavity loss-parameter in the Sandia Model, $\alpha_{Sandia} = \frac{k^3 V}{2\pi Q}$, differs from the Random Coupling Model 3-D cavity loss-parameter ($\alpha = \frac{k^3 V}{2\pi^2 Q}$) by a factor of $1/\pi$. The Sandia model, which is formulated for a three-dimensional enclosure, introduces an impedance-normalization scheme similar to the one described in Fig. 2.2 for uncovering the universal fluctuations in the cavity impedance. The Sandia group also has a similar expression as Eq. (2.6) for the variance of the real and imaginary parts of the universal fluctuating cavity impedance and does a good job of estimating the asymptotic tails of these distributions.

The Random Coupling Model incorporates all the predictions of the Sandia model, and goes further to include complicated enclosures excited by multiple ports (see section 2.4). This makes it possible to explicitly consider the distribution of voltages and currents on a target port due to a given excitation stimulus at a source port (see chapter 8), which is of key interest to the HPM and Electromagnetic Compatibility community. The extension to multiple ports as well as the effects of non-reciprocal media within the cavity, which is incorporated into the Random Coupling Model, leads to qualitatively new and different predictions which are not available to the Sandia model. Further, the Sandia model uses a single numerical value for the resistive and reactive parts of the terminal impedance of the antenna. This restricts their normalization scheme to narrow frequency ranges (5 or 10 MHz at 200 to 900 MHz). The Random Coupling Model, on the other hand, makes use of the measured frequency-dependent radiation-impedance of the relevant ports. Thereby making it possible to gather normalized impedance data over an arbitrarily large frequency range (3 to 20 GHz- as will be shown in subsequent chapters). The Random Coupling Model also includes predictions for the fluctuations in the scattering and admittance matrices of quasi-two-dimensional and three-dimensional complicated enclosures, which is again not included in the Sandia model.

2.4 Extending the "Radiation Impedance" Normalization to Multi-Port Systems

In general, for a N-port system, the radiation impedance is now an $N \times N$ complex-valued, symmetric matrix ($\ddot{Z}_{rad}$). If the N ports are very far apart, $\ddot{Z}_{rad}$ is diagonal, but that is not assumed here. Reference **[26]** has shown that the measured $N \times N$ impedance matrix of a N-port, wave-chaotic cavity ($\ddot{Z}$) has a mean-part

given by the radiation impedance matrix ($\ddot{Z}_{rad}$) and a universal fluctuating part ($\ddot{z}$), which is scaled by the radiation resistance matrix ($\mathrm{Re}[\ddot{Z}_{rad}]$). Thus,

$$\ddot{Z} = j\,\mathrm{Im}[\ddot{Z}_{rad}] + (\mathrm{Re}[\ddot{Z}_{rad}])^{1/2}\,\ddot{z}\,(\mathrm{Re}[\ddot{Z}_{rad}])^{1/2}. \tag{2.9}$$

From Eq. (2.9), $\ddot{z}$ can be easily extracted,

$$\ddot{z} = (\mathrm{Re}[\ddot{Z}_{rad}])^{-1/2}(\ddot{Z} - j\,\mathrm{Im}[\ddot{Z}_{rad}])(\mathrm{Re}[\ddot{Z}_{rad}])^{-1/2}. \tag{2.10}$$

The normalized scattering matrix $\ddot{s}$ is ,

$$\ddot{s} = (\ddot{z} - \ddot{1})(\ddot{z} + \ddot{1})^{-1}, \tag{2.11}$$

where $\ddot{1}$ is the $N \times N$ identity matrix.

The normalized scattering matrix $\ddot{s}$ can also be obtained from the cavity scattering matrix $\ddot{S}$ and the radiation scattering matrix $\ddot{S}_{rad}$ by converting these quantities to the cavity and radiation impedances, $\ddot{Z}$ and $\ddot{Z}_{rad}$, respectively through

$$\ddot{Z} = \ddot{Z}_o^{1/2}(\ddot{1} + \ddot{S})(\ddot{1} - \ddot{S})^{-1}\ddot{Z}_o^{1/2} \text{ and}$$

$$\ddot{Z}_{rad} = \ddot{Z}_o^{1/2}(\ddot{1} + \ddot{S}_{rad})(\ddot{1} - \ddot{S}_{rad})^{-1}\ddot{Z}_o^{1/2}, \tag{2.12}$$

and by then using Eqs.(2.10) and (2.11). The matrix $\ddot{Z}_o$ is a real diagonal matrix whose elements are the characteristic impedances of the transmission lines connected to the driving ports.

The normalized quantities $\ddot{z}$ and $\ddot{s}$ represent the impedance and scattering matrix when the N ports are perfectly coupled to the cavity, i.e., when $\ddot{Z}_{rad} = \ddot{Z}_o$. Since, in general, $\ddot{Z}_{rad}$ is a smoothly varying function of frequency and of the coupling-port structure, Eqs. (2.10) and (2.11) yield the perfectly-coupled (ideally

matched) impedance and scattering matrix over any arbitrarily large range of frequency and for any port geometry.

Reference **[26]** predicts that the marginal PDFs of the eigenvalues of $\vec{\vec{z}}$ which are contained in the diagonal matrix $\vec{\vec{\lambda}}_{\vec{z}}$, and marginal PDFs of the eigenvalues of $\vec{\vec{s}}$ which are contained in the diagonal matrix $\vec{\vec{\lambda}}_{\vec{s}}$ are qualitatively similar to the PDFs of z and s in the 1-port case (see Fig. 2.3) and that they are dependent only on the loss-parameter (α) of the cavity.

2.5 Generating Normalized Impedance and Scattering matrices using Random Matrix Monte Carlo Simulations

As mentioned previously, in the experimental results that follow in chapters 5 through 8, my objective is to test the applicability of Random Matrix Theory to describe the universal statistical aspects of wave-chaotic scattering. It turns out that there exist several exact analytic predictions for the functional form of the PDFs of the universal impedance and scattering fluctuations as a function of the cavity loss-parameter α in the BTRS case **[47, 48]**. However, for the TRS case, the mathematical formalism is often too involved to obtain such succinct and exact, α-dependent analytic predictions for the universal impedance and scattering fluctuation PDFs. Thus, in situations where no α-dependent analytic prediction exists, I compare my experimentally obtained normalized impedance and scattering matrix fluctuation PDFs for one or two port wave-chaotic cavities with corresponding numerical PDFs generated using random matrix Monte Carlo Simulations. This section presents the algorithms which I employ for numerically generating the TRS universal impedance

and scattering matrices as a function of α, from which the required universal fluctuation PDFs are derived.

It has been identified previously that in a one-port lossy wave-chaotic cavity, the cavity impedance can be written in the form of Eq.(2.1). Based on Eq.(2.1), the assumption that $Q_{ul} \cong Q$ and, in the limit that the ports are perfectly coupled to the cavity at all frequencies, the normalized cavity impedance (z) can be written as,

$$z = \frac{-j}{\pi} \sum_{n=1}^{M} \Delta k_n^2 \frac{w_n^2}{k^2(1-j/Q) - k_n^2}, \tag{2.13}$$

where the significance of each term in this expansion has been previously explained (see section 2.2).

By defining the cavity loss-parameter $\alpha = k^2/(\Delta k_n^2 Q)$ as before, Eq.(2.13) can be written as,

$$z = \frac{-j}{\pi} \sum_{n=1}^{M} \frac{w_n^2}{\frac{k^2 - k_n^2}{\Delta k_n^2} - j\alpha}. \tag{2.14}$$

Equation (2.14) is then evaluated numerically using MATLAB. In the MATLAB simulations, M is taken to be a large value on the order of 1000. Also M independent zero-mean and unit-variance Gaussian-distributed random numbers are generated for w_n using the random-number generator in MATLAB. Next, M values of the normalized eigenvalues $k_n^2/\Delta k_n^2$ corresponding to the GOE ensemble need to be generated. Two approaches are possible for obtaining these quantities; (i) an approximate approach (which I call the "Wigner-Distribution Approach") that makes use of the TRS normalized nearest neighbor eigenfrequency spacing distribution - Eq.

(1.1) and (ii) a full-fledged "Random Matrix Theory Approach" that makes use of the eigenvalues of an ensemble of large random matrices. The values of k^2 are picked to be the median-value of the obtained spectra of k_n^2.

For the method (i), M independent values of the TRS normalized nearest neighbor eigenfrequency spacing (ε) are generated using the TRS normalized nearest neighbor eigenfrequency spacing distribution in Eq. (1.1). The quantity $k_n^2/\Delta k_n^2$ is then defined as $k_n^2/\Delta k_n^2 = \sum_{i=1}^{n} \varepsilon_i$. This approach is computationally fast and has been found to yield satisfactory outcomes for one-port wave-chaotic systems. It is noteworthy to point out that this approach has also been adopted by **[49]**. However, the approach is approximate in the sense that long-range correlations in the eigenspacings are neglected. I have found that these long-range correlations play a significant role particularly in the case of joint-distributions of the normalized impedance and scattering matrices eigenvalues, for two-port wave-chaotic systems (see chapter 5). Thus, to account for these long-range correlations, method (ii) is always adopted when pertaining to two-port systems.

For method (ii), in order to obtain the M values of the normalized eigenvalues $k_n^2/\Delta k_n^2$ corresponding to the GOE ensemble, a $M \times M$ random matrix is first generated. The elements of the random matrix satisfy the criteria for GOE ensemble, i.e. the matrix is real symmetric with each element being an independent zero-mean, Gaussian-distributed random number. The on-diagonal elements are of unit-variance while the variance of the off-diagonal elements is 0.5. For large M, the eigenvalues of this $M \times M$ random matrix have non-uniform spacing and are

distributed as per "Wigner's Semi-Circle law" **[23]**, i.e, $P(\lambda_M) = \frac{1}{\pi}\sqrt{2M - \lambda_M^2}\,; |\lambda_M| < \sqrt{2M}$, where λ_M corresponds to one of the M eigenvalues of the $M \times M$ random Matrix. The distribution of the eigevalues of one such $M \times M$ random matrix (with $M = 2000$) is shown in Fig. 2.4 (a). In order to generate a sequence of eigenvalues with approximately uniform spacing, Ref. **[50]** resorts to selecting the middle $M/5$ levels and then normalizing the selected eigenvalues by multiplying with $\sqrt{2M}/\pi$ to create a sequence of $k_n^2/\Delta k_n^2$ with average spacing of approximately unity. However, by following this procedure, the remaining $4M/5$ eigenvalues and the computational effort required to obtain these quantities is unutilized.

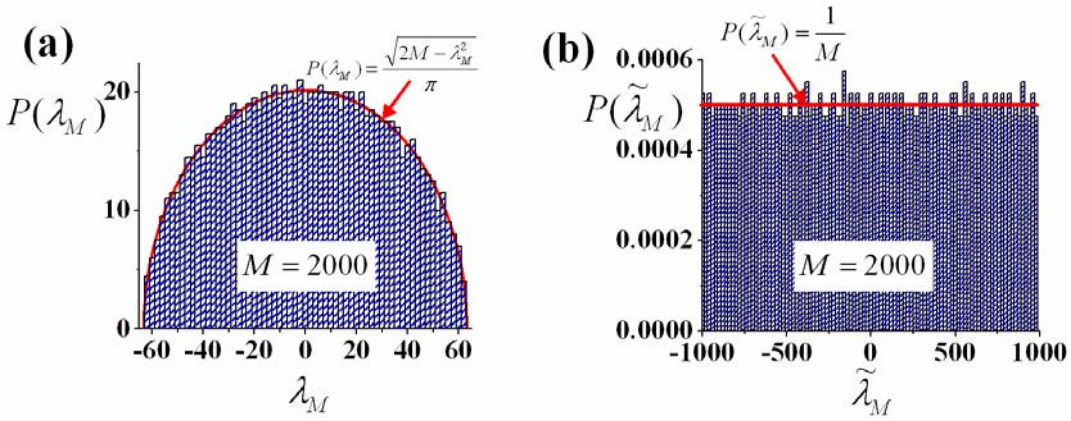

Fig.2.4: (a) Histogram (in blue) showing the distribution of the eigenvalues (λ_M) of a $M \times M$ sized random matrix of the GOE ensemble with $M = 2000$. The red curve is the "Wigner's Semi-Circle Law" prediction for $M = 2000$. (b) Histogram (in blue) showing the distribution of the mapped-eigenvalues ($\tilde{\lambda}_M$) obtained from the

eigenvalues (λ_M) shown in (a) and Eq. (2.12). The red line represents a uniform distribution $P(\widetilde{\lambda}_M) = 1/M$ for $M = 2000$.

An alternative procedure involves introducing a mapping function $\varsigma(\lambda_M, M)$ which maps each λ_M possessing the semi-circle distribution, into a new variable $\widetilde{\lambda}_M$ which is uniform distributed between $-M/2$ and $M/2$ and having an average spacing of unity (Fig. 2.4(b)). The functional form of the mapping function $\varsigma(\lambda_M, M)$ is,

$$\widetilde{\lambda}_M = \frac{M}{2\pi}\left(\pi + 2\sin^{-1}\left(\frac{\lambda_M}{\sqrt{2M}}\right) + 2\frac{\lambda_M}{\sqrt{2M}}\frac{\sqrt{2M-\lambda_M^2}}{\sqrt{2M}}\right) - \frac{M}{2}. \tag{2.15}$$

In this procedure, all of the M eigenvalues (λ_M) are utilized thereby making the algorithm computationally more efficient. To my knowledge, the mapping function $\varsigma(\lambda_M, M)$ does not alter the long-range correlation properties of the eigenvalues λ_M .

Once the normalized impedance z is obtained, it can be converted to the normalized one-port scattering coefficient s using Eq. (2.11). By repeating this procedure about 100,000 times, a sufficiently large ensemble of z and s is generated from which the statistical descriptions of these quantities are determined.

For random matrix Monte Carlo simulations pertaining to wave-chaotic systems driven by more than one port, a similar formalism for the $N \times N$ normalized impedance matrix ($\vec{\vec{z}}_{N\times N}$) as in Eq. (2.14) is adopted, i.e.,

$$\vec{\vec{z}}_{N\times N} = \frac{-j}{\pi}\vec{\vec{W}}\frac{1}{\vec{\vec{\lambda}} - j\alpha\vec{\vec{1}}}\vec{\vec{W}}^T, \tag{2.16}$$

where N is the number of driving ports. The matrix $\vec{\vec{W}}$ is a $N \times M$ coupling-matrix with each element W_{ij} representing the coupling between the i^{th} driving port $(1 < i \leq N)$ and the j^{th} eigenmode of the cavity $(1 \leq j \leq M)$. Each W_{ij} is an independent Gaussian-distributed random number of zero mean and unit variance. The matrix $\vec{\vec{W}}^T$ corresponds to the transpose of matrix $\vec{\vec{W}}$, and $\vec{\vec{1}}$ is a $M \times M$ identity-matrix. The matrix $\vec{\vec{\lambda}}$ is a $M \times M$ diagonal matrix with a set of M $\tilde{\lambda}_M$ -values generated as discussed previously.

The $N \times N$ normalized scattering matrix is then defined as $\vec{\vec{s}}_{N\times N} = (\vec{\vec{z}}_{N\times N} - \vec{\vec{1}}_{N\times N})(\vec{\vec{z}}_{N\times N} + \vec{\vec{1}}_{N\times N})^{-1}$, where the $^{-1}$ indicates a matrix inversion operation. By repeating this procedure about 100,000 times, a sufficiently large ensemble of $\vec{\vec{z}}$ and $\vec{\vec{s}}$ is generated from which the statistical descriptions of these quantities are determined.

Chapter 3: Experimental Setup and Data Analysis

Until about 1990, apart from the nuclear spectra studies of **[51],** only a very small number of experiments on wave-chaotic scattering existed. The studies of irregularly shaped microwave cavities by Stockmann and Stein **[52]**, Doron, Smilansky and Frenkel **[53]** have provided an impetus to wave-chaotic scattering research. Microwave cavities with irregular shapes (having chaotic ray dynamics) have proven to be very fruitful for the study of wave-chaos, where not only the magnitude, but also the phase of scattering coefficients, can be directly measured from experiments. In this chapter, I present a detailed account of my experimental setup for a quasi-two-dimensional, quarter-bow-tie shaped wave-chaotic cavity which is driven by one-port (section 3.1) or two-ports (section 3.2). I also present the procedure for normalizing the measured cavity impedance and scattering data using the "radiation impedance" normalization process from Chapter 2.

3.1 Experimental Setup and Data Analysis- One Port

My experimental setup consists of an air-filled quarter bow-tie shaped chaotic cavity (Fig. 3.1(a)) which acts as a two dimensional resonator below about 19.05 GHz **[54]**. Ray trajectories in a closed cavity of this shape are known to be chaotic. This cavity has previously been used for the successful study of the eigenvalue spacing statistics **[22]** and eigenfunction statistics **[41, 55]** for a wave chaotic system. In order to investigate a scattering problem, the cavity is excited by means of a single coaxial probe whose exposed inner conductor, with a diameter ($2a$) extends from the top plate and makes electrical contact with the bottom plate of the cavity (Fig. 3.1(b)). In

chapter 4, the scattering properties of the time-reversal symmetric cavity over a frequency range of 6 - 12 GHz are discussed, where the spacing between two adjacent resonances is on the order of 15 – 30 MHz over this frequency range.

As in the numerical experiments in Refs.**[25, 26]** and Chapter 2, my experiment involves a two-step normalization procedure to account for the system-specific details of non-ideal port coupling. The first step is to collect an ensemble of cavity scattering coefficients S over the frequency range of interest. Ensemble averaging is realized by using two rectangular metallic perturbations with dimensions 26.7 x 40.6 x 7.87 mm^3 (about 1% of the cavity volume), which are systematically scanned and rotated throughout the volume of the cavity (Fig.3.1(a)). Each configuration of the perturbers within the cavity volume results in a different value for the measured value of S. This is equivalent to measurements on cavities having the same volume, loss and coupling geometry for the port, but with different shapes. The perturbers are kept far enough from the antenna so as not to alter its near-field characteristics. For each configuration, the scattering coefficient S is measured in 8000 equally spaced steps over a frequency range of 6 to 12 GHz using a Hewlett Packard 8510C Vector Network Analyzer. In total, one hundred different configurations are measured, resulting in an ensemble of 800,000 S values. I refer to this step as the "Cavity Case".

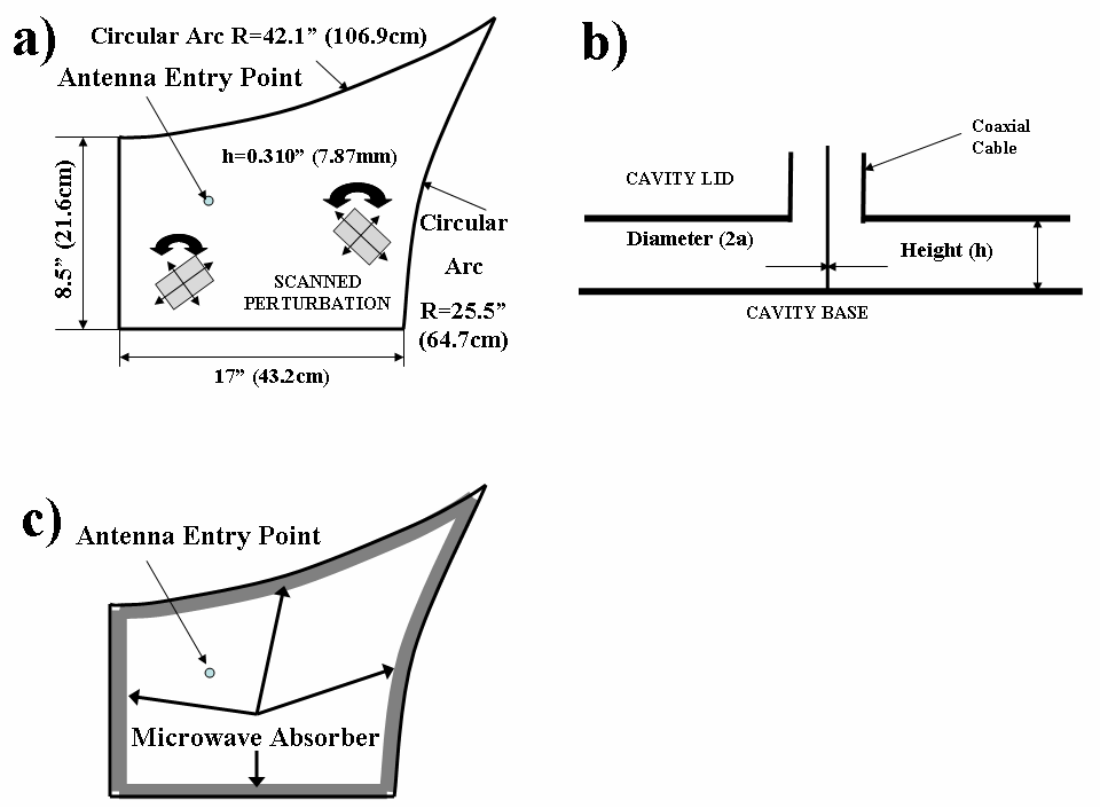

Fig 3.1: (a) The physical dimensions of the quarter bow-tie chaotic microwave resonator are shown along with the position of the single coupling port. Two metallic perturbations are systematically scanned and rotated throughout the entire volume of the cavity to generate the cavity ensemble. (b) The details of the coupling port (antenna) and cavity height *h* are shown in cross section. (c) The implementation of the radiation case is shown, in which commercial microwave absorber is used to line the inner walls of the cavity to minimize reflections.

The second step, referred to as the "Radiation Case", involves obtaining the scattering coefficient for the excitation port when waves enter the cavity but do not return to the port. In the experiment, this condition is realized by removing the perturbers and lining the side-walls of the cavity with commercial microwave

absorber (ARC Tech DD10017D) which provides about 25dB of reflection loss between 6 and 12 GHz (Fig. 3.1.(c)). The finite reflection-loss presented by the microwave absorber results in systematic errors in the measured radiation-case scattering coefficient, which is discussed in section 9.1.3. Note that in the radiation-case setup, the side-walls of the cavity are outside the near field zone of the antenna. Using the same frequency stepping of 8000 equally spaced points over 6 to 12 GHz, I measure the radiation scattering coefficient S_{rad} for the cavity. Such an approach approximates the situation where the side-walls are moved out to infinity; therefore S_{rad} does not depend on the chaotic ray trajectories of the cavity, and thus gives a characterization of the coupling independent of the chaotic system. Because the coupling properties of the antenna depend on the wavelength and thus vary over frequency, S_{rad} is usually frequency dependent.

Having measured the cavity S and S_{rad}, I then transform these quantities into the corresponding cavity and radiation impedances (Z and Z_{rad}) respectively using,

$$Z = Z_0 \frac{(1+S)}{(1-S)} \tag{3.1}$$

$$Z_{rad} = Z_0 \frac{(1+S_{rad})}{(1-S_{rad})} \tag{3.2}$$

where Z_0 is the characteristic impedance of the transmission line feeding the antenna and is assumed to be 50Ω for the results that follow.

The normalized impedance z is then obtained by,

$$z = \frac{Z - j\,\mathrm{Im}[Z_{rad}]}{\mathrm{Re}[Z_{rad}]} \tag{3.3}$$

In order to obtain z, every value of the determined cavity impedance Z is normalized by the corresponding value of Z_{rad} at the same frequency. The transformation,

$$s = \frac{z-1}{z+1} \tag{3.4}$$

or equivalently,

$$s = \frac{(1+S_{rad}^{*})}{(1+S_{rad})}\frac{(S-S_{rad}^{*})}{(1-SS_{rad}^{*})} \tag{3.5}$$

yields the normalized scattering coefficient s.

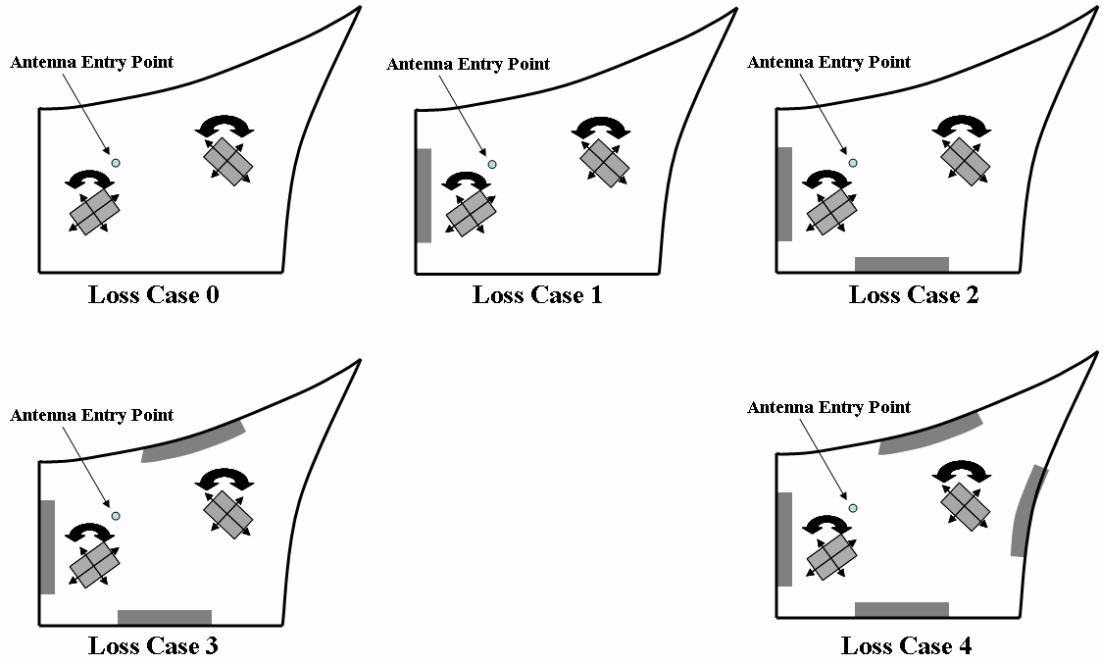

Fig 3.2: Implementation of the different cavity "Loss Cases". The gray lines indicate 15.2 cm-long strips of microwave absorber placed along the inner walls of the cavity. The figure is not drawn to scale.

In order to test the validity of the theory for systems with varying loss, I create different "cavity cases" with different degrees of loss. Loss is controlled and parameterized by placing 15.2 cm-long strips of microwave absorber along the inner walls of the cavity (see section 4.1.4). These strips cover the side walls from the bottom to top lids of the cavity. I thus generate five different loss scenarios (Loss Case 0, Loss Case 1, Loss Case 2, Loss Case 3 and Loss Case 4) shown schematically in Fig 3.2. The numbers 0, 1, 2, 3 and 4 correspond to the number of 15.2 cm -long strips placed along the inner cavity walls**.**. The total perimeter of the cavity is 147.3 cm. I also create two different coupling geometries by using coaxial cables with two different inner diameters (2a=1.27mm and 2a=0.625mm, schematically shown in Fig. 3.1(b)).

Experimental results for the marginal probability density functions (PDFs) of normalized impedance z and normalized scattering coefficient s, and its agreement with corresponding predictions from Random Matrix Theory is presented in chapter 4.

3.2 Experimental Setup and Data Analysis- Two Ports

In this section, I present my experimental setup and data-analysis for an air-filled, quasi-two-dimensional, quarter bow-tie shaped billiard cavity (Fig. 3.3 (a)) driven by two-ports. As in section 3.1, the cavity is 7.87 mm deep and behaves as a two-dimensional resonator when the driving frequency is less than 19.05 GHz. The curved walls ensure that the ray trajectories are chaotic and that there are only isolated classically periodic-orbits.

To set up the investigation, I introduce two driving ports (Fig. 3.3(b)) which are placed roughly 20 cm apart, and are labeled Port-1 and Port-2. The ports are located sufficiently far away from the side-walls of the cavity so that the near-field structure of each port is not altered by the walls. Both ports are sections of coaxial transmission lines, where the exposed center-conductor extends from the top plate of the cavity and makes contact with the bottom plate, injecting current into the bottom plate (Fig. 3.3(c)). The ports are non-identical; the diameter of the inner conductor is 2a=1.27 mm for Port-1 and 2a=0.635 mm for Port-2.

The measurements are made using an Agilent E8364B Vector Network Analyzer which is far superior to the HP8510C (used in section 3.1) in terms of frequency resolution, improved signal noise-floor and the ability to electronically calibrate the device rather than the conventional mechanical calibration used in the HP8510C. As in chapter 2 and section 3.1**,** the normalization of the measured data is a two-step procedure. The first step, what I refer to as the "Cavity Case" involves measuring a large ensemble of the full-2x2 scattering matrix $\vec{\vec{S}}_{cav} = \begin{bmatrix} S_{11} & S_{12} \\ S_{21} & S_{22} \end{bmatrix}$.To realize this large ensemble, two metallic perturbers (shown as gray solids in Fig. 3.3(a)), each of typical dimensions 6.5 cm x 4 cm x 0.78 cm are used. The perturbers are roughly the order of a wavelength in size at 5 GHz. The edges of the perturbers are intentionally serrated to further randomize the wave scattering within the cavity by preventing the formation of standing waves between the straight wall segments of the cavity and the edges of the perturbations. The perturbers are systematically translated and rotated through one-hundred different locations within the volume of the cavity. Hence each orientation of the two perturbers results in a different internal

field structure within the cavity. Thus, in effect, I measure one-hundred cavity configurations all having the same volume, coupling geometry for the driving ports, and almost exactly the same cavity conduction loss. For each configuration of the perturbers, $\vec{\vec{S}}$ is measured as a function of frequency from 3 to 18 GHz in 16000 equally spaced steps. An ensemble of 1,600,000 cavity scattering matrices $\vec{\vec{S}}$ is thus collected. Special care is taken not to bring the perturbers too close to the ports so as not to alter the near-field structure of the ports.

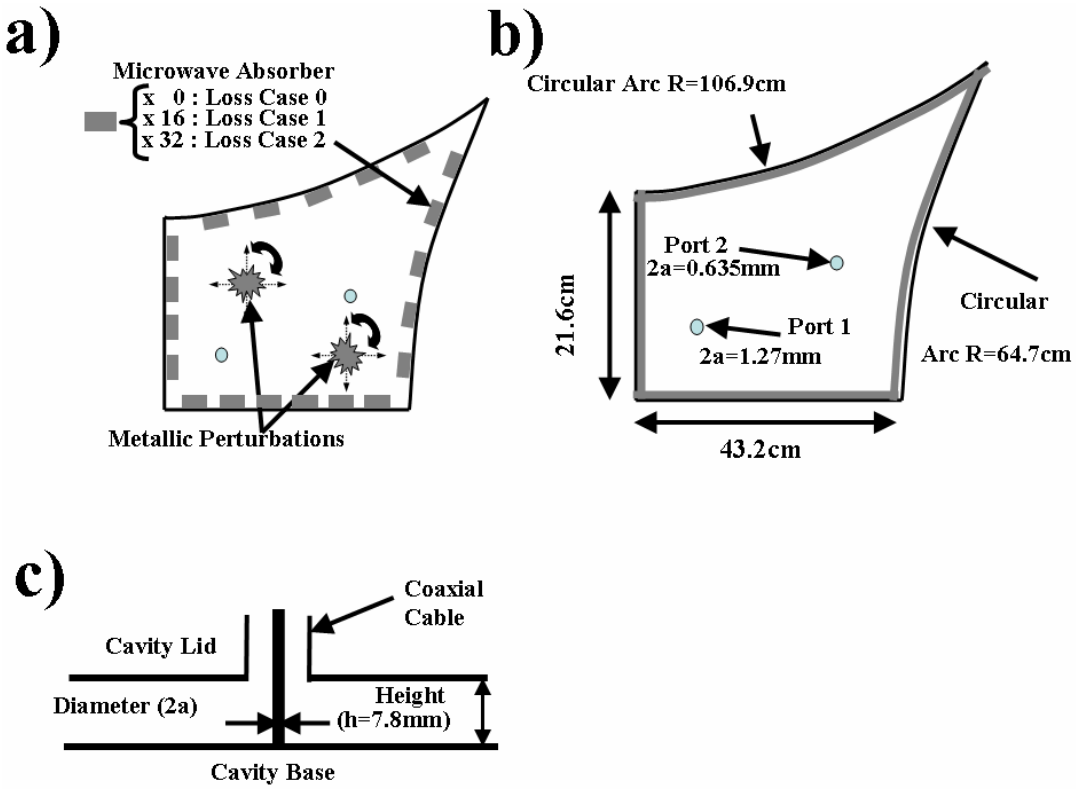

Fig.3.3: (a) Top view of quarter-bow-tie microwave cavity used for the experimental "Cavity Case". The two perturbations with serrated edges are shown as the gray shapes. The small, gray, uniformly-spaced rectangles lining the side-walls of the cavity represent 2cm-long strips of microwave absorber which are used to control the

loss in the cavity.(Loss Case 0 : 0 strips, Loss Case 1: 16 strips, Loss Case 2: 32 strips). (b) The implementation of the experimental "Radiation Case" is shown. The gray lining on the side-walls is a homogenous layer of microwave absorber (about 2 mm thick). The physical dimensions of the cavity are shown in the schematic. The approximate locations of the two driving-ports are also shown. (c) Cross-section view of both driving-ports inside the cavity. The cavity is 7.87 mm in depth. The diameter of the inner conductor is $2a$ (=1.27 mm for Port 1; =0.635 mm for Port 2).

The dominant loss mechanism in the empty cavity is ohmic loss in the broad top and bottom plates of the cavity. The fluctuations in loss from mode-to-mode are small and come from differences in field configurations around the side walls **[56]**. The degree of loss can be increased in a controlled manner by partially lining the inner side-walls with 2 cm-long strips of microwave absorber (Fig. 3.3(a)) having uniform spacing. I believe this creates a more homogenously distributed loss-profile as compared to the lossy cavity cases of section 3.1 (see section 9.1.2). Three lossy Cavity Cases are measured at room temperature– labeled "Loss Case 0" : with no absorbing strips, "Loss Case 1" : with 16 absorbing strips and "Loss Case 2" : with 32 absorbing strips. A fourth experimental Loss Case is created by placing the Loss Case 0 cavity in a bath of dry-ice (solid CO_2 at -78.5^{o}C). This has the effect of slightly increasing the overall Loss Case 0 cavity Q value by about 10% (taking into account the small decrease in the cavity volume and changes in the cavity mode-spacing due to thermal contraction of the cavity). I refer to this case as the "dry-ice case". Along

with frequency, these four loss cases lead to an experimental control over the value of α from 0.9 to 25.

To make a quantitative assessment of the degree of "non-ideal coupling" or "mismatch" of the two ports with the cavity, I compute the transmission coefficient T_{coup} of the ports **[36]** as a function of frequency from 3 to 18 GHz. I define $T_{coup} = 1 - |\hat{\lambda}_{<\vec{\vec{S}}>}|^2$, where $\hat{\lambda}_{<\vec{\vec{S}}>}$ are the two complex scalar eigenvalues of $<\vec{\vec{S}}>$. Here, $<\vec{\vec{S}}>$ is the configuration average over the measured ensemble of $\vec{\vec{S}}$ at each frequency. $T_{coup} = 1(0)$ represents the case when the ports are perfectly matched (mismatched) to the cavity. The inset in Fig. 3.4 shows the PDF of the measured T_{coup} (i.e. $P(T_{coup})$) for a Loss Case 0 cavity from 3 to 18 GHz. The PDF is fairly widely spread over the range 0 to 1 with a mean value of about 0.7, and with a standard deviation of about 0.3. An analysis of the coupling and loss for the scattering matrix in similar microwave cavities is presented in Ref. **[56]**.

The degree to which the two perturbations produce a change in the internal field structure of the cavity can be qualitatively inferred by looking at the frequency correlations in the measured $\vec{\vec{S}}$ data. In Fig. 3.4 for Loss-Case 0, the frequency correlation function $\rho(\delta f) = \dfrac{\langle |S_{11}(f_o)||S_{11}(f_o+\delta f)|\rangle - \langle |S_{11}(f_o)|\rangle\langle |S_{11}(f_o+\delta f)|\rangle}{\sigma_{|S_{11}(f_o)|}\sigma_{|S_{11}(f_o+\delta f)|}}$ with $f_o = 3GHz$ is shown as the red circles. The averaging $\langle ... \rangle$ is done over the one hundred different configurations of the perturbations inside the cavity, and $\sigma_{|S_{11}(f)|}$ represents the standard deviation of the one-hundred different measurements for cavity $|S_{11}(f)|$ at frequency f. The frequency $f_o = 3GHz$ represents the lowest of

the frequencies that is experimentally tested; and therefore the worst-case scenario for performing the approximation to true ensemble averaging. Based on the area and perimeter of the cavity, the Weyl formula **[15]** yields a typical mean-spacing of $\Delta f_{Weyl} \cong 42MHz$ between the eigenmodes of the cavity around f_o. From Fig. 3.4, it is observed that the experimentally determined correlations in frequency die off within one mean-spacing Δf_{Weyl}. However, the correlation function in Fig. 3.4 is similar to those obtained under local, rather than global, perturbations of the system **[57]**. It has previously been identified that the short ray orbits inside the cavity will produce systematic deviations of the finite configuration averaging from a true ensemble average **[25]**. I therefore invoke ergodicity and also employ frequency averaging of the data. Since the frequency averaging ranges that I use are very much larger than Δf_{Weyl} (typically by a factor of about 20), this confirms that the frequency (in addition to perturber configuration averaging) is an effective means of approximating a true ensemble average.

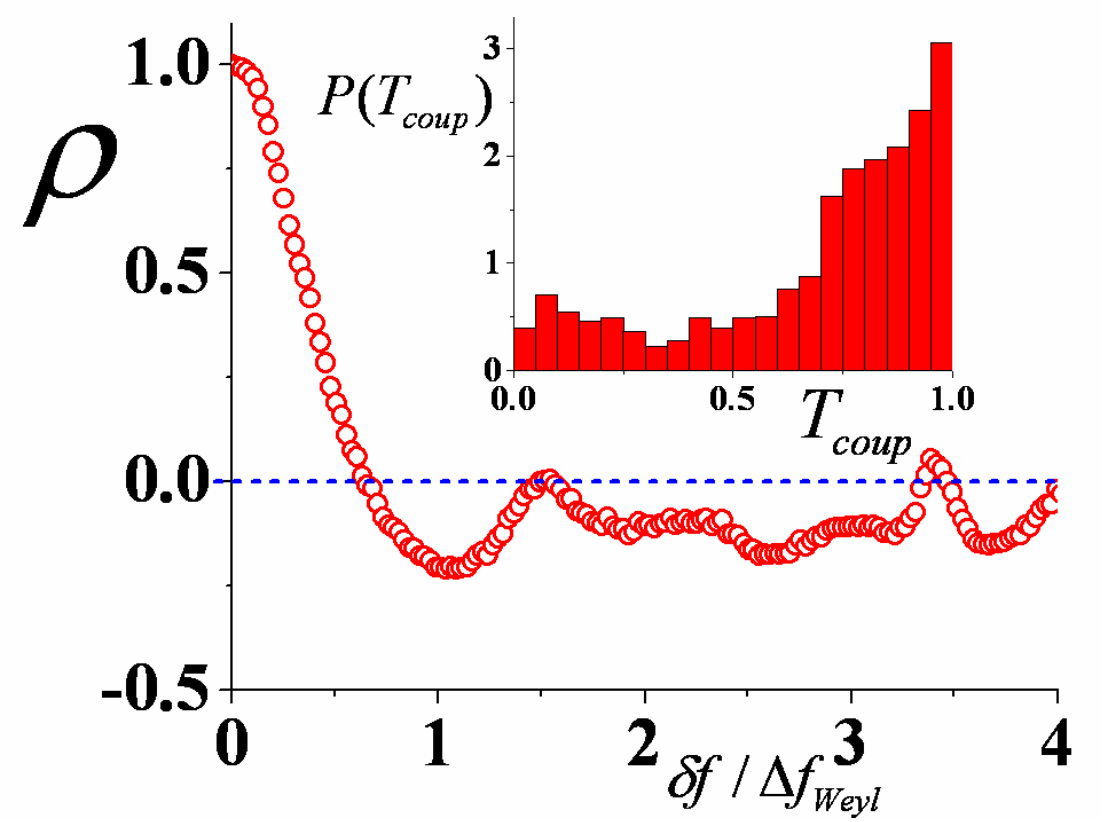

Fig.3.4: Spectral correlation function $\rho(\delta f) = \frac{\langle |S_{11}(f_o)||S_{11}(f_o+\delta f)|\rangle - \langle |S_{11}(f_o)|\rangle\langle |S_{11}(f_o+\delta f)|\rangle}{\sigma_{|S_{11}(f_o)|}\sigma_{|S_{11}(f_o+\delta f)|}}$ of the measured cavity reflection coefficient. Each red-circle symbol represents the correlation between the one hundred different renditions of the Loss-Case 0 cavity $|S_{11}|$ at frequency $f_o = 3GHz$ with the one-hundred different renditions of the same cavity $|S_{11}|$ at frequency $f_o + \delta f$. The mean mode-spacing is determined to be $\Delta f_{Weyl} \approx 42MHz$. Inset: The PDF of the raw-data transmission coefficient of the two ports ($P(T_{coup})$) is shown for Loss-Case 0 cavity from 3 to 18 GHz. Note the broad range of coupling values present in the un-normalized data.

The second step of the normalization procedure is what I refer to as the "Radiation Case" (Fig. 3.3(b)). In this step, the side-walls of the cavity are completely lined with microwave absorber (ARC-Tech DD 10017- about 2mm thick) which gives about 20-25 dB reflection loss between 3 and 18 GHz for normal incidence. The perturbers are removed so as not to produce any reflections back to the ports. Port-1 and Port-2 are left untouched- so that they retain the same coupling geometry as in the "Cavity Case". The radiation measurement now involves measuring the resultant 2x2-scattering matrix, which I label $\vec{\vec{S}}_{rad} = \begin{bmatrix} S_{11rad} & S_{12rad} \\ S_{21rad} & S_{22rad} \end{bmatrix}$, from 3 to 18 GHz with the same 16000 frequency steps as in the "Cavity Case". The microwave absorber serves to severely suppress any reflections from the side-walls. This effectively simulates the situation of the side-walls of the cavity being moved out to infinity (radiation-boundary condition). The off-diagonal terms in $\vec{\vec{S}}_{rad}$ correspond to direct-path processes between the two ports. The contribution of these terms has been taken into account in the analysis and results that are presented in section 5.1 and section 5.3. The hazards associated with ignoring these terms in the normalization process deserves special mention and are discussed in section 5.2.

Having measured the ensemble of cavity $\vec{\vec{S}}$ and the corresponding radiation $\vec{\vec{S}}_{rad}$, I convert these quantities into the corresponding cavity impedance $\vec{\vec{Z}}$ and radiation impedance $\vec{\vec{Z}}_{rad}$ matrices respectively using Eq. (2.12), where each port has a single operating mode with characteristic impedance of 50Ω over the frequency range of the experiment.

Every measured $\vec{\vec{Z}}$ is then normalized with the corresponding measured $\vec{\vec{Z}}_{rad}$ at the same frequency using Eq. (2.10). Having obtained the normalized impedance matrix $\vec{\vec{z}}$, it is then converted to the normalized scattering matrix $\vec{\vec{s}}$ using Eq. (2.11); and the normalized admittance matrix $\vec{\vec{y}}$ ($\vec{\vec{y}} = \vec{\vec{z}}^{-1}$). These normalized quantities represent the corresponding electromagnetic response of the chaotic-cavity in the limit of perfect coupling between the driving ports and the cavity over the entire frequency range of the experiment from 3 to 18 GHz. Experimental results for the joint and marginal probability density functions of $\vec{\vec{z}}$, $\vec{\vec{y}}$ and $\vec{\vec{s}}$, and its agreement with corresponding predictions from Random Matrix Theory is presented in chapter 5.

Chapter 4: Universal Fluctuations in One-Port Impedance and Scattering Coefficients of Wave-Chaotic Systems

In this chapter, I present my experimental results for the universal fluctuations in the normalized impedance z and normalized scattering coefficient s for the quasi-two-dimensional, quarter-bow-tie shaped wave-chaotic cavity introduced in section 3.1. My experimental results, in this chapter, are presented in two sections. In section 4.1, I show my experimental results for the Probability Density Functions (PDFs) of the normalized impedance z. I first experimentally validate that the radiation impedance Z_{rad} accurately quantifies the non-ideal coupling between the port and the cavity. I then compare the experimentally obtained histogram approximations to the PDFs of z with predictions from Random Matrix Theory. In section 4.2, I convert the normalized impedance z to the normalized scattering coefficient s and experimentally validate statistical predictions for the magnitude and phase of the normalized s from Random Matrix Theory. Section 4.3 concludes this chapter with a summary of my experimental findings and its implications.

4.1 Experimental Results for One-Port Normalized Impedance z

This section is broadly divided into four parts. In the first part, I examine the effects of increasing loss on the raw cavity impedance Z. I show the advantage of using the radiation impedance, which is a non-statistical quantity, rather than the ensemble averaged cavity impedance $< Z >$ to quantify the non-ideal coupling

between the port and the cavity. In the second part of this section, I show the insensitivity of the "radiation–impedance" normalization process to system-specific details and uncover the universal fluctuations in the cavity impedance. I then show the agreement between the experimentally determined histogram approximations to the PDFs of the normalized impedance z and those numerically generated using Random Matrix Theory. In the third part, a prediction for the variances of the real and imaginary parts of these normalized impedance PDFs and their dependence on the cavity loss-parameter (α) is experimentally tested. Finally, in the fourth part, I experimentally derive an empirical relation between the cavity loss-parameter (α) and the number of microwave absorbing strips within the cavity, thereby showing my ability to control the value of α in the cavity.

4.1.1 Effect of loss on cavity impedance and strength of the radiation impedance to quantify non-ideal port coupling

Figure 4.1 demonstrates how the cavity impedance evolves with increasing loss **[58]**. Shown are impedance magnitude data versus frequency for Loss-Case 0 (black squares), Loss-Case 1 (blue circles) and Loss-Case 4 (green triangles) cavities excited by an antenna with inner diameter $2a = 1.27mm$. These data sets are for a single rendition of the cavity in the frequency range of 6-7.2 GHz. Also shown is the measured radiation impedance magnitude (red line in Fig. 4.1) for the same antenna as in the Loss-Case cavities with $2a = 1.27mm$. As losses increase, it can be observed that the fluctuations in |Z| clearly decrease, and approach the radiation case.

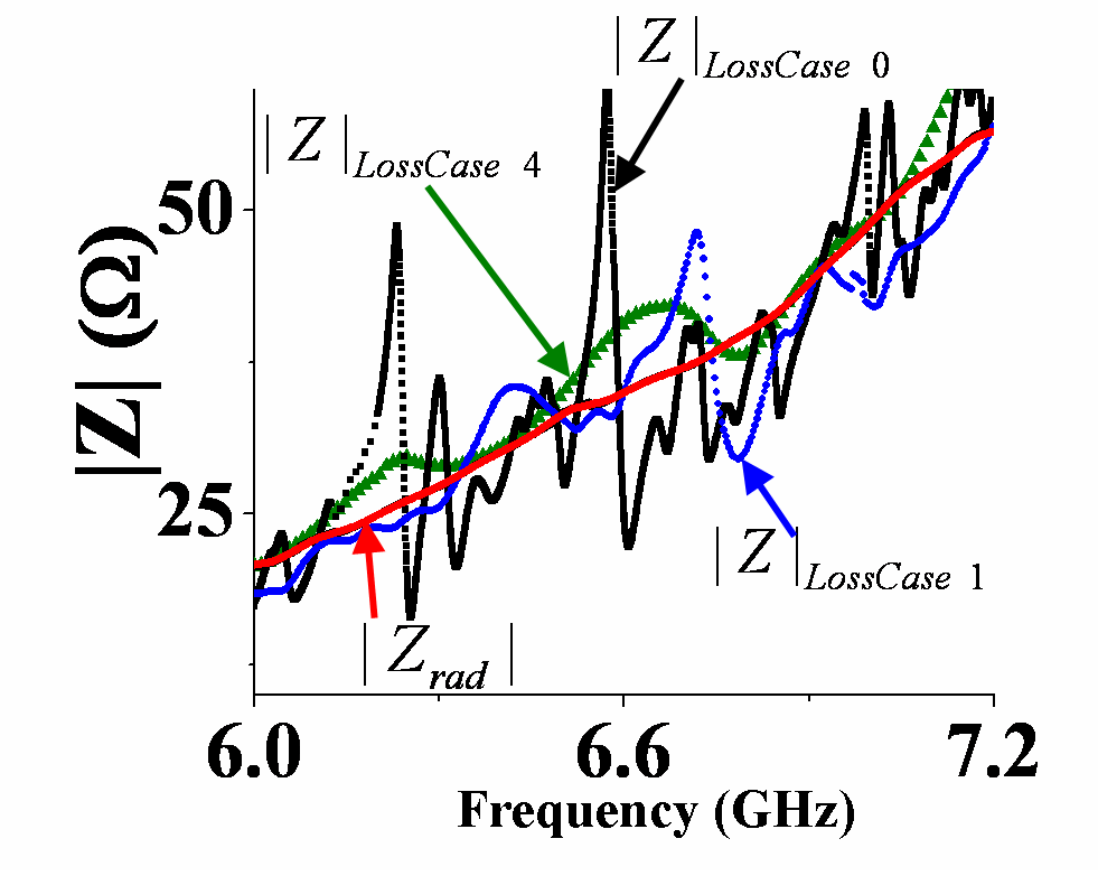

Fig. 4.1: The magnitude of a single rendition of the cavity impedance (Loss Case 0-black squares, Loss Case 1-blue circles, Loss Case 4-green triangles) is shown as a function of frequency. The solid red line is the magnitude of the measured radiation impedance for the same antenna and coupling detail as shown in the Loss-Case cavities . As losses within the cavity increase, the cavity resonances are dampened out and the measured cavity impedance approaches the radiation impedance.

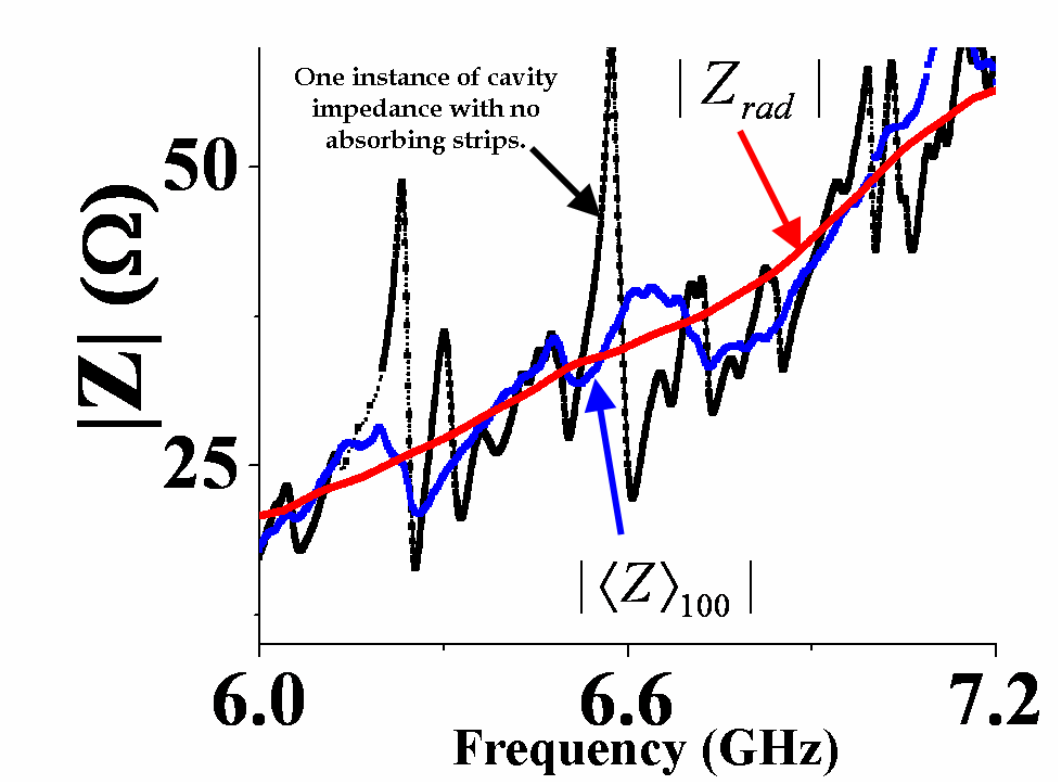

Fig. 4.2: The magnitude of the Loss-Case 0 cavity impedance is shown as a function of frequency. The black squares indicate a single rendition of the cavity impedance and perturbations. The blue line is the magnitude of the complex cavity impedance obtained after configuration averaging over 100 different perturbation positions within the cavity. The solid red line is the magnitude of the measured radiation impedance for the same antenna and coupling detail as shown in Fig. (3.1 (b)) and with $2a = 1.27mm$. Note that even after 100 renditions of the perturbers within the cavity, $|\langle Z\rangle_{100}|$ is still a poor approximation to $|Z_{rad}|$.

In Fig. 4.2, I examine the degree to which configuration averaging to estimate $\langle\langle S\rangle\rangle$ and $\langle\langle Z\rangle\rangle$, as employed in the Poisson Kernel, can reproduce the radiation

cases S_{rad} and Z_{rad}. Figure 4.2 shows typical data for the magnitude of the cavity impedance versus frequency for several cases. The black squares show the cavity impedance for one particular rendition of the Loss Case 0 cavity and its perturbers. The blue line shows the result of averaging the complex impedance of 100 renditions of the Loss Case 0 cavity. The solid red line is the measured radiation impedance $|Z_{rad}|$, which should be equivalent to the ensemble average of the cavity impedance $\langle\langle Z\rangle\rangle$. It is clear that even after configuration averaging the properties of 100 cavities, the value of $\langle Z\rangle_{100}$ has not yet approached the radiation case. This demonstrates the importance of obtaining very high quality statistics before the Poisson Kernel can be used on real data. It also illustrates the relative ease with which the radiation impedance can be used to characterize the non-ideal coupling of real wave-chaotic systems **[58]**.

4.1.2 Uncovering the Normalized Impedance (z) PDFs

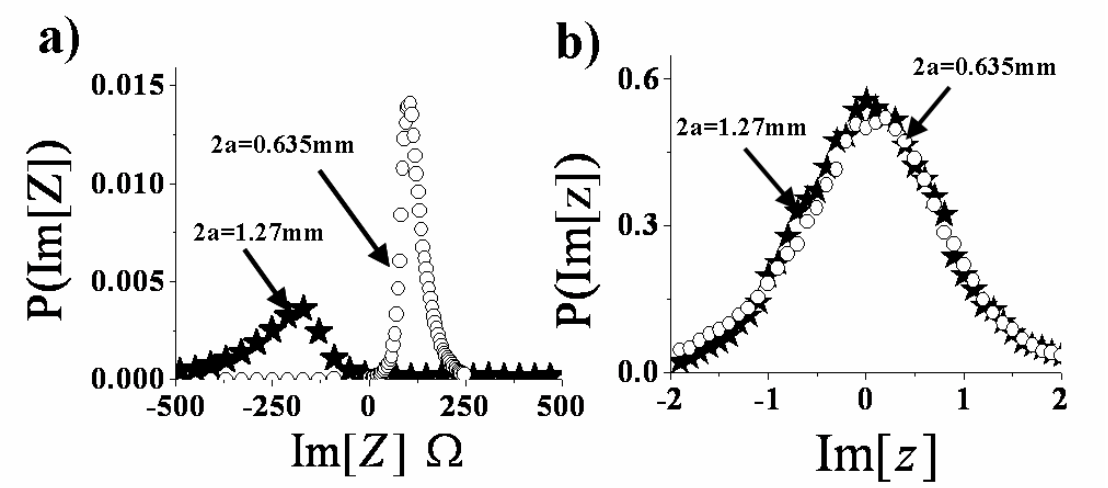

Fig.4.3: (a) shows the PDFs of the imaginary part of cavity impedance (Im[Z]) for two different antenna diameters, 2a=0.635mm (circles) and 2a=1.27mm (stars), from 9 GHz to 9.6 GHz. (b) The two curves in (a) scale together after using the prescription of **[25]** for the imaginary normalized cavity impedance (Im[z]).

Here, I test the degree of insensitivity of the universal properties of the normalized impedance PDFs to system-specific details and non-universal quantities **[45]**. Working in the 9 to 9.6 GHz range, I take two identical cavities and change only the diameter of the coupling wire in the antenna from $2a$ = 1.27 mm to 0.635 mm. As seen in Fig. 4.3(a), this difference causes a dramatic change in the raw Im[Z] PDF. However, this difference essentially disappears in the PDFs for the appropriately scaled impedance z as shown in Fig. 4.3(b).

Figure 4.4 shows the evolution of the PDFs for the normalized cavity impedance in the frequency range of 7.2-8.4 GHz for increasing loss **[45]**. The red

error bars which are roughly the size of the symbols in Fig. 4.4 are representative of the typical statistical binning error in the experimental PDFs. The data shows that as the losses within the cavity increase, the PDF of the normalized imaginary part of the impedance loses its long tails and begins to sharpen up, developing a Gaussian appearance. The normalized PDF of the real part smoothly evolves from being peaked below 1, into a Gaussian-like distribution that peaks at 1 and sharpens with increasing loss (also see Fig.2.3). The data-sets represented by the stars, triangles and hexagons in Fig. 4.4 correspond to α values of about 0.8, 4.2 and 7.6 respectively. These values of α $(=k^2A/(4\pi Q))$ were determined from first principles by specifying the values of the wave-number $k \approx 163\ m^{-1}$ corresponding to the center frequency of 7.8 GHz, enclosed physical-area of the cavity $A \approx 0.115\ m^2$ and typical loaded Q of the cavity within this frequency range. The typical loaded Q values for the cavity of about 300 , 60 and 35, for the data-sets represented by the stars, triangles and hexagons respectively, were extracted from $S_{11}(\omega)$ measurements for these different loss scenarios (see **Appendix [C]**). The experimentally obtained PDFs are overlaid with numerically generated PDFs from random matrix Monte Carlo simulations, shown in blue, for the real and imaginary parts of the normalized impedance (see section 2.5) for the same choice of α = 0.8, 4.2 and 7.6. There is a close overlap between the numerical results and the experimental results in all cases indicating that Random Matrix Theory satisfactorily describes both the real and imaginary parts of the normalized impedance PDFs for the same value of α .

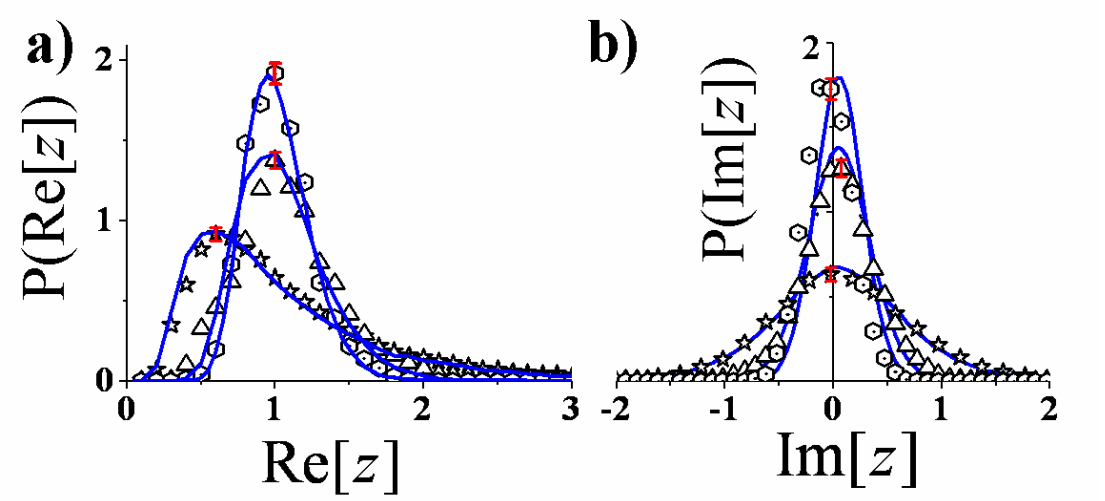

Fig.4.4: PDFs for the (a) real and (b) imaginary parts of the normalized cavity impedance z for a wave chaotic microwave cavity between 7.2 and 8.4 GHz with h = 7.87 mm and $2a$ = 1.27 mm, for three values of loss in the cavity (open stars: Loss-Case 0, triangles: Loss-Case 2, hexagons: Loss-Case 4). The red error bars which are roughly the size of the symbols indicate the typical statistical binning error in the experimentally obtained PDFs. Also shown in blue are single parameter numerical predictions from Random Matrix Theory for the choice of α corresponding to the data-sets represented by the stars, triangles and hexagons.

4.1.3 Universal Relation between the cavity loss-parameter α and the Variance of Re[z] and Im[z]

Having established that the "radiation-impedance" normalization procedure is valid and the universal fluctuations in the normalized impedance are well represented by Random Matrix Theory, I proceed to test another prediction of **[25]** which pertains to the relation between the variance of the real and imaginary parts of the TRS normalized impedance PDFs and the loss-parameter α (Eq.(2.6)).

My first step is to determine the value of α for my experimental Loss-Cases. I employ a sliding window of width 1 GHz wide (over which I assume that the value of α does not change significantly) that steps every 500 MHz over the frequency range of 6-12 GHz for my measured Loss-Case data. I define each 1 GHz window as a "data-set". Since it is a tedious process to determine the value of the cavity Q for each of these data-sets from the $S_{11}(\omega)$ measurements, I resort to an alternate method which involves fitting the experimentally determined normalized impedance PDFs to those generated numerically from Random Matrix Theory.

I numerically generate PDFs of the real and imaginary parts of the normalized impedance using random-matrix Monte-Carlo (MC) simulations with square matrices of size $N = 400$, and the value of $\alpha(=\alpha_{MC})$ in the simulations ranging from 0.1 to 15 in steps of 0.1 (see section 2.5). I then define a "PDF-error" function $\Delta e_\theta = -\sum_\theta |P_{MC}(\theta,\alpha_{MC}) - P_{\exp}(\theta,f)|$, which quantifies the error between the PDFs of the normalized impedance generated numerically from Monte-Carlo simulations (MC) and those determined experimentally (exp). Here, θ corresponds to either the real (Re[z]) or imaginary (Im[z]) parts of the normalized impedance PDFs ($P(\theta)$). Instances where there is good agreement between the normalized z PDFs obtained experimentally and the corresponding PDFs generated through random matrix Monte Carlo simulations for a given choice of α_{MC}, result in small magnitudes for the PDF-error function.

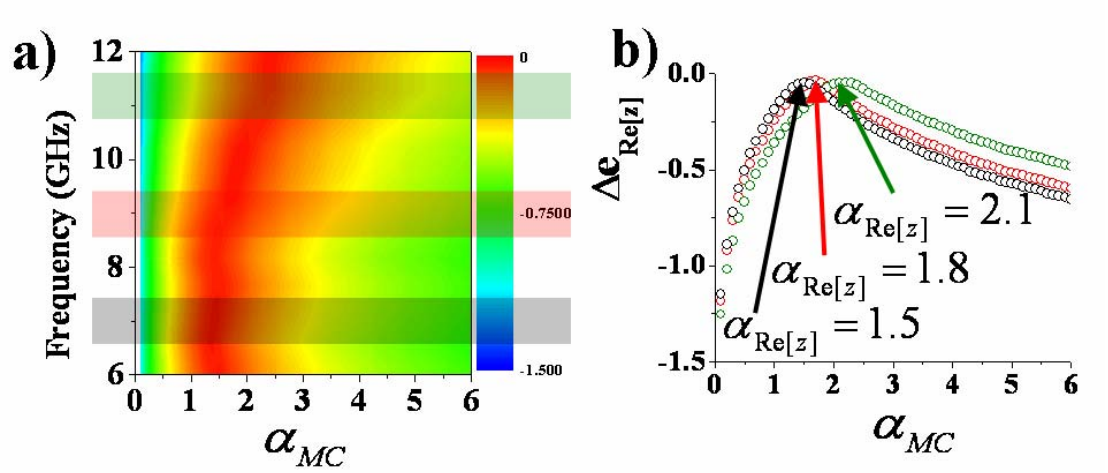

Fig.4.5: (a) Contour plot for the Loss-Case 0 PDF-error function $\Delta e_{\mathrm{Re}[z]}$ with the color-scale indicating the magnitude of the PDF-error function (blue=large error, red=small error). The red region indicates choices of α_{MC} in the numerical simulations for which there is good agreement (small error) between the experimentally obtained PDF for $\mathrm{Re}[z]$ and the corresponding PDF generated from random matrix Monte Carlo simulations. The black, red and green horizontal bands indicate 1GHz wide cavity data-sets for which the value of α is to be determined in (b). (b) The value of α_{MC} that results in the smallest error for $\Delta e_{\mathrm{Re}[z]}$ corresponding to the data-sets represented by the black, red and green horizontal bands in (a) is taken as the representative loss-parameter value ($\alpha_{\mathrm{Re}[z]}$) for that data-set.

Figure 4.5 (a) shows a contour plot of the PDF-error function $\Delta e_{\mathrm{Re}[z]}$ for a Loss-Case 0 cavity in the frequency range of 6 to 12 GHz. The experimental setup is as described in section 3.1, but the metallic perturbations used for generating the cavity-ensemble are of the type used in section 3.2. The color-scale indicates the

magnitude of the error function (blue=large error, red=small error). The red region indicates where there is good agreement between the experimentally obtained PDF for Re[z] and the corresponding PDF generated numerically from Monte-Carlo simulations for a specified value of α_{MC}. By taking 1GHz wide cavity data-sets, which are represented as the lightly-colored rectangular-bands parallel to the α_{MC}-axis in Fig. 4.5(a), I can uniquely determine the most-likely value of $\alpha_{MC}(=\alpha_{\mathrm{Re}[z]})$ which results in the smallest error for $\Delta e_{\mathrm{Re}[z]}$ corresponding to a given data-set. This is shown in Fig. 4.5(b) for three cavity data-sets in the frequency range of 6.6-7.6 GHz (black circles), 8.5-9.5 GHz (red circles) and 10.8-11.8 GHz (green circles) corresponding to the black, red and green horizontal bands in Fig. 4.5(a) respectively. As shown in Fig. 4.5(b), the most likely value of $\alpha_{MC}(=\alpha_{\mathrm{Re}[z]})$ that corresponds to the data-set represented by the black, red and green horizontal bands in Fig. 4.5(a) is $\alpha_{\mathrm{Re}[z]}=1.5\pm0.1$, $\alpha_{\mathrm{Re}[z]}=1.8\pm0.1$ and $\alpha_{\mathrm{Re}[z]}=2.1\pm0.1$ respectively. A similar analysis showing the contour plot of the PDF-error function $\Delta e_{\mathrm{Im}[z]}$ obtained by fitting the imaginary part of the normalized impedance PDFs is shown in Fig. 4.6(a), and is used for determining the most-likely value of $\alpha_{MC}(=\alpha_{\mathrm{Im}[z]})$ corresponding to the same three cavity data-sets in the frequency range of 6.6-7.6 GHz (black circles) with $\alpha_{\mathrm{Im}[z]}=1.4\pm0.1$, 8.5-9.5 GHz (red circles) with $\alpha_{\mathrm{Im}[z]}=1.7\pm0.1$ and 10.8-11.8 GHz (green circles) with $\alpha_{\mathrm{Im}[z]}=2.0\pm0.1$, that correspond to the black, red and green horizontal bands in Fig. 4.6(b) respectively. As indicated by the nature of the red-region in Fig. 4.5(a) (and Fig. 4.6(a)), it can be inferred that the value of $\alpha_{\mathrm{Re}[z]}$(and

$\alpha_{\mathrm{Im}[z]}$) smoothly increases as a function of frequency. This frequency-trend for $\alpha_{\mathrm{Re}[z]}$ and $\alpha_{\mathrm{Im}[z]}$ is expected considering that the losses within the cavity are also frequency-dependent and increase with frequency.

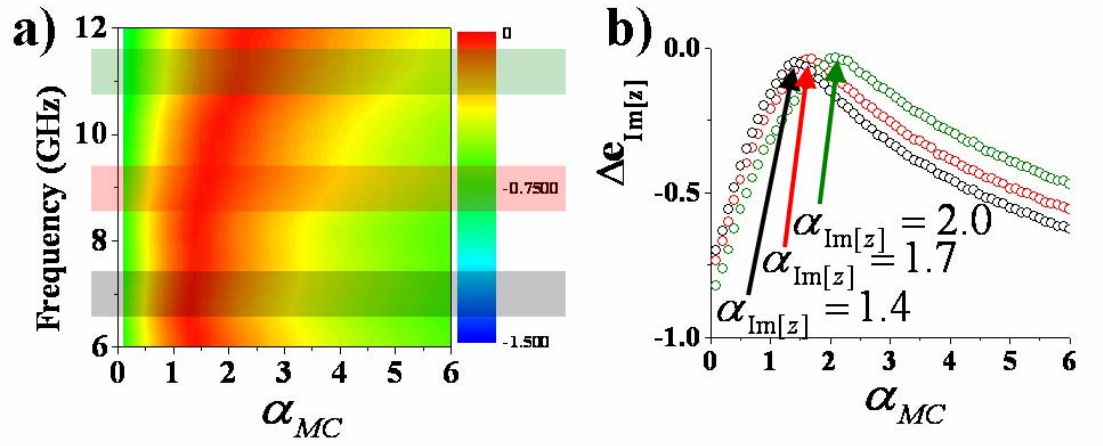

Fig.4.6: (a) Contour plot for the Loss-Case 0 PDF-error function $\Delta e_{\mathrm{Im}[z]}$ with the color-scale indicating the magnitude of the PDF-error function (blue=large error, red=small error). The red region indicates choices of α_{MC} in the numerical simulations for which there is good agreement (small error) between the experimentally obtained PDF for $\mathrm{Im}[z]$ and the corresponding PDF generated from random matrix Monte Carlo simulations. The black, red and green horizontal bands indicate 1GHz wide cavity data-sets for which the value of α is to be determined in (b). (b) The value of α_{MC} that results in the smallest error for $\Delta e_{\mathrm{Im}[z]}$ corresponding to the data-sets represented by the black, red and green horizontal bands in (a) is taken as the representative loss-parameter value ($\alpha_{\mathrm{Im}[z]}$) for that data-set.

The black circles in Fig. 4.7 show the derived values of $\alpha_{\mathrm{Re}[z]}$ and $\alpha_{\mathrm{Im}[z]}$ for all the 1GHz wide data-sets in Fig. 4.5 and Fig. 4.6 form 6 to 12 GHz. The red horizontal and vertical error bars indicate the estimated error in my determination of $\alpha_{\mathrm{Re}[z]}$ and $\alpha_{\mathrm{Im}[z]}$ respectively for each data-set. A linear fit (blue line) constrained to go through the origin gives the relation $\alpha_{\mathrm{Im}[z]} = (1.0 \pm 0.1)\alpha_{\mathrm{Re}[z]}$, which again testifies to the fact that a single loss-parameter simultaneously fits both the real and imaginary parts of the normalized impedance PDFs (within the limits of experimental error). In the results that follow in this chapter, I define the experimentally determined loss-parameter (α) to be the average value of $\alpha_{\mathrm{Re}[z]}$ and $\alpha_{\mathrm{Im}[z]}$ obtained from the PDF fitting procedure for that data-set.

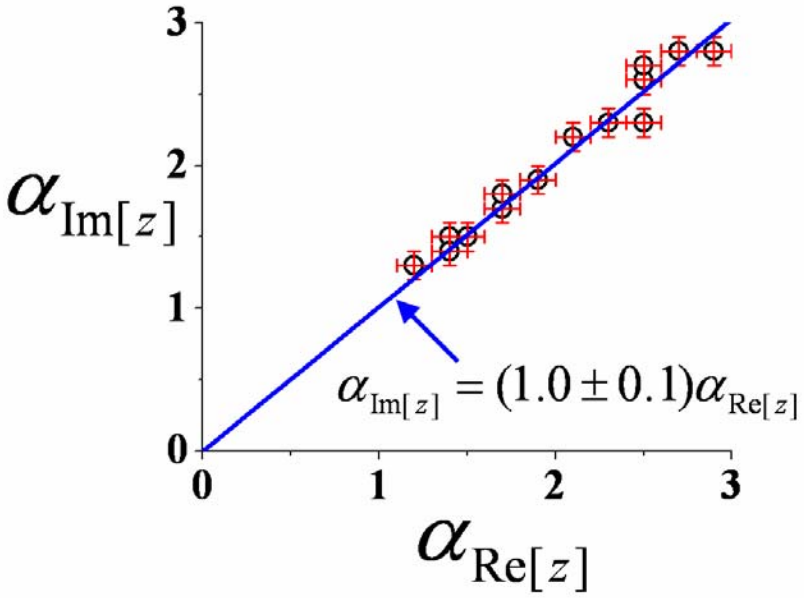

Fig. 4.7: Comparison of the derived loss-parameter values $\alpha_{\mathrm{Re}[z]}$ and $\alpha_{\mathrm{Im}[z]}$ for the data-sets shown in Fig. 4.5(a) and Fig. 4.6(a) are shown as the black circles and are obtained by fitting the PDFs of the real and imaginary parts of the normalized

impedance with those generated numerically from random matrix Monte Carlo simulations. The red errors bars indicate the estimated error in the determination of $\alpha_{\mathrm{Re}[z]}$ and $\alpha_{\mathrm{Im}[z]}$. The blue line which is a linear fit to all the black circles shows that for all data-sets $\alpha_{\mathrm{Re}[z]} \cong \alpha_{\mathrm{Im}[z]}$.

The black, red and green circles in Fig. 4.8 show the experimentally obtained PDFs of the real (Fig. 4.8 (a)) and imaginary (Fig. 4.8 (b)) parts of the normalized impedance z for the 1GHz wide data-sets corresponding to the black (6.6-7.6 GHz), red (8.5-9.5 GHz) and green (10.8-11.8 GHz) lightly-colored rectangular-bands, respectively, shown in Fig. 4.5(a) and Fig. 4.6(a). The solid black, red and green solid lines in Fig. 4.8 are numerically generated PDFs from random matrix Monte Carlo simulations for values $\alpha = 1.45$, $\alpha = 1.75$ and $\alpha = 2.05$ respectively. It can be seen that in all three cases, the agreement between the experimentally obtained PDFs and those generated numerically are in good agreement.

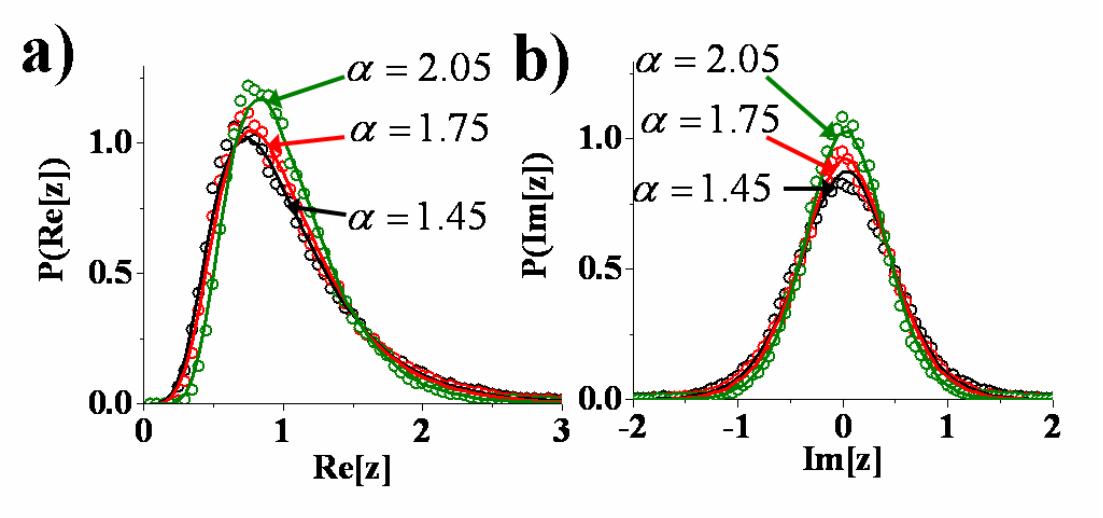

Fig. 4.8: (a) Experimentally obtained PDFs of the real part of the normalized impedance z for the data-sets represented by the lightly-colored rectangular-bands in Fig. 4.5(a)- black circles: 6.6-7.6 GHz; red circles: 8.5-9.5 GHz, green circles: 10.8-11.8 GHz. (b) Experimentally obtained PDFs of the imaginary part of the normalized impedance z for the data-sets represented by the lightly-colored rectangular-bands in Fig. 4.6(a)- black circles: 6.6-7.6 GHz; red circles: 8.5-9.5 GHz, green circles: 10.8-11.8 GHz. The black, red and green solid lines in (a) and (b) are predictions from Random Matrix Theory for the values of α (=1.45, 1.75 and 2.05) derived from the PDF fitting method for each of the data-sets indicated by the black, red and green circles respectively.

Now that I have established a robust method to determine the value of the loss-parameter α corresponding to my data-sets, I proceed to the second step of the analysis for experimentally testing the relation between the variance of the real and imaginary parts of the normalized impedance and the loss-parameter α **[45]**. Reference **[25]** predicts that in the limit $\alpha >> 1$, the variance (σ^2) of the real and

imaginary parts of the time-reversal symmetric normalized impedance PDFs is related to α through Eq.(2.6).

In Fig. 4.9, the hollow stars (circles) represent the variance σ^2 of the real (imaginary) part of the normalized impedance for Loss-Case 0 and Loss-Case 2 cavities with cavity height *h*=7.87mm. The red "+"("×") represent the variance σ^2 of the real (imaginary) part of the normalized impedance for Loss-Case 0 cavity with cavity height *h*=1.78 mm. In all cases, the variance of the real and imaginary parts of the normalized impedance PDFs are in close agreement. The values of the loss-parameter α for each of the symbols which correspond to a particular data-set between 6 and 12 GHz was determined by the PDF fitting method discussed previously.

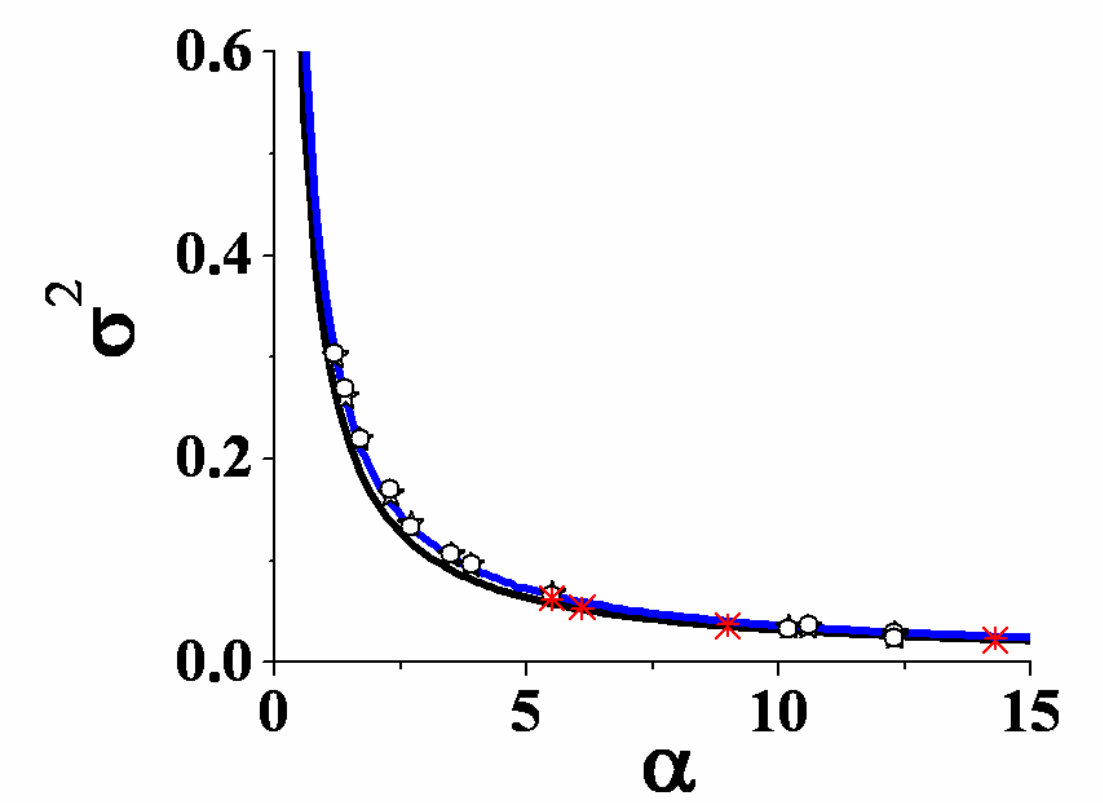

Fig. 4.9: Plot of variances of $\mathrm{Re}[z]$ (stars) and $\mathrm{Im}[z]$ (circles) versus fit parameter α for Loss-Case 0 and Loss-Case 2 cavities of height $h = 7.87mm$. Plot of variances of $\mathrm{Re}[z]$ ("+") and $\mathrm{Im}[z]$ ("×") versus fit parameter α for Loss-Case 0 cavity of height $h = 1.78mm$. The black curve is the function $\sigma^2 = 1/(\pi\alpha)$. The blue curve is generated numerically from Random Matrix Theory.

The black curve in Fig. 4.9 is the function $\sigma^2 = 1/(\pi\alpha)$. It can be observed that for values of $\alpha < 5$, the experimental data (shown by the symbols) does not conform with the black curve. This is expected considering Eq. (2.6) is valid in the limit of large α ($\alpha >> 1$). The blue curve is generated numerically from random matrix Monte-Carlo simulations with square matrices of size $N = 400$, and the value

of α in the simulations ranging from 0.1 to 15 in steps of 0.1 (see section 2.5). There is good agreement between the experimental data shown by the symbols and the blue curve for values of $\alpha < 5$. For values of $\alpha > 5$, the difference between the black and the blue curve is difficult to differentiate given the current experimental precision. However, overall there is good agreement between the data and the theoretical predictions of **[25]** (for $\alpha > 5$) and with predictions from Random Matrix Theory (for $\alpha < 5$). This suggests another method to determine the value of the loss-parameter α for the data-sets based on the variances of the normalized impedance PDFs, which is elucidated in Chapter 5.

4.1.4 Absorber Perimeter Ratio (Ξ)

This subsection presents results that show my ability to experimentally fine-tune the value of the cavity loss-parameter α by controlling the number of microwave absorbing strips placed within the cavity. As explained in chapter 3, the degree of loss in the cavity can be controlled by placing 15.2 cm long microwave-absorbing strips along the inner side-walls of the cavity. I thus introduce an α-control parameter called the "Absorber Perimeter Ratio"(Ξ), which is defined as the ratio of the perimeter of the cavity covered with absorbing strips to the total cavity perimeter. The parameter Ξ can vary from 0 to 1 corresponding to the Loss-Case 0 or the "Radiation-Case" cavity setups respectively. Figure 4.10 examines the dependence of the experimentally determined value of α versus Ξ. Each symbol corresponds to the value of α for a given Loss-Case cavity in the frequency range of 7.2-8.4 GHz, i.e., Loss Case 0- hollow star; Loss Case 1- hollow circle; Loss Case 2- hollow triangle; Loss Case 3- hollow square; Loss Case 4- solid star. The α values

were determined by the PDF fitting method described in section 4.1.3. The red error bars, which are roughly the size of the symbols in Fig. 4.10, indicate the estimated error in the determination of α. The data shows a clear linear relationship of α on the absorber perimeter ratio Ξ. This linear relationship is expected because $1/Q$ is proportional to the dissipated power in the cavity, which scales with the amount of microwave absorber placed in the cavity. A linear fit (blue line) of the data is quite accurate and shows a zero-crossing for α at $\alpha = -0.035$. This suggests that the empty cavity losses correspond to covering the walls of a perfectly conducting cavity with 3.5% coverage of microwave absorber **[58]**.

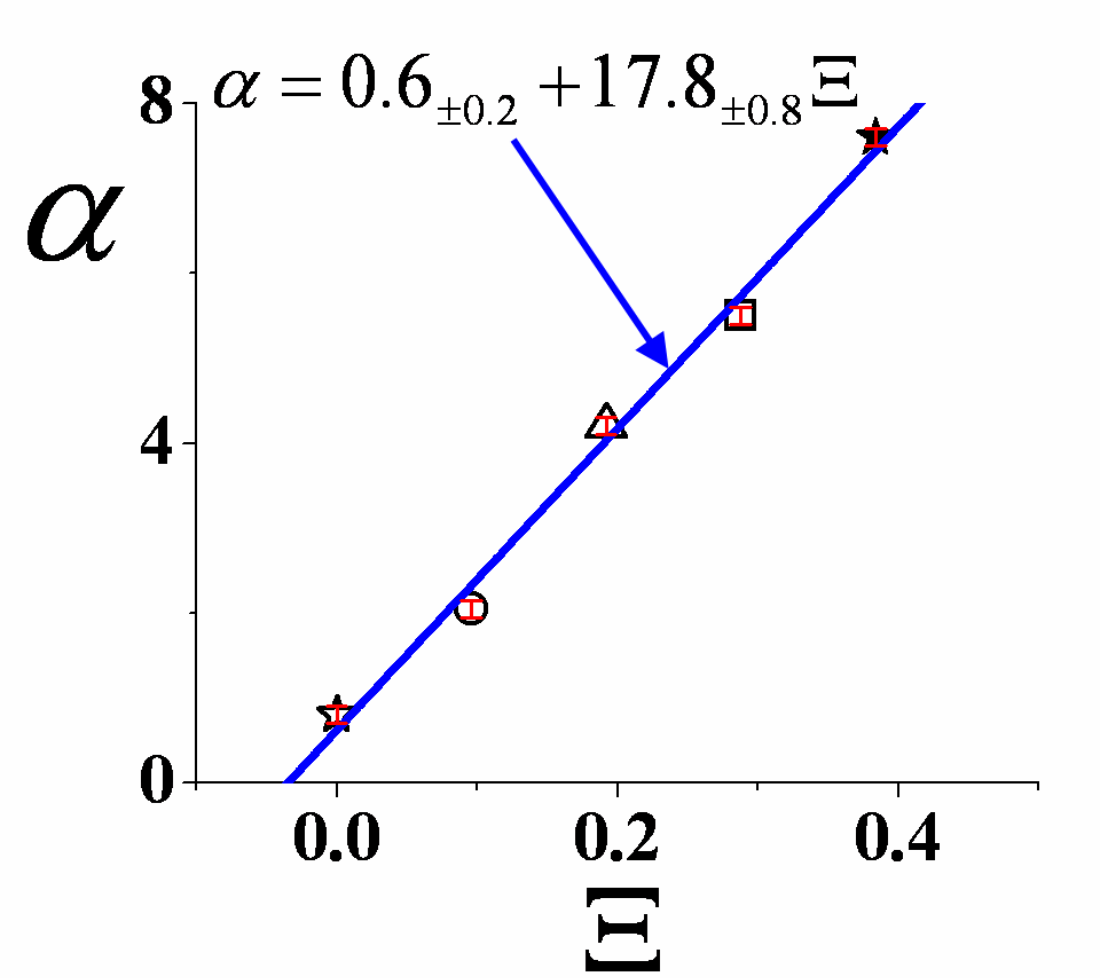

Fig. 4.10: The relationship between the cavity loss-parameter α and the absorber perimeter ratio (Ξ) is shown between 7.2 and 8.4 GHz. The symbols represent Loss Case 0- hollow star; Loss Case 1- hollow circle; Loss Case 2- hollow triangle; Loss Case 3- hollow square; Loss Case 4- solid star. The best linear fit to all the data points is shown as the solid blue line. The x-intercept of this line indicates the Ξ-value required to make a loss-less cavity have the same α-value as the experimental Loss-Case 0 cavity of Fig. 3.1(a).

4.2 Experimental Results for Normalized Scattering Coefficient s

In this section, I present my experimental findings for the statistical properties of the normalized scattering coefficient *s,* for different coupling geometries and degrees of loss. This section is divided into five parts. In the first part, I give an example for the PDF of *s* at a specific degree of quantified loss and a certain coupling geometry. In the second part, I fix the degree of quantified loss, but vary the coupling by using coaxial cable antennas having inner conductors of different diameters (2a=1.67mm and 2a=0.635mm). The PDF histograms for the magnitude and phase of *s* in these two cases will be compared. The third part tests the trend of the PDF of $|s|^2$ for a given coupling geometry and for three different degrees of quantified loss. Good agreement with Random Matrix Theory is found in all cases. In the fourth part, I experimentally test a relation between the cavity and radiation power reflection coefficients as predicted by **[25]**. Finally, in the fifth part, I show that it is possible to accurately reconstruct the statistical aspects of the raw cavity scattering coefficient (magnitude and phase) given only the value of α and the measured radiation scattering coefficient.

4.2.1 Statistical Independence of $|s|$ and ϕ_s

The first example I give is based on Loss-Case 0 (i.e., no absorbing strips in the cavity) and coupling through a coaxial cable with inner diameter 2a=1.27mm **[46]**. Having obtained the normalized impedance *z*, I transform *z* into the normalized scattering coefficient *s* using Eq. (2.8). Since the walls of the cavity are not perfect conductors, the normalized scattering coefficient *s* is a complex scalar with modulus

less than 1. (In Loss-Case 0, most of the loss occurs in the top and bottom cavity plates since they have much larger area than the side walls.) Based on Dyson's circular ensemble, one of the most important properties of s is the statistical independence of the scattering phase ϕ_s and the magnitude $|s|$. Figure 4.11(a) shows a contour density plot of s in the frequency range of 6 to 9.6 GHz for Loss Case 0. The grayscale level at a given point in Fig. 4.11(a) indicates the number of points for $\{\mathrm{Re}[s], \mathrm{Im}[s]\}$ that fall within a local rectangular region of size 0.02×0.02. Next, arbitrary angular slices of this distribution that subtend an angle of $\pi/4$ radians at the center are taken and the histogram approximations to the PDF of $|s|$ using the points within those slices are computed. The corresponding PDFs of $|s|$ for the three slices are shown in Fig. 4.11(b). It can be observed that these PDFs are essentially identical, independent of the angular slice. Figure 4.11 (c) shows PDFs of ϕ_s computed for all the points that lie within two annuli defined by $0 \le |s| \le 0.3$ (stars) and $0.3 < |s| \le 0.6$ (hexagons). These plots support the hypothesis that the magnitude of s is statistically independent of the phase ϕ_s of s and that ϕ_s is uniformly distributed in $-\pi$ to π. To my knowledge, this represents the first experimental test of Dyson's circular ensemble hypothesis for wave-chaotic scattering.

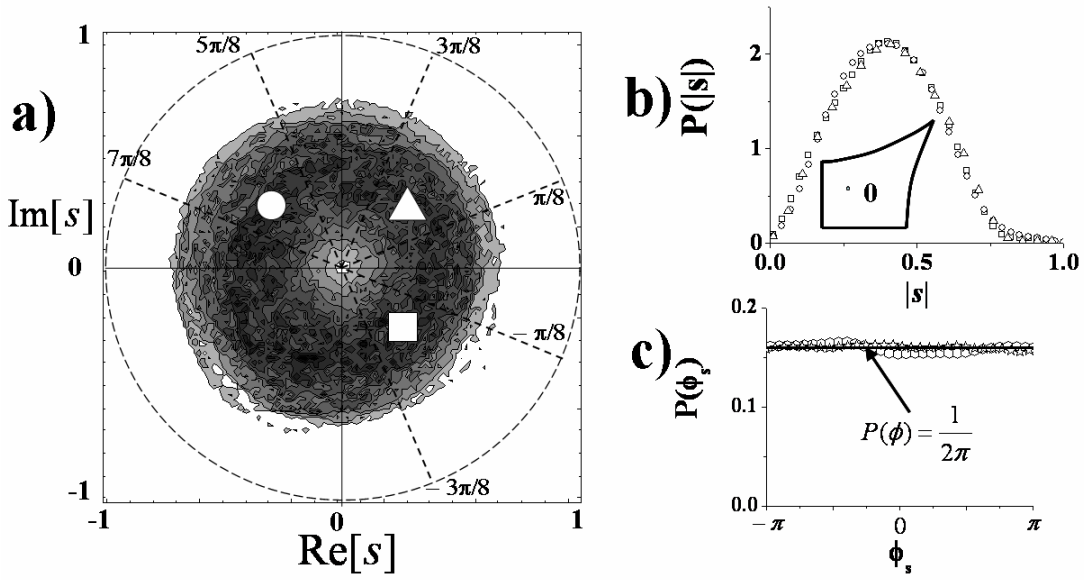

Fig. 4.11: (a) Polar contour density plot for the real and imaginary components of the normalized cavity s ($s = |s| \exp(i\phi_s)$) for Loss-Case 0 in the frequency range of 6 to 9.6 GHz. The angular slices with the symbols (triangles, circles, squares) indicate the regions where the PDF of $|s|$ is calculated and shown in (b). Observe that the PDF of the three regions are essentially identical. (c) The PDF of the phase ϕ_s of the normalized scattering coefficient s for two annuli defined by $0 \le |s| \le 0.3$ (stars) and $0.3 < |s| \le 0.6$ (hexagons). Observe that these phase PDFs are nearly uniform in distribution. The uniform distribution is shown by the solid line ($P(\phi) = 1/2\pi$). This is consistent with the prediction that the $|s|$ is statistically independent of the phase ϕ_s, of s.

4.2.2 Detail-Independence of s

As shown in the previous section for the normalized impedance z, here I verify that the normalized s also does not include any artifacts of system-specific, non-ideal

coupling **[46]**. I take two identical wave chaotic cavities and change only the inner diameter of the coupling coaxial cable from 2a=1.27 mm (represented as the blue stars in Fig. 4.12) to 2a=0.635 mm (represented as the red circles in Fig. 4.12). Since the modification of the coaxial cable size barely changes the properties of the cavity, I assume that the loss parameters in these two cases are the same. The difference in the coupling geometry manifests itself as gross differences in the distribution of the raw cavity scattering coefficients S. This is clearly observable for the PDFs of the cavity power reflection coefficient $|S|^2$ as shown in Fig. 4.12(a) and the PDFs for the phase of S (denoted ϕ_S) shown in Fig. 4.12(c), for Loss-Case 0 over a frequency range of 6 to 11.85 GHz. However, after measurement of the corresponding radiation impedance and the normalization procedure described above, I observe that the PDFs for the normalized power reflection coefficients are nearly identical, as shown in Fig. 4.12 (b) for $|s|^2$ and the phase (ϕ_s) in Fig. 4.12(d). This supports the theoretical prediction that the normalized scattering coefficient *s* is a universal quantity whose statistics does not depend on the nature of the coupling antenna. Similarly, in Fig. 4.12(c), the phase ϕ_S of the cavity scattering coefficient S shows preference for certain angles. This is expected because of the non-ideal coupling (impedance mismatch) that exists between the antenna and the transmission line. After normalization, the effects of non-ideal coupling are removed and only the scattering phase of an ensemble of ideally coupled chaotic systems (in which all scattering phases are equally likely) is seen. Hence, consistent with theoretical expectations of **[25]**, the phase ϕ_s of normalized *s* data show an approximately uniform distribution (Fig.4.12(d)).

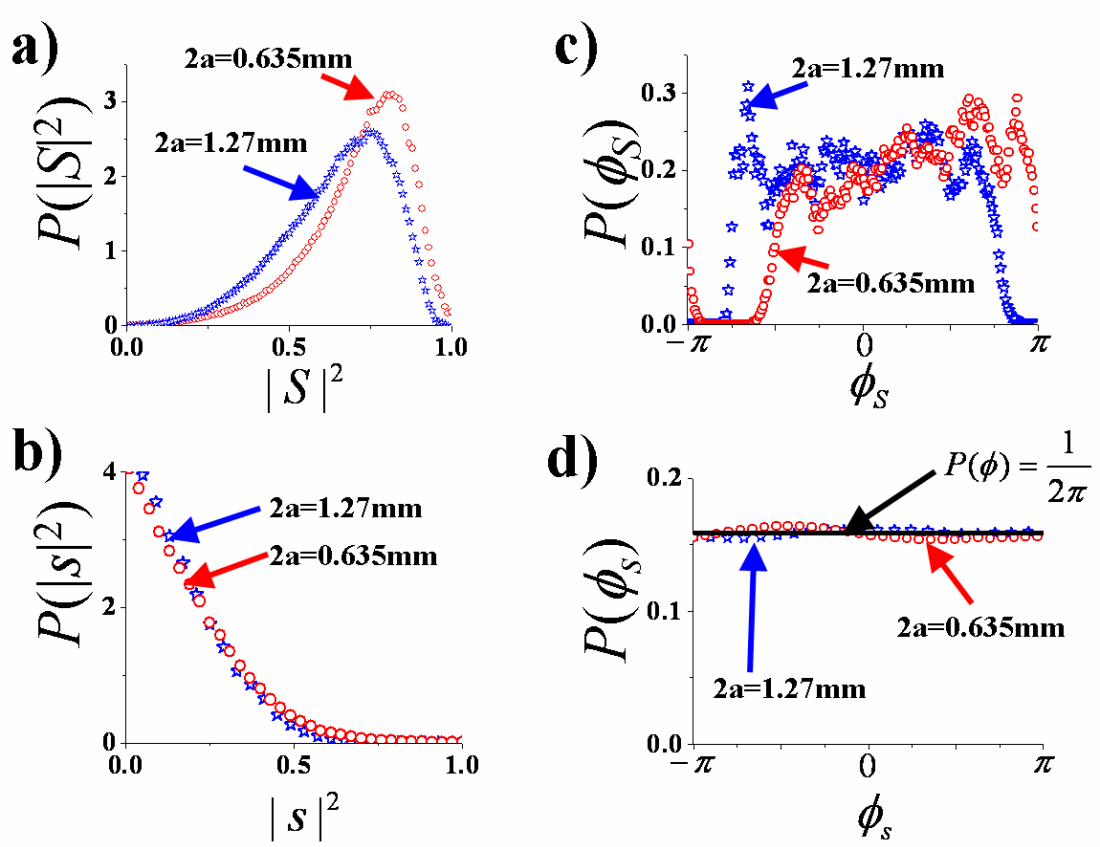

Fig. 4.12: (a) PDF for the un-normalized Loss-Case 0 cavity $|S|^2$ in the frequency range of 6 to 11.85 GHz for two different coupling antenna diameters 2a = 0.635 mm (red circles) and 2a = 1.27 mm (blue stars). (b) PDF for the normalized cavity $|s|^2$ in the frequency range of 6 to 11.85 GHz for two different coupling antenna diameters 2a = 0.635 mm (red circles) and 2a = 1.27 mm(blue stars). Note that the disparities seen in (a) on account of the different coupling geometries disappear after normalization. (c) PDF for the un-normalized cavity phase (ϕ_S) for Loss Case 0 in the frequency range of 6 to 11.85 GHz for two different coupling antenna diameters 2a = 0.635 mm (red circles) and 2a = 1.27 mm (blue stars). (d) PDF for the normalized cavity phase (ϕ_s) in the frequency range of 6 to 11.85 GHz for two different coupling antenna diameters 2a = 0.635 mm (red circles) and 2a = 1.27 mm

(blue stars). The normalized phase PDFs for the stars and circles in (d) are nearly uniformly distributed (the black line in (d) shows a perfectly uniform distribution $P(\phi) = 1/2\pi$).

4.2.3 Variation of s with loss

Having established that the coupling geometry is irrelevant for the distribution of s, I fix the coupling geometry (coaxial cable with inner diameter 2a=1.27 mm) and vary the degree of quantified loss within the cavity. Three loss cases will be considered, namely, Loss-Case 0, 1 and 3 **[46]**.

The symbols in Fig. 4.13 (presented on a semi-log scale) show the PDF of the normalized power reflection coefficient ($r = |s|^2$) in the frequency range 6.5 to 7.8 GHz for three different Loss-Cases (stars: Loss-Case 0, circles: Loss-Case 1, squares: Loss-Case 3). These data-sets correspond to α-values of 0.8 ± 0.1(stars), 2.4 ± 0.1(circles) and 6.5 ± 0.1(squares), which were obtained from the PDF fitting method described in section 4.1.3. The solid blue lines are the numerical PDFs of r, i.e., $P(r)$ (presented on a semi-log scale) generated from random matrix Monte Carlo simulations (see section 2.5) for values of α=0.8, 2.4 and 6.5. I observe that the predictions from Random Matrix Theory conforms well to my experimental data for all degrees of loss.

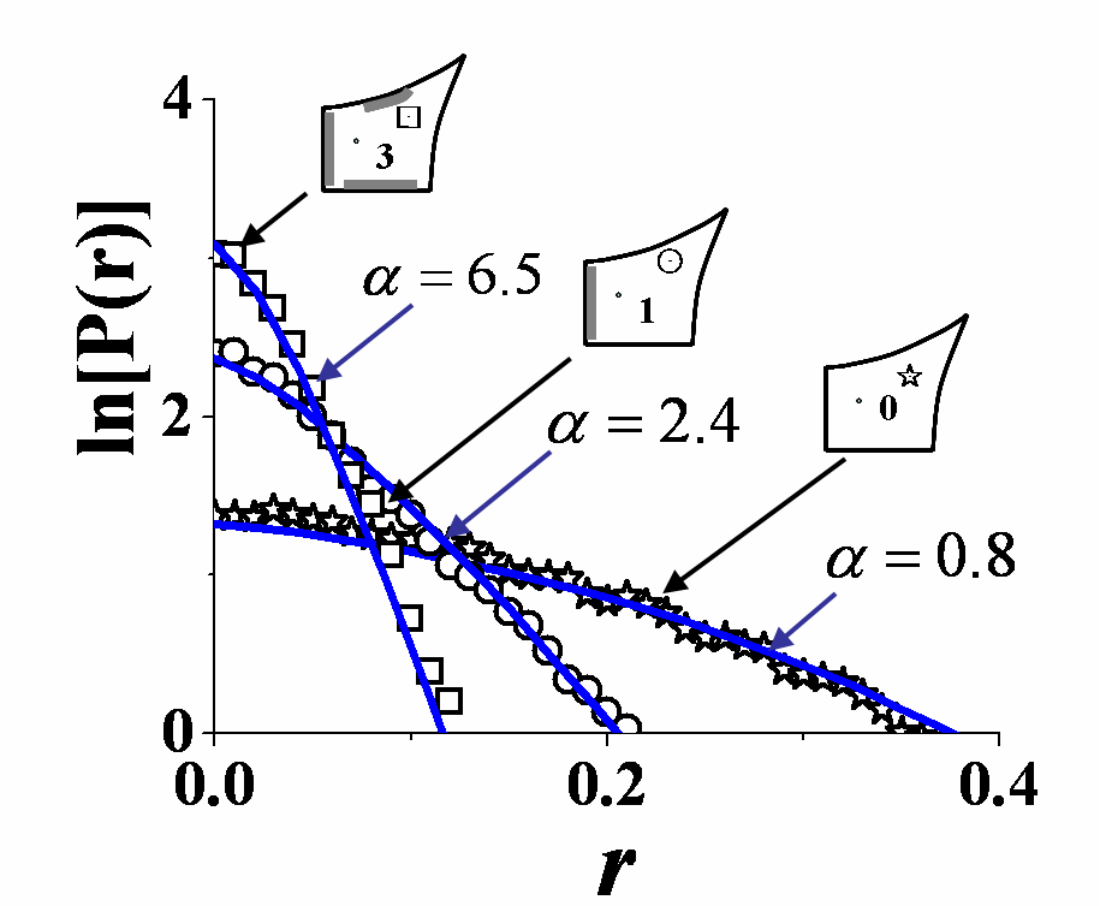

Fig.4.13: PDF for the normalized power reflection coefficient $r = |s|^2$ on a natural log scale for Loss Case 0, 1, 3 (stars, circles and squares respectively) in the frequency range of 6.5 to 7.8 GHz. Also shown is the prediction from Random Matrix Theory (solid lines) for $P(r)$ using the values of α obtained from the PDF fitting method described in section 4.1.3.

4.2.4 Relation Between Cavity and Radiation Reflection Coefficients

In this subsection, I would like to examine how the measured cavity power reflection coefficient depends only on the radiation scattering coefficient and losses in

the cavity **[46]**. Reference **[25]** predicts that the average value of the cavity power reflection coefficient $\overline{|S|^2}$ depends only on the magnitude of the radiation scattering coefficient ($|S_{rad}|$) and the loss parameter α, and is independent of the phase of S_{rad}. The quantity $|S_{rad}|$ is related to the radiation impedance ($Z_{rad} = \mathrm{Re}[Z_{rad}] + j\,\mathrm{Im}[Z_{rad}]$) through the transformation,

$$|S_{rad}| = \sqrt{\frac{(\mathrm{Re}[Z_{rad}] - Z_o)^2 + (\mathrm{Im}[Z_{rad}])^2}{(\mathrm{Re}[Z_{rad}] + Z_o)^2 + (\mathrm{Im}[Z_{rad}])^2}}\,. \tag{4.1}$$

I consider a cavity having quantified loss (Loss Case 0, 1 and 3), with a coupling port of diameter 2a=1.27 mm and over the frequency range of 6.5 to 7.8 GHz. Having experimentally obtained the normalized z as described in section 3.1, I then simulate an ensemble of similar cavities but with different coupling "geometries". This is done by means of a lossless two-port impedance transformation **[25]** of the z data, as described by the relation,

$$z' = \frac{1}{(1/z + j\xi)}\,. \tag{4.2}$$

which corresponds to adding a reactive impedance $-j/\xi$ in parallel with the impedance z.

The quantity z' thus simulates the impedance of a hypothetical cavity that is non-ideally coupled to the excitation port, and the coupling geometry is characterized by the real factor ξ, which can be varied in a controlled manner. I also define a transformed radiation impedance (z'_{rad}) given by,

$$z'_{rad} = \frac{1}{(1 + j\xi)}\,. \tag{4.3}$$

For the generation of z'_{rad}, the factor ξ is varied over the same range of values as used to generate z'. Having determined z' and its corresponding z'_{rad}, I determine the scattering coefficients s' and s'_{rad} through the transformations,

$$s' = (z' - 1)/(z' + 1) \tag{4.4}$$

$$s'_{rad} = (z'_{rad} - 1)/(z'_{rad} + 1) \tag{4.5}$$

A range of ξ values are chosen to cover all possible coupling scenarios. I then plot the average of $|s'|^2$ (i.e., $\overline{|s'|^2}$) as a function of s'_{rad}. This approach is followed for all three loss cases (Loss case 0, 1 and 3) resulting in the data sets with star, circles and squares, respectively, in Fig. 4.14.

First note that all curves originate from the point $\overline{|s'|^2} = |s'_{rad}| = 1$, which may be thought of as the perfectly mismatched case. Next consider $|s'_{rad}| < 1$, and observe that as the losses increase, the curves shift downwards for a fixed coupling (characterized by $|s'_{rad}|$). This is intuitively reasonable because, as the absorption (losses) within the cavity increases, less signal is expected to return to the antenna (i.e. smaller $\overline{|s'|}$) for a given coupling $|s'_{rad}|$. From the PDF fitting method described in section 4.1.3, I determine α to be 0.8 ± 0.1(stars), 2.4 ± 0.1(circles) and 6.5 ± 0.1(squares) for Loss-Case 0, 1 and 3 respectively. The solid blue lines in Fig. 4.14 are obtained from the Random Matrix Theory using Monte Carlo simulations (see section 2.5) by first generating an ensemble of the normalized impedance z with the appropriate values for α (=0.8, 2.4 and 6.5). Next, this ensemble of z is transformed using Eq. (4.2) and Eq.(4.3) with the same range of coupling factors (ξ)

as used for the experimentally determined z'. Finally, these values of z' are converted to s' using Eq.(4.4). Good agreement between the numerical simulations from Random Matrix Theory (solid blue lines in Fig. 4.14) and the experimentally derived points is observed.

For a given lossy cavity one can also consider its lossless N-port equivalent. By the lossless N-port equivalent I mean that the effect of the losses distributed in the walls of our cavity can be approximated by a lossless cavity with $N-1$ extra perfectly-coupled (pc) ports through which power coupled into the cavity can leave. The point $|S_{rad}|=|s'_{rad}|=0$ in Fig. 4.14 corresponds to perfect coupling. In this case, Ref. **[25]** predicts that the vertical axis intercept of these curves corresponds to the lossless N-port equivalent of the distributed losses within the cavity; i.e., at $|s'_{rad}|=0$, **[25]** predicts that $\overline{|s'|^2}\Big|_{pc}=2/(N+1)$ (for time-reversal symmetric wave chaotic systems). Thus, in the experiment the quantified loss in Loss-Case 0, 1 and 3 is equivalent to about 11, 24 and 45 perfectly-coupled ports, respectively. In other words, for all intents and purposes, the cavity can be considered loss-less but perfectly coupled to this number of ports.

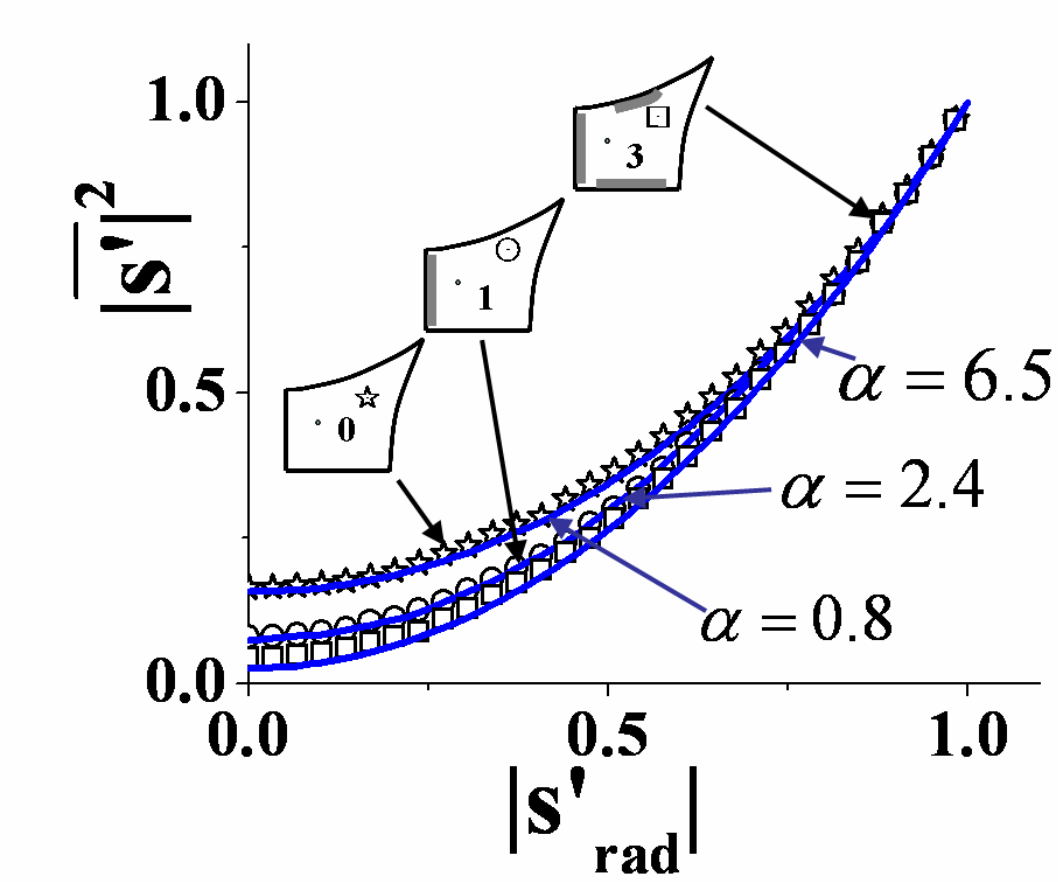

Fig. 4.14: Dependence of the average of the cavity power reflection coefficient $\overline{|s'|^2}$ on the magnitude of the radiation scattering coefficient $|s'_{rad}|$, for different loss cases (Loss Case 0: stars; Loss Case 1: circles; Loss Case 3: squares). The data is shown for the frequency range of 6.5 to 7.8 GHz and corresponds to estimated α-values of 0.8 ± 0.1 (stars), 2.4 ± 0.1 (circles) and 6.5 ± 0.1 (squares). Also shown are the numerical simulations from Random Matrix Theory based upon α-values of 0.8, 2.4 and 6.5 (solid blue lines).

4.2.5 Recovering Raw Cavity S given S_{rad} and α

In sections 4.2.1 through 4.2.4, I used the radiation impedance (Z_{rad}), or the radiation scattering coefficient (S_{rad}), as a tool to characterize the non-ideal coupling (direct processes) between the antenna and the cavity. This quantity is measurable and is only dependent on the local geometry around the port. References **[35, 36]** use configuration and frequency averaged scattering data to obtain an approximation to the true ensemble average, $<< S >>$. For a given center frequency f_0, this procedure relies on the satisfaction of two requirements: first the range of Δf must be large enough to include a large number of modes; second, S_{rad} must vary little over the range of Δf.

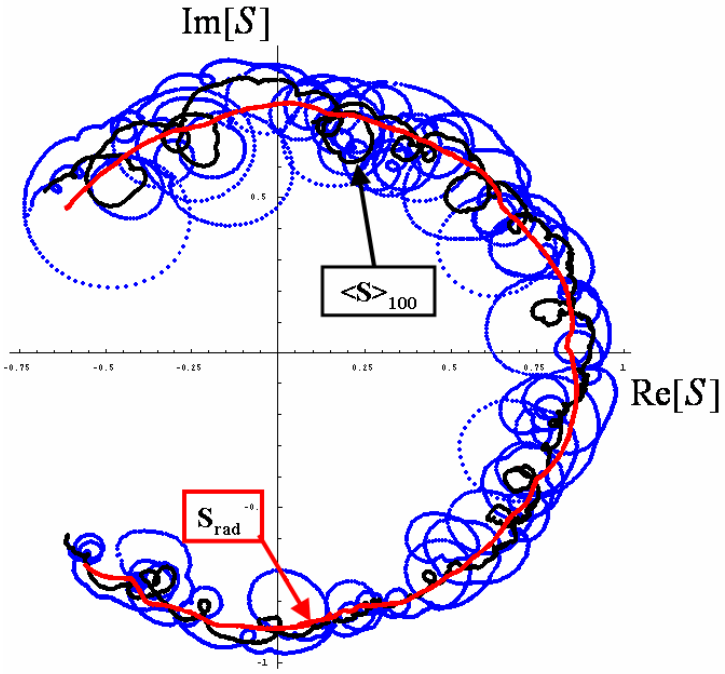

Fig. 4.15: Polar plot for the cavity scattering coefficient $S = \mathrm{Re}(S) + j\,\mathrm{Im}(S)$ is shown for a frequency range of 6 to 12 GHz for Loss-Case 0 and with a coupling port of diameter 2a = 1.27 mm. The blue trace represents one single rendition of the cavity for a selected position and orientation of the perturbers. The black trace is the configurational average $\langle S \rangle_{100}$ over one hundred different locations and orientations of the perturbers within the cavity. The red trace shows the radiation scattering coefficient for the same port.

The nature of the variation of S with frequency is illustrated in Fig. 4.15, where a plot $\{\mathrm{Re}(S), \mathrm{Im}(S)\}$ of the complex scattering coefficient for a cavity in the frequency range of 6 to 12 GHz is shown **[46]**. The blue trace shows results for S for a single configuration of the cavity corresponding to a given position and orientation of the perturbers (Fig. 3.1(a)). Isolated resonances are seen as circular loops in the

polar plot. The degree of coupling is indicated by the diameter of the loops. Frequency ranges where the coupling is good would manifest themselves as large loops, while those frequency ranges with poor coupling result in smaller loops. By averaging one-hundred such different configurations of this cavity for different positions and orientations of the perturber, the black trace denoted as $\langle S \rangle_{100}$ is obtained. Note that even with one hundred cavity renditions, the fluctuations in $\langle S \rangle_{100}$ are still present and are seen as the meanders in the black trace. The red trace, which corresponds to the radiation scattering coefficient for this antenna geometry, is devoid of such fluctuations (because there are no reflected waves from the far walls back to the port) and is easily obtainable in practice without resorting to generating large configurationally averaged sets of cavities. Moreover, since the radiation impedance of the port is also a function of frequency, there is no constraint on the frequency span where the analysis for obtaining the universal statistics of s (or z) can be carried out.

To quantitatively illustrate this point, I simulate the non-universal scattering statistics of a given cavity for a given type of coupling using only the measured radiation impedance of the coupling port and the numerically generated normalized impedance z from Random Matrix Theory, which depends only upon the net losses within the cavity **[46]**. I consider a Loss Case 0 cavity, over a frequency range of 6 to 7.5GHz, which is excited by means of a coaxial cable of inner diameter (2a=1.27mm). The variation in $|< S >_{100}|$ (inset of Fig. 4.16 (b)) indicates that the coupling characteristics for this setup fluctuate over the given frequency range, undergoing roughly four or five oscillations over a range in $|< S >_{100}|$ of order 0.2.

Thus the frequency averaged $|< S >_{100}|$ would be expected to be an unreliable estimate to parameterize the coupling over this frequency range.

I can estimate the value of α $(= k^2 A/(4\pi Q))$ from first principles by specifying the values of the wave-number $k(\approx 142\ m^{-1})$ corresponding to the center frequency of 6.75 GHz, enclosed physical-area of the cavity $A \approx 0.115\ m^2$ and typical loaded $Q \sim 225$ (from $S_{11}(\omega)$ measurements) of the cavity within this frequency range (see **Appendix [C]**); thereby yielding an estimated $\alpha \cong 0.8$. I use this α–value to generate an ensemble of z from random-matrix Monte-Carlo simulations with square matrices of size $N = 400$ (see section 2.5). I then combine it with the measured $Z_{rad}(\omega)$ of the antenna using Eq.(2.4), and finally employ Eq.(3.1) to obtain an estimate of the non-universal system-specific scattering coefficient, which I denote as $\tilde{S}$.

In Fig. 4.16(a), the PDF of $|\tilde{S}|^2$ is shown as the solid red trace, while the experimentally measured PDF of $|S|^2$ is shown as the black stars. While in Fig. 4.16 (b), the PDF of $\phi_{\tilde{S}}$ is shown as the solid red trace with experimentally measured PDF of ϕ_S shown as the black stars. I observe relatively good agreement between the numerically generated estimate and the actual data. This result validates the use of the radiation impedance (scattering coefficient) to accurately parameterize the system-specific, non-ideal coupling of the ports and also provides a way to predict beforehand the statistical properties of other complicated enclosures non-ideally

coupled to external ports. An extension of this result to predict the range of voltages induced within a computer box (three dimensional cavity) is explained in Chapter 8.

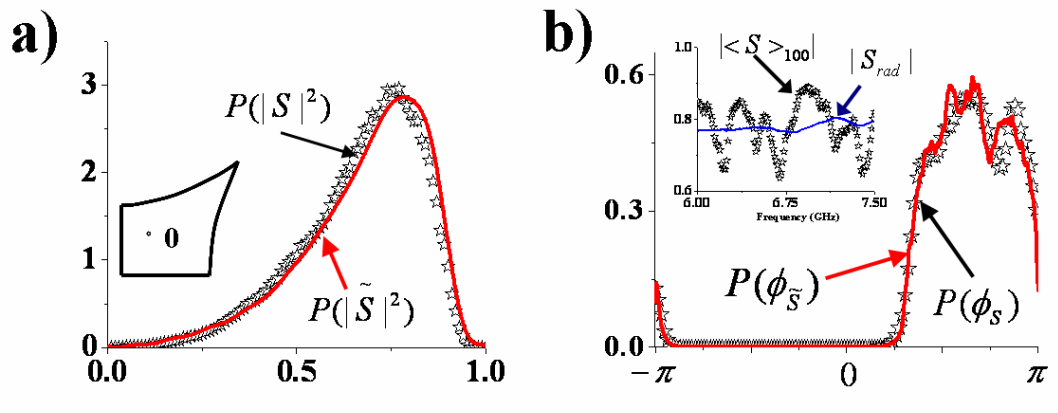

Fig. 4.16: (a) The experimental PDF for the Loss-Case 0 cavity power reflection coefficient ($|S|^2$) (black over a frequency range of 6 to 7.5GHz. Also shown is the numerical estimate $P(|\tilde{S}|^2)$ (solid red trace) determined from Random Matrix Theory and the experimentally measured radiation impedance of the port (Z_{rad}). (b) The experimental PDF for the Loss-Case 0 cavity scattering phase (ϕ_s) (black stars) over a frequency range of 6 to 7.5GHz. Also shown is the numerical estimate $P(\phi_{\tilde{S}})$ (solid red trace) determined from Random Matrix Theory and the experimentally measured radiation impedance of the port (Z_{rad}). The inset shows the fluctuation in $|\langle S\rangle_{100}|$ (black stars) over the frequency range of 6 to 7.5GHz, while the solid blue trace shows the magnitude of the experimentally measured radiation scattering coefficient ($|S_{rad}|$).

4.4 Summary of Chapter 4 and Conclusions

The results tested in this chapter are based on very general considerations and should apply equally well to conductance measurements through quantum dots (see Chapter 6), impedance or scattering matrix measurements on electromagnetic or acoustic enclosures (see Chapter 8), and scattering experiments from nuclei and Rydberg atoms. In conclusion, I have examined key testable predictions for the universal statistics of impedance and scattering fluctuations for one-port time-reversal symmetric wave-chaotic systems and found satisfactory agreement on all experimental issues directly related to the theory in Chapter 2 **[25]**. I find that a single control parameter characterizing the cavity loss fully describes the shapes and scales of these fluctuations in accordance with Random Matrix Theory and is independent of system specific details of port-coupling, shape of the wave-chaotic cavity, etc.

Chapter 5: Universal Fluctuations in 2-port Impedance, Admittance and Scattering Matrices of Wave-Chaotic Systems

In this chapter, I experimentally extend the "radiation impedance" approach of Refs. **[25, 26]** and chapter 4 to two-port wave-chaotic cavities. The quantities of interest here are the eigenvalues of the normalized impedance ($\vec{z}$), admittance ($\vec{y}$) and scattering matrices ($\vec{s}$) of wave-chaotic systems. For a wave-chaotic cavity driven by two-ports, each $\vec{z}$, $\vec{y}$ or $\vec{s}$ matrix produces two complex-eigenvalues with certain α-dependent statistical properties that are assumed to be explained by Random Matrix Theory, where α represents the cavity loss-parameter as explained in chapter 2. The experimental validation of this assumption is the focus of this chapter. The experimental setup and data analysis to obtain $\vec{z}$, $\vec{y}$ and $\vec{s}$, for the results presented in this chapter has been explained in section 3.2.

Reference **[26]** has shown that the marginal Probability Density Functions (PDFs) of the real and imaginary parts of the eigenvalues of $\vec{z}$ (denoted as $\mathrm{Re}[\vec{\lambda}_{\vec{z}}]$ and $\mathrm{Im}[\vec{\lambda}_{\vec{z}}]$ respectively), for a given value of α, are statistically identical to the PDFs of $\mathrm{Re}[z]$ and $\mathrm{Im}[z]$ respectively for the same value of α. Here z represents the one-port normalized impedance (see chapter 4). Using this fact, I resort to an alternative method to determine the value of α for my experimental data-sets, for the results presented in this chapter. This new method is based on an extension of Eq.(2.6) to two-port systems, and states that the variance(σ^2) of $\mathrm{Re}[\vec{\lambda}_{\vec{z}}]$ and $\mathrm{Im}[\vec{\lambda}_{\vec{z}}]$ for time-reversal symmetric systems are related to α through,

$$\sigma^2_{\mathrm{Re}[\vec{\lambda}_{\vec{z}}]} \cong \sigma^2_{\mathrm{Im}[\vec{\lambda}_{\vec{z}}]} \cong \frac{1}{\pi\alpha} \qquad \text{for } \alpha >> 1. \tag{5.1}$$

The one-port version of Eq.(5.1) i.e, Eq.(2.6), has been verified experimentally in Ref. **[45]** and chapter 4. Accordingly, Eq.(5.1) will be assumed to hold true for the 2-port results discussed in this paper for data-sets with $\alpha > 5$. For data-sets with $\alpha < 5$, the following procedure is employed. First, I numerically generate marginal PDFs of the real and imaginary parts of the normalized impedance eigenvalues using random-matrix Monte-Carlo simulations with square matrices of size $N = 1000$, and the value of α in the simulations ranging from 0.1 to 5 in steps of 0.1 (see section 2.5). I determine the variance(σ^2) of these numerically generated PDFs and fit their dependence on α to a polynomial function $\sigma^2 = \Theta(\alpha)$ of high order (see blue curve in Fig. 4.9). I then determine the variance of the PDF of the real part, i.e. $\sigma^2_{\mathrm{Re}[\vec{\lambda}_{\vec{z}}]}$ (which is equal to the variance of the PDF of the imaginary part $\sigma^2_{\mathrm{Im}[\vec{\lambda}_{\vec{z}}]}$ to good approximation **[25, 26, 45];** also see Chapter 4) of the experimentally-determined normalized impedance eigenvalues and solve the inverse polynomial function $\alpha = \Theta^{-1}(\sigma^2_{\mathrm{Re}[\vec{\lambda}_{\vec{z}}]})$ to obtain a unique estimate of α corresponding to that experimental data-set.

This chapter is organized into the following sections. Sections 5.1 through 5.3 present my experimental results on the universal fluctuations in the eigenvalues of $\vec{z}$, $\vec{y}$ and $\vec{s}$. Firstly, in section 5.1, I present experimental data showing the similarity in the PDFs for the eigenvalues of $\vec{z}$ and $\vec{y}$, and also compare these experimentally obtained PDFs with those from Random Matrix Theory for increasing values of α. A technical issue encountered in these 2-port experiments is the presence of non-zero,

off-diagonal terms in the measured $\vec{\vec{Z}}_{rad}$. These terms account for the direct-path processes ("cross-talk") between the two ports and come about because of the finite physical separation between the two-ports in the experiment during the radiation measurement. The role of these non-zero, off-diagonal $\vec{\vec{Z}}_{rad}$ terms in determining the universal PDFs of $\vec{z}$ is explained in section 5.2. Section 5.3 is dedicated to the universal fluctuations in the eigenvalues of $\vec{s}$, and is divided into three parts. In sub-section 5.3.1, the statistical independence of the magnitude and phase of the eigenvalues of $\vec{s}$ is experimentally established. The marginal distributions for the magnitude and phase of the eigenvalues of $\vec{s}$ are then compared with predictions from Random Matrix Theory. Sub-section 5.3.2 then explores the evolution of the joint PDF of the $\vec{s}$-eigenphases as a function of increasing loss. In sub-section 5.3.3, I experimentally test the predictions for the joint PDF of $\vec{s}\vec{s}^{\dagger}$ (where † denotes the conjugate transpose) from Ref. **[59]** as a function of cavity loss. Section 5.4 concludes this chapter with a summary of my experimental findings and its implications.

5.1 Experimental Results for the PDFs of the $\vec{z}$ and $\vec{y}$ eigenvalues

5.1.1 Marginal PDFs of the $\vec{z}$ and $\vec{y}$ eigenvalues

In this section I determine the marginal PDFs of the eigenvalues of the normalized impedance $\vec{z}$ and normalized admittance $\vec{y}$**.** It has been theorized in **[60]** that these two quantities have identical distributions for their eigenvalues. References **[25, 26]** show that attaching an arbitrary lossless two-port network at the interface

between the plane of measurement, and the cavity does not alter the statistics of $\tilde{z}$. If this lossless two-port is assumed to be a transmission line with an electrical-length equal to one-quarter wavelength at the driving frequency, then the lossless two-port acts as an "impedance inverter" **[61]** thereby presenting a cavity admittance at the plane of measurement. This similarity in the statistical description of $\tilde{z}$ and $\tilde{y}$ is predicted to be extremely robust and independent of loss in the cavity, coupling, driving frequency, etc.

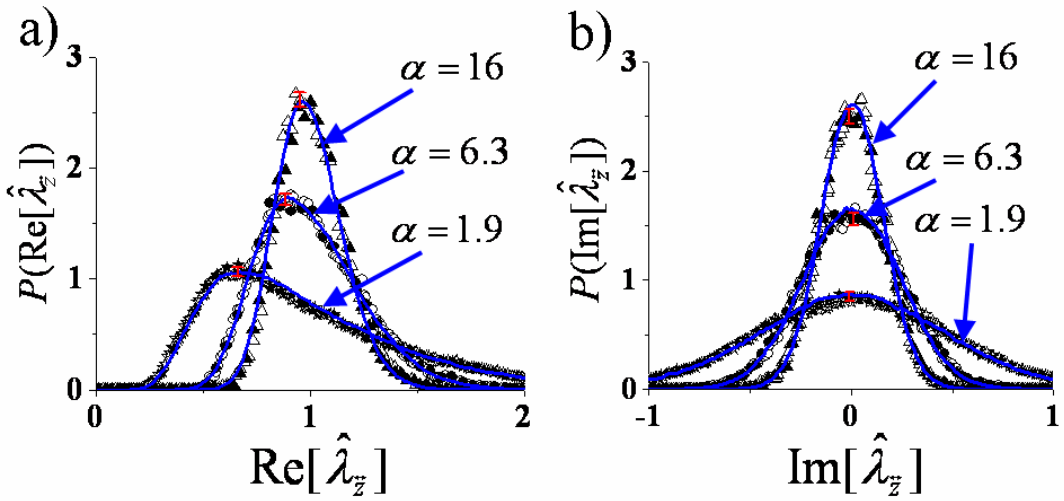

Fig. 5.1: PDFs for the real (a) and imaginary (b) parts of the grouped eigenvalues of the normalized cavity impedance $\hat{\lambda}_{\tilde{z}}$ (hollow stars : Loss-Case 0; hollow circles : Loss-Case 1; hollow triangles : Loss-Case 2) in the frequency range of 10.5-12 GHz. The PDFs for the real (a) and imaginary (b) parts of the grouped eigenvalues of the normalized cavity admittance $\hat{\lambda}_{\tilde{y}}$ (solid stars : Loss-Case 0; solid circles : Loss-Case 1; solid triangles : Loss-Case 2) in the frequency range of 10.5-12 GHz are also shown. The red error bars indicate the typical statistical binning error of the data. Also shown are the single parameter, simultaneous fits for both impedance and

admittance PDFs (blue solid lines), where the loss parameter α is obtained from the variance of the data in (a).

For my experimental test of this prediction, I consider the three loss cases, Loss-Case 0, 1 and 2, in the frequency range 10.5-12GHz. By an eigenvalue decomposition, each $\vec{z}$ and $\vec{y}$ matrix yields two complex eigenvalues, which I group together to form $\hat{\lambda}_{\vec{z}}$ and $\hat{\lambda}_{\vec{y}}$ respectively. I observe that grouping the two eigenvalues together as opposed to randomly considering one of the two eigenvalues separately does not alter the statistical results that follow. Histograms of the real and imaginary parts of $\hat{\lambda}_{\vec{z}}$ and $\hat{\lambda}_{\vec{y}}$ are plotted in Fig. 5.1. The hollow stars, circles and triangles in Fig.5.1(a) (Fig.5.1(b)) correspond to the histogram approximations of the PDF of $\mathrm{Re}[\hat{\lambda}_{\vec{z}}]$ ($\mathrm{Im}[\hat{\lambda}_{\vec{z}}]$) for Loss-Case 0, 1 and 2 respectively. The evolution of these PDFs for $\mathrm{Re}[\hat{\lambda}_{\vec{z}}]$ and $\mathrm{Im}[\hat{\lambda}_{\vec{z}}]$ with increasing loss, are in qualitative agreement with the description given in Ref. **[26]** and chapters 2 and 4. As losses increase, it can be observed that the PDFs of $\mathrm{Re}[\hat{\lambda}_{\vec{z}}]$ shifts from being peaked at $\mathrm{Re}[\hat{\lambda}_{\vec{z}}]\sim 0.6$ (Loss-Case 0) to developing a Gaussian-type distribution that peaks near $\mathrm{Re}[\hat{\lambda}_{\vec{z}}]\sim 1$ (Loss-Case 2). While in Fig. 5.1(b), as losses increase, the PDFs lose their long tails and become sharper. The solid stars, circles and triangles in Fig. 5.1(a) (Fig. 5.1(b)) correspond to the histogram approximations of the PDF of $\mathrm{Re}[\hat{\lambda}_{\vec{y}}]$ ($\mathrm{Im}[\hat{\lambda}_{\vec{y}}]$) for Loss-Case 0, Loss-Case 1 and Loss-Case 2 respectively. The agreement between the PDF approximations for $\mathrm{Re}[\hat{\lambda}_{\vec{z}}]$ and $\mathrm{Re}[\hat{\lambda}_{\vec{y}}]$ ($\mathrm{Im}[\hat{\lambda}_{\vec{z}}]$ and $\mathrm{Im}[\hat{\lambda}_{\vec{y}}]$) is good for all the three Loss-Cases. The red error bars are representative of the statistical error

introduced from the binning of the data in the histograms. By computing the variance of the PDFs for $\mathrm{Re}[\hat{\lambda}_{\bar{z}}]$ and by using the inverse polynomial function $\alpha = \Theta^{-1}(\sigma^2_{\mathrm{Re}[\hat{\lambda}_{\bar{z}}]})$, I obtain a loss parameter of $\alpha = 1.9 \pm 0.1$ (Loss-Case 0-stars); From the variance of the PDFs for $\mathrm{Re}[\hat{\lambda}_{\bar{z}}]$ and by Eq. (5.1), I obtain a loss parameter of $\alpha = 6.3 \pm 0.1$ (Loss-Case 1-circles) and $\alpha = 16 \pm 0.1$ (Loss-Case 2-triangles). Using these loss parameter values, a random matrix Monte Carlo computation (see section 2.5) yields the solid blue lines which simultaneously fit the data shown in both Fig. 5.1(a) and Fig. 5.1(b) for the three loss cases. The agreement between the experimentally observed values and the Random Matrix Theory result are in good agreement for all three cases and within the bounds of the error bars.

I also observe a robust agreement between the distributions for $\mathrm{Re}[\hat{\lambda}_{\bar{z}}]$ and $\mathrm{Re}[\hat{\lambda}_{\bar{y}}]$ as well as between $\mathrm{Im}[\hat{\lambda}_{\bar{z}}]$ and $\mathrm{Im}[\hat{\lambda}_{\bar{y}}]$ over a broad range of frequencies, coupling conditions and loss. To highlight this robust nature, in Fig. 5.2, I plot the variance of $\mathrm{Re}[\hat{\lambda}_{\bar{z}}]$ (blue squares), $\mathrm{Re}[\hat{\lambda}_{\bar{y}}]$ (green hexagons), $\mathrm{Im}[\hat{\lambda}_{\bar{z}}]$ (red stars) and $\mathrm{Im}[\hat{\lambda}_{\bar{y}}]$ (black circles) distributions for a Loss-Case 0 cavity measurement. Each symbol corresponds to a 1 GHz wide sliding window that steps every 500 MHz over the frequency range from 6 to 18 GHz. It can be seen that the four symbols closely overlap each other over the entire frequency range. The agreement between the symbols (as predicted by Ref. **[25, 26, 60]**) is remarkable despite the variation in coupling, frequency and loss (which varies from an α-value of about 1 to 3.5 over this frequency range) within the cavity **[62]**.

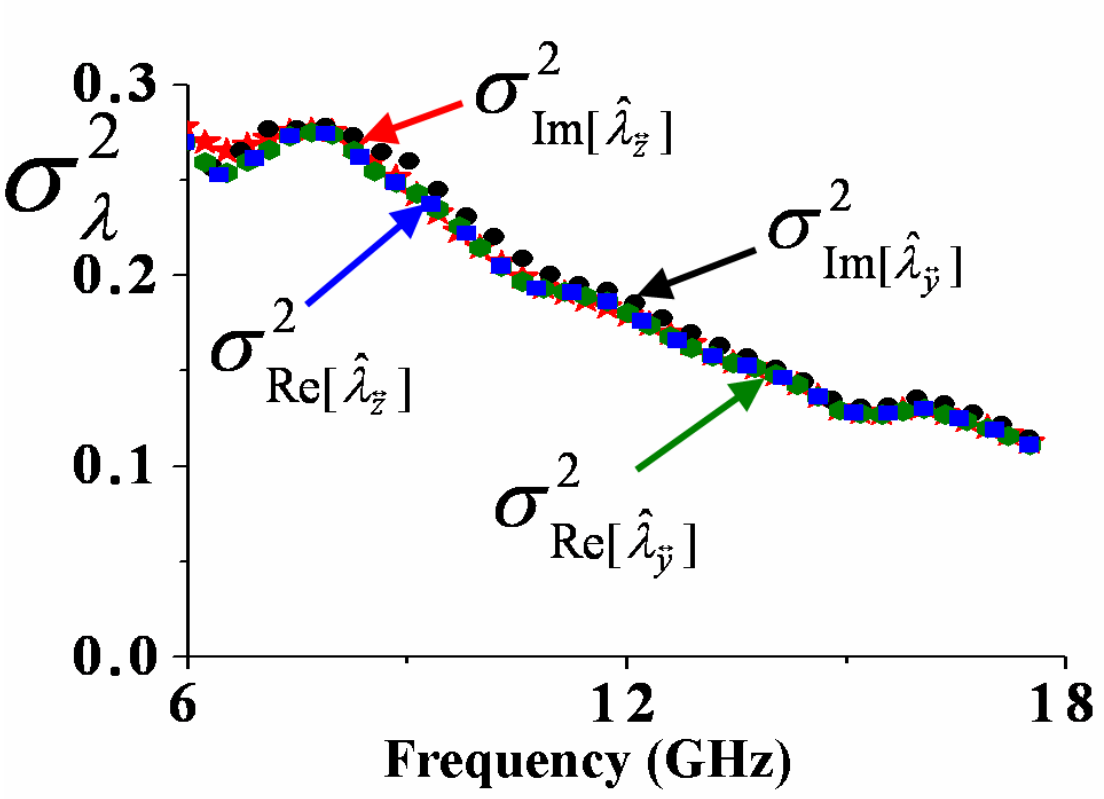

Fig. 5.2: The variance of $\mathrm{Re}[\hat{\lambda}_{\tilde{z}}]$ (blue squares), $\mathrm{Re}[\hat{\lambda}_{\tilde{y}}]$ (green hexagons); $\mathrm{Im}[\hat{\lambda}_{\tilde{z}}]$ (red stars) and $\mathrm{Im}[\hat{\lambda}_{\tilde{y}}]$ (black circles) distributions are shown as a function of frequency from 6 to 18 GHz for Loss-Case 0. The agreement between these four quantities is good and robust over the entire frequency range despite the change in cavity Q and coupling.

5.1.2 Variation of α with frequency for the different experimental loss-cases

In this sub-section, I resort to the PDF-fitting method, which was described in Chapter 4, to quantify the evolution of the cavity loss-parameter α (for the different cavity- Loss-Cases) with increasing frequency. As in Chapter 4, I employ a sliding window of width 1 GHz wide (over which I assume that the value of α does not

change significantly) that steps every 500 MHz over the frequency range of 3-18 GHz for my measured Loss-Case data. I define each 1 GHz window as a "data-set".

I then numerically generate PDFs of the real and imaginary parts of the 2-port normalized impedance eigenvalues using random-matrix Monte-Carlo (MC) simulations with square matrices of size $N = 1000$, and the value of $\alpha (= \alpha_{MC})$ in the simulations ranging from 0.1 to 35 in steps of 0.1 (see section 2.5). I define a "PDF-error" function $\Delta e_\theta = -\sum_\theta | P_{MC}(\theta, \alpha_{MC}) - P_{\exp}(\theta, f) |$, which quantifies the error between the marginal PDFs of the normalized impedance eigenvalues generated numerically from Monte-Carlo simulations (MC) and those determined experimentally (exp). Here, θ corresponds to either the real ($\mathrm{Re}[\hat{\lambda}_{\bar{z}}]$) or imaginary ($\mathrm{Im}[\hat{\lambda}_{\bar{z}}]$) parts of the normalized impedance eigenvalue PDFs ($P(\theta)$). Instances where there is good agreement between the experimentally determined marginal PDFs and those generated numerically for a given value of α_{MC} result in small magnitudes for the PDF-error functions $\Delta e_{\mathrm{Re}[\hat{\lambda}_{\bar{z}}]}$ and $\Delta e_{\mathrm{Im}[\hat{\lambda}_{\bar{z}}]}$.

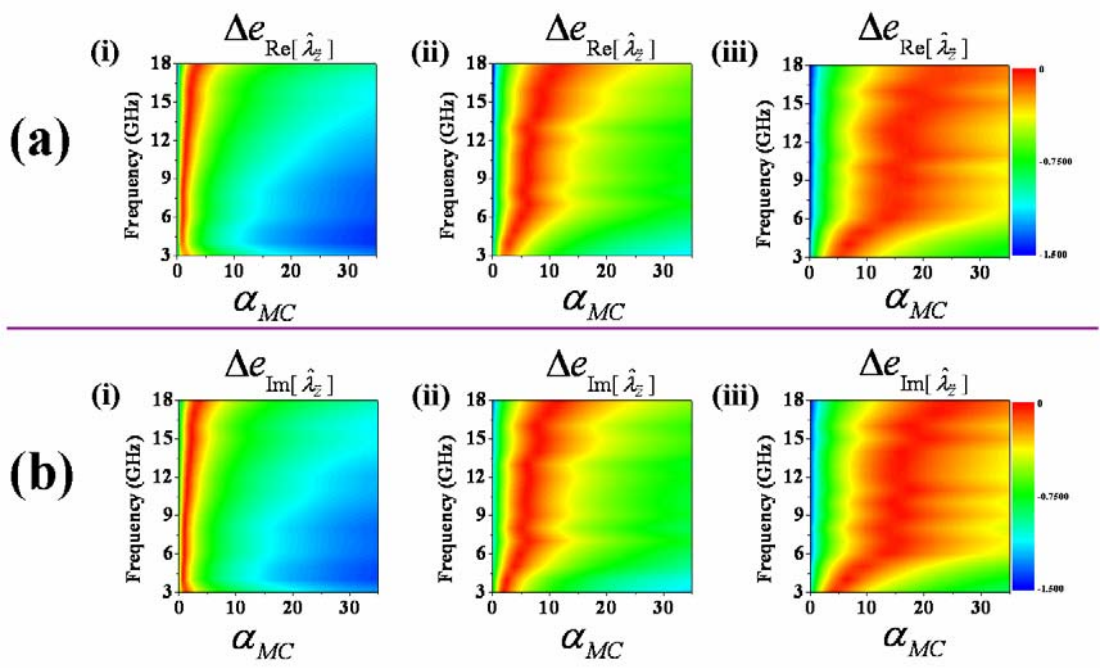

Fig. 5.3: (a) Contour plot for the (i) Loss-Case 0, (ii) Loss-Case 1, (iii) Loss-Case 2 PDF-error function $\Delta e_{\mathrm{Re}[\hat{\lambda}_{\tilde{z}}]}$. The common color-scale for (i),(ii) and (iii) is shown in (iii) and indicates the magnitude of the PDF-error function $\Delta e_{\mathrm{Re}[\hat{\lambda}_{\tilde{z}}]}$ (blue=large error, red= small error). (b) Contour plot for the (i) Loss-Case 0, (ii) Loss-Case 1, (iii) Loss-Case 2 PDF-error function $\Delta e_{\mathrm{Im}[\hat{\lambda}_{\tilde{z}}]}$. The common color-scale for (i), (ii) and (iii) is shown in (iii) and indicates the magnitude of the PDF-error function $\Delta e_{\mathrm{Im}[\hat{\lambda}_{\tilde{z}}]}$ (blue=large error, red= small error). The red regions indicate those choices of α_{MC} for which there is good agreement (small error) between the experimentally obtained PDFs and the corresponding PDFs generated from random matrix Monte Carlo simulations.

Figure 5.3 (a) shows contour plots of the PDF-error function $\Delta e_{\mathrm{Re}[\hat{\lambda}_{\bar{z}}]}$ for (i) Loss-Case 0, (ii) Loss-Case 1 and (iii) Loss-Case 2 cavities in the frequency range of 3 to 18 GHz. The color-scale indicates the magnitude of the error function (blue=large error, red=small error). The red region indicates where there is good agreement between the experimentally obtained PDF for $\mathrm{Re}[\hat{\lambda}_{\bar{z}}]$ and the corresponding PDF generated numerically from Monte-Carlo simulations for a specified value of α_{MC}. A similar analysis in shown in Fig. 5.3(b) for the contour plots of the PDF-error function $\Delta e_{\mathrm{Im}[\hat{\lambda}_{\bar{z}}]}$ corresponding to (i) Loss-Case 0, (ii) Loss-Case 1 and (iii) Loss-Case 2 cavities in the frequency range of 3 to 18 GHz.

As in Chapter 4, I define the experimentally determined loss-parameter (α) for a given data-set to be the average value of $\alpha_{\mathrm{Re}[\hat{\lambda}_{\bar{z}}]}$ and $\alpha_{\mathrm{Im}[\hat{\lambda}_{\bar{z}}]}$, obtained from the PDF fitting procedure; where, $\alpha_{\mathrm{Re}[\hat{\lambda}_{\bar{z}}]}$ and $\alpha_{\mathrm{Im}[\hat{\lambda}_{\bar{z}}]}$ are defined as those choices of α_{MC} that result in the smallest error-value for $\Delta e_{\mathrm{Re}[\hat{\lambda}_{\bar{z}}]}$ and $\Delta e_{\mathrm{Im}[\hat{\lambda}_{\bar{z}}]}$ respectively for that data-set. I then examine the trend of α for each Loss-Case data-set, represented in Fig. 5.3, as a function of frequency. This trend is shown in Fig. 5.4. The increasing value of α for each of the Loss-Cases (Loss-Case 0: red stars, Loss-Case 1: blue stars, Loss-Case 2: green stars) as a function of frequency in Fig. 5.4 is expected as the cavity-losses are frequency dependent and monotonically increase with frequency. The small fluctuations in the data represented by the blue (Loss-Case 1) and green (Loss-Case 2) stars between 7.5 GHz and 15 GHz are attributed to the frequency-dependent absorptive properties of the microwave absorber used to line the inside of the cavity walls for the Loss-Case 1 and Loss-Case 2 cavity setups. The error bars in

Fig. 5.4, are indicative of the estimated experimental error in determining α, as explained in chapter 4.

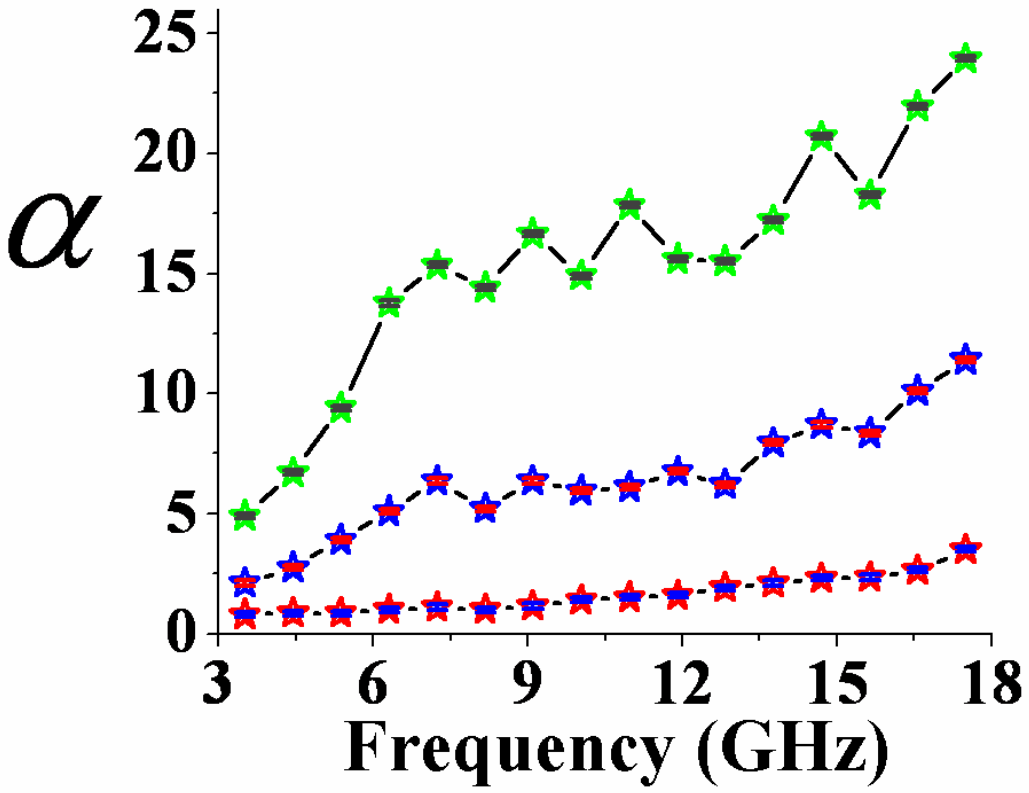

Fig. 5.4: Variation in the cavity loss-parameter (α) as a function of frequency for different cavity Loss-Cases (Loss-Case 0: red stars, Loss-Case 1: blue stars, Loss-Case 2: green stars). Note the similar trend of the fluctuations in the data represented by the blue and green stars, which arises from the frequency-dependent absorptive properties of the microwave absorber used to create the cavity Loss-Case 1 and Loss-Case 2 respectively. The error bars indicate the estimated experimental error in determining α for each data-set.

5.2 Importance of The Off-Diagonal Radiation Elements in $\ddot{Z}_{rad}$

The "radiation impedance" approach to filter out the direct processes involved in a chaotic scattering experiment relies on the accuracy of the measured radiation impedance matrix. This section explains a key technical issue faced while experimentally measuring the radiation impedance matrix of the driving ports; specifically, the presence of non-zero, off-diagonal terms in the measured radiation impedance matrix.

The conjecture that the statistical properties of real-world, physically realizable, wave-chaotic scattering systems can be modeled by an ensemble of large matrices with random elements (governed by certain system symmetries) is applicable only in the semi-classical or short wavelength limit (ray limit). For the purpose of this conjecture, in the presence of ports, a consistent definition of the short wavelength limit is that, when taking this limit, the size of the ports connecting to the cavity remain constant in units of wavelength. With this definition of the limit, the ratio of the distance between the ports to their size approaches infinity. Thus $\ddot{Z}_{rad}$ becomes diagonal and approaches a constant at short wavelength.

The conjecture that Random Matrix Theory describes the scattering properties in a specific case assumes that, in the short wavelength limit, rays entering the cavity bounce many times before leaving (i.e., they experience the chaotic dynamics). With the above definition of the short wavelength limit of the ports, this would be the case since the fraction of power reflected back to a port via short (e.g., one or two bounce) paths approaches zero. At finite wavelength, however, it can be anticipated that there could be noticeable deviations from the Random Matrix Theory predictions and that

these would be associated with short ray paths. In my experimental determinations of $\vec{\vec{Z}}_{rad}$, I have effectively eliminated the largest source of such non-universal behavior, namely, the short ray paths that go directly between ports 1 and 2. This is the case because these ray paths are already included in the experimental $\vec{\vec{Z}}_{rad}$.

In particular, lining the inner walls of the cavity with microwave absorber for the "Radiation Case" of the experiment, serves to essentially eliminate reflections off the side-walls, but plays no role in suppressing the direct-path interaction (cross-talk) between the two ports. This cross-talk is manifested primarily as non-zero, off-diagonal terms in the measured $\vec{\vec{Z}}_{rad}$ with enhanced frequency dependence relative to the one-port case.

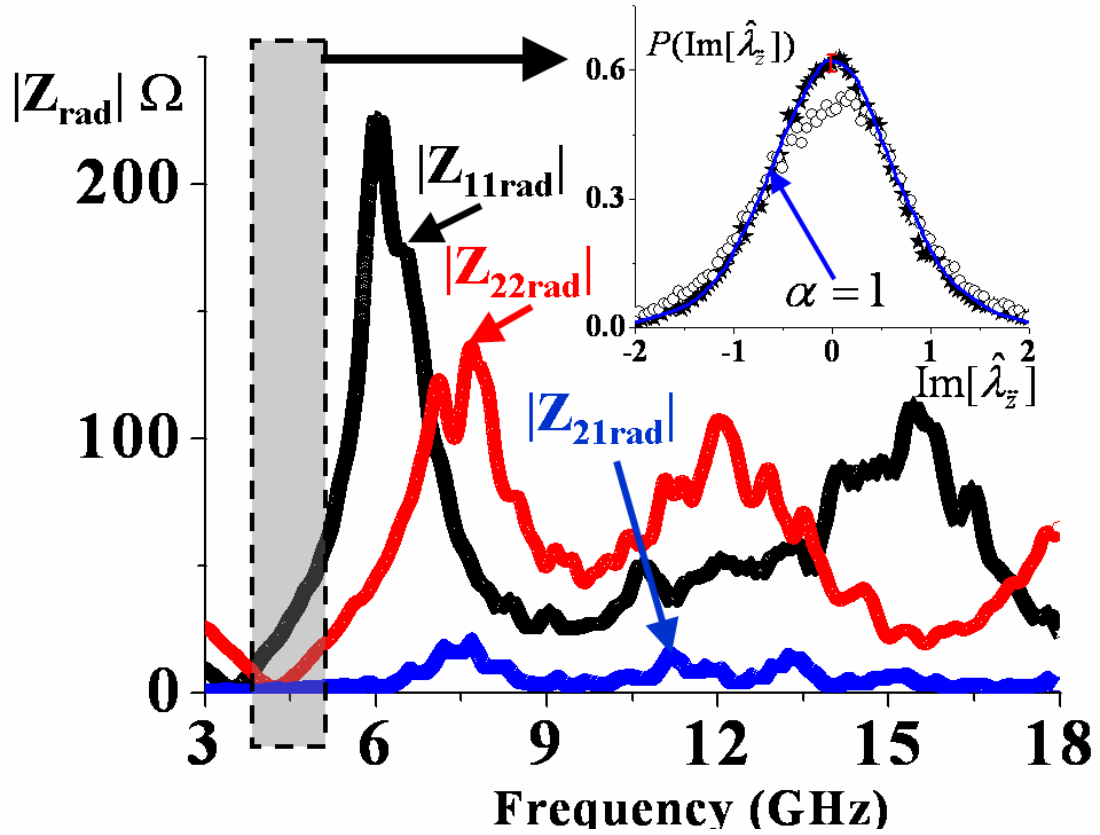

Fig. 5.5: Magnitude of the elements of the measured radiation impedance matrix are shown as a function of frequency from 3 to 18 GHz for the setup in Fig.3.3. Inset: PDF of $\mathrm{Im}[\hat{\lambda}_{\tilde{z}}]$ for the Loss Case 0 cavity in the frequency range 4-5 GHz, which is obtained by considering the full 2x2 radiation impedance matrix (stars) and by considering only the contribution of the diagonal elements of the radiation impedance matrix (circles). The blue solid line is the Random Matrix Theory numerical prediction for α =1 which is obtained from the variance of the data represented by the stars.

Figure 5.5 shows the magnitudes of the elements of the radiation impedance matrix $\ddot{Z}_{rad}$ for the two-port setup shown in Fig. 3.3. Frequency ranges where there is

significant cross-talk between the two ports are manifested as large values of $|Z_{21rad}| = |Z_{12rad}|$. Note the complicated structure of the measured elements of $\ddot{\vec{Z}}_{rad}$.

To highlight the contribution of short ray paths, the inset of Fig. 5.5, shows the PDF of the eigenvalues of the normalized impedance for two scenarios of the Loss-Case 0 cavity in the 4-5 GHz frequency range. The circles represent the PDF of $\mathrm{Im}[\hat{\lambda}_{\vec{z}}]$ that is obtained by setting the off-diagonal terms of the measured radiation impedance matrix to zero. The solid stars however, represent the PDF of $\mathrm{Im}[\hat{\lambda}_{\vec{z}}]$ which is obtained by considering <u>all</u> the elements of the measured radiation impedance matrix during the normalization process (Eq. (2.10)) to obtain $\vec{\vec{z}}$. The red error bars are representative of the statistical error introduced from the binning of the data in the histograms indicated by the solid stars. I observe a clear discrepancy between the two curves and also note that the PDF represented by the circles does not peak at 0. Using the variance of the measured $\mathrm{Im}[\hat{\lambda}_{\vec{z}}]$ (stars) and the inverse polynomial function $\alpha = \Theta^{-1}(\sigma^2_{\mathrm{Im}[\hat{\lambda}_{\vec{z}}]})$, I obtain a loss parameter value of $\alpha = 1.0 \pm 0.1$ for this frequency range. I use this value to generate the PDF of $\mathrm{Im}[\hat{\lambda}_{\vec{z}}]$ using Random Matrix Monte Carlo simulation (see section 2.5). The resultant numerical prediction is shown as the solid blue line. Good agreement between the numerical Random Matrix Theory prediction and the experimentally determined PDF of $\mathrm{Im}[\hat{\lambda}_{\vec{z}}]$ by considering the full 2x2 radiation impedance matrix is thus observed. My choice of the 4-5 GHz range is motivated by the fact that in this range, the ratio of $|Z_{21rad}|/|Z_{22rad}|$ is the largest. This result establishes the importance of off-

diagonal terms in $\vec{\vec{Z}}_{rad}$, and helps to validate the approach to removing short-path direct processes between the ports.

5.3 Marginal and Joint PDFs of $\vec{s}$ eigenvalues

In this section, I give my experimental results on the universal statistical fluctuations in the eigenvalues of $\vec{s}$ **[62]**. Each 2x2 $\vec{s}$ matrix yields two complex eigenvalues – which possess certain universal statistical properties in their marginal and joint PDFs.

5.3.1 Statistical Independence of $|\hat{\lambda}_{\vec{s}}|$ and $\phi_{\hat{\lambda}_{\vec{s}}}$

Having obtained the ensemble of normalized $\vec{s}$, I diagonalize $\vec{s}$ using an eigenvalue decomposition, $\vec{s} = \vec{V}_{\vec{s}}\vec{\lambda}_{\vec{s}}\vec{V}_{\vec{s}}^{-1}$;where, $\vec{V}_{\vec{s}}$ is the 2x2 eigenvector matrix of $\vec{s}$; and $\vec{\lambda}_{\vec{s}}$ is a diagonal matrix containing the two complex eigenvalues of $\vec{s}$. In the time-reversal symmetric, lossless limit, $\vec{s}$ is unitary. This dictates that $\vec{V}_{\vec{s}}$ be an orthogonal matrix and $\tilde{\vec{\lambda}}_{\vec{s}} = \begin{bmatrix} Exp[j\tilde{\phi}_1] & 0 \\ 0 & Exp[j\tilde{\phi}_2] \end{bmatrix}$. In the presence of loss, $\vec{V}_{\vec{s}}$ is no longer orthogonal and $\vec{s}$ now has complex, sub-unitary eigenvalues, i.e. $\vec{\lambda}_{\vec{s}} = \begin{bmatrix} |\lambda_1| e^{j\phi_1} & 0 \\ 0 & |\lambda_2| e^{j\phi_2} \end{bmatrix}$, where $|\lambda_{1,2}| < 1$. Reference **[46]** (see Chapter 4) has shown that for a 1-port system, the magnitudes and phases of the normalized 1-port scattering coefficient s are statistically independent. The independence was shown to be extremely robust and is unaffected by the presence of loss. For a two-port setup, as

in the experiments presented in this chapter, this would imply statistical independence of the magnitude and phases of the eigenvalues of $\vec{s}$.

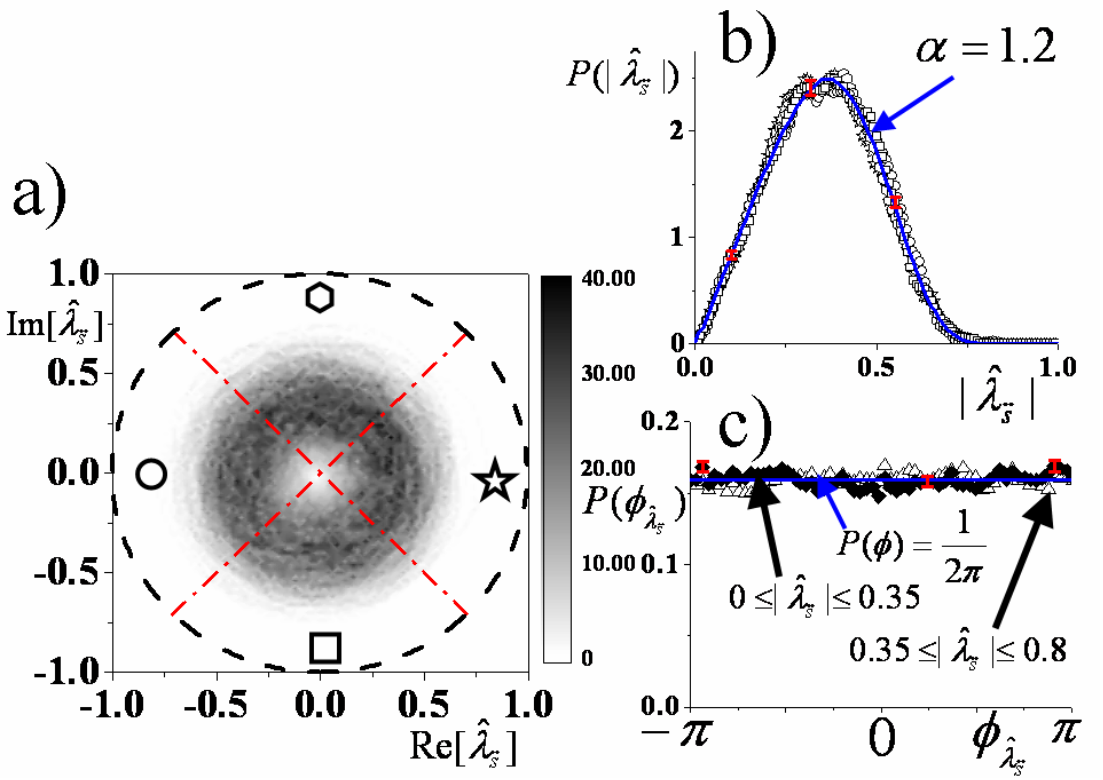

Fig.5.6: (a) The density of eigenvalues of $\hat{\lambda}_{\vec{s}}$ in the complex plane is shown for frequencies in the range 7.6 GHz to 8.1 GHz for Loss-Case 0. The gray-scale code white, light gray, dark gray, black are in ascending density order. (b) Angular slices (90^o) with the symbols (stars, hexagons, circles, squares) indicate regions where the PDF of $|\hat{\lambda}_{\vec{s}}|$ of the data in (a) is calculated and shown. Observe that the four PDFs are nearly identical. The blue solid line is the numerical prediction from Random Matrix Theory using the loss parameter $\alpha = 1.2$. The red error bars indicate the statistical binning error in the histograms. (c) Experimental histogram approximations to the PDF of the eigenphase of $\vec{s}$ (i.e., $\phi_{\hat{\lambda}_{\vec{s}}}$). Two annular rings

defined by $0 \leq |\hat{\lambda}_{\vec{s}}| \leq 0.35$ and $0.35 \leq |\hat{\lambda}_{\vec{s}}| \leq 0.8$ of the data in (a) are taken and the histograms of the phase of the points within these regions are shown as the solid diamonds and hollow triangles respectively. The red error bars indicate typical statistical binning errors for the data. The blue solid line is a uniform distribution ($P(\phi) = 1/(2\pi)$).

To test this hypothesis, the two complex eigenvalues of the $\vec{s}$ ensemble are grouped into one list, which I shall refer to as "$\hat{\lambda}_{\vec{s}}$". I observe that grouping the two eigenvalues together as opposed to randomly choosing one of the two eigenvalues does not change the statistical properties of the results that follow. Figure 5.6(a) shows a plot in the complex plane of the eigenvalue density for a representative set of measured $\vec{s}$ ranging between 7.6 to 8.1 GHz where the loss-parameter is roughly constant. The gray-scale level at any point in Fig. 5.6(a) indicates the number of points for $\{\mathrm{Re}[\hat{\lambda}_{\vec{s}}], \mathrm{Im}[\hat{\lambda}_{\vec{s}}]\}$ that lies within a local rectangular region of size 0.01 x 0.01. Next, angular slices which subtend a polar-angle of $\pi/2$ are taken and histogram approximations to the PDF of $|\hat{\lambda}_{\vec{s}}|$ of the points lying inside each of the four slices are computed. This is shown by the stars, hexagons, circles and squares in Fig. 5.6(b). It can be observed that the PDF approximations are essentially identical and independent of the angular-slice. By grouping the real part of the eigenvalues of $\vec{z}$ in to one list and computing its variance (i.e. $\sigma^2_{\mathrm{Re}[\hat{\lambda}_{\vec{z}}]}$), I solve the inverse polynomial function $\alpha = \Theta^{-1}(\sigma^2_{\mathrm{Re}[\hat{\lambda}_{\vec{z}}]})$ to yield an estimate of $\alpha = 1.2 \pm 0.1$ for this data set. The blue solid line shows the numerical Random Matrix Theory prediction

(see section 2.5) which is computed using a single value of $\alpha = 1.2$. The red error bars in Fig. 5.6(b) which are representative of the typical statistical binning error of the experimental histograms show that the data agrees well with the numerical Random Matrix Theory PDF.

In Fig. 5.6(c), the histogram approximations of the phase of the points lying within two-annular rings defined by $0 \leq |\hat{\lambda}_{\vec{s}}| \leq 0.35$ (solid diamonds) and $0.35 \leq |\hat{\lambda}_{\vec{s}}| \leq 0.8$ (hollow triangles) are shown. A nearly uniform distribution is obtained for both cases indicating that the PDF of the phase of $\hat{\lambda}_{\vec{s}}$ is independent of the radius of the annular ring. Also shown in blue is the uniform distribution with $P(\phi) = 1/(2\pi)$. Figure 5.6 thus supports the hypothesis that the magnitude and phase of the eigenvalues of $\vec{s}$ are statistically independent of each other and that the eigen-phase of $\vec{s}$ is uniformly distributed from 0 to 2π **[62]**.

5.3.2 Joint PDF of $\vec{s}$ eigenphases

Sub-section 5.3.1 has established the uniform distribution of the marginal PDF of the eigenphases of $\vec{s}$. Here I explore the statistical inter-relationships between the two eigenphases of $\vec{s}$ by looking at their joint PDFs i.e., $P(\phi_1, \phi_2)$. In the lossless limit the eigenvalues of $\vec{s}$ are of unit modulus and their marginal distribution is uniform in phase along the unit-circle. Reference **[23]** has shown that the joint PDF of the eigenphases ϕ_1 and ϕ_2, shows a clear anti-correlation, i.e. $P(\phi_1, \phi_2) \propto |e^{j\phi_1} - e^{j\phi_2}|^{\beta}$, where $\beta = 1(2)$ for a time-reversal(broken) GOE(GUE) system. In the lossless GOE case this anti-correlation is $<\phi_1 \phi_2> \cong -0.216$, where $-\pi \leq \phi_{1,2} \leq \pi$ **[26]**. As losses

are introduced, the eigenvalues of $\vec{s}$ are no longer confined to move along the unit-circle; but rather are distributed inside the unit circle in a manner dependent upon the loss in the system (as was shown in Fig. 5.6(a)). The sub-unitary modulus of the eigenvalues thus presents an extra degree of freedom for eigenvalue avoidance, hence a reduced anti-correlation of the eigenphases as the losses increase can be expected. To my knowledge, there exists no analytic formula for the evolution of the joint PDF of the eigenphases of $\vec{s}$ as a function of loss. In the following paragraphs, I thus compare my experimental results for the joint PDF of the eigenphases of $\vec{s}$ with numerical computations of results from Random Matrix Theory.

In order to make comparisons of the data with numerical computations from Random Matrix Theory, I transform the eigenphases ϕ_1 and ϕ_2 to κ_1 and κ_2, as follows,

$$\begin{aligned} \kappa_1 &= \phi_1 - \phi_2 - \pi + 2\pi H(\phi_2 - \phi_1) \\ \kappa_2 &= \phi_2 \end{aligned} \tag{5.2}$$

where $H(x)$ is the Heaviside step function ($H(x) = 0$ for $x < 0$; $H(x) = 1$ for $x > 0$). This transformation of variables has the effect of making κ_1 and κ_2 statistically independent, with all the correlation information between ϕ_1 and ϕ_2 being contained in κ_1; and κ_2 being uniformly distributed (as shown in Fig. 5.6(c)). In the lossless case, it can be easily deduced from $P(\phi_1, \phi_2) \propto | e^{j\phi_1} - e^{j\phi_2} |^{\beta}$, that $P(\kappa_1) = Cos(\kappa_1 / 2)/4$ for $\beta = 1$.

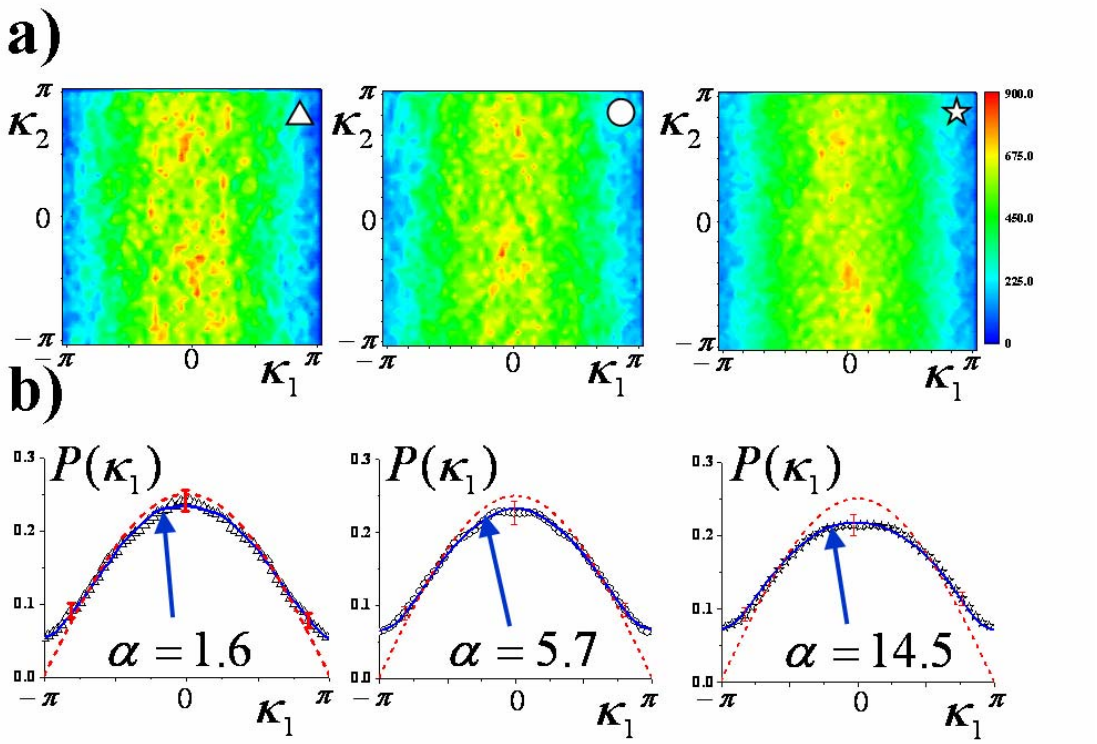

Fig. 5.7: (a) The joint PDF ($P(\kappa_1,\kappa_2)$) of the transformed eigenphases κ_1 and κ_2 for Loss Case 0 (triangles: left), Loss Case 1 (circles: center) and Loss Case 2 (stars: right) in the frequency range of 10.4-11.7 GHz. The color-scale levels blue, green, yellow and red are in ascending density order. (b) Marginal PDFs for κ_1 (Loss Case 0 (triangles: left), Loss Case 1 (circles: center) and Loss Case 2 (stars: right)) of the data shown in the top row. The dashed red line is the lossless prediction $P(\kappa_1) = Cos(\kappa_1/2)/4$. The blue solid lines are the numerical Random Matrix Theory prediction for $P(\kappa_1)$ with α =1.6 (left); 5.7 (center) and 14.5 (right).

The top row of Fig. 5.7 shows the density plots of κ_1 and κ_2 for the three different loss-cases (Loss-Case 0: triangles, Loss-Case 1: circles, Loss-Case 2: stars) in the frequency range of 10.4-11.7 GHz. This corresponds to $\alpha = 1.6 \pm 0.1, 5.7 \pm 0.1$

and 14.5 ± 0.1 respectively. For the data set represented by the triangles, the value of α was determined by computing the variance of the real part of the grouped eigenvalues of $\vec{z}$ (i.e. $\sigma^2_{\mathrm{Re}[\hat{\lambda}_{\vec{z}}]}$) and solving the inverse polynomial function $\alpha = \Theta^{-1}(\sigma^2_{\mathrm{Re}[\hat{\lambda}_{\vec{z}}]})$. For the data sets represented by the circles and stars, the value of α was determined by computing the variance of the real part of the grouped eigenvalues of $\vec{z}$ and Eq. (5.1). As the plots indicate, the statistical variation is entirely contained in the κ_1 direction, with κ_2 being nearly uniformly distributed. The color-scale level on the plots indicates the number of points for $\{\kappa_1, \kappa_2\}$ which lie within a local rectangular region of size 0.01 x 0.01. The corresponding anti-correlation of the eigenphases $<\phi_1, \phi_2> \cong -0.17, -0.16, -0.15$ $(-\pi \le \phi_{1,2} \le \pi)$ for the triangles, circles and stars respectively.

The bottom row of Fig. 5.7 shows histogram approximations to the Marginal PDFs of κ_1 for all three cases of loss (Loss-Case 0: triangles, Loss-Case 1: circles, Loss-Case 2: stars) for the data shown in the top row. The blue solid line is the numerical Random Matrix Theory computation for $P(\kappa_1)$ which is based upon the loss parameters stated above. The red dashed-line is the predicted PDF of κ_1 in the lossless case. The red error-bars indicate the typical statistical binning error for the experimental PDF histograms. The agreement between the experimentally determined $P(\kappa_1)$ (symbols) and the numerically generated $P(\kappa_1)$ (blue trace) is good and well within the error-estimates. I observe that as the losses increase, the histograms for $P(\kappa_1)$ tends to grow progressively wider and develop smooth tails - which results in a reduced anti-correlation between ϕ_1 and ϕ_2, as expected **[62]**.

5.3.3 Joint PDF of eigenvalues of $\vec{\vec{s}}\vec{\vec{s}}^{\dagger}$

I now consider the joint PDF of the eigenvalues of $\vec{\vec{s}}\vec{\vec{s}}^{\dagger}$, where † denotes the conjugate transpose. Since $\vec{\vec{s}}\vec{\vec{s}}^{\dagger}$ is Hermitian, its eigenvalues are purely real. The matrix $\vec{\vec{s}}\vec{\vec{s}}^{\dagger}$ is of significant interest in the quantum-transport community as it determines the conductance fluctuations of ballistic quantum-dots in the presence of dephasing/loss. Owing to the analogy between the time-independent Schrödinger equation and the two-dimensional Helmholtz equation, the microwave billiard experiment presents itself as an ideal platform to test statistical theories for these quantum fluctuations without the complicating effects of thermal smearing **[63]** and Coulomb interactions, as discussed in Ref. **[64]** (also see Chapter 6).

Models have been introduced to quantify the loss of quantum phase coherence (dephasing) of transport electrons in quantum dots **[65, 66, 67, 68]**. These models generally utilize a fictitious lead attached to the dot that has a number of channels N_{ϕ} each of which contains a tunnel-barrier with transmission probability Γ_{ϕ}, for the electrons that enter the channel from the dot. Electrons that enter one of the channels of this lead are re-injected into the dot with a phase that is uncorrelated with their initial phase, and there is no net current through the fictitious lead. An alternative model of electron transport employs a uniform imaginary term in the electron potential **[69, 70]**, leading to loss of probability density with time, similar to the loss of microwave energy in a cavity due to uniformly distributed losses in the walls and lids. As far as the conductance is concerned, it was shown that these two models are equivalent in the limit when the number of channels in the dephasing lead $N_{\phi} \to \infty$

and $\Gamma_\phi \to 0$, with the product $\gamma = N_\phi \Gamma_\phi$ remaining finite **[59, 66, 71]**. In this case, the dephasing parameter γ is equivalent to a loss parameter describing the strength of uniformly distributed losses in the system. Other models have been proposed that consider parasitic channels **[66, 72]** or an "absorbing patch" or "absorbing mirror" **[73]** to describe losses in a microwave cavity. Here I examine the predictions of Brouwer and Beenakker using the dephasing lead model in the limit mentioned above. In this case the dephasing parameter γ is treated as a loss-parameter describing fairly uniformly distributed losses in the microwave cavity, and is found to be proportional to the loss-parameter α**.**

Reference **[59]** has shown that the eigenvalues of $\vec{s}\vec{s}^{\,\dagger}$ can be denoted as $1-T_1$ and $1-T_2$ (where T_1 and T_2 determine the absorption strength of this fictitious port) with the statistical properties of T_1 and T_2 dependent on the parameter γ. When $\gamma = 0$, T_1 and T_2 equal zero and $\vec{s}$ is unitary. As γ increases, T_1 and T_2 migrate towards 1. Equation 17(a) (Eq.(5.3) below) and Eq.17(b) of Ref. **[59]** are exact analytic expressions for the joint PDF of T_1 and T_2 in terms of γ for both the GOE and GUE cases respectively. At all values of γ, the analytic expression for $P(T_1, T_2; \gamma)$ shows strong anti-correlation between T_1 and T_2 **[59]**,

$$
\begin{aligned}
P(T_1,T_2;\gamma) &= \frac{1}{8} T_1^{-4} T_2^{-4} Exp\left(-\frac{1}{2}\gamma(T_1^{-1}+T_2^{-1})\right) |T_1 - T_2| (\gamma^2(2-2e^{\gamma}+\gamma+\gamma e^{\gamma}) \\
&- \gamma(T_1+T_2)(6-6e^{\gamma}+4\gamma+2\gamma e^{\gamma}+\gamma^2) \\
&+ T_1 T_2 (24-24e^{\gamma}+18\gamma+6\gamma e^{\gamma}+6\gamma^2+\gamma^3)).
\end{aligned}
\tag{5.3}
$$

For my experiment, once the ensemble of $\vec{s}$ has been obtained, T_1 and T_2 can be easily determined by computing the eigenvalues of $\vec{s}\vec{s}^{\,\dagger}$. In Fig. 5.8, contour

density plots of $P(T_1, T_2)$ is shown for the Loss-Case 0 (Fig. 5.8(a) : 3.2-4.2 GHz) and Loss Case 0 (Fig. 5.8(b): 13.5-14.5 GHz). This corresponds to α values of 1.0 ± 0.1 for Fig. 5.8(a) and 2.9 ± 0.1 for Fig. 5.8 (b). These values of α are determined from estimating the variance of the real part of the grouped eigenvalues of $\tilde{z}$ (i.e. $\sigma^2_{\mathrm{Re}[\hat{\lambda}_{\tilde{z}}]}$) and solving the inverse polynomial function $\alpha = \Theta^{-1}(\sigma^2_{\mathrm{Re}[\hat{\lambda}_{\tilde{z}}]})$ for both data sets. The color-scale level indicates the number of points that lie in a local rectangular region of size 0.01 x 0.01 for Fig. 5.8 (a) and 0.005 x 0.005 for Fig. 5.8 (b) (note the change in scales for the plots). I observe that as losses increase the cluster of T_1 and T_2 values which are centered around ~0.75 for Fig. 5.8 (a) migrates towards values of T_1 and T_2 approaching 1 (Fig. 5.8 (b)). I also observe a strong anti-correlation in $P(T_1, T_2)$ for $T_1 = T_2$. This anti-correlation is manifested in all the data measured at varying degrees of loss from α =0.9 to 25 **[62]**.

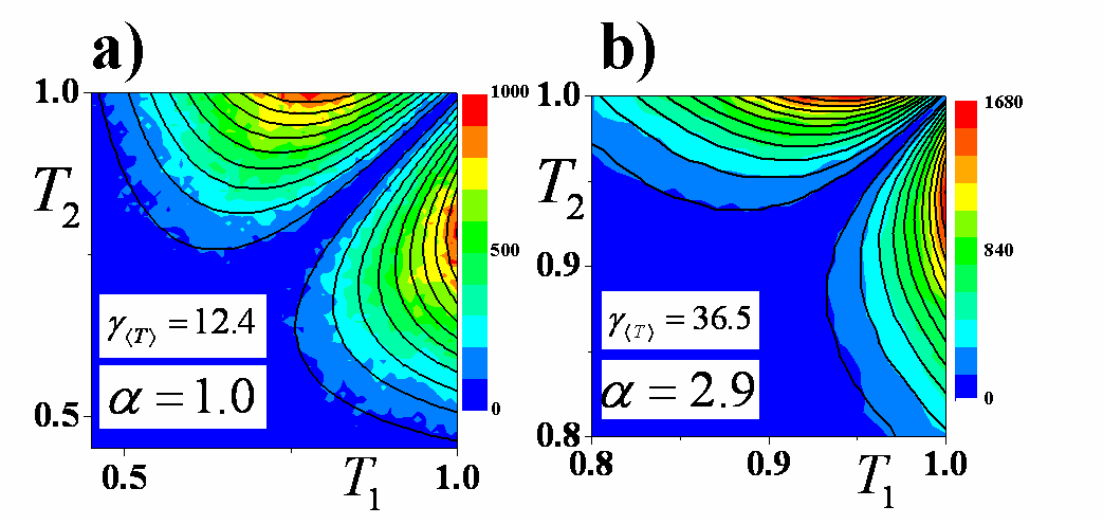

Fig.5.8: The experimental joint PDF of T_1 and T_2 (i.e., $P(T_1,T_2)$) for Loss-Case 0: 3.2-4.2 GHz ($\alpha = 1.0$) (a) and 13.5-14.5 GHz ($\alpha = 2.9$) (b). The color-scale levels blue, green, yellow and red are in ascending density order. The black contours are theoretical predictions for $P(T_1,T_2;\gamma)$ obtained from Eq. 5.3 for $\gamma = 12.4$ (a) and $\gamma = 36.5$ (b).

To estimate the value of γ for my experimental data-sets, I use an analytic expression for $\langle T_1\rangle$ (or equivalently $\langle T_2\rangle$ since T_1 and T_2 are symmetric) in terms of γ from Eq. (4.7) **[59]** which was derived by James Hart for the TRS case,

$$\langle T_1\rangle = \langle T_2\rangle = \langle T\rangle = \frac{1}{4\gamma}(e^{-\gamma}(4(e^{\gamma}-\gamma-1)+4e^{\gamma}(2e^{\gamma}-2-\gamma(2+\gamma))\xi(-\gamma) - 2e^{\gamma/2}(e^{\gamma}(2+\gamma(\gamma-2))-2)\xi(-\gamma/2))) \tag{5.4}$$

where $\xi(z) = -\int_{-z}^{\infty}\frac{e^{-t}}{t}dt$ is the exponential integral function. Figure 5.9 shows the relation between $\langle T\rangle$ and γ.

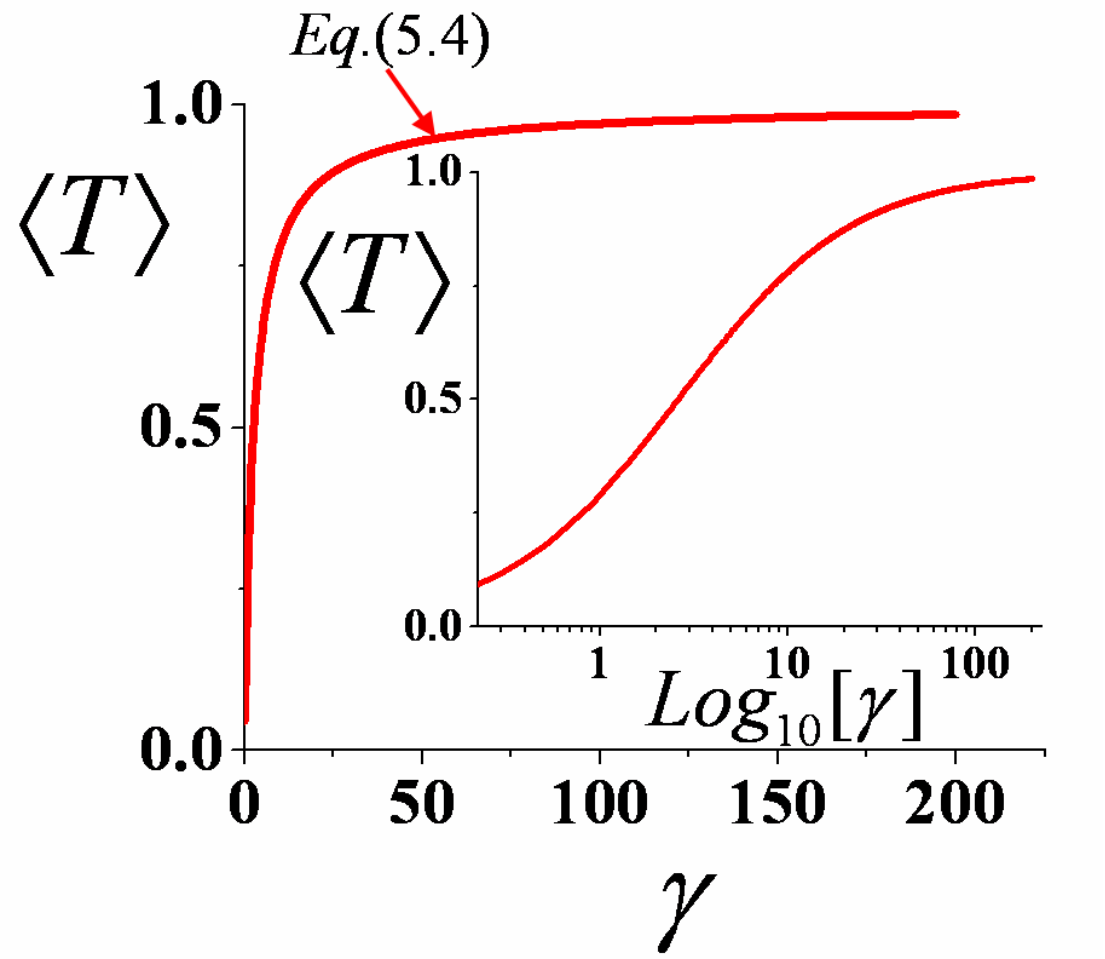

Fig. 5.9: Relation between $\langle T \rangle$ and γ as described in Eq. (5.4). Inset: Relation between $\langle T \rangle$ and γ as described in Eq. (5.4) shown on a semi-log plot.

By determining the value of $\langle T \rangle$ from the measured data set, Eq.(5.4) then uniquely determines the corresponding value of $\gamma\,(\equiv \gamma_{\langle T \rangle})$. This approach yields values of $\gamma_{\langle T \rangle} = 12.4 \pm 0.1$ and $\gamma_{\langle T \rangle} = 36.5 \pm 0.1$ for the data in Fig. 5.8(a) and Fig. 5.8(b), respectively. Using these values of $\gamma_{\langle T \rangle}$, I plot the analytic contour curves defined by Eq. (5.3) for the two loss cases, shown as the solid black lines in Fig. 5.8. The theoretical curves reflect the same number of contour levels shown in the data. I

observe relatively good agreement between the theoretical prediction of Ref. **[59]** and the experimental data. This agreement between the experimental data and the theoretical prediction is also observed to extend over other loss-cases and frequency ranges. Comparing the value of α from each experimental data set with the corresponding value of $\gamma_{\langle T \rangle}$, I empirically determine a linear relation between α and γ, i.e $\gamma = (12.5 \pm 0.1)\alpha$ using 70 points for $\gamma_{\langle T \rangle}$ between about 11 and 300 **[62, 64]** (also see chapter 6).

5.4 Summary of Chapter 5 and Conclusions

The results discussed in this chapter are meant to provide conclusive experimental evidence in support of the "radiation impedance" normalization process introduced in Ref. **[26]** for multiple-port, wave-chaotic cavities. The close agreement between the experimentally determined PDFs and those generated numerically from random matrix Monte Carlo simulations, support the use of Random Matrix Theory to model statistical aspects of real-world wave-chaotic systems. This chapter is a natural two-port extension of the one-port experimental results of Chapter 4 **[45, 46]**. The extension to two-ports makes these results of much broader appeal to other fields of physics and engineering where wave-transport through complex, disordered media is of interest.

In this chapter, I have shown that the full 2x2 radiation impedance matrix of the two-driving ports can accurately quantify the non-ideal and system-specific coupling details between the cavity and the ports as well as the cross-talk between

ports, over any frequency range. Hence, given the experimentally-measured, non-ideally coupled cavity data, this normalization procedure allows the retrieval of the universal statistical fluctuations of wave-chaotic systems which are found only in the limit of perfect coupling. I have experimentally tested the evolution of these universal fluctuations traversing from the regime of intermediate to high loss and for different coupling geometries. I find good agreement between the PDFs obtained experimentally to those generated numerically from Random Matrix Theory. Of particular significance is the joint PDF of the eigenphases of $\tilde{s}$, and the eigenvalues of $\tilde{s}\tilde{s}^{\dagger}$ which lead to the universal conductance fluctuations statistics of quantum-transport systems. The results are not restricted to microwave-billiard experiments but also apply to other allied fields, such as quantum-optics, acoustics and electromagnetic compatibility.

Chapter 6: Experimental Test of Universal Conductance Fluctuations By Means Of Wave-Chaotic Microwave Cavities

Much attention has been focused on the problem of mesoscopic transport through a quantum dot in which a two-dimensional electron gas system contained within an arbitrarily-shaped potential-well boundary is connected to two electron reservoirs through leads– the source (s) and drain (d). Recently it has been possible to fabricate quantum dots with low impurity content where the elastic mean free paths of the enclosed electrons are typically much larger than the physical size of the dot **[27]**. Electron transport through such "ballistic dots" is governed by elastic collisions off the enclosing potential-well boundaries. It has been observed that the terminal conductance of such dots, defined as $\hat{G} = I_s /(V_s - V_d)$ where I_s is the source current flowing into the dot and $(V_s - V_d)$ is the potential difference between these two leads, exhibits strong, reproducible fluctuations on the order of the quantum of conductance ($G_0 = e^2 / h$) **[63, 74, 75]**. These fluctuations arise from quantum-interference effects due to the phase-coherent electron transport within such dots and have been explained using the hypothesis that the fluctuations are governed by Random Matrix Theory **[23].** Similar universal conductance fluctuations (UCF) have also been observed in other systems such as quasi-one-dimensional metal wires **[75, 76]**.

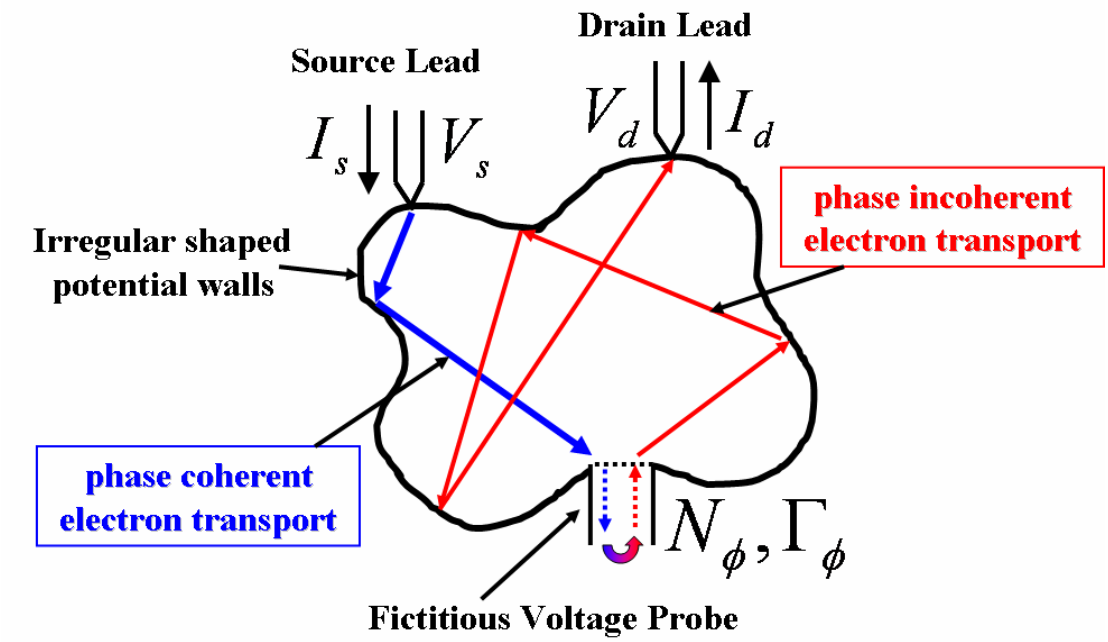

Fig. 6.1: Schematic representation of a ballistic quantum dot showing the "fictitious voltage probe" dephasing model. Electrons enter the dot through the source-lead and leave the dot through the drain-lead. V_s and I_s (V_d and I_d) denote the potential and the current at the source(drain) lead respectively. The electron transport within the interior of the dot is chaotic due to the irregularly shaped potential-well boundaries of the dot. The phase coherent transport is represented as the blue arrows while the red arrows indicate the loss of phase-coherence (dephasing) transport. The dephasing process is modeled as a fictitious voltage probe ϕ with N_ϕ propagating modes and Γ_ϕ being the transmission probability for the electrons entering each fictitious mode from the interior of the dot. The electrons that enter the fictitious probe are then re-injected into the interior of the dot with an arbitrary phase, thereby giving rise to phase-incoherent transport (indicated by the curved arrow).

In a quantum dot, this phase coherence is partly lost by opening the system to the outside world during the process of measurement of the conductance. Quantum phase decoherence (dephasing) can also be induced due to the presence of impurities within the dot, thermal fluctuations, or electron-electron interactions, all of which lead to more classical properties for electron transport **[77]**. Significant theoretical and experimental effort has been devoted to studying the dephasing of the transport electrons in quantum dots **[63, 65, 67]**. One class of theoretical dephasing models utilizes a "fictitious voltage probe (ϕ)" attached to the dot that has a number of channels (modes) N_ϕ, each of which contains a tunnel-barrier with transmission probability Γ_ϕ for the electrons that enter the channel from the dot (Fig. 6.1). Electrons that enter one of the channels of this fictitious probe are re-injected into the dot with a phase that is uncorrelated with their initial phase, and there is no net current through the fictitious probe. An alternative model of electron transport employs a uniform imaginary term in the electron potential **[69, 70]**, leading to loss of probability density with time. It was shown that **[59]**, as far as the conductance is concerned, these two models yield equivalent predictions in the limit when the number of channels in the dephasing lead $N_\phi \to \infty$ and $\Gamma_\phi \to 0$, with the product $\gamma = N_\phi \Gamma_\phi$ remaining finite ("the locally weak absorbing limit"**) [71]**. A similar idea exists for describing ohmic losses in the microwave cavity in terms of non-ideally coupled "parasitic channels" **[66]**. Since the ohmic losses in the microwave cavity are to good approximation uniformly distributed, the equivalence of the imaginary potential and voltage leads models mentioned above can be used to relate the de-phasing parameter γ employed by electron-transport theory **[59]** to the loss

parameter of the microwave cavity ($\alpha = k^2/(\Delta k_n^2 Q)$) which was introduced in Chapter 2. Using the prescription outlined by ref. **[59]** it is possible to determine the analog of conductance for the microwave cavity and make detailed comparisons of data to theory.

For the results presented in this chapter, I make use of an electromagnetic analog of a quantum dot in the form of a two-dimensional chaotic microwave cavity. In the case of a cavity thin in one dimension, Maxwell's equations reduce to a two-dimensional scalar Helmholtz equation. Owing to the analogy between the scalar Helmholtz equation and the Schrödinger equation **[13]**, the chaotic microwave cavity is an ideal surrogate for a ballistic quantum dot without the complicating effects of thermal fluctuations **[63]**, Coulomb interactions, or impurities. The experimental setup of the microwave cavity from which the results discussed in this chapter were obtained has been presented in section 3.2. The microwave cavity is driven by two ports (Port 1 and Port 2) - see Fig.3.3, both of which support a single propagating mode and are analogous to the source and drain leads in the quantum dot. The microwave analog also permits detailed measurements of the eigenvalues **[52, 78, 79]**, eigenfunctions **[41, 55]**, scattering and reaction matrices **[35, 36, 39, 45, 46, 58, 62, 64]**, in a system where every detail of the potential and the port-coupling can be controlled (see chapters 4 and 5).

Adopting a variant of the Landaeur-Buttiker formalism, the normalized conductance ($G = \hat{G}/2G_o$) can be expressed in terms of the scattering matrix

$\vec{\vec{s}} = \begin{pmatrix} s_{11} & s_{12} \\ s_{21} & s_{22} \end{pmatrix}$ of a chaotic cavity when the leads (ports) are perfectly coupled to the cavity **[59]**. i.e.,

$$G = |s_{12}|^2 + \frac{(1-|s_{11}|^2-|s_{12}|^2)(1-|s_{22}|^2-|s_{21}|^2)}{2-|s_{11}|^2-|s_{12}|^2-|s_{21}|^2-|s_{22}|^2}, \tag{6.1}$$

where the first term describes the direct (phase coherent) transport through the microwave-cavity and corresponds to the conductance of the quantum-dot due to the electrons that did not enter the fictitious voltage probe. The second term is a correction that describes the conductance due to the electrons that are re-injected into the dot from the phase-breaking fictitious voltage-probe, thereby ensuring particle conservation in the voltage-probe model **[59]**.

In the time-reversal symmetric case with single-mode leads, Ref. **[59]** has shown that as γ increases the probability density function of G (i.e. $P(G;\gamma)$) becomes more and more sharply peaked around the classical value of $G = 1/2$. In the limit of large γ, an asymptotic analytic expression for $P(G;\gamma)$ is predicted to be **[59],**

$$P(G;\gamma) = \frac{1}{2}\gamma(1+|x|-x)e^{-|x|} \quad \text{with } x = 2\gamma(G-1/2). \tag{6.2}$$

This yields a large-γ asymptotic expression for the mean and variance of G which are predicted to be **[59],**

$$< G >= \frac{1}{2} - \frac{1}{2\gamma} + O(\gamma^{-2}), \tag{6.3},$$

$$\text{var}(G) = \frac{3}{4\gamma^2} + O(\gamma^{-3}). \tag{6.4}.$$

This chapter is divided into the following sections. In section 6.1, I derive an empirical relation between the dephasing parameter γ and the cavity loss-parameter α based on my experimental results. Section 6.2 then explores the PDFs of the experimentally derived universal conductance fluctuations for increasing values of γ and compares them with predictions from **[59]** and Random Matrix Theory. In section 6.3, I experimentally test the predictions from **[59]** for the mean and variance of these universal conductance fluctuation PDFs as a function of γ. Finally, section 6.4 concludes the chapter with a summary of my experimental findings and its implications.

6.1 Relation between the dephasing parameter(γ) and the cavity loss-parameter(α)

To report my experimental results, I begin by examining the relationship between the estimated dephasing parameter $\gamma_{\langle T \rangle}$ (see section 5.3.3) and the estimated cavity loss parameter α which is determined as per the procedure explained in chapter 5. By employing a sliding frequency window 1 GHz wide that runs over each of the three Loss-Cases - 0, 1, 2 from 3 to 18 GHz, I estimate the value of $\gamma_{\langle T \rangle}$ and the corresponding value of α for each window. The comparison is shown as the black circles in Fig. 6.2. A linear fit yields the empirical expression $\gamma_{\langle T \rangle} = (12.5 \pm 0.1)\alpha$ for nearly 70 points with values for $\gamma_{\langle T \rangle}$ ranging from about 11 to about 300. By comparing the Poynting theorem for the electromagnetic cavity with the continuity equation for the probability density in the quantum system **[80, Appendix D]**, I find $\gamma = 4\pi\alpha$, with $4\pi \cong 12.56...$. This result can be considered an empirical confirmation of the proposed equivalence of the imaginary potential

(uniform volume losses) and de-phasing lead models in the limit considered in **[59]**. The 1 GHz width of my sliding window was chosen to be large enough to overcome the effects of short-ray paths (which are not removed by only configuration averaging **[25, 26, 62]**), but at the same time small enough that the cavity losses can be assumed to be approximately constant over this frequency range **[64]**.

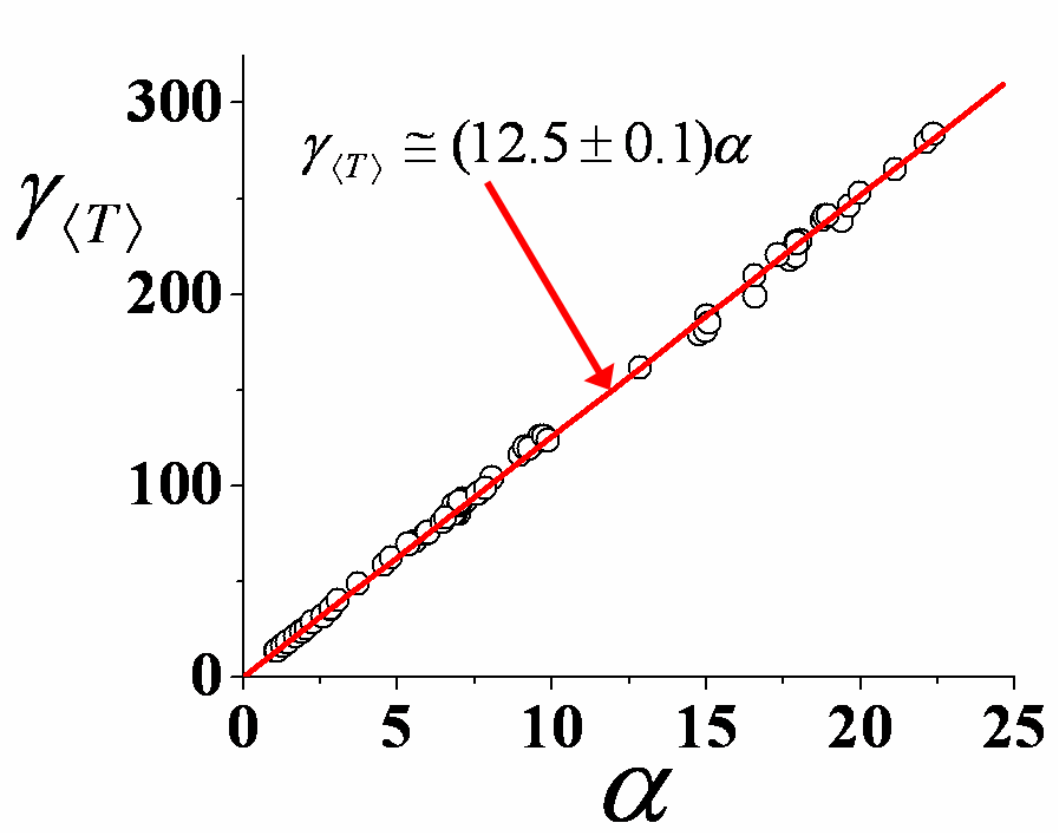

Fig. 6.2: The relation between the experimentally determined $\gamma_{\langle T\rangle}$ and α is shown as the circles. A linear fit (red line) yields the empirical expression $\gamma_{\langle T\rangle} = (12.5 \pm 0.1)\alpha$.

6.2 Uncovering the Universal Conductance Fluctuations PDFs

In Fig. 6.3, the experimentally obtained histogram approximation (symbols) to the PDF of the normalized conductance ($P(G;\gamma)$) derived from the normalized scattering matrix $\vec{s}$ and Eq. (6.1) is shown for four cavity data sets - dry-ice case : 4.1-4.7 GHz (hexagons) with $\alpha = 0.9 \pm 0.1$ and $\gamma_{\langle T \rangle} = 11.2 \pm 0.1$, Loss Case 0 : 16.8-17.6 GHz (stars) with $\alpha = 2.8 \pm 0.1$ and $\gamma_{\langle T \rangle} = 35.1 \pm 0.1$, Loss Case 1 : 8.3-9.5 GHz (circles) with $\alpha = 6.6 \pm 0.1$ and $\gamma_{\langle T \rangle} = 82.2 \pm 0.1$, and Loss Case 2 : 16.8-17.6 GHz (squares) with $\alpha = 21.7 \pm 0.1$ and $\gamma_{\langle T \rangle} = 272.1 \pm 0.1$. The colored solid lines (magenta, black, green, red) are the asymptotic analytic expression for $P(G,\gamma)$ (Eq. (6.2)) with values of γ that correspond to the estimated $\gamma_{\langle T \rangle}$ values obtained from the data-sets represented by the hexagons, stars, circles and squares respectively. The purple-colored solid line in Fig. 6.3(a) is a random matrix Monte-Carlo simulation (see section 2.5) for values of $\gamma_{\langle T \rangle} = 11.2$ corresponding to the data set in Fig. 6.3(a). The red error bars (roughly the size of the symbols) in Fig. 6.3 which are representative of the typical statistical binning error of the experimental histograms show that the agreement between the data (shown by the symbols) and the theoretical predictions (shown by the solid curves) improves as the value of $\gamma_{\langle T \rangle}$ increases. This is to be expected as Eq. (6.2) is valid only in the high dephasing limit ($\gamma >> 1$). Similar good agreement between the data and Eq. (6.2) is obtained for all of the nearly 40 data sets that I examined in which the frequency ranges and cavity loss cases resulted in an estimate of the $\gamma_{\langle T \rangle}$ parameter to be greater than about 18 **[64]**.

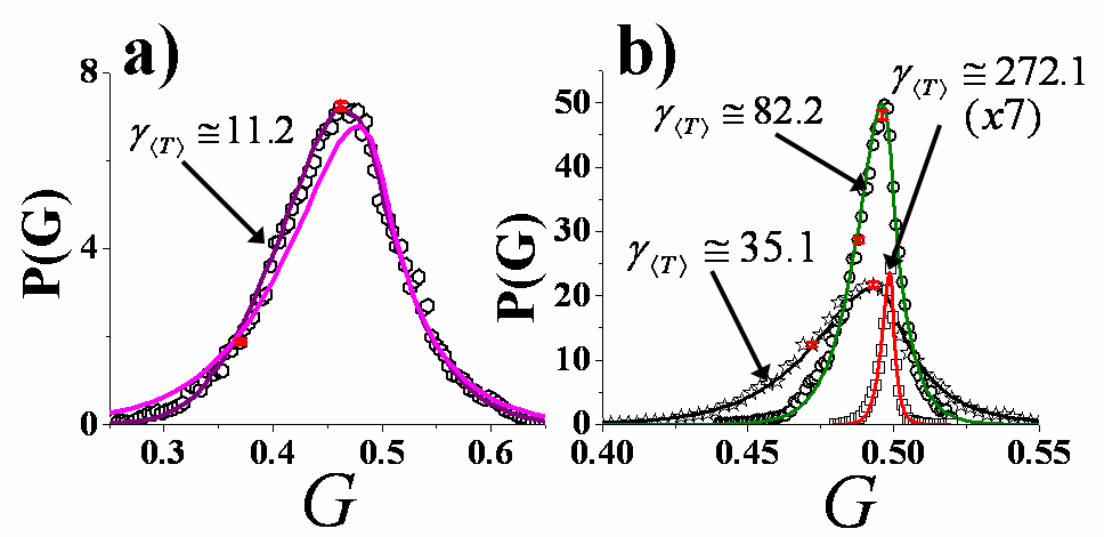

Fig. 6.3: (a) PDFs for the normalized conductance $P(G;\gamma)$ obtained from a chaotic cavity for dry-ice case : 4.1-4.7 GHz (hexagons) ($\alpha = 0.9 \pm 0.1; \gamma_{\langle T\rangle} = 11.2 \pm 0.1$). The magenta solid line is the analytic prediction Eq.(6.2) for $\gamma = 11.2$. The purple solid line is numerically generated from Random Matrix Theory for $\gamma = 11.2$. (b) PDFs for the normalized conductance $P(G;\gamma)$ for Loss Case 0 : 16.8-17.6 GHz (stars) ($\alpha = 2.8 \pm 0.1; \gamma_{\langle T\rangle} = 35.1 \pm 0.1$); Loss Case 1 : 8.3-9.5 GHz (circles) ($\alpha = 6.6 \pm 0.1; \gamma_{\langle T\rangle} = 82.2 \pm 0.1$) and Loss Case 2 : 16.8-17.6 GHz (squares) ($\alpha = 21.7 \pm 0.1; \gamma_{\langle T\rangle} = 272.1 \pm 0.1$). The black, green and red solid lines are analytic predictions Eq.(6.2) for $\gamma = 35.1, \gamma = 82.2$ and $\gamma = 272.1$. The red error bars (roughly the size of the symbols) are representative of the typical statistical binning error of the experimental histograms

In order to bring out the universal scaling behavior of the $P(G;\gamma)$ distributions (Eqs. (6.2)) and also to test that these distributions remain strictly non-

Gaussian for increasing values of γ (as predicted by **[59]**), I rescale the $P(G;\gamma)$ distributions by plotting $Log_{10}[\frac{P(G;\gamma)}{\gamma}]$ versus $x = 2\gamma(G - 1/2)$ in Fig. 6.4 for three representative data sets with $\gamma_{\langle T \rangle}$ ranging from about 56 to about 220. I observe that the three data sets roughly fall on top of each other. The solid blue curve is the theoretical curve, Eq.(6.2) which is in good agreement with the data. Some deviation of the symbols from the theoretical curve near $x \cong +2$ can be observed. This is attributed to the lack of adequate statistics in the tails of the experimentally determined histogram approximations to the probability density functions of the conductance. Overall, for values of x ranging from -4 to $+2$, the agreement is qualitatively good and applies over other data sets where $\gamma_{\langle T \rangle}$ ranges from about 18 to 330. The asymmetric (non-parabolic) nature of the experimental data (symbols) confirms that the experimentally obtained $P(G;\gamma)$ remains strictly non-Gaussian and negatively skewed even for large values of γ, as predicted by **[59]** (see **[64]**).

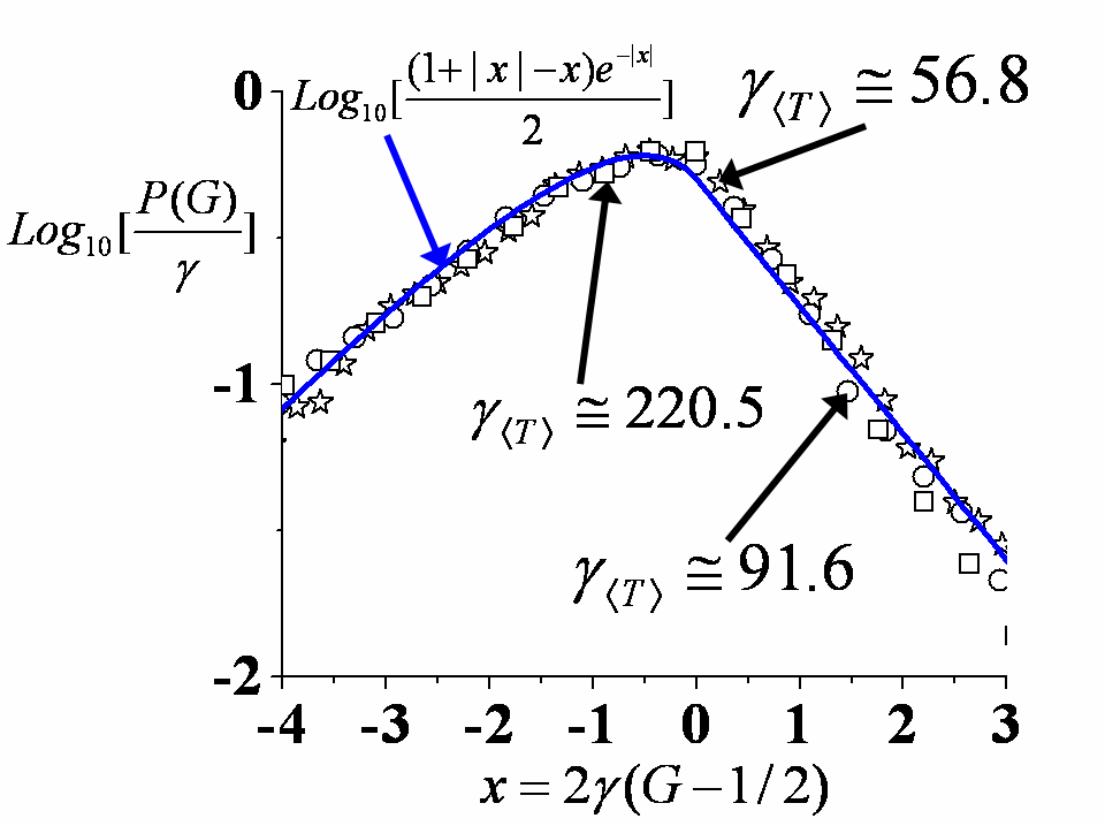

Fig.6.4: Universal scaling behavior of the conductance distributions is shown. The vertical-axis represents $Log_{10}[\frac{P(G,\gamma)}{\gamma}]$ with the corresponding $x = 2\gamma(G-1/2)$ along the horizontal-axis for three representative data sets consisting of Loss Case 1 : 5.01-6.08 GHz (stars) ($\alpha = 4.5 \pm 0.1; \gamma_{\langle T\rangle} = 56.6 \pm 0.1$); Loss Case 1 : 13.6-14.6 GHz (circles) ($\alpha = 7.3 \pm 0.1; \gamma_{\langle T\rangle} = 91.6 \pm 0.1$) and Loss Case 2 : 13.6-14.6 GHz (squares) ($\alpha = 17.7 \pm 0.1; \gamma_{\langle T\rangle} = 220.5 \pm 0.1$).The solid blue curve is the theoretical curve, Eq.(6.2).

6.3 Validating Theoretical Predictions for the Mean and Variance of the UCF PDFs

In Fig. 6.5, I again employ the sliding frequency window of width 1 GHz to test the asymptotic ($\gamma >> 1$) relations for the mean $< G >$ (Eq. 6.3) and variance $\mathrm{var}(G)$ (Eq. 6.4) of $P(G;\gamma)$ as a function of dephasing (loss) parameter γ. As before, I determine the value of $\gamma_{\langle T \rangle}$ for each frequency window data set that runs from 3 to 18 GHz for the three Loss Cases. I then determine the corresponding values of the mean and variance of the corresponding conductance distributions $P(G;\gamma)$ of each frequency window. In the inset of Fig. 6.5, each star indicates the experimentally estimated mean value of G (i.e., $< G >$) for the corresponding value of $\gamma_{\langle T \rangle}$. The standard deviation about the experimentally determined mean is of order 10^{-5}. I observe that as $\gamma_{\langle T \rangle}$ increases, the stars asymptotically approach the classical value of $< G >= 1/2$. The solid black curve represents the leading terms in Eq. (6.3)**.**

The circles in Fig. 6.5 show a similar analysis for the variance ($\mathrm{var}(G)$) of the normalized conductance distributions $P(G;\gamma)$ as a function of γ. The solid black curve represents the leading term in Eq. (6.4)**.** It can be observed that the circles closely follow the functional approximation for the theoretical curve (Eq. (6.4)) for the range of $\gamma_{\langle T \rangle}$ values from about 18 to about 330, with no adjustable parameters **[64]**.

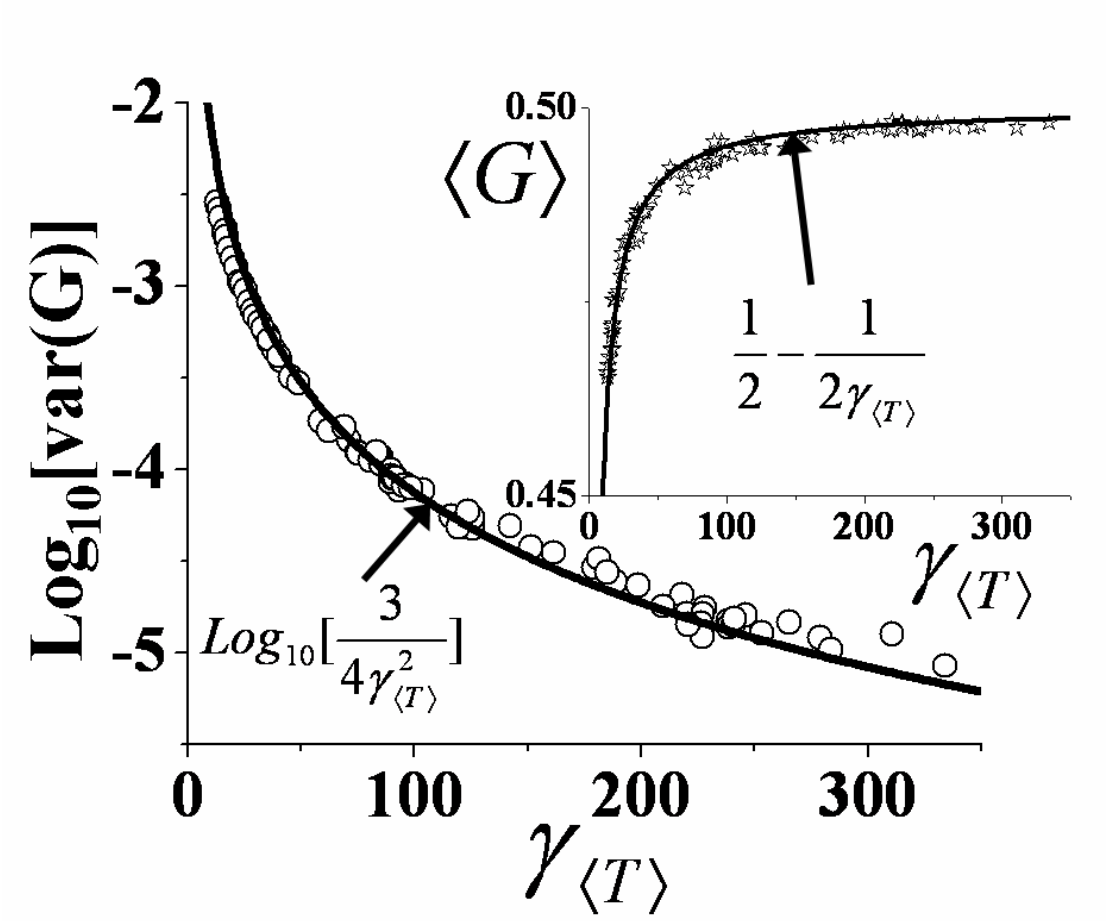

Fig.6.5: Evolution of the variance of the experimentally determined $P(G;\gamma)$ distributions (i.e., $\mathrm{var}(G)$) for increasing values of $\gamma_{\langle T\rangle}$ plotted on a logarithmic scale. The solid black line represents the leading terms of the prediction in Eq.(6.4). Inset: Evolution of the mean of the experimentally determined $P(G;\gamma)$ distributions (i.e., $\langle G\rangle$) for increasing values of $\gamma_{\langle T\rangle}$. The solid black line represents the leading terms of the prediction in Eq.(6.3). These are zero-parameter fits.

6.4 Summary of Chapter 6 and Conclusions

The results discussed in this chapter provide experimental evidence in support of the theoretical arguments proposed by **[59]** and the hypothesis that Random Matrix Theory provides a good description of the conductance fluctuation statistics in a ballistic chaotic quantum-dot in the presence of dephasing. I have shown that in the "locally weak absorbing limit" as discussed in **[59]**, the dephasing parameter can be related to the cavity loss parameter. I have derived an empirical linear relation between γ and the cavity loss-parameter α based on my experimental data. The finite conductivity of the metallic walls of the cavity translates to a minimum-possible experimentally accessible γ-value of about 11 for my experiments (at least for the present cavity geometry and temperatures of -78.5^{o}C and above). I have also shown that my experimentally determined conductance distributions and the asymptotic analytic functional forms for the PDF of G ($P(G)$), its mean value ($< G >$) and variance ($\mathrm{var}(G)$) are in good agreement over a broad range of large γ values. These results serve to establish the microwave analog as a method to study detailed theories of non-interacting quantum transport and de-coherence in quantum coherent systems.

Chapter 7: Characterization of Impedance and Scattering Matrix Fluctuations of Wave-Chaotic Systems

Statistical variations of the elements of the cavity impedance matrix ($\vec{\vec{Z}}$) and the cavity scattering matrix ($\vec{\vec{S}}$) due to small random variations in the scattering are of great interest. These statistics are found to be influenced by two fundamental aspects, (i) universal aspects as described by Random Matrix Theory, and (ii) non-universal, system-specific aspects that are dependent on the details of the coupling of input channels (e.g., transmission lines, waveguides,etc) to the scatterer. In this chapter, the quantity

$$R_Z = \frac{Var[Z_{ij}]}{\sqrt{Var[Z_{ii}]Var[Z_{jj}]}} \ , i \neq j \tag{7.1}$$

is considered. Here $Var[A]$, the variance of the complex scalar A is defined as the sum of $Var[\mathrm{Re}[A]]$ and $Var[\mathrm{Im}[A]]$.The variance is taken over the ensemble of configurations of the system. Reference **[81]** has shown that this result is of the form,

$$R_Z = \begin{cases} (3 - 2\int_0^\infty dx g(x) \frac{4}{4 + (x/\alpha)^2})^{-1} & (TRS) \\ \\ (1 + \frac{1 - e^{-4\pi\alpha}}{4\pi\alpha})^{-1} & (BTRS) \end{cases} \tag{7.2}$$

where g(s) is given by $g(s) = f^2(s) - [\int_0^s d(s') f(s') - 1/2](df/ds)$, with $f(s) = \sin(\pi s)/(\pi s)$; and α is the cavity loss-parameter introduced in chapter 2.The terms TRS and $BTRS$ stands for cavities with Time-Reversal Symmetry or Broken Time-Reversal Symmetry respectively. Reference **[81]** has shown that the quantity

R_Z is universal in that its value depends only upon the value of the loss-parameter (α). In specific, the asymptotic values for R_Z is given as,

$$R_Z = \begin{Bmatrix} 1/2 & (TRS) \\ \\ 1 & (BTRS) \end{Bmatrix} \qquad \text{for } \alpha >> 1, \tag{7.3}$$

and,

$$R_Z = \begin{Bmatrix} 1/3 & (TRS) \\ \\ 1/2 & (BTRS) \end{Bmatrix} \qquad \text{for } \alpha << 1, \tag{7.4}$$

The nature of R_Z as a function of α is shown in Fig. 7.1.

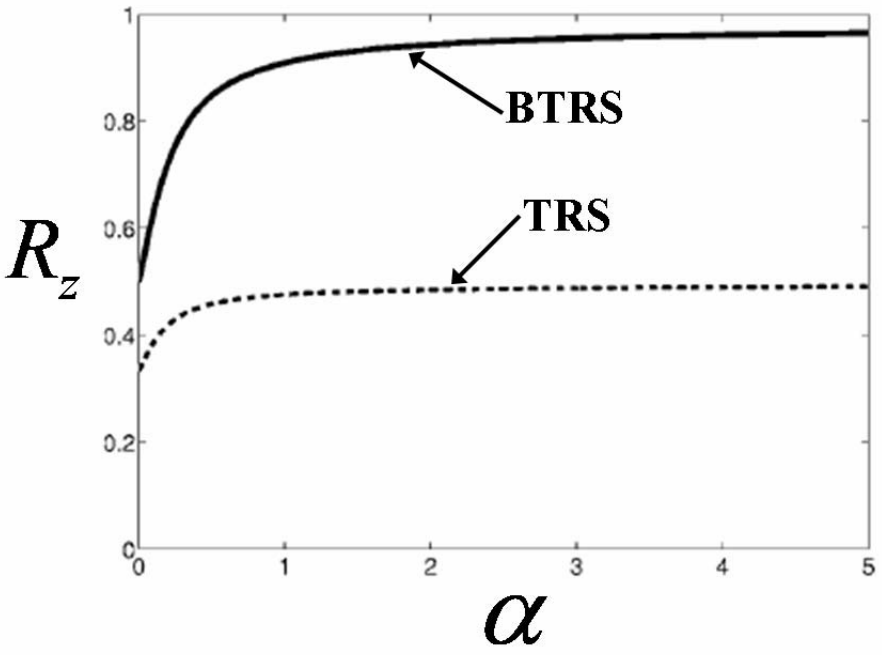

Fig. 7.1: R_Z vs the loss parameter α, as specified in Eq. (7.2). Figure reproduced from **[81]**.

A ratio similar to Eq.(7.1) can also be considered for the scattering matrix of the wave-chaotic cavity ($\vec{S}$),

$$R_S = \frac{Var[S_{ij}]}{\sqrt{Var[S_{ii}]Var[S_{jj}]}} \ , i \neq j \ . \tag{7.5}$$

In contrast to Eq.(7.2), **[81]** has shown that R_S in general depends upon both the coupling to the cavity and the loss parameter α. This non-universal aspect (dependence on the coupling) of R_S is shown in Fig.7.2. The quantities $\bar{\gamma}_r = \mathrm{Re}[Z_{rad}]/Z_0$ and $\bar{\gamma}_x = \mathrm{Im}[Z_{rad}]/Z_0$ are scalar quantities that determine the degree of coupling between the port and the cavity. In this figure both ports are symmetrically coupled to the cavity. Perfect coupling implies $\bar{\gamma}_r = 1$ and $\bar{\gamma}_x = 0$ as was mentioned in chapter 2. Figure 7.2(a) shows R_S vs $\bar{\gamma}_r$ for $\bar{\gamma}_x = 0$ in a loss-less case, with $\alpha = 0$ (circles), and in a high loss case, $\alpha = 5$ (thick black line). While in Fig. 7.2(b), R_S vs $\bar{\gamma}_x$ for $\bar{\gamma}_r = 1$ in a loss-less case, with $\alpha = 0$ (circles), and in a high loss case, $\alpha = 5$ (thick black line) is shown. Note the dependence of R_S on $\bar{\gamma}_r$ and $\bar{\gamma}_x$ in the loss-less case. However, in the limit of high loss, R_S also becomes universal **[81]** i.e., independent of coupling,

$$R_S = \left\{ \begin{matrix} 1/2 & (TRS) \\ \\ 1 & (BTRS) \end{matrix} \right\} \qquad \text{for } \alpha >> 1 . \tag{7.6}$$

Hence from Eq.(7.3) and Eq.(7.6), for $\alpha >> 1$, $R_S = R_Z$.

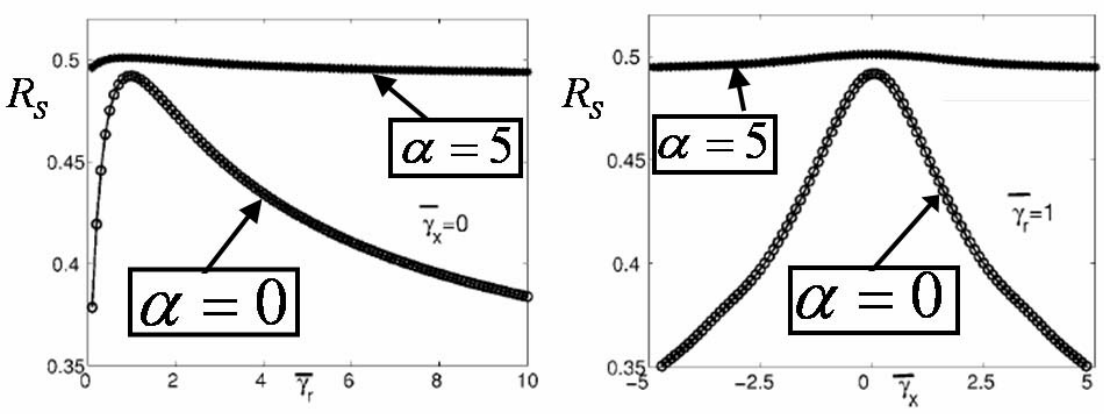

Fig. 7.2: (a) R_S vs $\bar{\gamma}_r$ for $\bar{\gamma}_x = 0$ in a loss-less case ($\alpha = 0$) and in a high loss case ($\alpha = 5$). (b) R_S vs $\bar{\gamma}_x$ for $\bar{\gamma}_r = 1$ in a loss-less case ($\alpha = 0$) and in a high loss case ($\alpha = 5$). The quantities $\bar{\gamma}_r = \mathrm{Re}[Z_{rad}]/Z_0$ and $\bar{\gamma}_x = \mathrm{Im}[Z_{rad}]/Z_0$ are scalar quantities that determine the degree of coupling between the port and the cavity. Reproduced from **[81]**.

Based upon their experiments on a mode-stirred electromagnetic cavity, Fiachetti and Michelsen **[82]** have recently conjectured the universality of Eq.(7.6) in the *TRS* case. More generally, Eq.(7.6) follows from classic results of Hauser and Feshbach describing fluctuations in the cross-section of inelastic neutron scattering **[83]**, and this result has been obtained by Friedman and Mello **[84]** using the concept of maximum entropy, and by Agassi *et.al.* using a random-matrix model **[31]**. The point to be reiterated is that the universal result for R_S i.e., Eq.(7.6), holds only for $\alpha >> 1$, while the universal result for R_Z (Eq.(7.2)) holds for arbitrary α **[81]**.

In this chapter my objective is to experimentally test the prediction of **[81]** for R_Z and R_S as a function of the cavity loss-parameter (α). In section 7.1, I provide

experimental results testing the theoretical predictions for the statistical fluctuations in the variance of the $\vec{\vec{S}}$ and $\vec{\vec{Z}}$ elements, in the limit of large damping. Then, in Section 7.2, I conclude with a summary of my results and its implications.

7.1 Experimental Results for R_Z and R_S

The experimental setup of the microwave cavity for the results to follow has been explained in section 3.2, but with the metallic perturbations of the type used in section 3.1. To eliminate the effect on the average of short ray orbits returning to the antenna (these lead to rapidly frequency-dependent systematic deviations of the average from the ensemble average, as discussed in **[25])** I perform frequency averaging over a sliding window of width 300MHz. I denote such sliding averages of impedance and scattering variance ratios by $\overline{R}_Z$ and $\overline{R}_S$ respectively. The inset in Fig. 7.3 shows $\overline{R}_Z$ (solid line) over a frequency range 4-12 GHz. Denoting the average of $\overline{R}_Z$ over the entire range, 4-12 GHz, by $\overline{\overline{R}}_Z$, I obtain $\overline{\overline{R}}_Z = 0.49$, and find that $|\overline{\overline{R}}_Z - \overline{R}_Z| \leq 0.02$ over the entire frequency range. This value of experimentally obtained $\overline{R}_Z$ is close to the theoretical value of ½ for large damping. Also shown in the inset is the variance ratio obtained with no frequency averaging (small circles). These are deviations from the frequency averaged ratio values with a standard deviation of 0.04. Nevertheless, the mean value of the variance ratio over the entire frequency range is 0.49.

The circles, stars and dashes in Fig. 7.3 show the variation in $\ln[Var[Z_{21}]]$, $\ln[\sqrt{Var[Z_{11}]Var[Z_{22}]}]$ and $\ln[\overline{\overline{R}}_Z\sqrt{Var[Z_{11}]Var[Z_{22}]}]$ respectively, as a function of

frequency. The agreement is quite good (i.e., the dashes overlie the open circles) at all frequencies **[81]**.

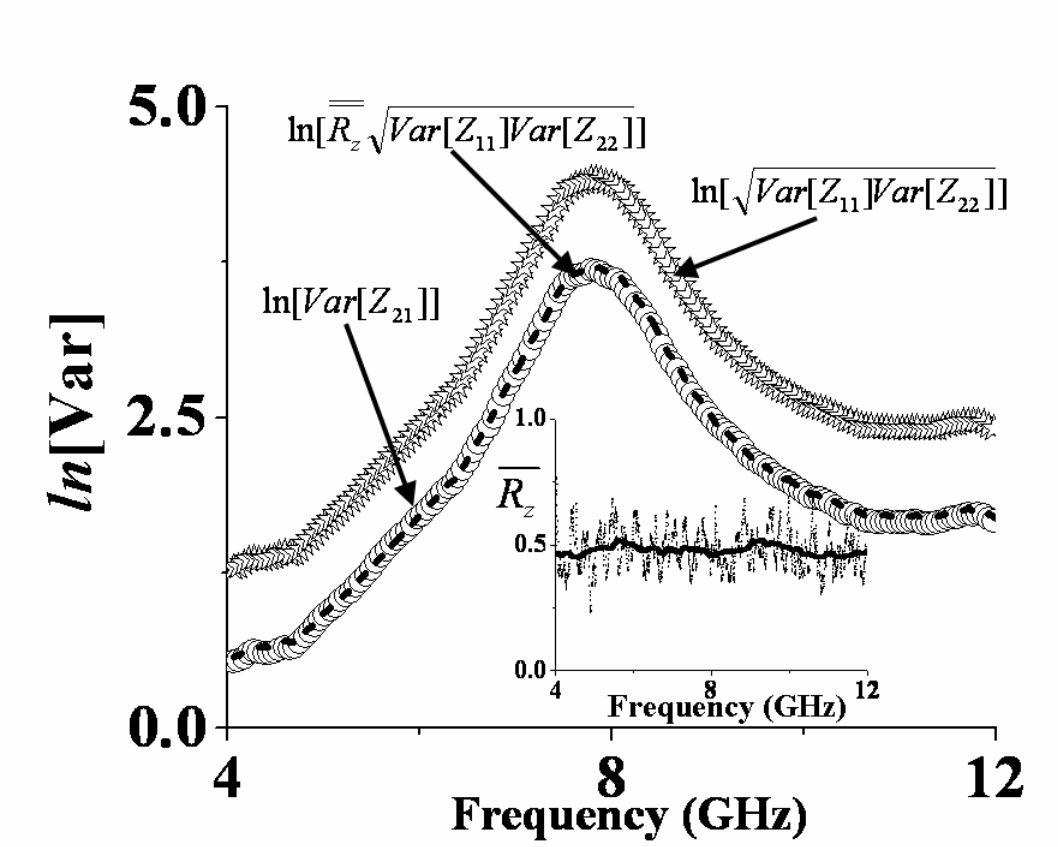

Fig.7.3: $Var[Z_{21}]$ (circles), $\sqrt{Var[Z_{11}]Var[Z_{22}]}$ (stars) and $\overline{\overline{R}}_Z\sqrt{Var[Z_{11}]Var[Z_{22}]}$ (dashes) are plotted on a natural-logarithmic scale as a function of frequency from 4 to 12 GHz. Inset shows the ratio $\overline{R}_Z$ as a function of frequency (solid line). The small circles show R_Z without any frequency averaging.

Similarly in Fig. 7.4, I present data for the scattering variance ratio. Experimentally I obtain $\overline{\overline{R}}_S = 0.5$ and $|\overline{\overline{R}}_S - \overline{R}_S| \leq 0.08$ over the frequency range 4-12 GHz. The circles, starts and dashes in Fig. 7.4 show the variation in $Var[S_{21}]$, $\sqrt{Var[S_{11}]Var[S_{22}]}$ and $\overline{\overline{R}}_S\sqrt{Var[S_{11}]Var[S_{22}]}$, respectively, as a function of

frequency. Similar to the impedance data (Fig. 7.3), I observe that the data for $\overline{\overline{R}}_S\sqrt{Var[S_{11}]Var[S_{22}]}$ (dashes) overlie the data for $Var[S_{21}]$ (open circles), again indicating that the experimentally obtained value for $\overline{R}_S$ shows good agreement with the asymptotic theoretical values for highly damped time-reversal symmetric systems over a large frequency range **[81]**.

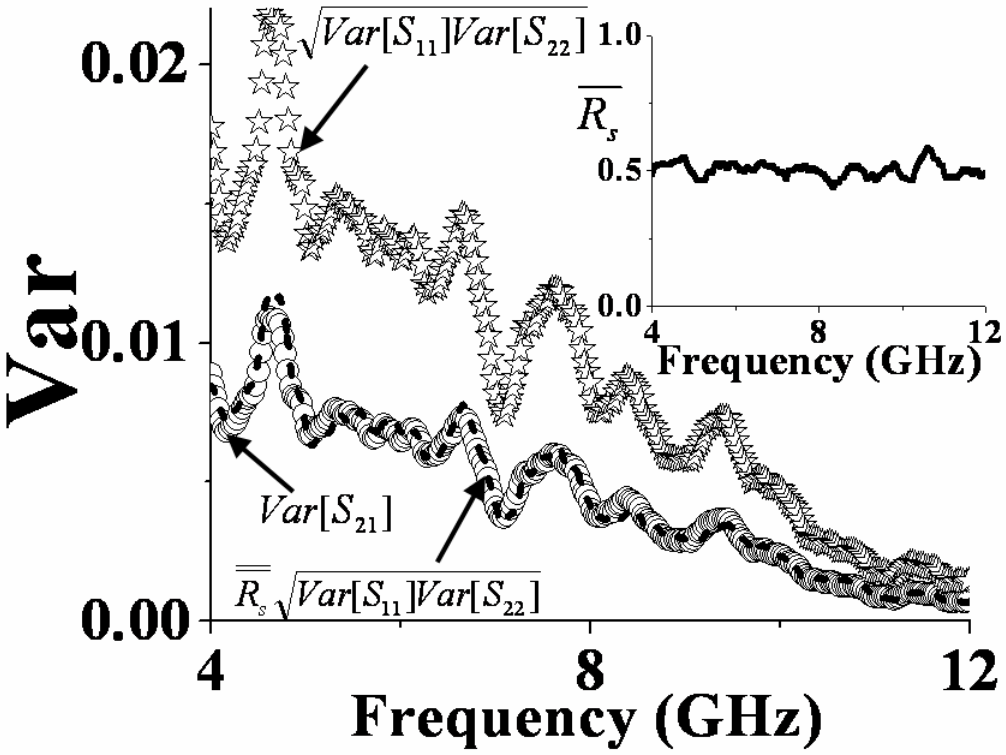

Fig. 7.4: $Var[S_{21}]$ (circles), $\sqrt{Var[S_{11}]Var[S_{22}]}$ (stars) and $\overline{\overline{R}}_S\sqrt{Var[S_{11}]Var[S_{22}]}$ (dashes) are plotted as a function of frequency from 4 to 12 GHz. Inset shows the ratio $\overline{R}_Z$ as a function of frequency (solid line).

An experimental study of the impedance and scattering variance ratios for low values of α ($\alpha < 0.5$) as well as for the BTRS case is currently not accessible with the present experimental setup and needs to be explored in the future.

7.2 Summary of Chapter 7 and Conclusions

In summary, I have experimentally tested the predictions of **[81]** for the impedance and scattering variance ratios in the limit of high loss and find good agreement between theoretical predictions and experimental data. The impedance and scattering ratios are of key significance in the field of HPM effects on electronics within complicated enclosures. These quantities determine the range of voltages that can be induced on the second port due to a given excitation at the first port - without the requirement of measuring the transmission properties of the enclosure. This point will be addressed in greater detail in Chapter 8.

Chapter 8: Applications of the Random Coupling Model to Predicting HPM-Effects in 3-D, Real World Enclosures

The "radiation impedance" normalization which was introduced through the "Random Coupling Model (RCM)" in Chapter 2 has proved to be extremely successful in accounting for the non-ideal coupling between the driving ports and the quasi-two-dimensional, quarter-bow-tie shaped wave-chaotic cavity of chapter 3. In chapters 4, 5 and 6, it was shown that the experimental results for the statistical descriptions of the normalized impedance, admittance and scattering matrices were in good agreement with corresponding predictions from Random Matrix Theory. However, these experimental results were validated on a microwave cavity which was specifically designed to have chaotic ray dynamics. The objective of the current chapter is to push the "Random Coupling Model" towards more real-world scenarios-namely, the coupling of electromagnetic radiation into complex enclosures, such as a computer-box, which is of key interest to researchers and engineers in the HPM-effects and Electromagnetic Compatibility community.

To achieve this objective, I first need to establish three aspects about the wave-scattering within the computer-box cavity. Firstly, I need to experimentally prove the existence of wave-chaotic scattering within the computer-box cavity (section 8.1). Secondly, the applicability of the "radiation impedance" normalization to account for non-ideal port coupling in a three-dimensional coupling-geometry, where polarization of the waves and the effects of field variations associated with the presence of a side-wall has to be established experimentally (section 8.2). Note that in

the experimental setups described in chapter 3, the driving ports were positioned many wavelengths away from the side-walls so that the near-field structure of the ports was not altered by the side-walls. This is not the case for the results presented in this chapter. Finally, the existence of universal fluctuations in the normalized impedance and normalized scattering matrices for the computer-box cavity (3-D geometry) has to be established and shown to be in agreement with corresponding predictions from Random Matrix Theory. This aspect is covered in section 8.3.

Once these three aspects of the wave-scattering within the computer-box cavity has been experimentally established, it is then possible to utilize the Random Coupling Model to introduce a prediction algorithm for the statistical nature (Probability Density Function) of the induced voltages at key points (such as a microprocessor-pin lead, a PCB track, etc.) within the computer-box cavity, for a given HPM attack scenario. This algorithm, which I call the "RCM Voltage Algorithm", is explained and experimentally validated in section 8.4. In section 8.5, another prediction algorithm for the variance of the induced voltages based upon the Hauser-Feshbach scattering ratios, which was introduced in chapter 7, is presented and experimentally validated. Then in section 8.6, based upon the insights gained from the Random Coupling Model, certain design-guidelines are presented to make a generic 3-D complicated enclosure more resistant to HPM attack. Finally, section 8.7 concludes this chapter with a summary of the results and its implications.

8.1 Proving the Existence of Wave-Chaotic Scattering in a Computer-Box Cavity

The three-dimensional cavity under study is a typical computer-box of physical dimensions 38 cm x 21 cm x 23 cm (Fig. 8.1(a)), which contains all the internal electronics – motherboard, memory chips, network card, etc (Fig.8.1(b)). The floppy-drive, CDROM-drive and SMPS power-supply unit were removed to increase the internal volume of the cavity and also to decrease the inherent cavity-loss. The cavity was excited by means of two ports, labeled Port 1 and Port 2 in Fig. 8.1(c), each uniformly radiating 7dBm of RF power over the frequency range of 4 to 20 GHz. The free-space wavelength at 4 GHz corresponds to about 7.5 cm which is about three times smaller than the smallest cavity dimensions. The ports are sections of coaxial transmission lines, with the exposed inner-conductor extending 13 mm into the volume of the cavity from the side walls. Each port has an inner-conductor diameter of 2a=1.27mm.

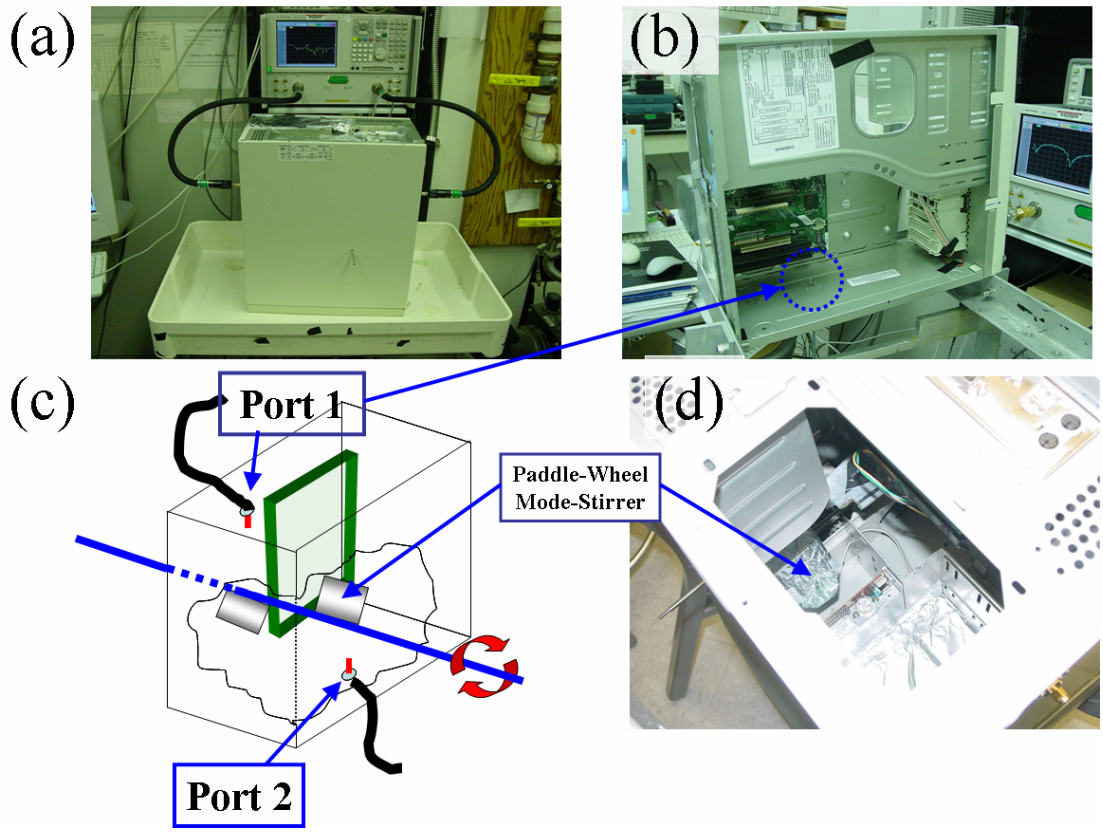

Fig. 8.1: (a) Photograph of the experimental setup of the computer-box used for testing the Random Coupling Model. The computer-box is connected to the Agilent E8364B Vector Network Analyzer (in background). (b) Photograph of the computer-box with the outer metallic-casing removed. The motherboard and one of the driving ports (port 1) on the bottom-plate of the computer-box cavity are clearly visible.(c) Schematic showing the location of the two driving ports, the paddle-wheel mode-stirrer used to generate an ensemble of cavity measurements. (d) Photograph showing one of the paddle-wheel blades of the mode-stirrer. The paddle-wheel blade is made of card-board paper coated with aluminum foil.

To make a statistical analysis of the electromagnetic response of the computer-box cavity, the first step involves measuring a large ensemble of the full

2x2 cavity scattering matrix ($\vec{\vec{S}} = \begin{bmatrix} S_{11} & S_{12} \\ S_{21} & S_{22} \end{bmatrix}$) using an Agilent E8364B Vector Network Analyzer. This is referred to as the "Cavity Case". To realize this large ensemble, a mode-stirrer is introduced into the volume of the cavity. The mode-stirrer (shown in schematic in Fig. 8.1(c)) consists of a central metallic shaft (shown as the blue line) of diameter about 5 mm with two paddle-wheel type blades (silver-colored rectangles) measuring approximately 10cm x 5cm and placed 7 cm apart. The two blades are made of cardboard-paper coated with aluminum foil (Fig. 8.1(d)) and are oriented perpendicular to each other on the shaft. Each orientation of the blades within the cavity results in a different internal field configuration. For each configuration, $\vec{\vec{S}}$ is measured as a function of frequency from 4 to 20 GHz in 16000 equally spaced steps. By rotating the shaft through twenty different positions, an ensemble of 320,000 computer-box cavity scattering matrices is thus collected. From the $S_{21}(\omega)$ measurements, it is inferred that the typical loaded-Q of the computer-box cavity ranges from about 45 at 4GHz to about 250 at 20 GHz.

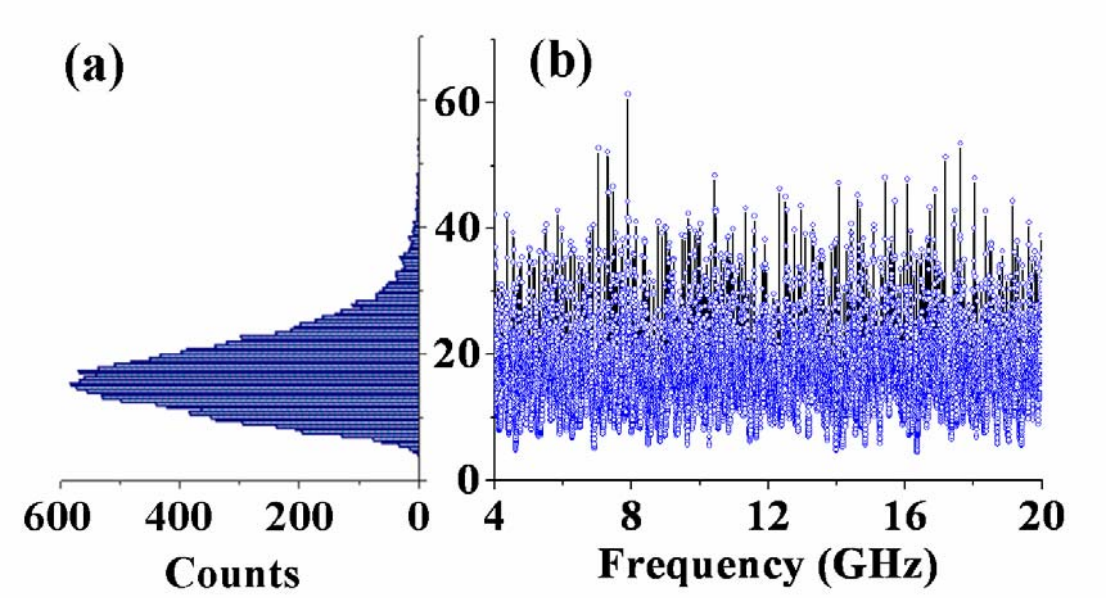

Fig. 8.2: (a) The histogram of the estimated ratio (Λ) of the maximum transmitted power to the minimum transmitted power at each frequency for the twenty different positions of the mode-stirrer. The histogram is fairly wide-spread with a mean of 17.3dB and a standard deviation of 6.2dB. (b) Variation in Λ with frequency (shown as the blue circles). A dynamic range of nearly 55dB is observed for Λ over the frequency range of 4 GHz to 20 GHz.

The extreme sensitivity of the internal field configurations to the orientation of the mode-stirrer position, which gives rise to wave-chaotic scattering, can be inferred by estimating the ratio of the maximum transmitted power to the minimum transmitted power at each frequency for the twenty different positions of the mode-stirrer. This power-ratio, denoted as Λ (Fig. 8.2), has a distribution which is fairly wide-spread with a mean of 17.3dB and a standard deviation of 6.2dB (Fig.8.2(a)).

The dynamic range of Λ is nearly 55dB over the frequency range of 4 to 20 GHz (shown as the blue circles in Fig. 8.2(b)). This indicates that there are significantly large field fluctuations within the computer-box cavity as the mode-stirrer is rotated, thereby creating an environment conducive to the formation of chaotic ray-dynamics. An even more conclusive validation of wave-chaotic scattering within the computer-box cavity, based upon the Dyson's circular ensemble, is explained in section 8.3.1.

8.2 Characterization of the Measured Radiation-Case Scattering Matrix Elements

To prove that the applicability of the "radiation impedance" normalization to three-dimensional port coupling geometries, it is necessary to make an estimate of the radiation impedance(or radiation scattering) matrix of the driving ports and show that this quantity incorporates the aspects of non-ideal port-coupling. As was described in chapter 3, the radiation measurement involves simulating an outward radiation condition for the two driving ports- but retaining the coupling structure as in the Cavity Case. To achieve this condition, all internal electronics and inner surfaces of the cavity side-walls are coated with microwave absorber (Eccosorb HR-25 and ARC-Tech DD10017D respectively) with the intent of preventing reflections within the computer-box cavity (Fig.8.3). A circular area of about 5 cm radius is left uncoated around each of the ports so as to retain the near-field structure of the ports. The "Radiation Case" now involves measuring the resultant 2x2 radiation-scattering matrix, $\ddot{\vec{S}}_{rad} = \begin{bmatrix} S_{11rad} & S_{12rad} \\ S_{21rad} & S_{22rad} \end{bmatrix}$, from 4 to 20 GHz with the same 16000 frequency steps as in the "Cavity Case".

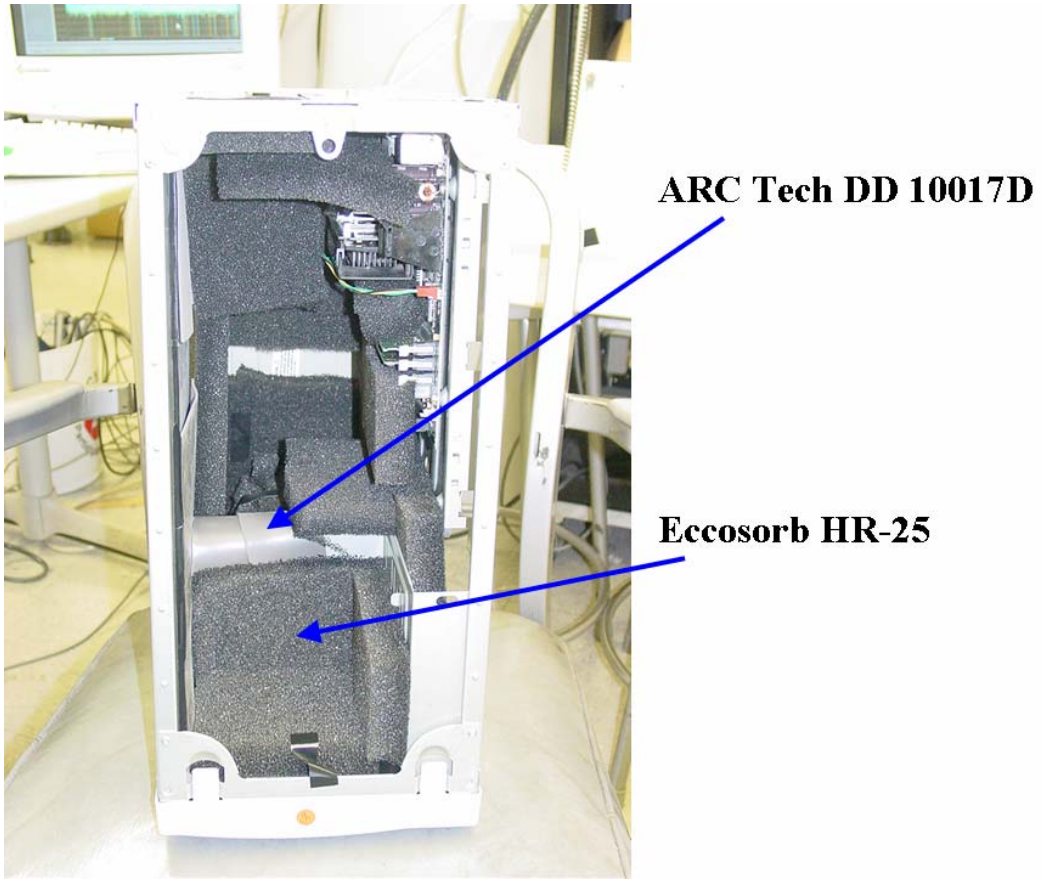

Fig. 8.3: Photograph of the experimental setup for the implementation of the "Radiation Case". All inner side-walls are coated with a dielectric absorber (ARC Tech DD 10017D), while the internal electronics are coated with a microwave foam absorber (Eccorsorb HR-25). A small circular region (about 5cms in radius) around each driving port (not visible in photograph) is left uncoated to retain the near-field structure of the driving ports.

In figure 8.4, the nature of the measured scattering matrix elements is shown as a function of frequency. The gray, pink and cyan circles represent the magnitude of the ensemble-averaged computer-box cavity S_{11}, S_{22} and S_{21} elements respectively. The magnitude of the ensemble averaged scattering matrix elements is indicative of

the degree of non-ideal coupling between the ports and the cavity. A frequency range where the coupling between port-*i* and the cavity is good, results in small values of $|\langle S_{ii} \rangle|^2 \, (i = 1,2)$. As can be seen in the figure, the two ports have vastly different frequency-dependent coupling characteristics (indicated by the gray and pink circles for port 1 and port 2 respectively). The solid black, red and blue lines represent the magnitude of the measured radiation-scattering elements S_{11rad}, S_{22rad} and S_{21rad} respectively. As was observed for the 1-port wave-chaotic cavity data in chapter 4, here too, the measured radiation scattering elements closely follow the general trend in the ensemble averaged scattering elements over the entire frequency range. This indicates that the radiation matrix elements accurately quantify the non-ideal coupling between the ports and the computer-box cavity at all frequencies. The slight oscillatory nature of the radiation-scattering matrix elements is attributed to short-ray reflected paths within the computer-box cavity. These short-ray paths arise mostly due to the flat side-walls of the cavity and imperfections in the absorptive properties of the microwave-absorber coating.

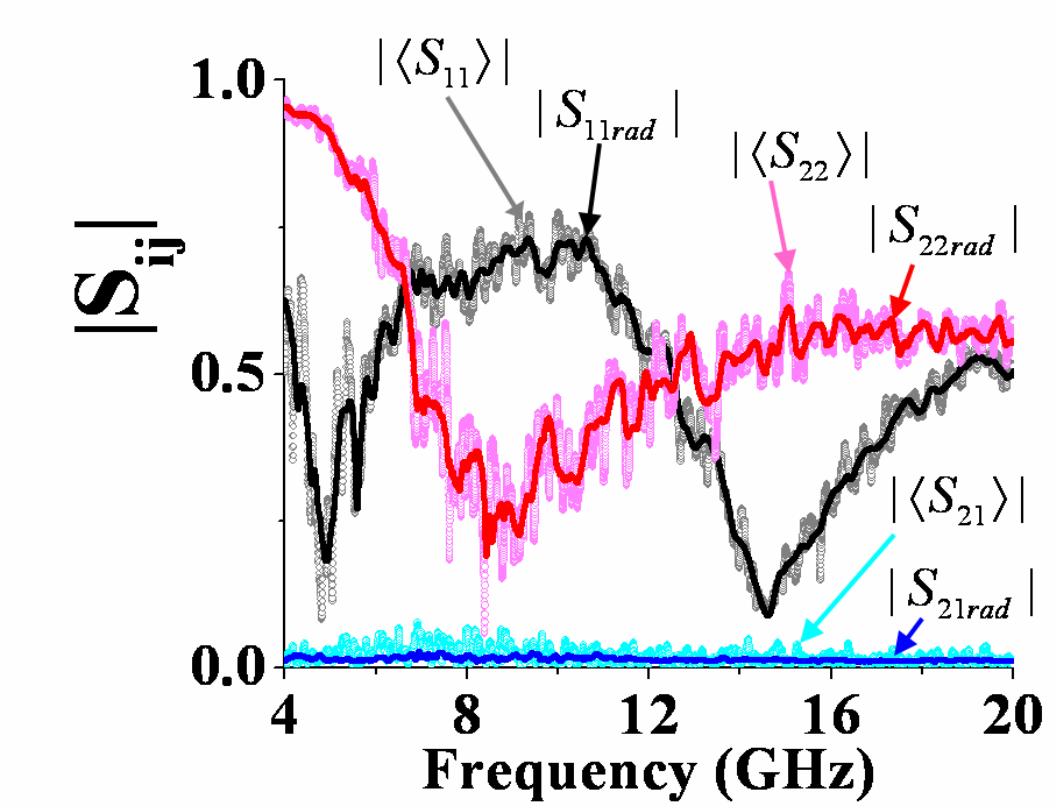

Fig. 8.4: Nature of the measured computer-box cavity scattering matrix elements as a function of frequency. The gray, pink and cyan circles represent the magnitude of the ensemble-averaged computer-box cavity S_{11}, S_{22} and S_{21} elements respectively. The solid black, red and blue lines represent the magnitude of the measured radiation-scattering elements S_{11rad}, S_{22rad} and S_{21rad} respectively, which closely follow the general trend in the corresponding ensemble-averaged cavity scattering matrix elements.

8.3 "Radiation Impedance" Normalization and the Applicability of Random Matrix Theory

Having measured the ensemble of the computer-box cavity scattering matrix $\vec{\vec{S}}$, and the corresponding radiation-scattering matrix $\vec{\vec{S}}_{rad}$, I convert these quantities into the corresponding cavity-case impedance matrices $\vec{\vec{Z}}$ and radiation-impedance matrices $\vec{\vec{Z}}_{rad}$, respectively using Eq.(2.12). Here each port is assumed to have a single operating mode with characteristic impedance of 50 ohms over the frequency range of the experiment. Each $\vec{\vec{Z}}$ is then normalized with the corresponding measured $\vec{\vec{Z}}_{rad}$ at the same frequency using Eq. (2.10). The normalized impedance matrix $\vec{\vec{z}}$, thus obtained, is then converted to the normalized scattering matrix $\vec{\vec{s}}$ using Eq. (2.11).

8.3.1 Dyson's Circular Ensemble for the Computer-Box Cavity

To prove conclusively the existence of wave-chaotic scattering within the computer-box cavity, I resort to experimentally verifying the statistical independence of the magnitude and phase of the normalized $\vec{\vec{s}}$ eigenvalues. This hypothesis, which is known as the Dyson's Circular Ensemble, is a hall-mark of wave-chaotic scattering and was shown to be extremely robust and unaffected by the presence of loss (See Chapters 4 and 5).

To validate this hypothesis, I diagonalize $\vec{\vec{s}}$ using an eigenvalue decomposition, $\vec{\vec{s}} = \vec{\vec{V}}_{\vec{\vec{s}}}\vec{\vec{\lambda}}_{\vec{\vec{s}}}\vec{\vec{V}}_{\vec{\vec{s}}}^{-1}$;where, $\vec{\vec{V}}_{\vec{\vec{s}}}$ is the 2x2 eigenvector matrix of $\vec{\vec{s}}$; and $\vec{\vec{\lambda}}_{\vec{\vec{s}}}$ is a diagonal matrix containing the two complex eigenvalues of $\vec{\vec{s}}$. Since the computer-

box cavity is sufficiently of low Q, $\vec{s}$ has complex, sub-unitary eigenvalues, i.e. $\vec{\lambda}_{\vec{s}} = \begin{bmatrix} |\lambda_1| e^{j\phi_1} & 0 \\ 0 & |\lambda_2| e^{j\phi_2} \end{bmatrix}$, where $|\lambda_{1,2}| < 1$. As in chapter 5, the two complex eigenvalues of the $\vec{s}$ ensemble are grouped into one list, which I shall refer to as "$\hat{\lambda}_{\vec{s}}$". I observe that grouping the two eigenvalues together as opposed to randomly choosing one of the two eigenvalues does not change the statistical properties of the results that follow. Figure 8.5(a) shows a plot in the complex plane of the eigenvalue density for a representative set of measured $\vec{s}$ ranging between 8 to 9 GHz. The color-scale level at any point in Fig. 8.5(a) indicates the number of points for $\{\mathrm{Re}[\hat{\lambda}_{\vec{s}}], \mathrm{Im}[\hat{\lambda}_{\vec{s}}]\}$ that lies within a local rectangular region of size 0.0025 x 0.0025. Next, angular slices (shown as dotted red lines in Fig. 8.5 (a)) which subtend a polar-angle of $\pi/2$ are taken and histogram approximations to the PDF of $|\hat{\lambda}_{\vec{s}}|$ of the points lying inside each of the four slices are computed. This is shown by the circles, squares, stars and triangles in Fig. 8.5(b). It can be observed that the PDF approximations are essentially identical and independent of the angular-slice.

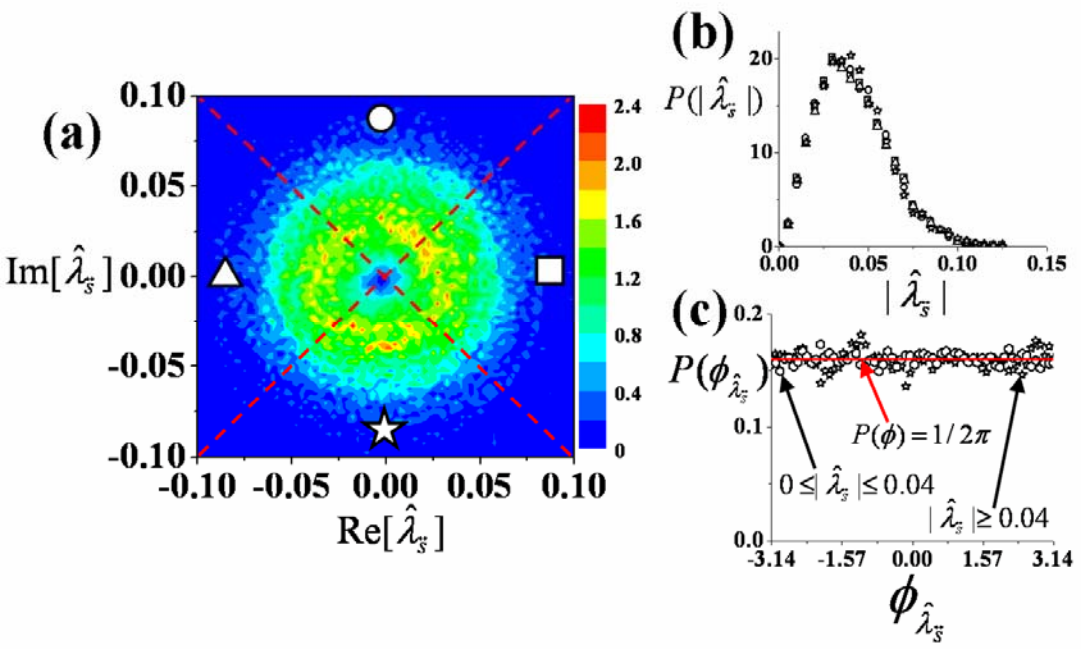

Fig. 8.5: (a) The density of eigenvalues of $\hat{\lambda}_{\vec{s}}$ in the complex plane is shown for frequencies in the range 8 GHz to 9 GHz for the computer-box cavity. The color-scale code blue, green, yellow, red are in ascending density order. (b) Angular slices (90^o) with the symbols (stars, triangles, circles, squares) indicate regions where the PDF of $|\hat{\lambda}_{\vec{s}}|$ of the data in (a) is calculated and shown. Observe that the four PDFs are nearly identical. (c) Experimental histogram approximations to the PDF of the eigenphase of $\vec{s}$ (i.e., $\phi_{\hat{\lambda}_{\vec{s}}}$). Two annular rings defined by $0 \le |\hat{\lambda}_{\vec{s}}| \le 0.04$ and $0.04 \le |\hat{\lambda}_{\vec{s}}| \le 0.1$ of the data in (a) are taken and the histograms of the phase of the points within these regions are shown as the solid diamonds and hollow triangles respectively. The red solid line is a uniform distribution ($P(\phi) = 1/(2\pi)$).

In Fig. 8.5(c), the histogram approximations of the phase of the points lying within two-annular rings defined by $0 \leq |\hat{\lambda}_{\vec{s}}| \leq 0.04$ (hexagons) and $0.04 \leq |\hat{\lambda}_{\vec{s}}| \leq 0.1$ (stars) are shown. A nearly uniform distribution is obtained for both cases indicating that the PDF of the phase of $\hat{\lambda}_{\vec{s}}$ is independent of the radius of the annular ring. Also shown in red is the uniform distribution with $P(\phi) = 1/(2\pi)$. Figure 8.5 thus supports the hypothesis that the magnitude and phase of the eigenvalues of $\vec{s}$ are statistically independent of each other and that the eigen-phase of $\vec{s}$ is uniformly distributed from 0 to 2π - thereby confirming that the scattering within the computer-box cavity is truly wave-chaotic. This result also establishes the effectiveness of the radiation-impedance normalization process to filter away the system-specific aspects of non-ideal port coupling in a complicated 3-D geometry.

8.3.2 Existence of Universal Impedance Fluctuations and applicability of Random Matrix Theory

Now that the existence of wave-chaotic scattering within the computer-box cavity has been established, in this section, I test the applicability of Random Matrix Theory to describe the universal fluctuations in the impedance matrices of such three-dimensional cavities.

I consider the experimentally determined normalized impedance $\vec{z}$ matrices that lie within a frequency range of 17 to 18 GHz. I define this set of $\vec{z}$ matrices as a "data-set". By an eigenvalue decomposition, each $\vec{z}$ matrix yields two complex eigenvalues, which I group into a single list denoted as $\hat{\lambda}_{\vec{z}}$. I observe that grouping the two eigenvalues together, as opposed to randomly considering one of the two

eigenvalues does not alter the statistical results that follow. Histogram approximations to the Probability Density Functions of the real and imaginary parts of $\hat{\lambda}_z$ are shown in Fig. 8.6(a) and Fig. 8.6(b) respectively. The variance (σ^2) of experimental PDFs in Fig. 8.6(a) and Fig. 8.6(b) are nearly identical in magnitude, i.e., $\sigma^2_{\mathrm{Re}[\hat{\lambda}_z]} \cong \sigma^2_{\mathrm{Im}[\hat{\lambda}_z]} = 13.5\times10^{-4}$. From the variance of the PDFs of the real and imaginary parts of $\hat{\lambda}_z$, and by using Eq.(5.1), I estimate a value of the cavity loss-parameter (α) for this data-set to be about $\alpha \cong 236$.

Using the value of $\alpha = 236$, a random matrix Monte Carlo simulation yields the red curves shown in Fig. 8.6(a) and Fig. 8.6(b) for the real and imaginary parts of $\hat{\lambda}_z$ PDFs. Relatively good agreement is observed between the experimentally derived PDFs and those generated numerically from Random Matrix Theory, thereby confirming the ability of Random Matrix Theory to explain the statistical aspects of the universal impedance fluctuations in the computer-box cavity.

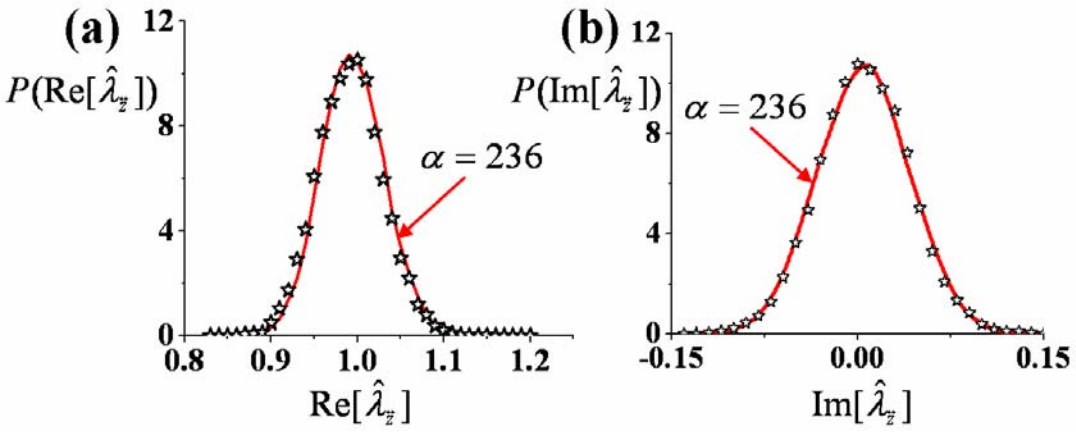

Fig. 8.6: Marginal PDFs for the real (a) and imaginary (b) parts of the grouped eigenvalues of the normalized computer-box cavity impedance $\hat{\lambda}_z$ (stars) in the

frequency range of 17-18 GHz. Also shown are the single parameter, simultaneous fits for both the real and imaginary normalized impedance PDFs (red solid lines), where the loss parameter α ($\alpha = 236$) is obtained from the variance of the data represented by the stars in (a) and (b).

8.3.3 Variation of α with Frequency for the Computer-Box Cavity

To determine the range of α values for the measured data on the computer-box cavity, I consider a sliding window of width 1GHz that steps every 500 MHz over the frequency range from 4 to 20 GHz. The black stars in Fig. 8.7 represent the variance of the real part of $\hat{\lambda}_z$ as a function of frequency. The red circles in Fig. 8.7 represent the variance of the imaginary part of $\hat{\lambda}_z$ as a function of frequency. Good agreement is observed between the black stars and the red circles over the entire frequency range of 4 to 20 GHz, as predicted by the Random Coupling Model (see chapter 2 and chapter 5).

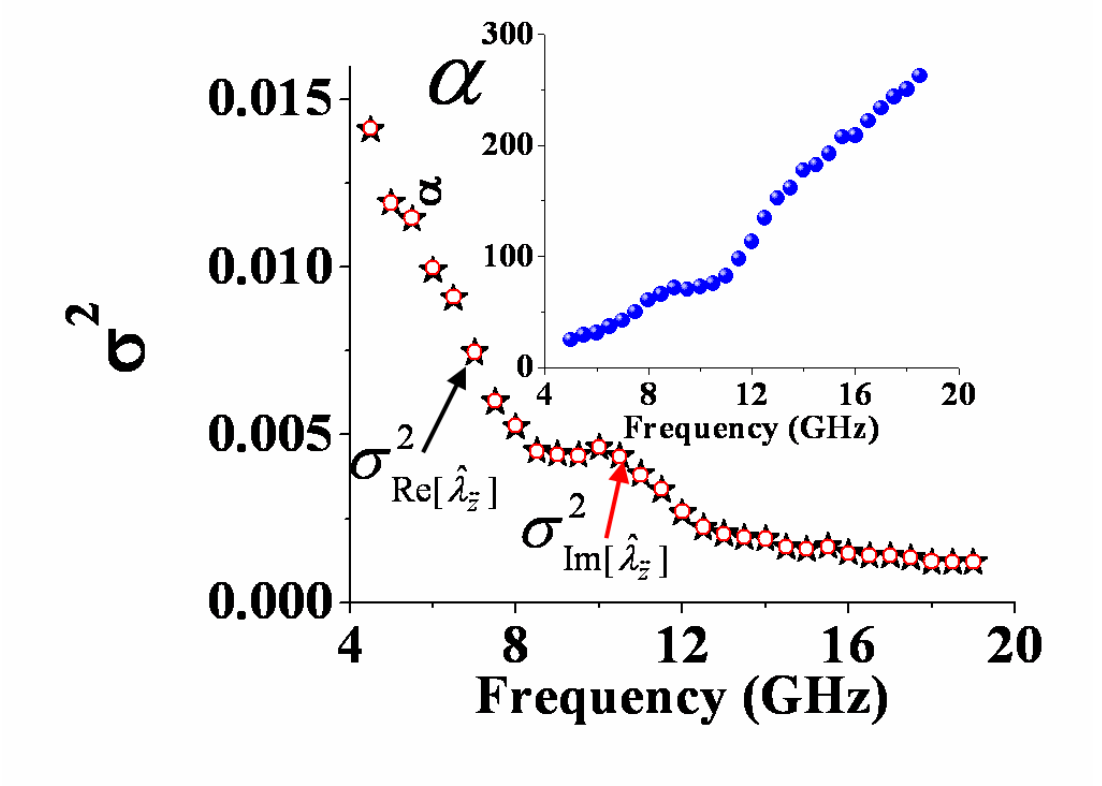

Fig. 8.7: The variance of $\mathrm{Re}[\hat{\lambda}_z]$ (black stars) and $\mathrm{Im}[\hat{\lambda}_z]$ (red circles) is shown as a function of frequency from 4 to 20 GHz for the computer-box cavity data. The agreement between these two quantities is good and robust over the entire frequency range despite the change in cavity Q and coupling. Inset: The estimated value of the cavity loss-parameter (α), which is derived from the mean of the variance of $\mathrm{Re}[\hat{\lambda}_z]$ (black stars) and $\mathrm{Im}[\hat{\lambda}_z]$ (red circles), and Eq.(5.1).

The solid blue circles in inset of Fig. 8.7 represent the resultant value of the cavity-loss parameter α, which was determined from the average of the variances of the real and imaginary parts of $\hat{\lambda}_z$, and Eq. (5.1). As the inset in Fig. 8.7 shows, the

estimated value of α increases as a smooth function of frequency from $\alpha \cong 22$ at 4GHz to $\alpha \cong 270$ at about 20GHz.The smooth frequency-dependent nature of α also indicates that the quality factor (Q) of such complicated enclosures does not fluctuate wildly as a function of frequency (this fact has also been established by **[56])**.

8.4 "RCM Induced Voltage Algorithm" for Prediction of Induced Voltage PDFs

In section 8.3, it was experimentally established that the computer-box cavity exhibits universal scattering and impedance fluctuations characteristic of wave-chaotic systems and that these universal fluctuations are well described, in a statistical sense, through Random Matrix Theory. This section builds upon the results of section 8.3, to formulate a prediction algorithm called the "RCM Induced Voltage Algorithm" for the PDF of induced voltages at specific target-ports within a complicated wave-chaotic cavity for a given excitation stimulus at some other driving source-port.

The challenge of predicting the PDF of induced voltages at specific ports (which could be a sensitive IC pin of a microprocessor within a computer-box) due to a certain incident RF power from a source-port (which could be a cooling vent on the computer-box casing) within complicated cavities such as a computer-box cavity is of significant interest to the HPM-effects and Electromagnetic Compatibility community. The "RCM Induced Voltage Algorithm" provides a quick statistical solution to this problem and works under the assumption that the cavity is wave-

chaotic, and that it possesses universal fluctuations in its scattering or impedance properties which are explained through Random Matrix Theory.

For a wave-chaotic cavity with a source-port and target-port, denoted as "port 1" and "port 2" respectively, the algorithm essentially requires only five pieces of information in order to make accurate statistical predictions for the induced voltages at the given target-port for a particular excitation at port 1. These five pieces of information are,

1. The frequency of interest (f).
2. The volume of the cavity (V).
3. The typical Q of the cavity-modes (Q) at the frequency of interest. The presence of other ports in the system modifies the Q of the cavity. Hence, their contribution is indirectly accounted for through the typical Q of the cavity.
4. An estimate of the 2x2 radiation-impedance matrix of the source and target ports within the cavity at the frequency of interest ($\ddot{Z}_{rad}$). This quantity can either be directly measured (as in the experiments presented in this chapter) or determined numerically using conventional EM-solver software. In certain cases, analytic expressions may exist for relatively simple coupling structures such as a horn antenna **[85],** a micro-strip antenna **[86]** or a Hertzian dipole **[49]**.
5. Mode of HPM attack- An estimate of the radiated power-spectrum profile at the source port $P_1(f)$.

The first three pieces of information determine the value of the cavity loss-parameter (α). For three-dimensional air-filled wave-chaotic cavities,

$\alpha = k^3 V/(2\pi^2 Q)$ as explained in chapter 2. The value of α in turn determines the shapes and scales of the normalized impedance $\vec{\vec{z}}$, and can be numerically generated using random matrix Monte Carlo simulations (see chapter 2). This numerically derived normalized impedance $\vec{\vec{z}}$ can then be combined with the estimated radiation-impedance matrix $\vec{\vec{Z}}_{rad}$ and Eq.(2.10), to yield a numerical estimate of the raw-cavity impedance $\left(\vec{\vec{Z}} = \begin{bmatrix} Z_{11} & Z_{12} \\ Z_{21} & Z_{22} \end{bmatrix}\right)$ ensemble. Finally, using the formalism of the ABCD-transmission parameters for a two-port microwave network as explained in **[87]**, it is possible to determine the induced voltage ensemble at the target-port (V_2) for the specified radiated power-spectrum profile $P_1(f)$ at the source-port through,

$$A = \left.\frac{V_1}{V_2}\right|_{I_2=0} = \frac{Z_{11}}{Z_{21}} \quad , \tag{8.1}$$

$$C = \left.\frac{I_1}{V_2}\right|_{I_2=0} = \frac{1}{Z_{21}} \quad , \tag{8.2}$$

and radiated-power at port-1, $P_1 = V_1 I_1$, (8.3)

yielding, $V_2 = \sqrt{P_1/AC} = \sqrt{P_1 Z_{21}^2 / Z_{11}}$. (8.4)

The steps of this algorithm are outlined in Fig. 8.8.

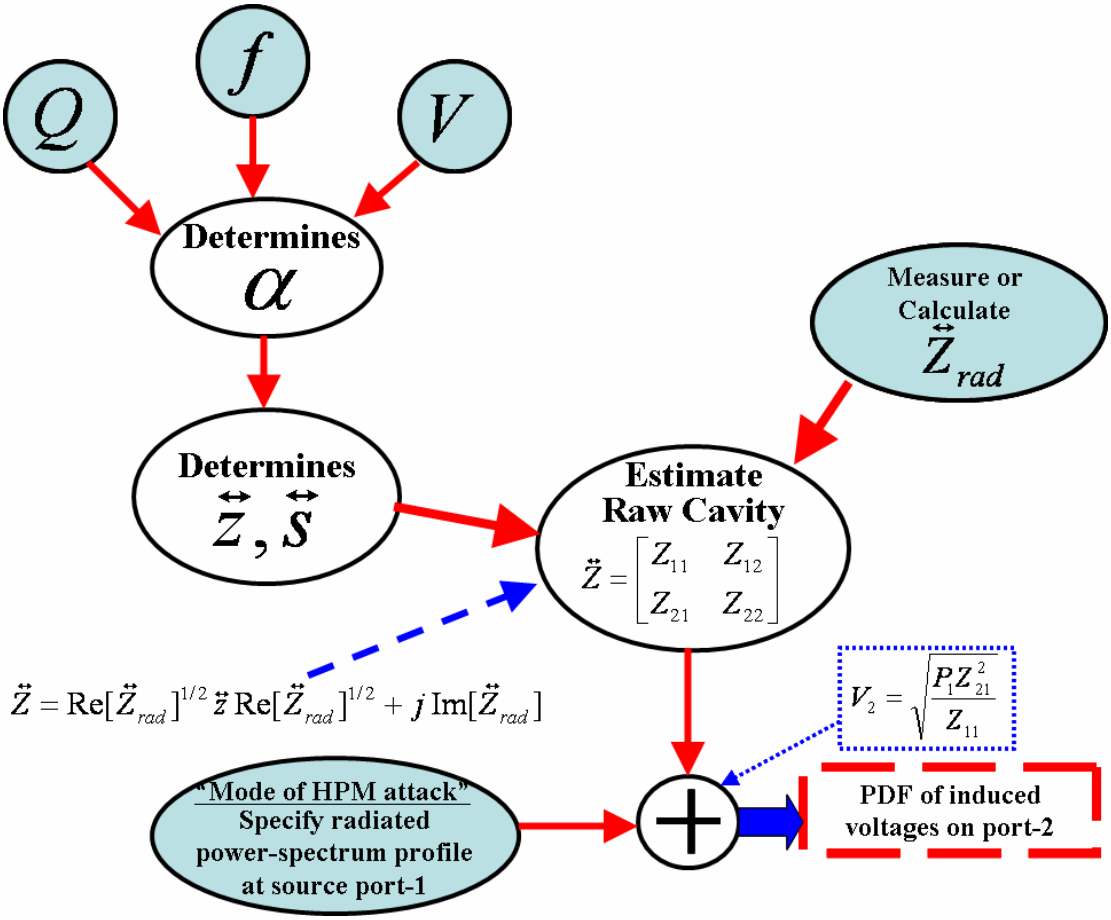

Fig. 8.8: Flowchart indicating the formalism of the "RCM Induced Voltage" algorithm. The inputs to the RCM Voltage algorithm, i.e., frequency (f), cavity volume (V), cavity Q, radiation impedance matrix of source and target ports ($\ddot{Z}_{rad}$), and the radiated power-spectrum profile at port-1(P_1), are indicated in blue.

To test the validity of this algorithm for the computer-box cavity, I first choose an arbitrary frequency range of 4.5 GHz to 5.5 GHz. I assume that the losses do not change significantly in this given frequency range. From the $S_{21}(\omega)$ measurements, I estimate that the typical Q for the computer-box cavity over this frequency range is about 45 (i.e., $Q \cong 45$). I then estimate the value of

$\alpha = k^3 V/(2\pi^2 Q)$ using $k = 2\pi f/c$ with $f = 5GHz$ and $V = 0.38 \times 0.21 \times 0.23 m^3$ (the physical volume of the computer-box cavity). This yields a value for α to be about 24. Note that since the computer-box cavity contains components of different dielectric constants (such as the FR-4 material used to fabricate the motherboard), the electromagnetic-volume of the computer-box cavity is different from the physical volume of the computer-box cavity. However, since the computer-box cavity is sufficiently lossy (thereby yielding values of $\alpha >> 1$), the statistics of the normalized impedance are relatively insensitive to small changes in α. This offsets the error in the estimate of the computer-box cavity volume.

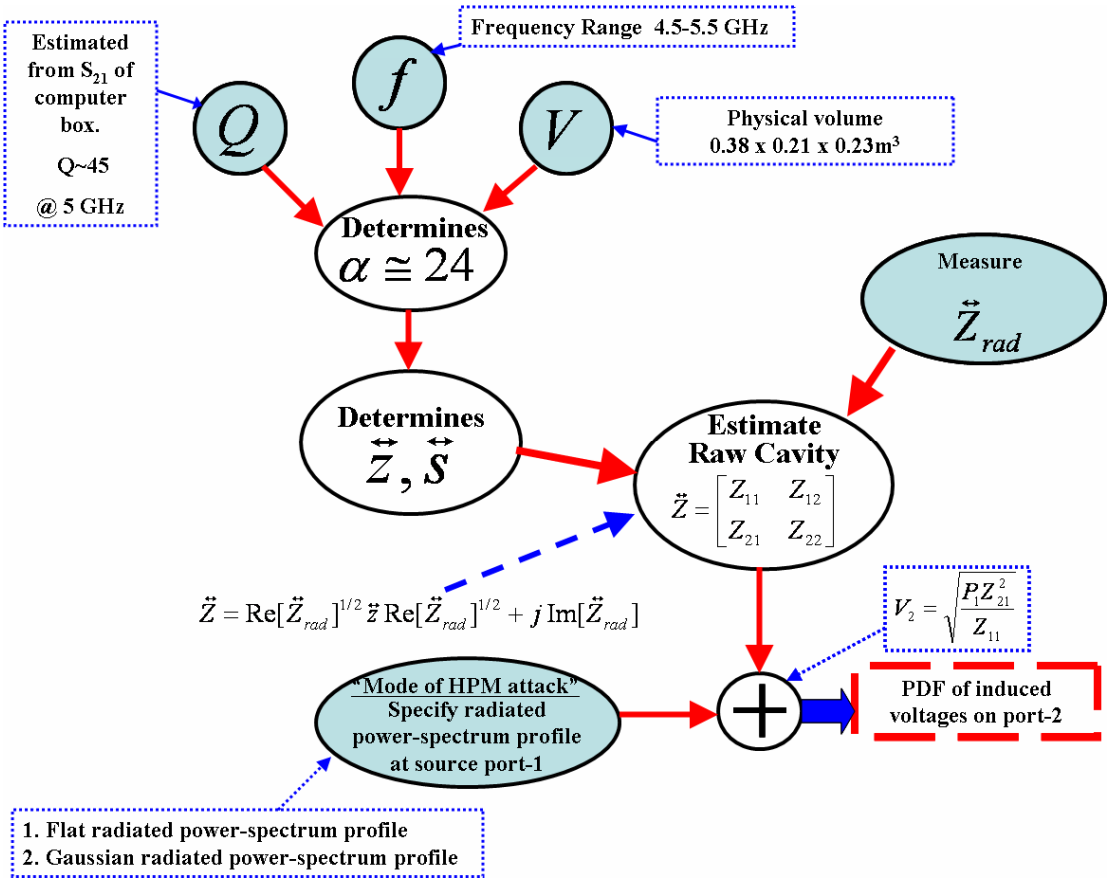

Fig. 8.9: Implementation of the RCM Voltage algorithm for the computer-box cavity in a frequency range of 4.5-5.5GHz. The value of $\alpha = k^3 V/(2\pi^2 Q)$ taking into account the volume of the computer-box cavity ($V = 0.38 \times 0.21 \times 0.23 m^3$), the estimated cavity Q (about 45) and the center frequency of 5 GHz, yields $\alpha \cong 24$. Using random matrix Monte Carlo simulations, an ensemble of 100,000 normalized impedance matrices ($\ddot{\vec{z}}$) which correspond to an α-value of 24, are generated. The measured radiation impedance matrix ($\ddot{\vec{Z}}_{rad}$) is then combined with the $\ddot{\vec{z}}$-ensemble to obtain an ensemble of cavity impedance matrices. This cavity impedance ensemble is then combined with the radiated power-spectrum profile at port-1 (P_1) to yield an

ensemble of induced port-2 voltage values ($V_2 = \sqrt{P_1 Z_{21}^2 / Z_{11}}$) from which the PDF of V_2 can be generated.

I then use random matrix Monte Carlo simulations with a random-matrix size of $M = 1000$, to generate an ensemble of 100,000 normalized impedance $\vec{\vec{z}}$ matrices which correspond to a value of $\alpha = 24$ (see section 2.5). Combining this ensemble of $\vec{\vec{z}}$ matrices with the measured radiation impedance matrix $\vec{\vec{Z}}_{rad}$ over the frequency range of 4.5GHz to 5.5GHz using Eq.(2.10), I obtain an estimate for the ensemble of the computer-box cavity impedance in the "Cavity case". In order to determine the nature of the induced voltage PDFs at port-2, I simulate two HPM attack scenarios by assuming two different radiated power-spectrum profiles at port-1,

(i) Flat power-spectrum profile of 1 Watt radiated uniformly over the frequency range from 4.5GHz to 5.5GHz, i.e., $P_1(f) = 1$ for $f = 4.5$GHz to 5.5 GHz (inset of Fig.8.10(a)).

(ii) Gaussian-shaped radiated power-spectrum profile centered at 5GHz and a standard-deviation of $\sqrt{0.03}$ GHz (inset of Fig. 8.10(b)).

Note: In cases (i) and (ii), I have assumed that the port-1 radiated power-spectrum profile is a purely real, scalar quantity. This assumption neglects any phase correlations between the frequency-components of the radiated signal from port-1.

The resultant PDF of the magnitude of the induced voltage at port-2 is shown as the red curve in Fig. 8.10(a) for the flat radiated power-spectrum profile (i). The red curve in Fig. 8.10(b) represents the resultant PDF of the magnitude of the induced

voltage at port-2 for the Gaussian-shaped radiated power-spectrum profile (ii). Note that the induced voltage PDFs in the two cases is very different.

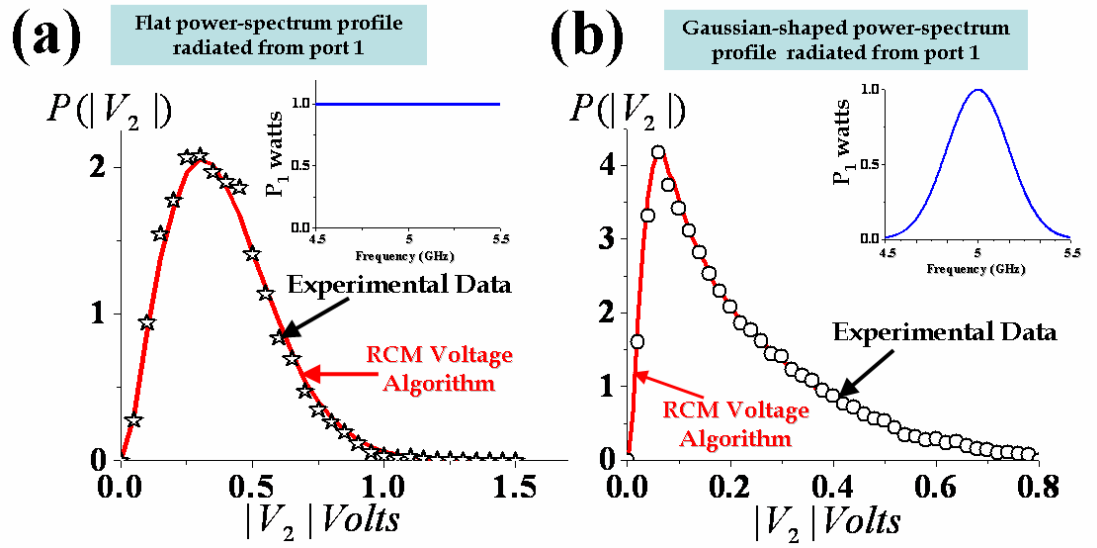

Fig. 8.10: (a) Numerically determined PDF of induced voltages at port-2 obtained using the RCM Voltage algorithm for a 1-watt flat power-spectrum profile radiated from port-1 (inset) is shown as the red curve. The black stars represent the experimentally derived PDF of induced voltages at port-2 obtained using the elements of the measured cavity impedance matrix and Eq.(8.4), for a 1-watt flat power-spectrum profile radiated from port-1. (b) Numerically determined PDF of induced voltages at port-2 obtained using the RCM Voltage algorithm for a Gaussian-shaped power-spectrum profile radiated from port-1(inset) is shown as the red curve. The black stars represent the experimentally derived PDF of induced voltages at port-2 obtained using the elements of the measured cavity impedance matrix and Eq.(8.4), for a Gaussian-shaped power-spectrum radiated from port-1. Good agreement is observed in both cases between the predictions for the induced voltage PDFs obtained

from the RCM Voltage algorithm and those generated using the measured cavity impedance data.

The stars in Fig. 8.10(a) represent the PDF of the induced voltage at port 2 for the flat radiated power-spectrum profile from port-1 (i) shown in inset and Eq.(8.4), where the terms Z_{11} and Z_{21} correspond to the experimentally measured Cavity-Case impedances of the computer-box cavity. Similarly, the circles in Fig. 8.10(b) represent the PDF of the induced voltage at port 2 for the Gaussian-shaped radiated power-spectrum profile from port-1 (ii) shown in inset and Eq.(8.4), where the terms Z_{11} and Z_{21} correspond to experimentally measured Cavity-Case impedances of the computer-box cavity. Relatively good agreement is found between the induced voltage PDFs which were determined numerically (red curves) using only the measured radiation impedance matrix and random matrix Monte Carlo simulations based upon a derived value of α, and those induced voltage PDFs (symbols) which were generated using the experimentally measured Cavity-case impedance matrix ensemble. This confirms the validity of the "RCM Voltage Algorithm" as an accurate and computational fast method to predict the statistical nature of induced voltages at a given target-port for a specified excitation at a source-port.

In the case of port-2 being a sensitive lead-pin of an integrated circuit which has several other lead-pins (other ports) in its near-field as might be the case for a high-density packaged VLSI chip, it might be possible to regard the other pins as passive-port components. Under this assumption, the presence of these passive-ports is incorporated into the wave-scattering dynamics within the enclosure through

modifications to the enclosure Q-value and the reduced volume of the enclosure. Complications to this assumption can arise if the near-by lead-pins are in different time-varying states i.e., logic-high state, logic-low state, or transitioning from one logic state to another. This aspect of the problem is presently beyond the capabilities of the RCM Voltage algorithm and deserves further investigation both from a theoretical and an experimental perspective.

8.5 Predicting the Variance of Induced Voltages Using Hauser-Feshbach Relations

This section is an extension of the scattering and impedance variance ratios (also known as Hauser-Feshbach relations) which were experimentally validated in Chapter 7 for the quarter-bow-tie shaped wave-chaotic cavity. In chapter 7, it was shown that in the limit of large α ($\alpha >> 1$), the impedance-variance ratio defined as $R_Z = \frac{Var[Z_{21}]}{\sqrt{Var[Z_{11}]Var[Z_{22}]}}$ (Eq.(7.1)), and the scattering-variance ratio defines as $R_S = \frac{Var[S_{21}]}{\sqrt{Var[S_{11}]Var[S_{22}]}}$ (Eq.(7.5)), were independent of coupling and were equal to ½ for a time-reversal symmetric cavity. Here, $Var[A]$ corresponds to the sum of the variance of the real and imaginary parts of the complex quantity A, with the averaging performed over the ensemble of the different measurements of A.

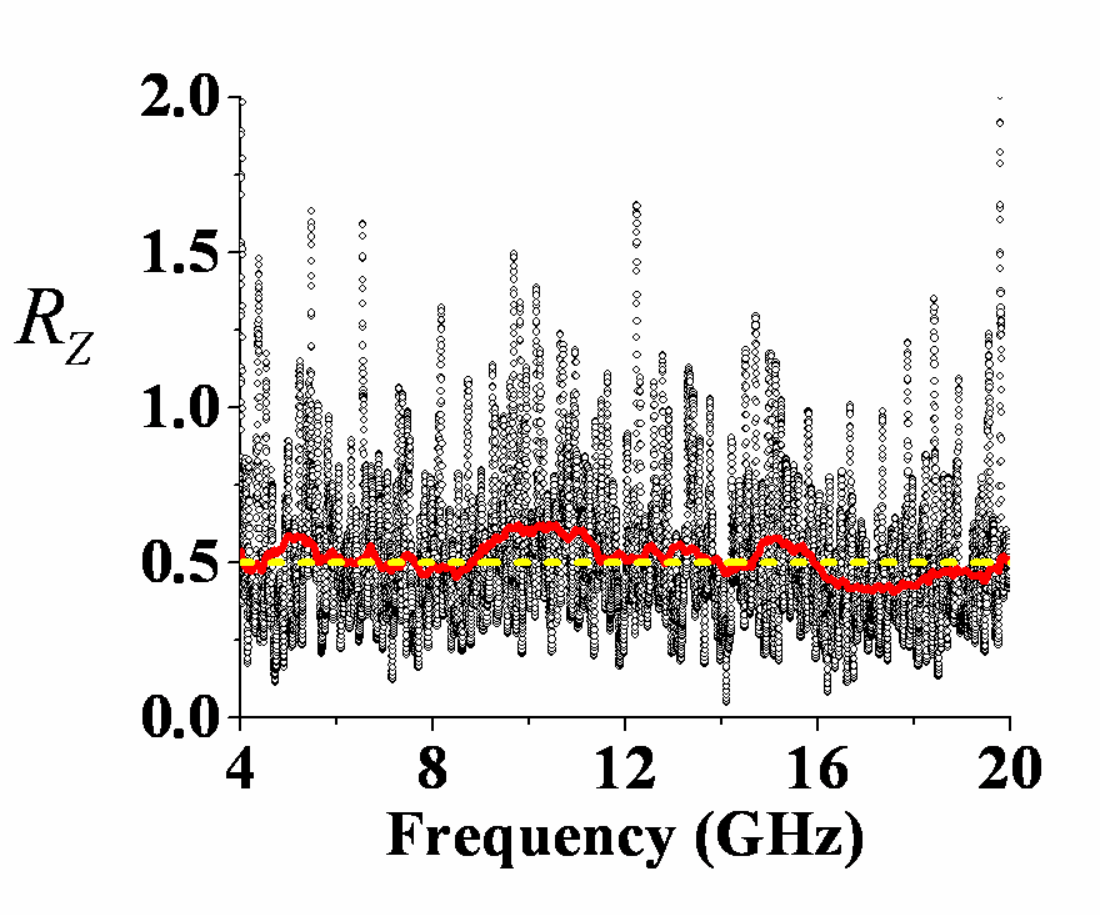

Fig. 8.11: Variation in R_Z as a function of frequency from 4 to 20 GHz for the computer-box cavity is shown as the black circles. The fluctuations are attributed to the presence of short-ray paths within the computer-box cavity. By frequency averaging the data represented by the black circles over a span of 1 GHz, the red line is obtained, which has a value of $\overline{R}_Z = 0.51 \pm 0.05$ over the entire frequency range from 4 to 20 GHz. The yellow dashed line represents the theoretical expected value of 0.5 for the high-loss limit.

For the computer-box cavity, Fig. 8.11 shows the nature of R_Z as a function of frequency from 4 to 20 GHz as the small black circles. The rapid fluctuations in

this quantity are on account of the short-ray paths within the computer-box cavity, as identified in chapter 7. By using a sliding window of width 1GHz, I obtain the red line which has a value of $\overline{R}_Z = 0.51 \pm 0.05$ over the entire frequency range from 4 to 20GHz. The yellow dashed line represents the theoretical expected value of 0.5. In Fig. 8.12, the nature of R_S as a function of frequency from 4 to 20 GHz is shown as the small black circles. As in Fig. 8.11, by using a sliding window of width 1GHz, I obtain the red line which has a value of $\overline{R}_S = 0.51 \pm 0.05$ over the entire frequency range from 4 to 20GHz. The yellow dashed line represents the theoretical expected value of 0.5. In both cases, Fig. 8.11 and Fig.8.12, I observe relatively good agreement between the frequency-averaged values $\overline{R}_Z$ and $\overline{R}_S$, and the theoretical prediction of 0.5 for the high-loss limit.

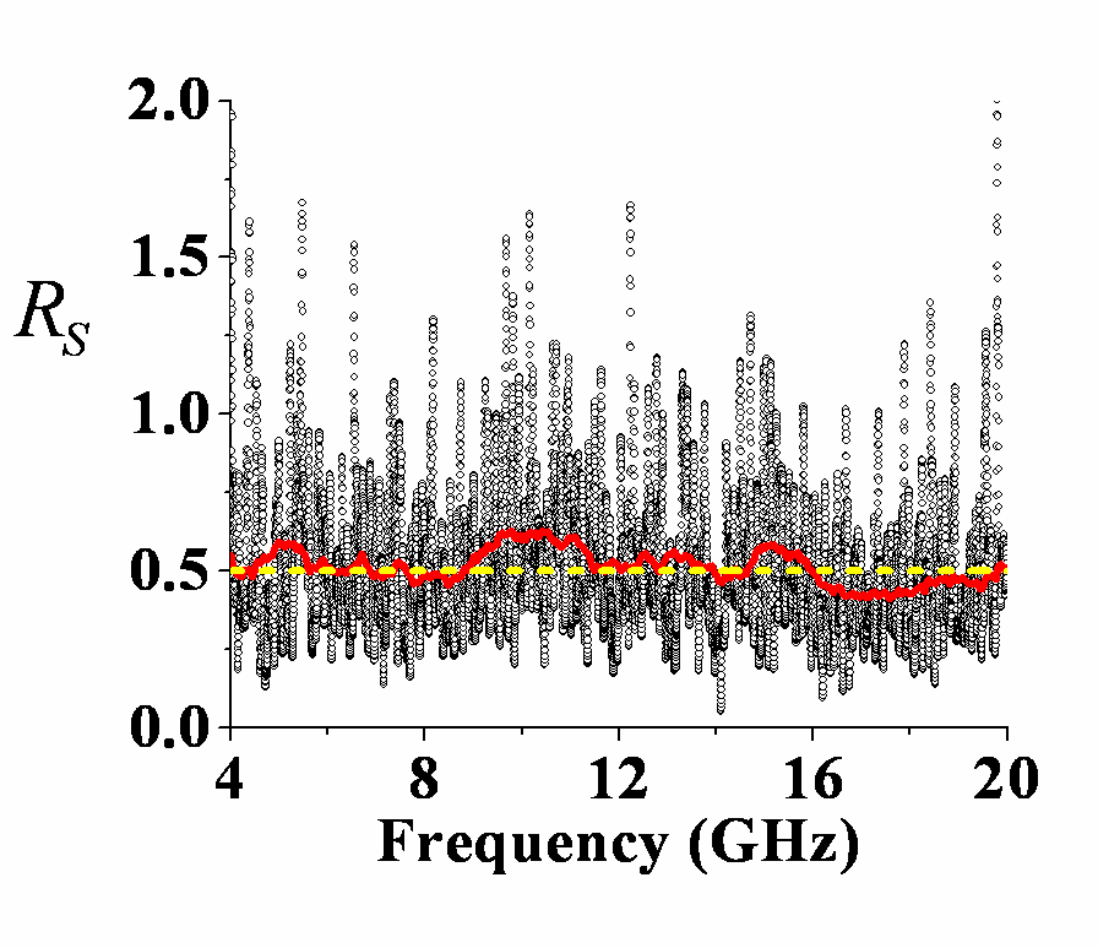

Fig. 8.12: Variation in R_S as a function of frequency from 4 to 20 GHz for the computer-box cavity is shown as the black circles. The fluctuations are attributed to the presence of short-ray paths within the computer-box cavity. By frequency averaging the data represented by the black circles over a span of 1 GHz, the red line is obtained, which has a value of $\overline{R}_S = 0.51 \pm 0.05$ over the entire frequency range from 4 to 20 GHz. The yellow dashed line represents the theoretical expected value of 0.5 for the high-loss limit.

Using this variance relation between the scattering elements of the computer-box cavity, it is possible to formulate a relation for the variance of the induced voltages at a target-port. In terms of the scattering matrix, the induced voltage at port-2 can be written as, $V_2 = S_{21}\sqrt{P_1 Z_{22rad}}$, where P_1 is the power radiated by port-1. If P_1 is assumed to be a constant (say 1 Watt) and since Z_{22rad} is determined only by the port-coupling geometry, the variance of the induced voltage can be written as,

$$Var[V_2] = P_1 Z_{22rad} Var[S_{21}]. \tag{8.5}$$

Provided port-1 and port-2 are correlated (i.e., communicate with each other), $Var[S_{21}]$ in Eq. (8.5) can be written in terms of R_S, $Var[S_{11}]$ and $Var[S_{22}]$ (Eq.(7.5)). It is therefore possible to determine the variance of the induced voltages at port-2 in a complicated, lossy ($\alpha >> 1$) cavity <u>without</u> measuring the transmission properties of the cavity, i.e.,

$$Var[V_2] = P_1 Z_{22rad} R_S \sqrt{Var[S_{11}]Var[S_{22}]}. \tag{8.6}$$

The equivalence of Eq.(8.5) and Eq.(8.6) is shown in Fig. 8.13. Assuming $P_1 = 1\ Watts$, I determine the variance of the induced voltage at port-2 of the computer-box cavity utilizing Eq.(8.5). This is indicated as the blue stars in Fig. 8.13, where the variance-values have been frequency-averaged over a sliding window of 1 GHz width. The red circles in Fig. 8.13 represent the variance of the induced voltage at port-2 of the computer box cavity for 1-Watt power radiated from Port-1 and utilizes Eq. (8.6), where $Var[S_{21}]$ from Eq.(8.5) was replaced with $\overline{R}_S\sqrt{Var[S_{11}]Var[S_{22}]}$ ($\overline{R}_S = 0.51$ and was obtained from Fig. 8.12). The same 1GHz frequency averaging is employed for the data represented by the red circles, as in the

case for the data represented by the blue stars. Relatively good agreement between the data represented by the blue stars and the red circles is observed over the entire frequency range from 4 to 20 GHz in spite of the variation in loss and coupling over this frequency-range.

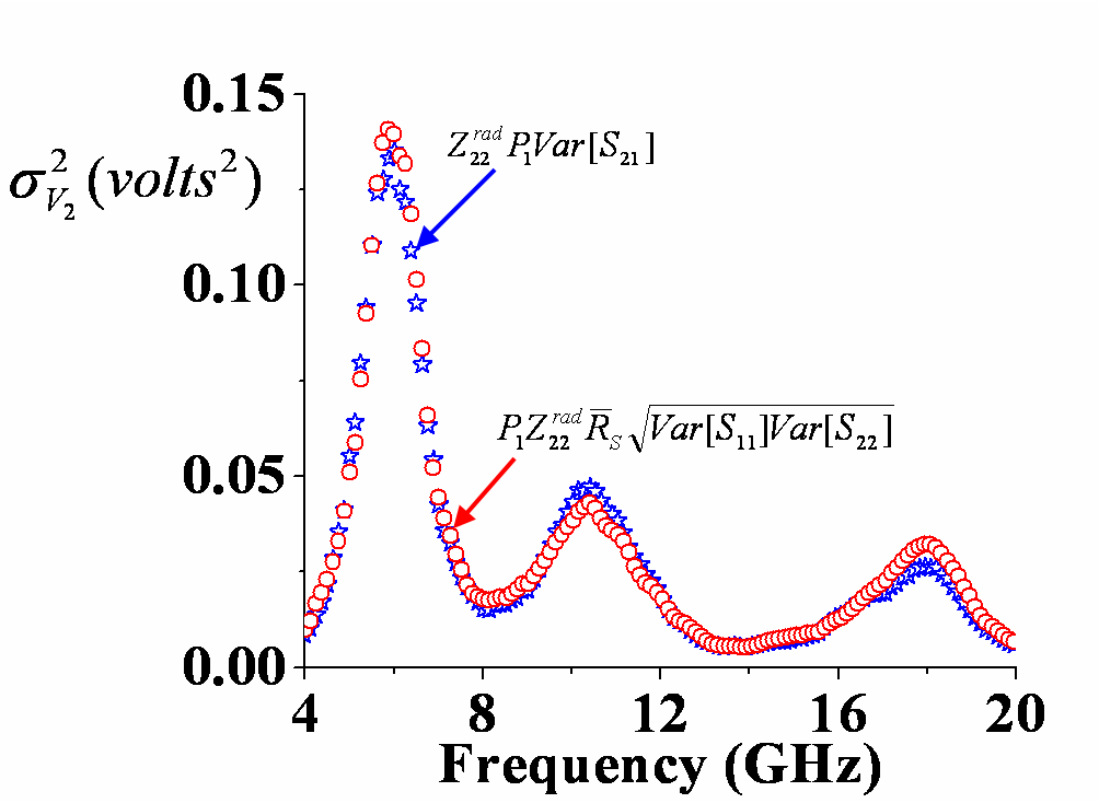

Fig. 8.13: The variance of the induced voltage at port-2 for 1-watt power radiated by port-1 determined using Eq.(8.5) and with 1GHz frequency-averaging is shown as the blue stars. The variance of the induced voltage at port-2 for 1-watt power radiated by port-1 determined using Eq.(8.6) and with 1GHz frequency-averaging is shown as the red circles, where the value of R_S in Eq.(8.6) is replaced with $\overline{R}_S = 0.51$. Good agreement is observed between the data represented by the blue stars and the red circles over the entire frequency range despite variations in loss and coupling.

8.6 Design Guidelines for HPM-Resistant Generic 3-D Complicated Enclosures

For complicated enclosures with chaotic ray-dynamics, the Random Coupling Model has shown that there exists certain universal statistical properties in the impedance, admittance and scattering matrices of these systems, which depends only upon the value of the dimension-less cavity loss-parameter (α). The Random Coupling Model has also shown that these universal statistical properties can be easily derived from experimental measurements of the cavity-enclosure by use of the radiation impedance of the driving ports. The radiation impedance is a non-statistical, frequency-dependent quantity which accurately quantifies the non-ideal coupling between the driving ports and the cavity-enclosure. Based on these lessons learnt from the Random Coupling Model, it is possible to deduce some simple design-guidelines for generic 3-D complicated enclosures such as computer-boxes or aircraft fuselages, which will make them more resilient to HPM attack.

a) Increasing the value of the cavity loss-parameter (α) :

   For a three-dimensional cavity-enclosure, $\alpha = k^3 V/(2\pi^2 Q)$, where the significance of the terms has been mentioned in chapter 2. As was shown in Fig. 4.1, increasing the value of α (e.g. by decreasing the cavity Q) decreases the fluctuations in the cavity impedance values. This in turn reduces the probability for large internal field fluctuations or equivalently large induced voltage swings on the components housed within the cavity-enclosure.

b) Radiation Impedance Engineering:

Through the Random Coupling Model it was shown that perfect coupling implies $Z_{rad} = Z_0$, where Z_{rad} and Z_0 represent the radiation impedance of the port coupled to the cavity, and Z_0 is the characteristic impedance of the transmission line connected to the port. This suggests that creating a large impedance mismatch between Z_{rad} and Z_0 (i.e, $Z_{rad} >> Z_0$ or vice versa) will result in very poor transfer of the incoming HPM energy on the port, to the interior of the cavity-enclosure.

c) Use of Non-Reciprocal Media:

Though it has not been discussed in this dissertation, the use of non-reciprocal media such as magnetized ferrites place within a cavity-enclosure can significantly decrease the amplitude of field intensities within the cavity-enclosure. In addition to being inherently lossy (increasing the α-value of the cavity-enclosure), non-reciprocal media restrict instances of constructive interference between the rays bouncing within the cavity-enclosure. This in turn reduces the formation of "hot-spots"(regions of high EM field intensities) **[55]** within the cavity-enclosure.

8.7 Summary of Chapter 8 and Conclusions

The results discussed in this chapter are meant to provide conclusive experimental evidence in support of the "Random Coupling Model" for multiple-port, real-world, three-dimensional complicated enclosures. The experimental results have

shown that the "radiation impedance" normalization process is extremely robust in quantifying the non-ideal port-coupling, even when polarization of the waves and field fluctuations due to the presence of side-walls in the near-field proximity of the driving ports, plays a role. The close agreement between the experimentally determined PDFs and those generated numerically from random matrix Monte Carlo simulations, support the use of Random Matrix Theory to model statistical aspects of real-world, three-dimensional complicated enclosures with chaotic ray dynamics.

In this chapter, I have shown that given an estimate of the cavity loss-parameter α and the full 2x2 radiation impedance matrix of the two-driving ports, it is possible to accurately predict the statistical nature of induced voltages on one of the two ports, for a specified excitation stimulus at the other port. I have also shown that using the Hauser-Feshbach scattering relation, it is possible to determine the variance of the induced voltage at a given port without the need for measuring the transmission characteristics of the cavity-enclosure. Based on the Random Coupling Model, I have also suggested certain design-guidelines to make a generic three-dimensional complicated enclosure (such as a computer-box or aircraft fuselage) more resistant to HPM attack. In an effort to make the Random Coupling Model accessible to the end-user, who is concerned with utilizing the model to address electromagnetic compatibility issues in a given setup, I have been compiled a stand-alone Graphic-User-Interface software called the "Terrapin RCM Solver v1.0" (see Appendix A). The current version of the software has several capabilities such as predicting the PDF of induced voltages at specific user-specified points within complicated enclosures for several HPM attack scenarios, and uncovering the universal

fluctuations in the impedance, admittance and scattering matrices of user-supplied measurements on real-world enclosures. More details on this software and its capabilities are elucidated in Appendix A.

Chapter 9: Final Conclusions and Scope for Future Work

The "Random Coupling Model", introduced in chapter 2, is a stochastic model which makes use of the Random Plane Wave hypothesis and Random Matrix Theory to formulate a statistical model for the impedance, admittance and scattering properties of time-reversal-symmetric (TRS) and broken-time-reversal-symmetric (BTRS) wave-chaotic systems. Perhaps the most important contribution of this model is its novel prescription of the "radiation impedance" normalization process which overcomes the issue of non-ideal port coupling. The non-ideal aspect of the port-coupling to the chaotic cavity has posed a difficult hurdle for experimentalists in the field of wave chaos. Most theoretical predictions for the statistical nature of wave-chaotic scattering exists in the limit that the driving ports are perfectly coupled to the cavity at all frequencies.

However, experimentally, it is practically impossible to design such a coupling structure. With the "radiation impedance" normalization prescription, experimentalists are equipped with a strategy to filter out the effects of non-ideal port coupling from their measured experimental data on a wave-chaotic cavity for any arbitrary port-coupling structure. Experimentalists are thus in a position to make clear-cut comparisons of their normalized (and, in essence "perfectly coupled") experimental data with theoretical predictions and/or numerical simulations from Random Matrix Theory.

In this dissertation, I have shown good agreement between the normalized experimental data for the one-port (chapter 4) and two-port (chapter 5) impedance, admittance and scattering fluctuations of a time-reversal-symmetric (TRS) wave-

chaotic cavity, and corresponding predictions from Random Matrix Theory. This agreement testifies to the potency of the "radiation impedance" normalization process as well as the applicability of Random Matrix Theory to describe the statistical aspects of wave-chaotic scattering. The results are generic in nature, and should apply to all systems showing instances of TRS wave-chaotic scattering- such as atomic nuclei, acoustic resonators, quantum corrals, quantum dots, etc. In chapter 6, I have utilized the Random Coupling Model along with the Schrödinger-Helmholtz analogy to conclusively test the predictions of **[59]** for the universal fluctuations in the conductance of dephased ballistic quantum-dots over a large range for the degree of dephasing, without the complicated effects of thermal fluctuations, impurity scattering or Coulomb interactions. Chapter 7 provided experimental validation for the impedance-based and scattering-based Hauser-Feshbach relations.

In chapter 8, I have experimentally proved the existence of wave-chaotic scattering and universal fluctuations in the impedance and scattering properties of real-world, three-dimensional cavity-enclosures taking the example of a typical computer-box cavity. The "radiation impedance" normalization prescription was shown to be remarkably effective for complicated three-dimensional geometries and shown to incorporate the polarization of the waves and field fluctuations associated with the presence of the side-walls in the near-field zone of the driving-ports. In the final sections of chapter 8, I have shown that given very minimal information about the cavity-enclosure or its inner details, the Random Coupling Model can provide a simple, fast and efficient algorithm to accurately predict the statistical nature of induced voltages at specific points within the enclosure for a specified HPM-attack

scenario. The Random Coupling Model has thus proved itself to be extremely valuable to engineers in the field of statistical electromagnetism, electromagnetic compatibility (EMC) or HPM-effects.

The Random Coupling Model, however, is still in its infancy- several extensions to the model are possible, as well as theoretical predictions for universal aspects of wave-chaotic scattering still remain experimentally untested. The next section introduces some ideas which, I strongly hope, are implemented in the future, thereby paving the way to make the Random Coupling Model a more versatile tool for wave-chaos experimentalists and EMC engineers alike.

9.1 Future Work

9.1.1 Cryogenic and 3-D Wave-Chaotic Cavity Design

The results that I have presented in this dissertation are restricted to TRS lossy wave-chaotic systems. The inherent ohmic losses present within the cavity translate to a minimum accessible α-value of about 0.8 (even when placed in a bath of solid CO_2 at -78.5^{o}C). Thus, the evolution of the normalized impedance, admittance and scattering probability density functions (PDFs) for small α-values ($\alpha < 0.5$) remains experimentally untested. Experimentally attaining small α-values is also crucial for proving the universal, coupling-independent aspect of the impedance-based Hauser-Feshbach ratio as compared to its scattering-based counter-part (as explained in chapter 7).

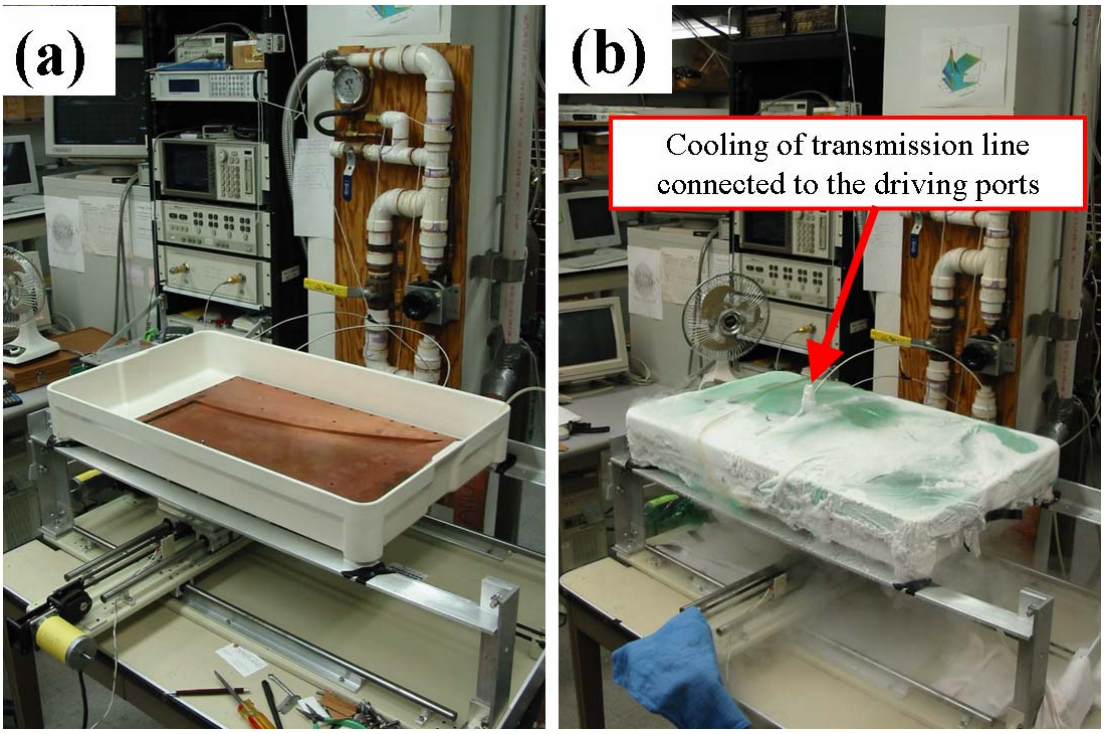

Fig. 9.1: (a) Photograph of the experimental setup for the wave-chaotic cavity, seen inside the white plastic tub, prior to filling the tub with liquid nitrogen. (b) Photograph of the wave-chaotic cavity inside the liquid-nitrogen bath. The tub is covered with a green plastic sheet so as to force the nitrogen vapors to exit only from a small tube on the side of the tub (not visible in photograph). The cooling (frost formation) on the transmission line connected to the driving-port is clearly visible. This cooling of the transmission line drastically alters its electrical properties thereby corrupting the room-temperature microwave calibration of the experimental setup.

Previously, I did attempt to lower the inherent cavity ohmic losses by immersing the quarter-bow-tie wave-chaotic cavity in a bath of liquid nitrogen (at -195.8^{o}C). This setup is shown in Fig. 9.1(a). However, this experiment was unsuccessful since the extremely cold temperature of the bath resulted in the cooling

of the transmission lines connected to the ports, thereby changing its electrical properties (Fig. 9.1(b)). As a result, the room-temperature microwave calibration of the experimental setup was severely compromised, yielding nonsensical values for the measured data. Another issue associated with this experiment was the implementation of the radiation-case at cryogenic temperatures. The microwave absorber (ARC Tech DD10017D) used to implement the room-temperature radiation case is not rated to work at -195.8^{o}C (also, I found the absorber becomes very brittle at cryogenic temperatures and loses its structural integrity). Thus the procurement of a new type of microwave absorber, rated to operate at cryogenic temperatures, would be needed to accomplish this radiation-measurement.

Another option for cryogenic-cavity experiments, which could be considered as an extension of the "dry-ice test" mentioned in chapter 3, would be to immerse the wave-chaotic cavity in a bath of solid CO_2 (at -78.5^{o}C) and then pour methanol on top of the dry-ice. The methanol serves to further cool the system down due to evaporation of the methanol vapors. I have never actually tested this approach. The present quarter-bow-tie wave-chaotic cavity could also be coated with a layer of superconducting material with a high critical temperature. This would also serve to reduce the ohmic losses in the cavity, thereby increasing the cavity-Q and yielding small α-values.

Small α-values can also be attained by designing a high-Q, three-dimensional enclosure in the shape of a rectangular box with a paddle-wheel mode-stirrer (similar to the computer-box cavity in chapter 8). The advantage of three-dimensional

enclosures is that the mode-density is much higher allowing for better stirring of the cavity-modes, which in turn, could result in better ensemble averaging.

9.1.2 Homogeneous versus Inhomogeneous Cavity Losses

Almost all theoretical work on wave-chaotic scattering (the "Random Coupling Model" included) makes the assumption that the losses within the cavity are uniformly distributed. While this assumption may be approximately true for a metallic microwave cavity uniformly filled with a single dielectric at high frequencies, the assumption can break down at lower frequencies. At lower frequencies, the resonance widths can vary from mode to mode due to the shape of the nodal-pattern and its interaction with the losses along the contour of the cavity. To qualitatively show the influence of inhomogeneous losses, I performed the following experiment.

For the one-port (diameter 2a=1.27mm) quarter-bow-tie chaotic-cavity presented in chapter 3, I created two different loss-case cavity profiles. In the first cavity case, what I refer to as the "Lumped Loss" cavity-profile, I placed two 15.2cm long strips of microwave absorber (ARC Tech DD10017D) along the curved inner side-walls of the cavity as shown in inset (a) of Fig. 9.2. Using the metallic perturbations of the type used in section 3.2, I measured the scalar scattering coefficient (S_{lump}) of an ensemble of one-hundred such cavity configurations in a frequency range of 3 to 18 GHz. In the second cavity case, what I refer to as the "Distributed Loss" cavity-profile, the same 15.2cm strips of microwave absorber (used in the Lumped-Loss cavity profile) were cut into 2cm long strips and placed with uniform spacing along the curved inner side-walls of the cavity as shown in inset

(b) of Fig. 9.2. Using the perturbation of the type used in section 3.2, I measured the scalar scattering coefficient (S_{dist}) of an ensemble of one-hundred such cavity configurations in a frequency range of 3 to 18 GHz. As explained in section 3.1, the radiation-case was also implemented where the inner side-walls of the cavity were totally covered with microwave absorber and the resultant radiation scattering coefficient (S_{rad}) was measured. Then, using the "radiation impedance" normalization process (as explained in section 3.1), the normalized impedance (z_{lump}) and (z_{dist}) corresponding to the Lumped-Loss cavity-profile and Distributed-Loss cavity-profile was obtained.

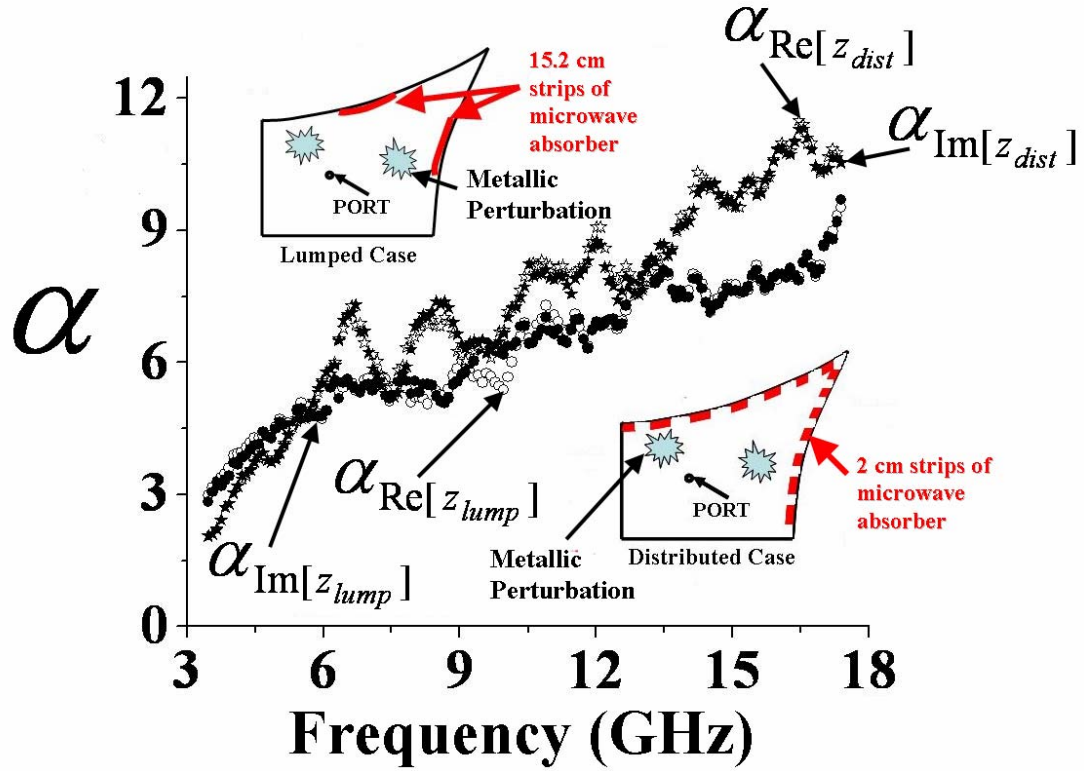

Fig. 9.2: The value of the cavity loss-parameter $\alpha_{\mathrm{Re}[z_{lump}]}$ (open circles), $\alpha_{\mathrm{Im}[z_{lump}]}$ (closed circles), $\alpha_{\mathrm{Re}[z_{dist}]}$ (open stars) and $\alpha_{\mathrm{Im}[z_{dist}]}$ (closed stars) determined

from the variance of $\mathrm{Re}[z_{lump}]$, $\mathrm{Im}[z_{lump}]$, $\mathrm{Re}[z_{dist}]$ and $\mathrm{Im}[z_{dist}]$, and Eq.(2.6). Note the disparity between the data sets represented by the stars and the circles. Inset (a) Schematic showing the implementation of the Lumped-Loss Cavity profile. Inset (b) Schematic showing the implementation of the Distributed-Loss Cavity profile.

By employing a sliding frequency window of width 1GHz which steps every 500 MHz, I computed the variance of $\mathrm{Re}[z_{lump}]$, $\mathrm{Im}[z_{lump}]$, $\mathrm{Re}[z_{dist}]$ and $\mathrm{Im}[z_{dist}]$ of the normalized impedance values that lie within each window for both the lumped-loss and distributed-loss cavity profiles. From these variance values and Eq.(2.6), I determined the corresponding value of the cavity loss-parameter $\alpha_{\mathrm{Re}[z_{lump}]}$ (open circles), $\alpha_{\mathrm{Im}[z_{lump}]}$ (closed circles), $\alpha_{\mathrm{Re}[z_{dist}]}$ (open stars) and $\alpha_{\mathrm{Im}[z_{dist}]}$ (closed stars) in Fig. 9.2. It can be observed that there is good agreement between the derived cavity loss-parameter values from the real and imaginary parts of the normalized impedance corresponding to a given loss-case cavity-profile (lumped-loss or distributed loss) over the entire frequency range. However, the α-values are significantly different for the two different loss-case cavity-profiles (stars and circles). I attribute this trend to the effects of non-uniformly distributed loss within the cavity. Further study on the effects of inhomogeneous distributed loss on the wave-scattering properties of such systems is necessary. Recently, there has been some effort to study the non-uniform spreading of the resonance widths due to inhomogeneous distribution of cavity losses **[88, 89].**

9.1.3 Effects of Short-Ray Periodic Orbits in the Measured Radiation Case

In the "radiation impedance" normalization process, the radiation-case theoretically assumes that the distant side-walls of the cavity are moved out to infinity thereby preventing any reflections of the waves back to the driving port (see chapter 2). Experimentally, the radiation-case is implemented by coating the side-walls of the cavity with commercial microwave-absorber ARC Tech DD10017D (see chapter 3). This microwave absorber has frequency dependent absorptive properties which provide at best 25dB of reflection loss over the frequency range of 3 to 18GHz for normal incidence of the waves onto the absorber. On account of these imperfections, there is some finite amount of reflected waves returning back to the port. These reflections are on account of "short-path orbits" where the wave, after leaving the port, bounces a finite number of times within the radiation-case cavity setup before returning to the port (Fig.9.3). The short-ray orbits manifest themselves as fluctuations in the measured radiation-scattering or impedance properties of the driving port (see chapter 8).

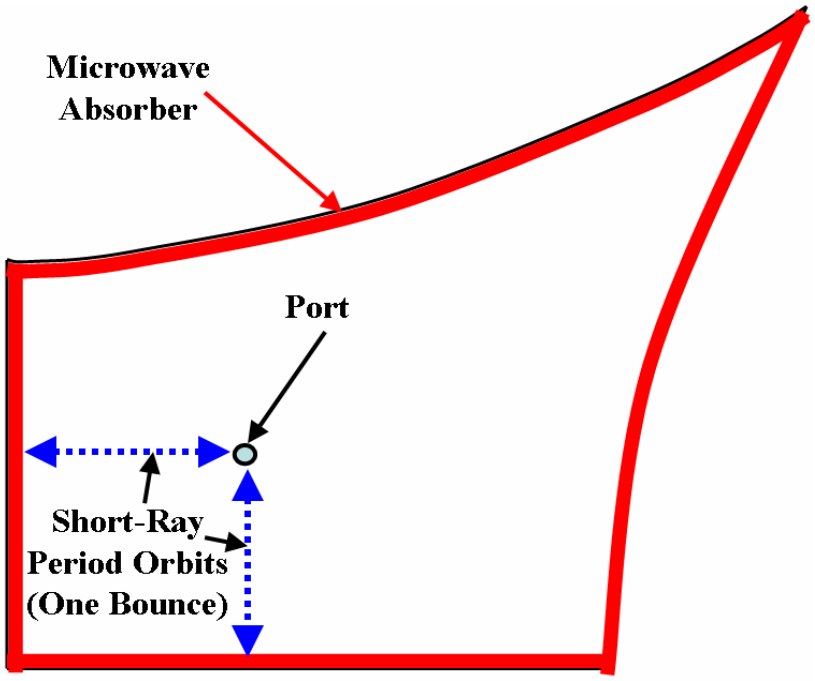

Fig. 9.3: Implementation of the experimental Radiation-Case. The red lining along the inner side-walls of the cavity represents the microwave absorber (see chapter 3). The one-bounce short-ray periodic orbits from the flat side-walls of the cavity are shown as the dashed blue lines.

To try to account for these short-ray orbits, I performed the following experiment on the quarter-bow-tie wave-chaotic cavity of chapter 3 driven by a single port with a coupling structure similar to that described in section 3.1. The port has an inner diameter of 2a=1.27mm. Using the perturbations of the type used in section 3.2, I measured one hundred configurations of the Loss-Case 0 cavity scattering coefficient S in a frequency range of 3 to 18 GHz. I also created the radiation-case as mentioned in chapter 3, where the entire length of the inner side-walls of the cavity was coated with microwave absorber, and measured the resultant radiation scattering

coefficient S_{rad}^{a} over the same frequency range as in the cavity-case (inset (a) in Fig. 9.4).

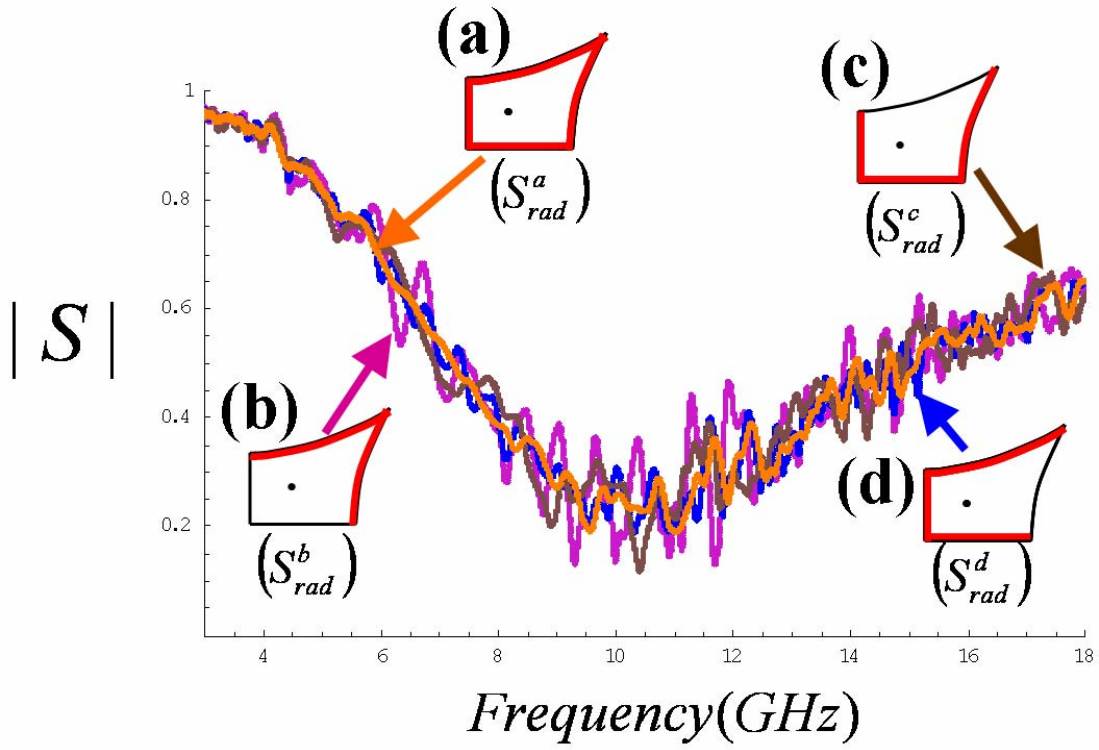

Fig. 9.4: Magnitude of the measured scattering coefficient for the cavity setup shown in inset (a)-orange, inset (b)-purple, inset (c)-brown, inset (d)- blue.

In addition, I also measured three "partial radiation-cases", wherein certain sections of the cavity side-walls were left uncoated with microwave absorber. This is shown schematically as the insets (b), (c) and (d) in Fig. 9.4. I then measured the resultant radiation scattering coefficients from 3 to 18 GHz for these three partial-radiation cases (labeling them as S_{rad}^{b}, S_{rad}^{c} and S_{rad}^{d} corresponding to the setup shown in insets (b), (c) and (d) respectively). The magnitude of these partial-radiation scattering coefficients is shown in Fig. 9.4. Note the fluctuations present in the

partial-radiation case measurements (purple, blue and brown curves), as compared to the radiation-case measurement (orange curve). The purpose of this exercise is to determine the contribution of a single-bounce short-ray orbit to the measured radiation case, i.e., the fluctuations introduced into the measured radiation case due to a wave that leaves the port bounces only once on the cavity side-walls before returning to the port.

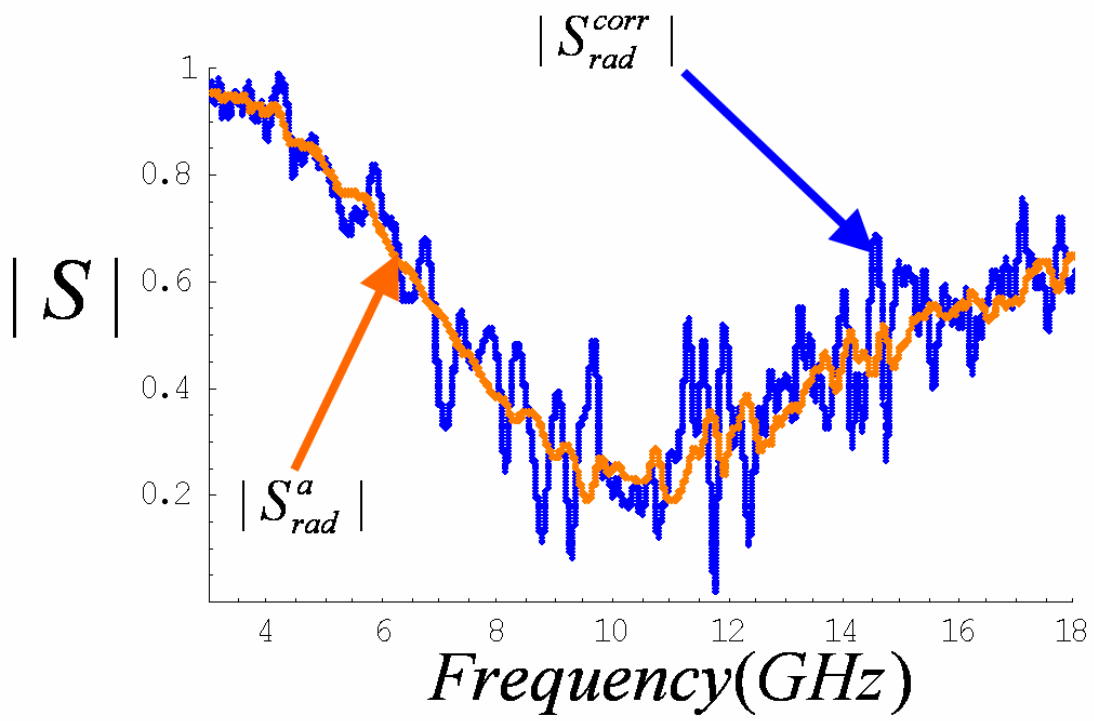

Fig. 9.5: Magnitude of the measured radiation-scattering coefficient for the cavity setup shown in inset (a)-orange, and the corrected-radiation scattering coefficient-blue. The fluctuations in the data represented by the blue line mostly come from one-bounce short-ray orbits.

From the measured data in Fig. 9.4, I construct a "corrected" radiation scattering coefficient $(S^{corr}_{rad} = S^{a}_{rad} + (S^{a}_{rad} - S^{a}_{rad}) + (S^{b}_{rad} - S^{a}_{rad}) + (S^{c}_{rad} - S^{a}_{rad}))$ which

should account for the contributions of the single-bounce short-ray orbits and is shown in Fig. 9.5 as the blue line. The orange line in Fig. 9.5 is the measured radiation scattering coefficient (S^a_{rad}). Using this corrected-radiation scattering coefficient, I normalize the measured cavity data by first converting them to the appropriate cavity impedances (using Eq.(3.1) and Eq.(3.2)) and then using the "radiation impedance" normalization process as mentioned in chapter 3 (Eq.(3.3)). In this manner, I obtain z^a and z^{corr} which correspond the normalized impedance values obtained after normalizing the cavity impedance (Z) with the measured radiation impedance (Z^a_{rad} - obtained from S^a_{rad}), and the corrected-radiation impedance (Z^{corr}_{rad} - obtained from S^{corr}_{rad}). I then convert z^a and z^{corr} to the appropriate normalized scattering coefficients s^a and s^{corr} respectively using Eq.(2.8).

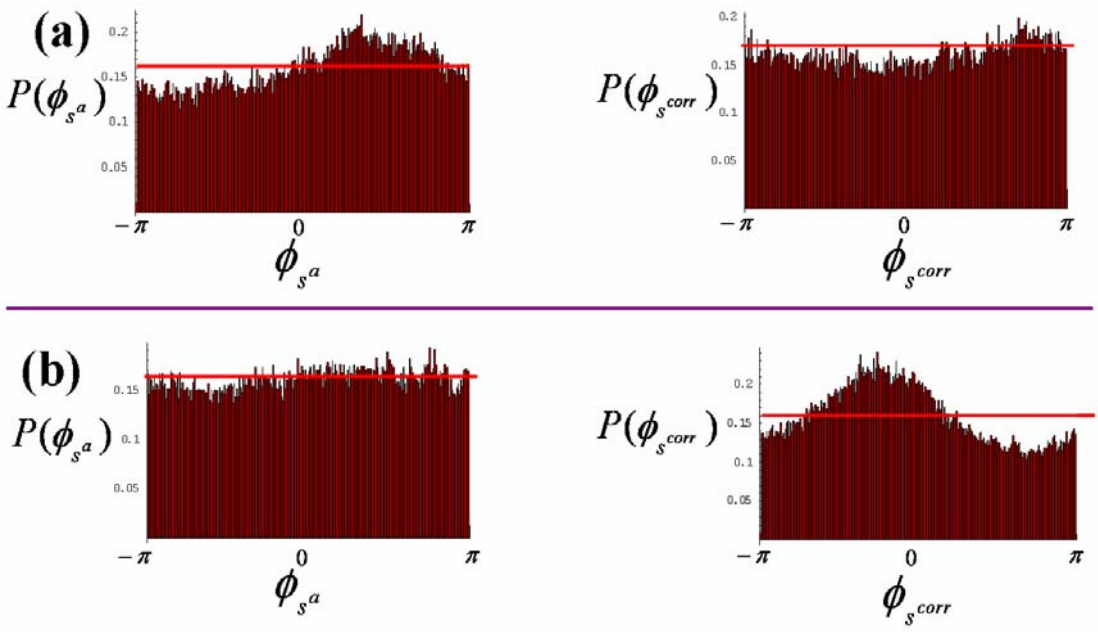

Fig. 9.6: (a) shows the probability density function (PDF) of the phase of s^a (left) and s^{corr} (right) in the frequency range of 6.8 to 7.8 GHz. (b) shows the probability

density function (PDF) of the phase of s^a (left) and s^{corr} (right) in the frequency range of 9.5 to 10.5 GHz.

To evaluate if the normalization process using the corrected-radiation measurement is effective, I look at the phase of the normalized scattering coefficient (which has been shown to be uniformly distributed between $-\pi$ and π). I take 1GHz frequency windows from the frequency range of 3 to 18 GHz, and determine the phase of s^a and s^{corr} values that lie in these windows. Figure 9.6 (a) shows the probability density function (PDF) of the phase of s^a (left) and s^{corr} (right) in the frequency range of 6.8 to 7.8 GHz. It can be observed that the short-ray orbits manifest themselves as deviations from the perfectly uniform distribution for the phase of s^a. However, the agreement with the perfectly uniform distribution seems to be much better for the PDF of the phase of s^{corr}. Encouraged by this result, I chose another frequency range of 9.5 to 10.5 GHz, and determined the phase of s^a and s^{corr} values that lie in this frequency window. The PDFs of the phase of s^a (left) and s^{corr} (right) are shown in Fig. 9.6(b). In this case, I observe that the PDF of the phase of s^a appears to be in much better agreement with the perfectly uniform distribution. Thus, I am presently not in a position to conclusively prove the effectiveness of the "radiation impedance" correction process due to the effects of short-ray orbits. This correction scheme would perhaps be more effective if performed in the impedance-domain rather than in the scattering-domain as shown above. The issue of short-ray orbits leading to systematic errors in the measured radiation-case data thus deserves further attention both on the theoretical and experimental fronts.

9.1.4 Experimentally Exploring Broken-Time-Reversal-Symmetric Wave-Chaotic Impedance, Admittance and Scattering Fluctuations

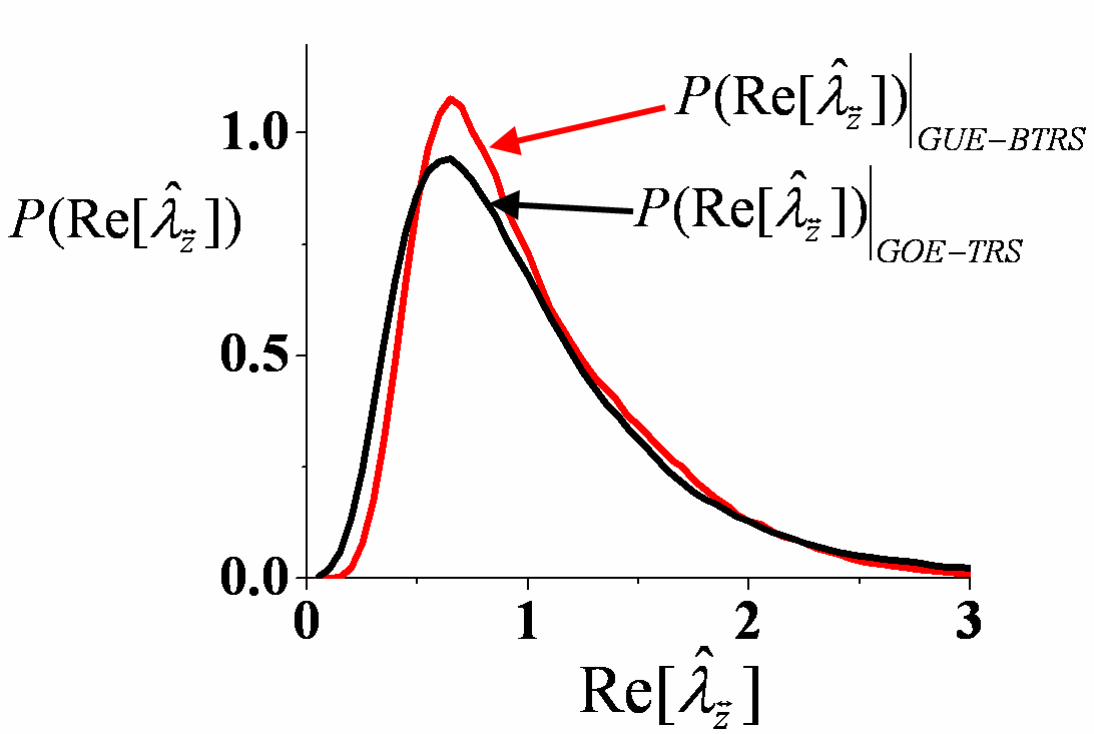

Fig. 9.7: Random Matrix Theory predictions for the PDF of the real part (black line- TRS, red line- BTRS) of the normalized impedance eigenvalues is shown for the same value of the cavity loss-parameter ($\alpha = 1$).

The breaking of time-reversal-symmetry presents a whole new series of theoretical predictions from Random Matrix Theory for the universal fluctuations in the impedance, admittance and scattering properties of wave-chaotic systems. These systems are now described by the Gaussian Unitary Ensemble (GUE) of random matrices (See chapter 1) and the universal fluctuations are predicted to be very different from corresponding predictions for the Time Reversal Symmetric case. An

example is shown in Fig. 9.7, where the PDF of the real part (black line- TRS, red line- BTRS) of the normalized impedance eigenvalues is shown for the same value of the cavity loss-parameter ($\alpha = 1$) (also see Eq.(2.5) and Eq. (2.6)). Another example, is shown in Fig. 9.8 for the universal conductance fluctuations PDFs for two wave-chaotic systems- TRS (blue line) and BTRS (red line) with the same degree of dephasing ($\gamma = 18$) within the quantum system **[59]**.

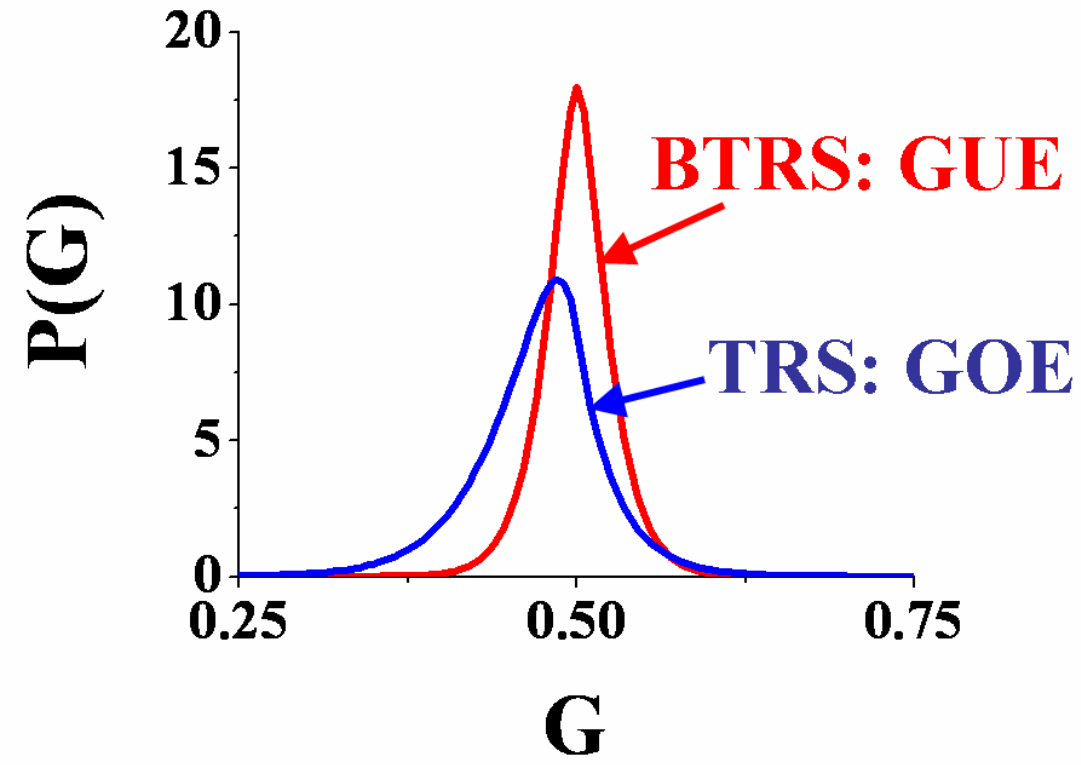

Fig. 9.8: Prediction from **[59]** for the PDF of the conductance (G) as defined in chapter 6 for the TRS case (blue) and the BTRS case (red) with the dephasing parameter ($\gamma = 18$).

In BTRS systems, the presence of an anisotropic media within the wave-chaotic cavity that has complex off-diagonal terms in its permittivity or permeability

tensors, results in the Helmholtz wave equation becoming complex (and therefore not symmetric upon the reversal of time i.e., $t \to -t$). Experimentally, this can be realized by placing a magnetized ferrite along one of the inner side-walls of the cavity **[55]**. One of the exciting phenomena induced upon breaking time reversal symmetry is the effect of "weak localization". Weak localization occurs in time reversal symmetric systems due to coherent back-scattering of the time-forward and time-reversed paths of the waves **[90]**, and leads to an enhancement of the average reflection coefficients in such systems. Thus, in essence, the waves seem to "remember" which port they entered the cavity from and prefer to exit the cavity through the same port. This is not true in BTRS systems.

Some experimental issues that should be considered when using ferrites to induce time reversal symmetry breaking is that ferrites tend to be very lossy, thereby inadvertently increasing the α-value of the system. The non-reciprocal phase shift introduced by the ferrites is also limited to small frequency ranges. Thus, in order to obtain experimental data over large frequency ranges, an array of different types of ferrites would perhaps be required.

9.1.5 Role of Scars

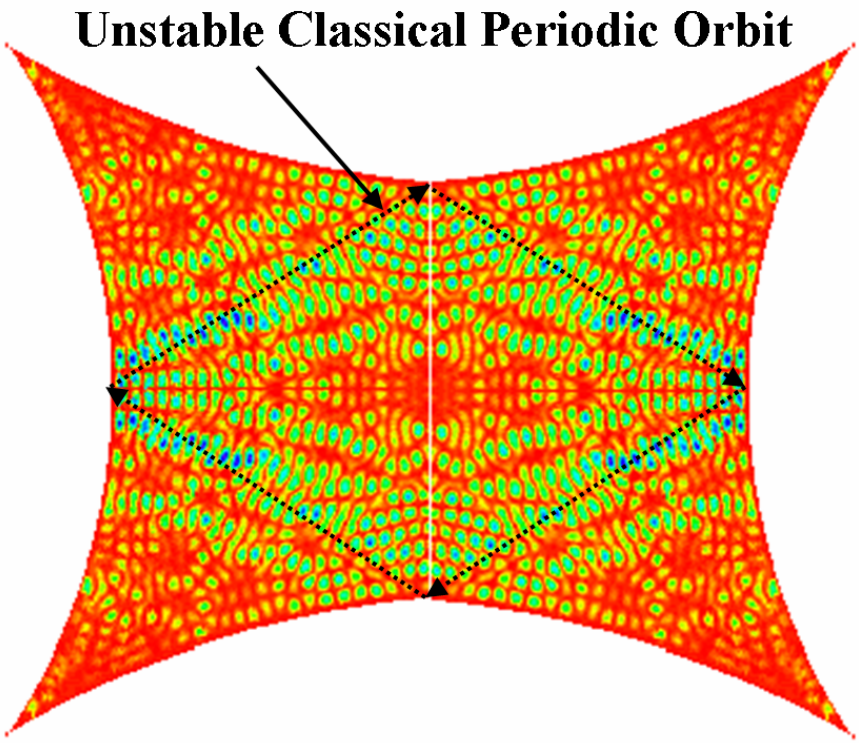

Fig. 9.9: A scarred wavefunction of the wave-chaotic cavity at 12.57 GHz is shown. The blue (red) regions indicate regions of high (low) field intensity (wavefunction magnitude). The enhanced wavefunction magnitudes (blue regions) are found in the vicinity of the unstable classical periodic orbit (shown as a dashed black line).

One of the basic assumptions of the Random Coupling Model is the applicability of the Random Plane Wave Hypothesis for the waves within the wave-chaotic cavity. Under this hypothesis, the energy is homogenously distributed amongst the different higher-order modes of the cavity. However, **[91, 92]** has shown that in certain cases, the eigenmodes of wave-chaotic cavities show deviations from the random plane wave hypothesis. Such eigenmodes, called "scars", have enhanced wavefunction magnitudes and are found in the vicinity of unstable classical periodic

orbits. An example of such a scarred eigenmode in the wave-chaotic cavity is shown in Fig. 9.9 at 12.57GHz. Scarred wavefunctions are not treated by the Random Coupling Model or Random Matrix Theory. The study of such wavefunctions requires a different mathematical approach using semi-classical techniques such as the Gutzwiller trace formula **[13]** which should be pursued and incorporated into the Random Coupling Model.

9.1.6 Formulating a Time-Domain Version of the Random Coupling Model

The Random Coupling Model as it stands now is formulated in the frequency domain. Extensions to the time domain are particularly interesting especially to the EMC and HPM-effects community, as it gives researchers and engineers the chance to study the effects of Pulsed RF and Electromagnetic Pulses on complicated enclosures. Recently, a strong theoretical and experimental endeavor has been initiated by Hart, Antonsen, Ott, Bertrand and Anlage to study the nature of voltage fluctuations and power-decay statistics in such wave-chaotic systems when excited by an electromagnetic pulse. Preliminary results have proved very promising and should eventually yield a novel insight into the interaction of pulses with complicated cavity-enclosures.

Appendix A- The "Terrapin RCM Solver v1.0" User's Guide

Fig. A.1: The "Terrapin RCM Solver v1.0" CD Label

Dept. of Electrical and Computer Engineering

University of Maryland-College Park, USA

Steven M. Anlage, anlage@umd.edu

Dept. of Physics, University of Maryland-College Park, USA

Work supported by AFOSR-MURI grant F496200110374

and AFOSR-DURIP grants FA95500410295 & FA95500510240

A.1 Introduction

The Terrapin RCM Solver v1.0 is a first generation stand-alone, GUI software that utilizes the "Random Coupling Model"(RCM) and the "RCM Induced Voltage Algorithm" to make statistical predictions for the induced voltages at specific points within a complicated, real-world 2D or 3D enclosure given a minimum of user-specified input information. In addition, the software has the capability to accurately determine universal and detail-independent impedance, admittance and scattering fluctuations in real-world 2D and 3D enclosures. The current version of the software is written for 2-port, 2D or 3D ray-chaotic enclosures. Extensions to this software to other cases can be explored in consultation with the authors.

We strongly encourage the user to evaluate this software and compare its predictions with independent measurements on real-world enclosures. We urge you to contact us regarding your comments/criticisms so that we may improve the design and functionality of future versions of this software.

A.2 Installation: Windows XP

The CD comes equipped with all the files necessary to run this software. In addition, the user is provided with some sample data-sets with which to familiarize himself/herself with the software and its functionality.

The software and all associated files are located in the folder "Terrapin RCM v1.0" on the CD.

1. Copy the folder “Terrapin RCM v1.0” on to your hard-disk.
2. Open the copied folder “Terrapin RCM v1.0” which is now present on your hard-disk.
3. Click on the file “MCRInstaller.EXE”. The contents of this file will now extract on to your hard-disk. This may take a few minutes depending upon processor speed. This is only a one-time operation. It is not required to run this step every time you use the software. During this extraction process, the Matlab Component Runtime (MCR) compiler and standard matlab libraries are installed.
4. Once the extraction process has completed, the software is now ready to use.
5. Click on the file “terprcm.EXE” to initiate the software. A status-prompt screen should appear for about 3 seconds following which the title screen of the Terrapin RCM v1.0 should open. See screenshot on next page.

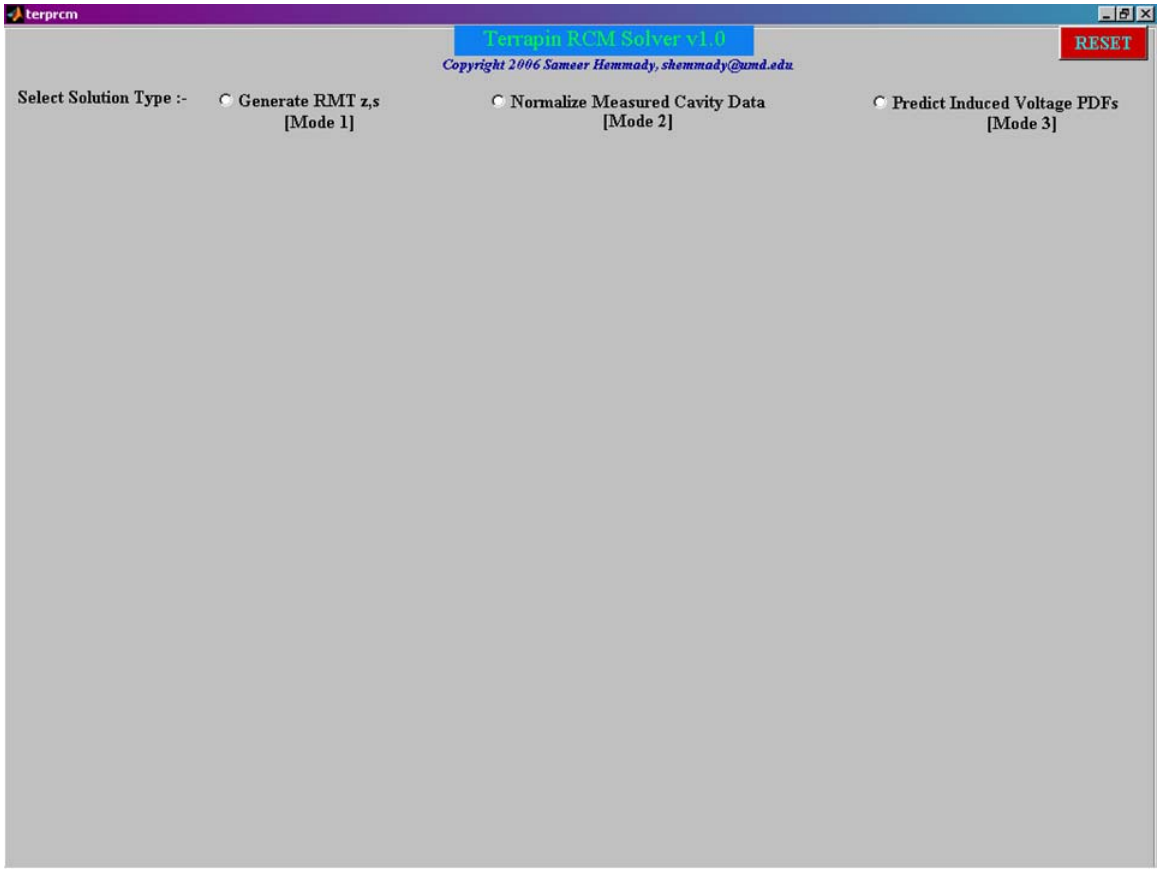

Fig. A.2: Title-screen of the "Terrapin RCM Solver v1.0"

A.3 Navigating "Terrapin RCM Solver v1.0"

The software is designed to operate in 3 modes of operation (also known as "solution types").

Generate RMT z, s [Mode 1]:

In this mode, the user is prompted to specify the value of the cavity loss-parameter α which determines the shapes and scales of the universally fluctuating impedance and scattering matrix of a complicated enclosure. The software then uses this value of α to numerically generate a large ensemble of these universally fluctuating quantities and allows the user to export these quantities to a file.

Normalize Measured Cavity Data [Mode 2]:

In this mode, the user is prompted to supply the measured cavity and radiation scattering matrix files of a real-world enclosure. The software then uses the "Random Coupling Model" to uncover the universal fluctuations in the impedance, admittance and scattering matrix of the real-world enclosure. The software also has the functionality of calculating the ONERA- Scattering Ratio and the Maryland-Impedance Ratio from the user-supplied data files.

Predict Induced Voltage PDFs [Mode 3]:

In this mode, the user is prompted to supply the measured/numerically generated radiation scattering matrix file for the ports of interest within a complicated real-world enclosure. The user is also prompted to specify the value of the cavity loss-parameter α. The software then determines the distribution of the induced voltages on the second port for a user-specified excitation at port-1. This mode works on the formalism of the "RCM Induced Voltage Algorithm".

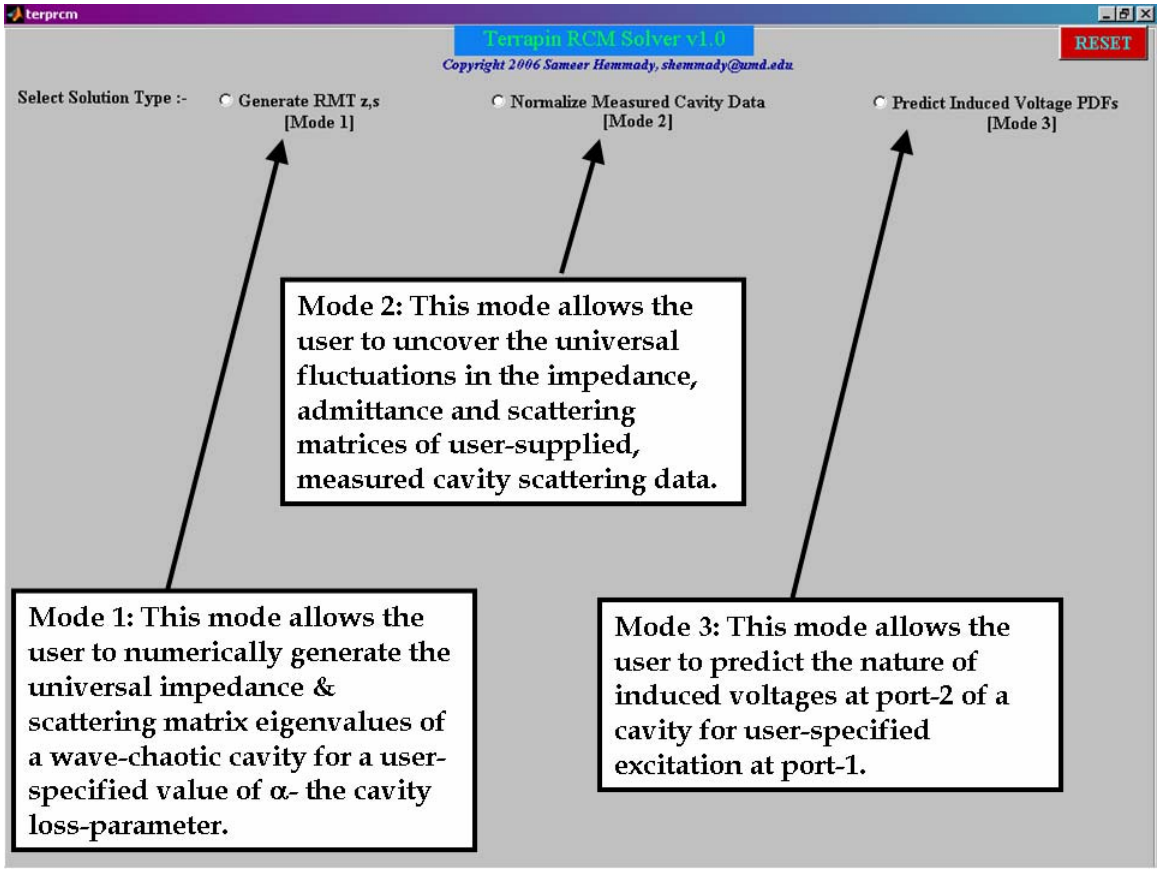

Fig. A.3: Navigating the "Terrapin RCM Solver v1.0"

Recovering from an unstable state:

In the event that the software enters an undesirable state. The user is provided with a red "**RESET**" button on the upper-right hand of the screen. This has the effect of terminating all current run-time processes associated with the Terrapin RCM Solver v1.0, clearing the memory and reinitiating the compiler. The software returns back to the initial title-screen and awaits further user action.

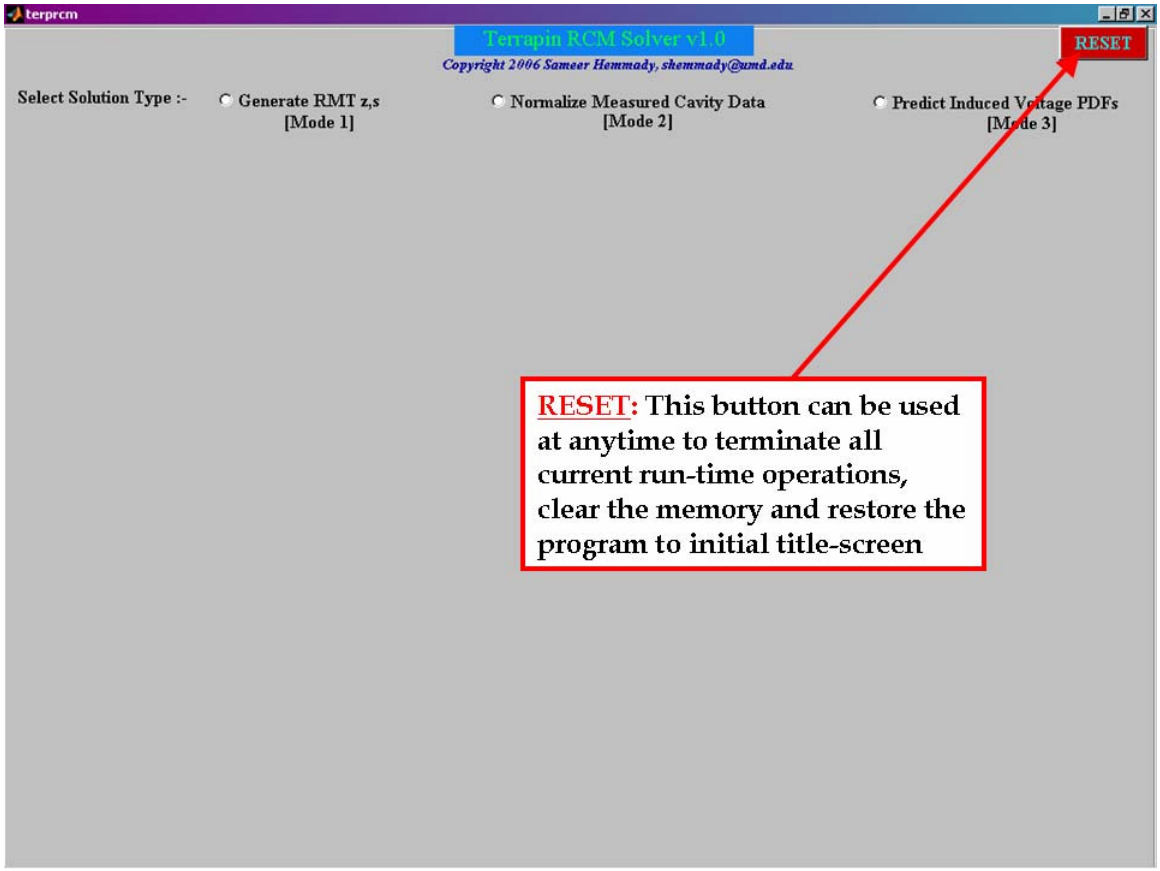

Fig. A.4: The use of the RESET button

A.4 Tutorial: Generating RMT z,s [Mode 1]

In this section we provide the user with a step-by-step procedure to operate the "Terrapin RCM Solver v1.0" in Mode 1. In this mode, the user is prompted to specify the value of the cavity loss-parameter α which determines the shapes and scales of the universally fluctuating impedance and scattering matrix of a complicated enclosure. The software then uses this value of α to numerically generate a large ensemble of these universally fluctuating quantities and allows the user to export these quantities to a file.

1. Upon executing the Terrapin RCM Solver v1.0 and arriving at the Title-screen, click the radio-button entitled "Generating RMT z,s [Mode 1]". The following screen will appear.

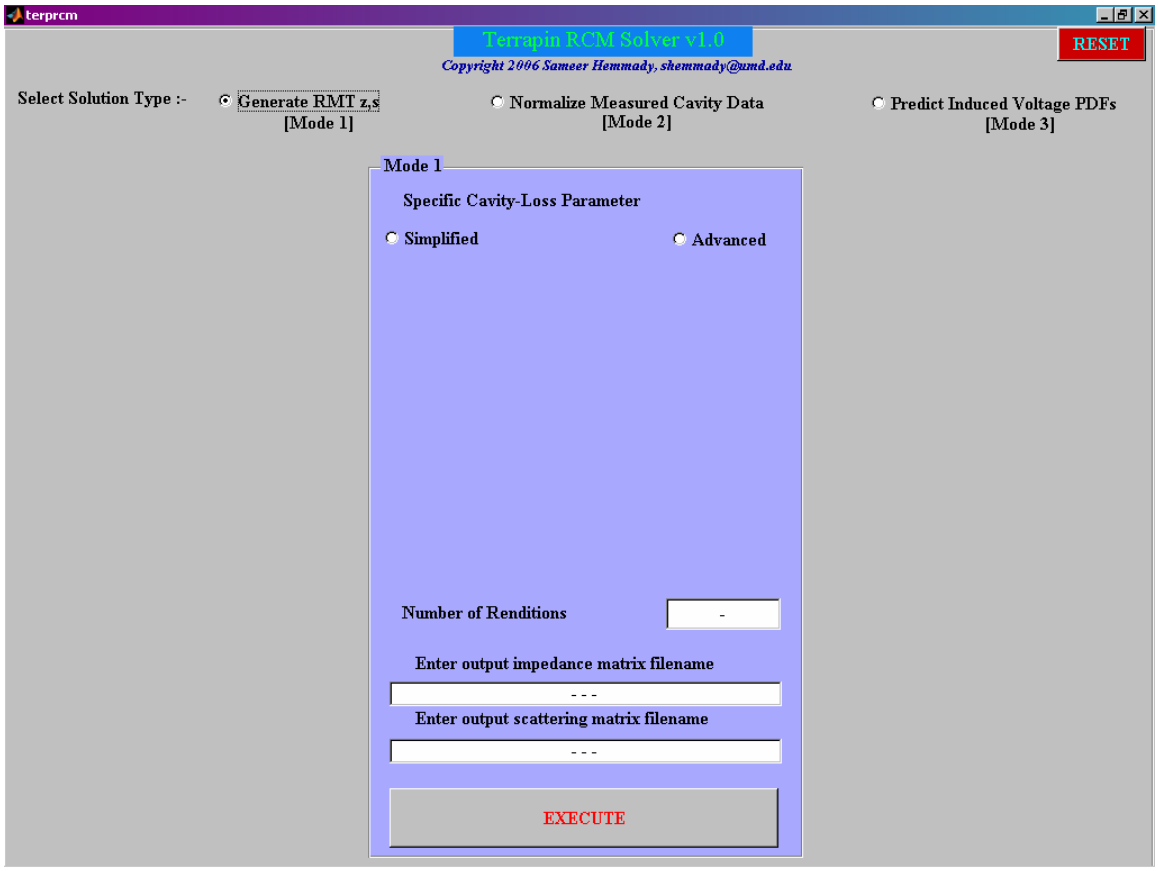

Fig. A.5: Screenshot of Mode 1

2. The user is prompted to specify the Cavity-Loss Parameter α. The software provides two options- Simplified **OR** Advanced. In the simplified mode, the user is prompted to directly specify the value of α. In the advanced mode, the user has greater flexibility and can use the software to calculate the value of α for a specific cavity setup. For

simplified mode operation go to step 3. For advanced mode operation go to step 7.

3. Clicking the radio-button marked “Simplified” will bring up the following screen. The user can now directly enter the value of the Cavity-Loss Parameter in the space provided. The Cavity-Loss Parameter is a non-negative real number, e.g. 0, 2.5, 3.154, etc.

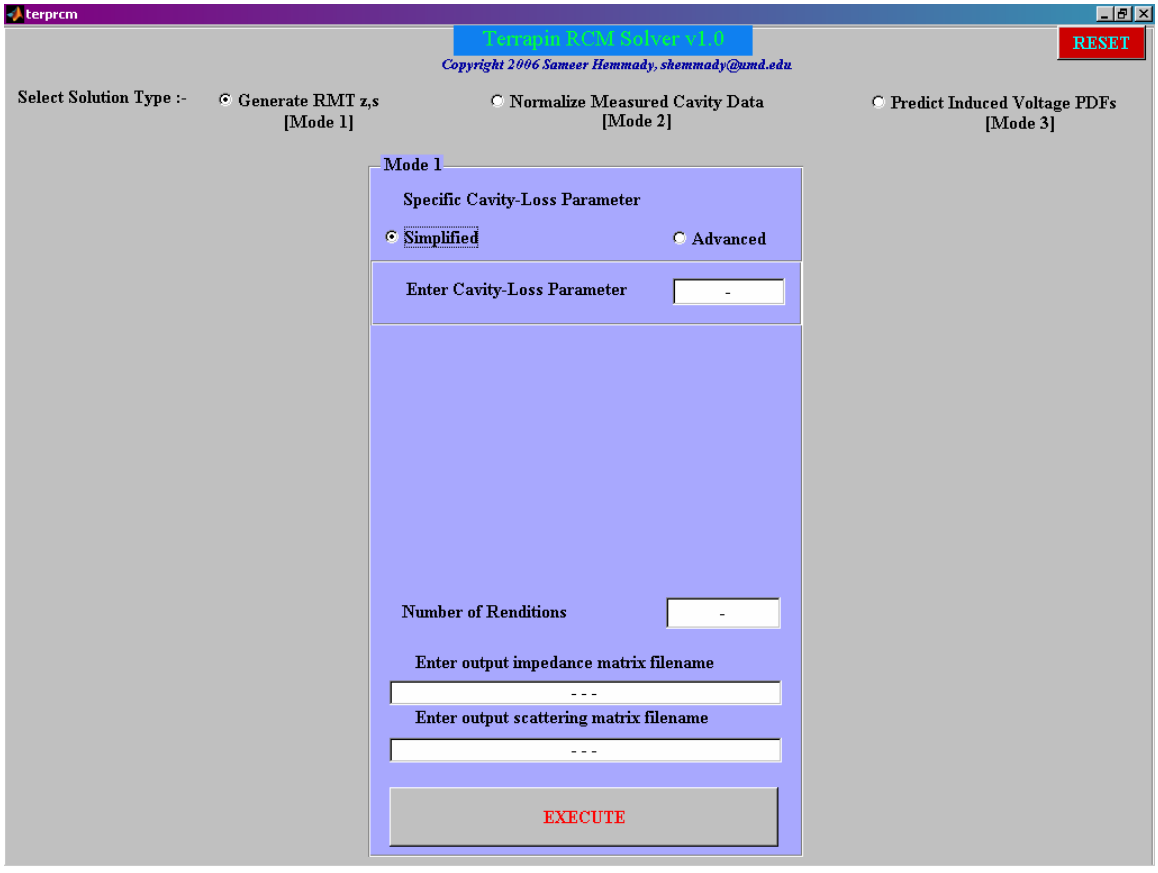

Fig. A.6: Screenshot of Mode 1-Simplified

4. The user can then specify the “Number of Renditions” in the space provided. Typically, a value of 50,000 or more provides a good statistical estimate for the quantities to be determined. This will result in 50,000 impedance or scattering matrices to be written to the output files.
5. The user can now specify the output impedance and scattering matrix filenames in the appropriate space provided. e.g. “zout.txt” and “sout.txt”. **NOTE:** the “.txt” extension is required. You can also specify a “.dat” extension if necessary.
6. Now press “EXECUTE” and sit back, relax... A progress bar should appear indicating the percentage of the process that has completed. When the process is finished, the resultant universal impedance and scattering matrix quantities are stored in the user-specified filenames in the same directory as the software.
7. Clicking the radio-button marked “Advanced” will bring up the following screen.

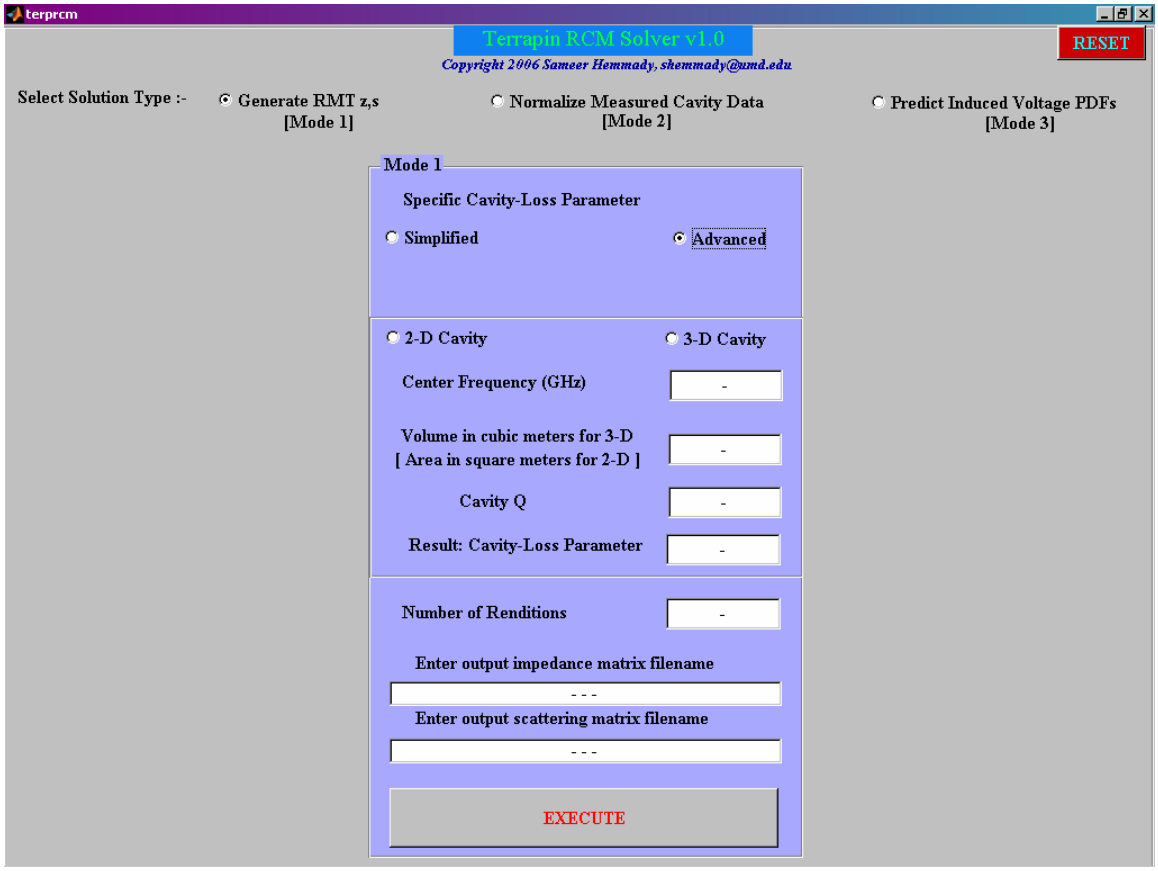

Fig. A.7: Screenshot of Mode 1- Advanced

8. In the "Advanced" mode, the user can allow the software to determine the value of the Cavity-Loss Parameter α, for a specific setup.
9. Click on either "2-D Cavity" **OR** "3-D Cavity" depending upon your desired setup.
10. Enter the Center Frequency in GHz in the space provided , e.g. 2, 0.075, etc.
11. Enter the Volume in cubic meters if you have chosen the "3-D Cavity" option in step 9; else enter the Surface-Area of the cavity in square meters if you have chosen the "2-D Cavity" in step 9.

12. Enter the typical value of Cavity Q that you would expect for your setup at the frequency specified in step 10.
13. Now follow steps 4, 5 and 6. At the end of the process, the resultant value of the Cavity-Loss Parameter that corresponds to your input parameters in steps 9,10,11 will be displayed in the space marked “Result: Cavity-Loss Parameter”.

Format of the output files from Solution Type 1 (Mode 1):

Assume that the filenames that correspond to the output impedance and output scattering matrix files are “zout.txt” and “sout.txt” respectively. Each file will contain a large number (as specified by the value of the “Number of Iterations”) of real-numbers that correspond to the normalized (universal) impedance and scattering matrices. A typical file structure will look as below:

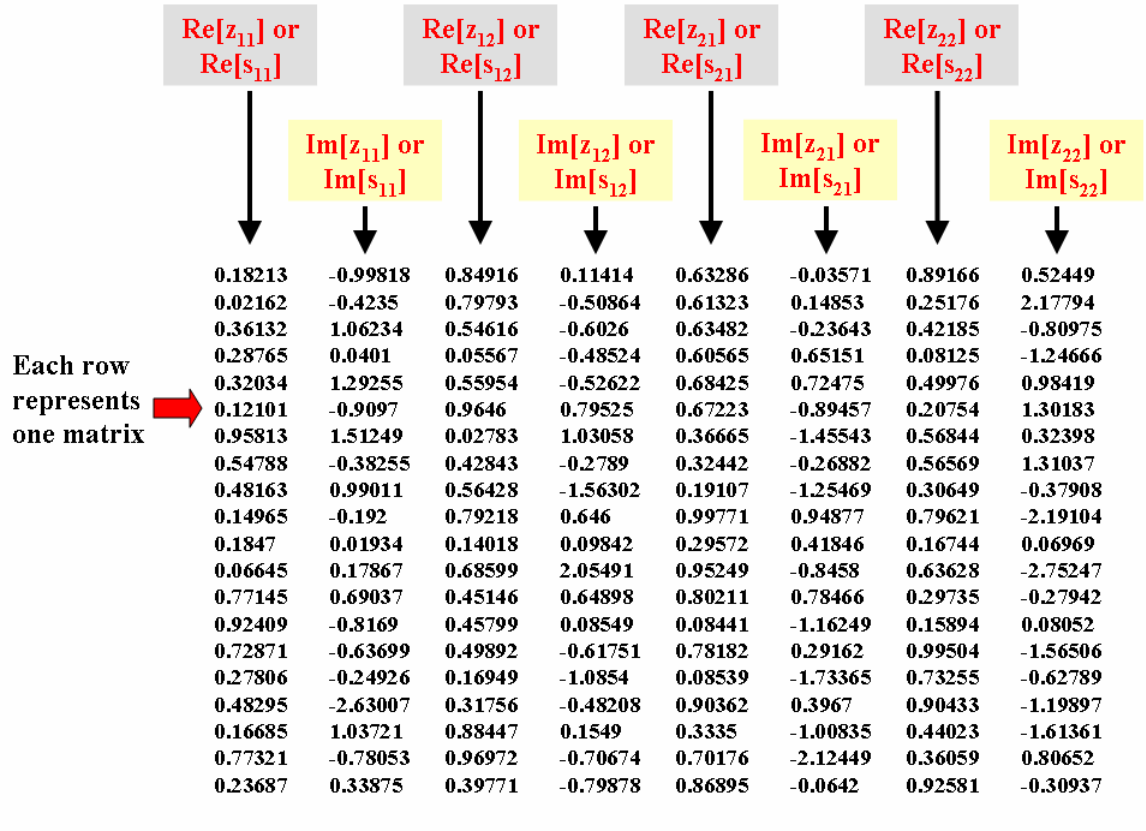

Fig. A.8: Format of the output ASCII file generated by Mode 1

where z_{xy} or s_{xy},(x,y=1,2) represent the elements of the z or s matrix with usual electromagnetic convention. Each row is a matrix that represents the cavity Impedance or Scattering matrix for a given value of α when the driving ports are perfectly-coupled (ideally-matched) to the cavity. The list of numbers shown in the figure above is purely for the purposes of showing the user how the output data file is formatted. It is **NOT** actual data generated by the software.

A.5 Tutorial: Normalize Measured Cavity Data [Mode 2]

In this section we provide the user with a step-by-step procedure to operate the "Terrapin RCM Solver v1.0" in Mode 2. In this mode, the user can use the software to uncover and plot universal fluctuations in the impedance, admittance and scattering matrices for a user-supplied cavity data-file. The software makes use of the measured cavity scattering matrix and the measured cavity radiation matrix files along the lines of the impedance-normalization process of the Random Coupling Model.

For the benefit of the first-time user, we have provided two sample data files- "Scav.txt" and "Srad.txt". The file "Scav.txt" contains 104 measurements of a 3D mode-stirred cavity which is driven by two ports in the frequency range of 4-5 GHz (in 300 equi-spaced frequency steps). The file "Srad.txt" contains a single measurement of the radiation scattering matrix of the two driving ports in the frequency range of 4-5GHz (in 300 equi-spaced frequency steps).

1. Upon executing the Terrapin RCM Solver v1.0 and arriving at the Title-screen, click the radio-button entitled "Normalize Measured Cavity Data [Mode 2]". The following screen will appear.

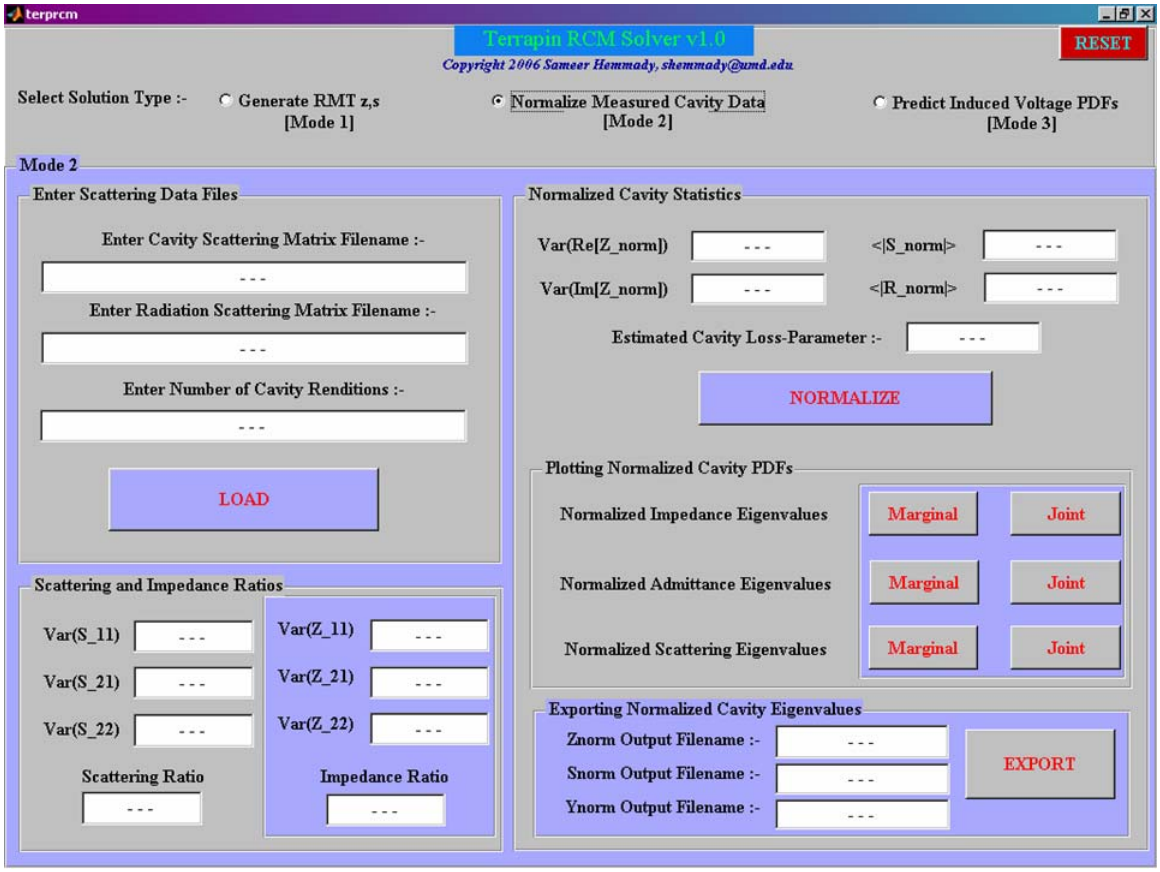

Fig. A.9: Screenshot of Mode 2

2. Type “Scav.txt” in the space provided for the Cavity Scattering Matrix file name.
3. Type “Srad.txt” in the space provided for the Radiation Scattering Matrix file name.
4. Type “104” in the space provided for the Number of Cavity Renditions.
5. Click “LOAD”. A progress bar should appear indicating the percentage of the process that has completed. When the process is finished, the relevant values for the variances of the cavity Scattering and Impedance matrix elements will appear in their respective spaces. The software will also compute the resultant ONERA Scattering and Maryland Impedance Ratio for the user-supplied data set.

6. Now click “NORMALIZE”. A progress bar should appear indicating the percentage of the process that has completed. When the process is finished, the relevant values for the quantities of the normalized (universal) cavity Scattering and Impedance matrix elements will appear in their respective spaces.
7. The user can now also click on any of the buttons marked “Marginal” or “Joint” to plot the resultant universal marginal or joint PDFs of the impedance, admittance or scattering eigenvalues. (PDF=Probability Density Function).
8. The user also has the option to export these normalized (universal) eigenvalues {real-part, imaginary-part} to a file. Specify the name of the files where you would like to store the normalized impedance,admittance and scattering eigenvalues and then click “EXPORT”. A progress bar should appear indicating the percentage of the process that has completed.

The formatting for the Scav.txt data file is shown on the next page. Please format your own measured cavity data sets as shown in order to successfully use this software. Make sure your measured cavity and radiation files are in the same directory as the software.

NOTE: The user-supplied Radiation Scattering Matrix data file should have the same format as above. However, there should be only one measured rendition of the radiation scattering matrix.

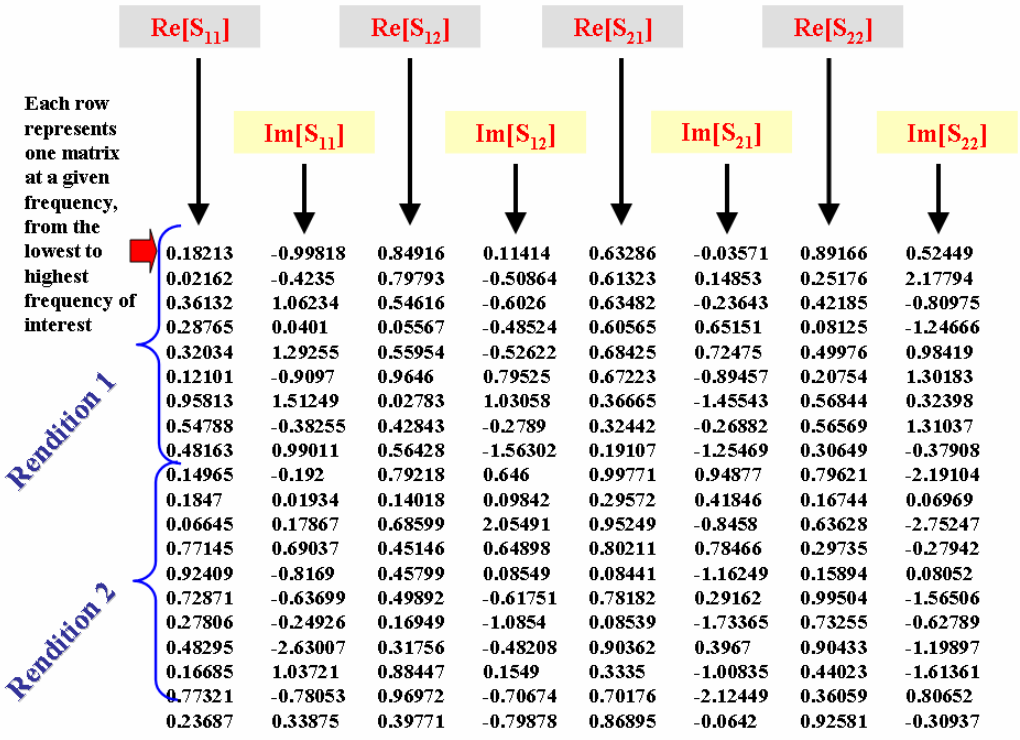

Fig. A.10: Formatting of user-supplied Cavity data files

Shown above is the typical format for arranging your measured cavity scattering matrix file in order to successfully use this software. The measured data is arranged into 8 columns as shown. Each row represents the elements of one scattering matrix at a given frequency. If you are measuring the cavity scattering response from 4 to 5 GHz in 1000 equi-spaced frequency steps, then there will be 1000 rows corresponding to the 1000 scattering matrix values measured at each frequency. This set of 1000 rows will correspond to the first measured rendition of the cavity. A similar set of 1000 rows which corresponds to your second measured rendition of the cavity will follow, as shown above. The difference between rendition sets is caused because of either moving some perturbation within the cavity such as a metal ball, or

a mode-stirrer which serves to significantly alter the field configurations within the cavity.

The radiation scattering matrix file should also be constructed to conform to the format above. However, only one measurement of the radiation scattering matrix rendition set is required.

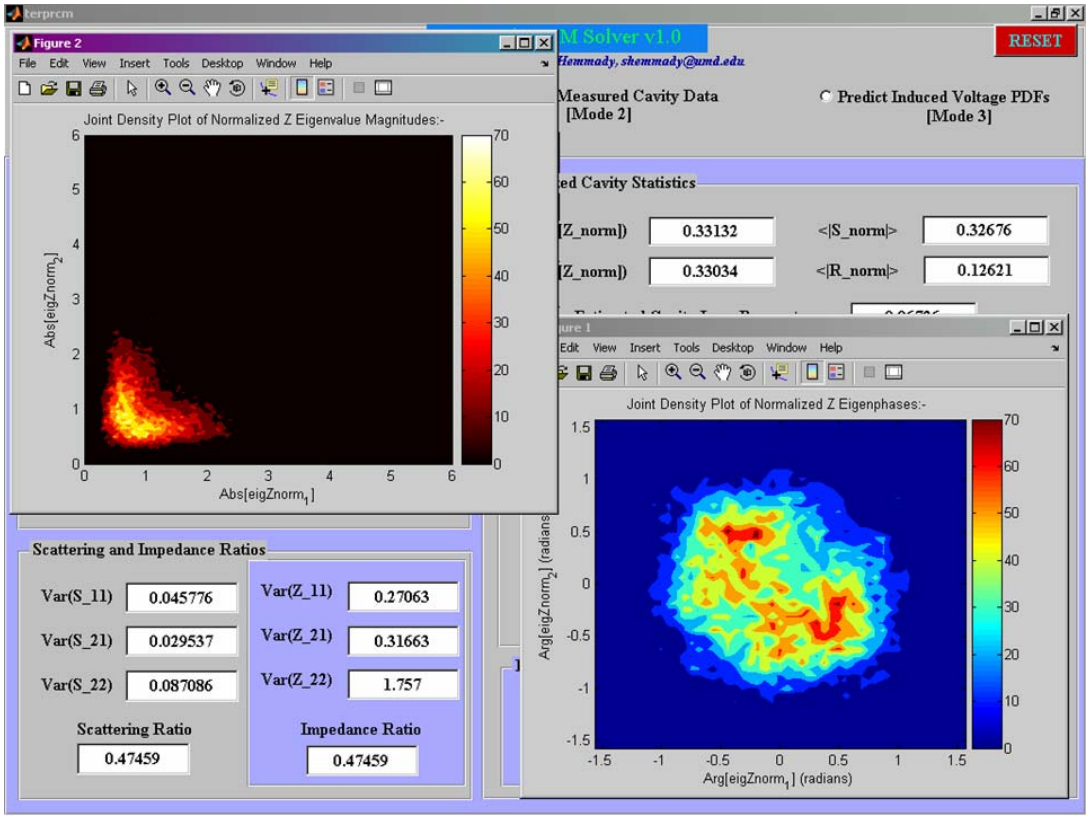

Fig. A.11: Screenshot of Mode 2 showing plots for the Joint PDF of the Universal Impedance eigenvalues

Shown above is a typical screenshot obtained upon successfully plotting the Joint PDF of the universal impedance eigenvalues. The figure in "yellow-red-black" color-code shows the joint PDF between the eigenvalue magnitudes of the normalized

(universal) impedance. The figure in the "red-green-blue" color-code shows the joint PDF between the eigenphases of the normalized (universal) impedance.

A.6 Tutorial: Predict Induced Voltage PDFs [Mode 3]

In this section we provide the user with a step-by-step procedure to operate the "Terrapin RCM Solver v1.0" in Mode 3. In this mode, the user can use the software to make statistical predictions for the nature of the induced voltages at Port-2 in a complicated 2D or 3D enclosure for a user-specified excitation at Port-1.

1. Upon executing the Terrapin RCM Solver v1.0 and arriving at the Title-screen, click the radio-button entitled "Predict Induced Voltage PDFs [Mode 3]". (PDF=Probability Density Function). The following screen will appear.

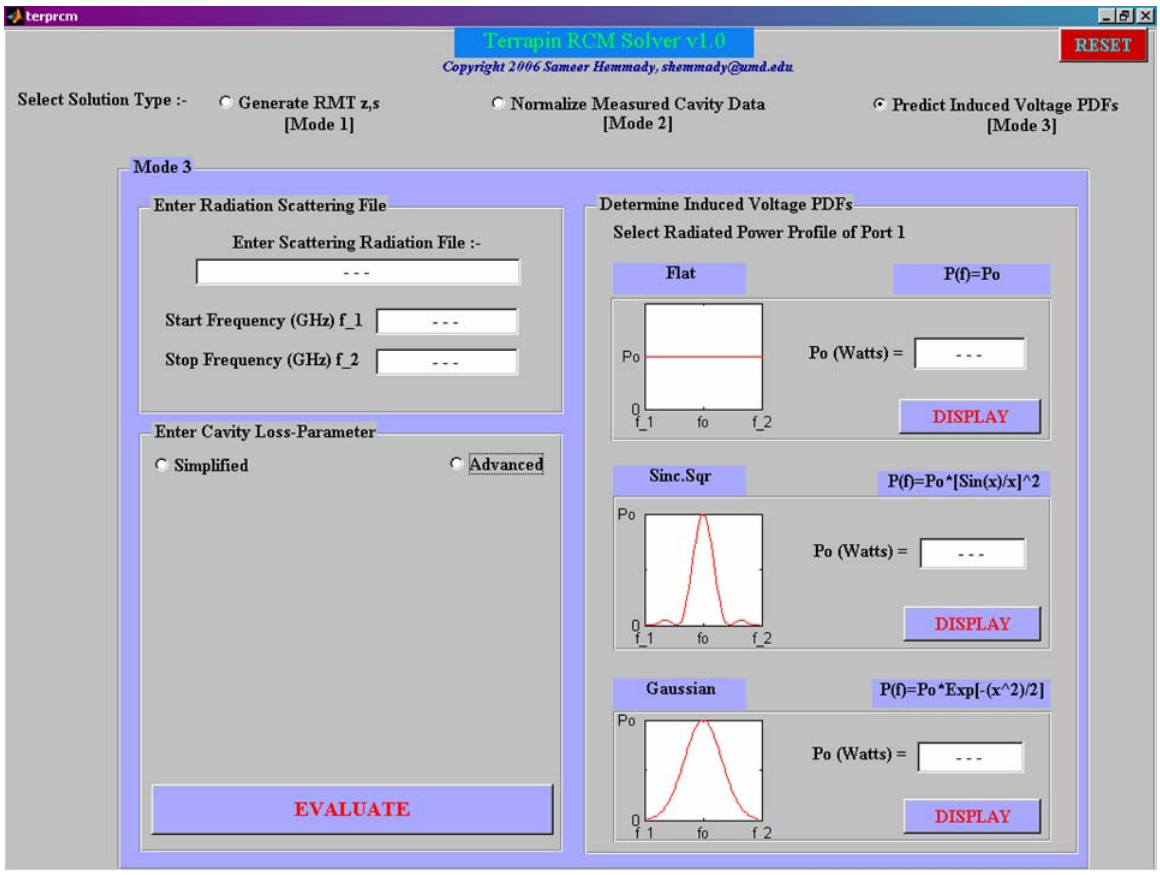

Fig. A.12: Screenshot of Mode 3

2. The user can then enter the file name of the user-supplied radiation scattering matrix file. For instructions on user-supplied files refer to pages 11, 12. For the benefit of the first-time user, we have provided the file "Srad.txt" which contains a single measurement of the radiation scattering matrix of two driving ports in a 3D mode-stirred cavity, in the frequency range of 4-5GHz (in 1000 equi-spaced frequency steps). Enter "Srad.txt" in the space provided.
3. Enter the start and stop frequencies in GHz in the appropriate spaces. Use "4" and "5" for Start and Stop frequency if using Srad.txt.

4. The user can then specify the Cavity-Loss Parameter in either the Simplified mode or Advanced Mode. Refer to pages 7,8 for further details.
5. Click "EVALUATE". A progress bar should appear indicating the percentage of the process that has completed. When the process is finished, the resultant value of the Cavity-Loss Parameter is displayed if the "Advanced" option is selected in step 4.
6. The user can then select an appropriate excitation at port-1 of the cavity. The current version supports three port-1 radiated power-profiles :
    a. Flat Response : User-specified value of P_o Watts from f_1 to f_2.
    b. Sinc-Squared Response: User-specified value of P_o Watts from f_1 to f_2.
    c. Gaussian Response: User-specified value of P_o Watts from f_1 to f_2.
7. Upon selecting the desired port-1 excitation by specifying the value of P_o (in Watts), the user can click the appropriate "DISPLAY" button to plot the distribution of the real, imaginary, magnitude and phase of the induced voltages at port-2 for the user-specified excitation at port-1.

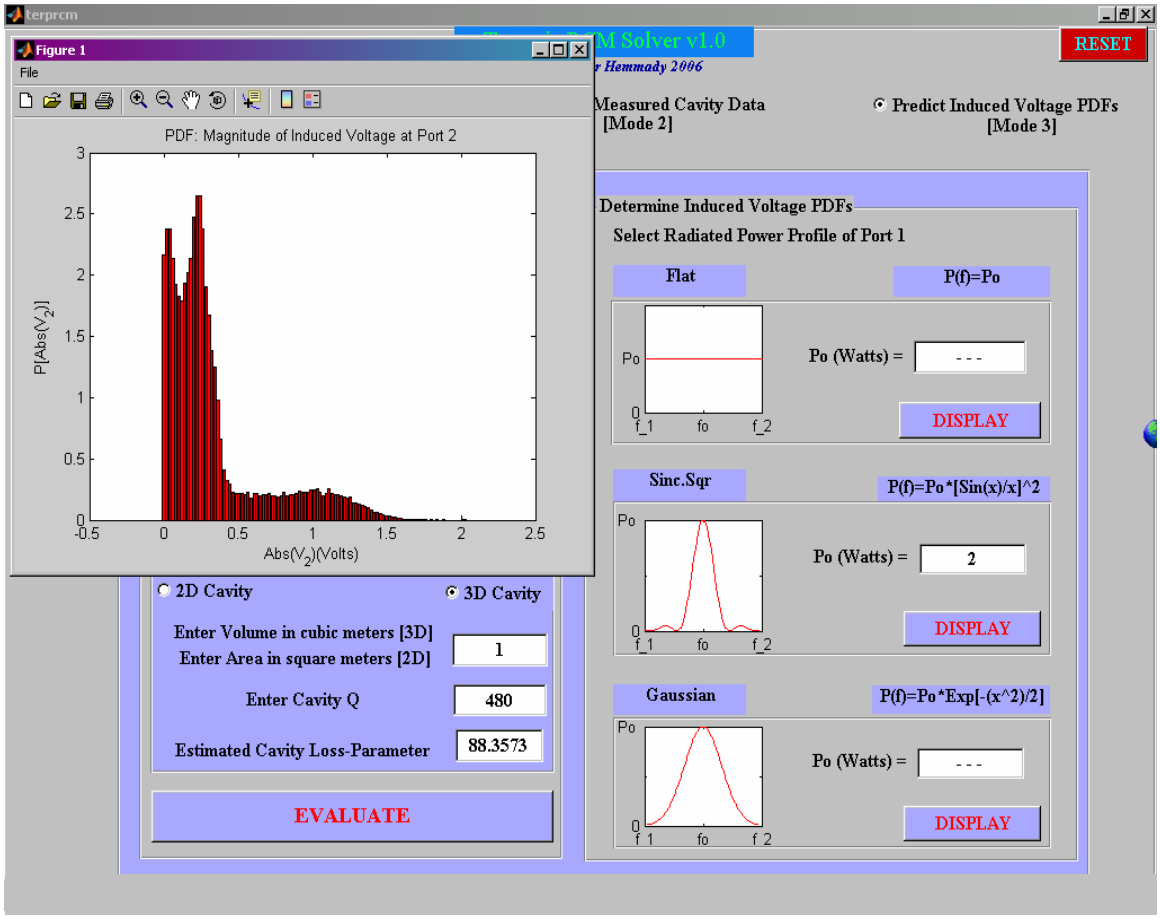

Fig. A.13: Screenshot of Mode 3 showing the PDF of induced voltages on port-2 for a 2-Watt peak Sinc-Square excitation at Port-1.

Shown above is a typical screenshot obtained upon successfully plotting the PDF of Induced Voltages on Port-2 for a 2-Watt peak Sinc-Square excitation from Port-1.

Appendix B: Summary of the different methods to estimate the cavity loss parameter - α

Method 1: Direct estimation of α from first principles: $\alpha = k^2/(\Delta k_n^2 Q)$

Procedure: **[See section 4.1.2 and appendix C]**

i) Determine : $k = 2\pi f / c$

ii) Estimate cavity Q (see appendix C)

iii) Determine : $\Delta k_n^2 \approx 4\pi / A$ $(2D)$ *or* $\Delta k_n^2 \approx 2\pi^2/(kV)$ $(3D)$

iv) Determine: $\alpha = k^2/(\Delta k_n^2 Q)$

Advantage:

i) Fast and easy to determine

ii) Useful as a quick estimate for α if cavity-losses are low and cavity resonances are not overlapping

Disadvantage:

i) Difficult to estimate the average Q of the resonator modes especially if the cavity-resonances overlap (high loss limit)

ii) For low frequencies, contributions from the lower order corrections due to the perimeter of the cavity must be taken into account when determining the value of Δk_n^2 in the quasi-two-dimensional cavity. Similar corrections are necessary in three-dimensions.

Fig. B.1 : Procedure, advantages and disadvantages of estimating the cavity loss-parameter from first principles.

Method 2:

Comparing the PDFs of Re[z] and Im[z] obtained from measurements with corresponding PDFs numerically generated from RMT using α as a fitting parameter.

Procedure: **[See section 4.1.3]**

i) Numerically generate PDFs of Re[z] and Im[z] using Random Matrix Monte Carlo simulations for different values of α.

ii) Experimentally determine the PDFs of Re[z] and Im[z] for a given frequency range (where α is approximately constant).

iii) Choose that value of α which minimizes the error between the PDFs in (i) and (ii).

Advantage:

i) More accurate than method-1

ii) Possible to estimate the error in determining α.

iii) Valid for lossy cavities with overlapping resonances.

Disadvantage:

i) Computationally intensive and time-consuming

ii) Need to numerically generate large ensembles of normalized impedance values using Random Matrix Monte Carlo simulations for a range of α-parameter values in order to perform the fitting procedure. Prone to statistical errors which could arise due to poor statistics (insufficient number of samples) of the numerically generated RMT z PDFs.

Fig. B.2: Procedure, advantages and disadvantages of estimating the cavity loss-parameter by comparing the PDFs of Re[z] and Im[z] obtained from measurements with corresponding PDFs numerically generated using α as a fitting parameter.

Method 3:

Estimating the loss-parameter for the data-set from the relation between the variance of Re[z] or Im[z] PDFs and α obtained from Random Matrix Monte Carlo simulations.

Procedure: **[See introduction to Chapter 5]**

(i) Numerically generate PDFs of Re[z] and Im[z] using Random Matrix Monte Carlo simulations for different values of α.

(ii) Fit the relation between the variance of the numerically-generated Re[z] or Im[z] PDFs and α to a polynomial (in α) of high order.

(iii) Determine the variance of experimentally measured Re[z] or Im[z] PDFs.

(iv) Solve the polynomial in (ii) to estimate the value of α for the experimental data-set.

Advantage:

i) More accurate than method-1

ii) Possible to estimate the error in determining α.

iii) Valid for lossy cavities with overlapping resonances.

Disadvantage:

i) Computationally intensive and time-consuming

ii) Need to numerically generate large ensembles of normalized impedance values using Random Matrix Monte Carlo simulations for a range of α-parameter values in order to perform the fitting procedure. Prone to statistical errors which could arise due to poor statistics(insufficient number of samples) of the numerically generated RMT z PDFs.

iii) Errors in the experimental calibration or imperfect impedance normalization can lead to systematic errors due to outlying data points, which give an erroneous value for the estimated variance of Re[z] or Im[z] PDFs. This will affect the determined α.

Fig. B.3: Procedure, advantages and disadvantages of estimating the cavity loss-parameter from the relation between the variance of Re[z] and Im[z] PDFs, and α obtained from Random Matrix Monte Carlo simulations.

Method 4:

Estimating the loss-parameter for the data-set from the relation between the variance of Re[z] or Im[z] PDFs and α obtained from the Random Coupling Model.

Procedure: **[See section 4.1.3]**

(i) Determine the variance of experimentally measured Re[z] or Im[z] PDFs.

(ii) Determine: $\alpha = \frac{1}{\pi\sigma^2_{\mathrm{Re}[z]}} = \frac{1}{\pi\sigma^2_{\mathrm{Im}[z]}}$

Advantage:

i) Fast and easy to determine

ii) Useful as a quick estimate for α.

iii) Valid for lossy cavities with overlapping resonances.

Disadvantage:

i) Valid only when $\alpha > 5$

ii) Errors in the experimental calibration or imperfect impedance normalization can lead systematic errors due to outlying data points, which give an erroneous value for the estimated variance of Re[z](or Im[z]). This will affect the determined α.

iii) Valid only for TRS systems. For BTRS systems use Eq.(2.5)

Fig. B.4: Procedure, advantages and disadvantages of estimating the cavity loss-parameter from the relation between the variance of Re[z] and Im[z] PDFs, and α obtained from the Random Coupling Model.

Method 5:

Estimating the loss-parameter for the data-set from the relation between the dephasing parameter (γ) and <T>, where <T>=1- <eigenvalues of $\ddot{\vec{S}}\ddot{\vec{S}}^{\dagger}$>

Procedure: **[See section 5.3.3]**

i) Determine <T> from eigenvalues of $\ddot{\vec{S}}\ddot{\vec{S}}^{\dagger}$, where $\ddot{\vec{S}}$ is the normalized scattering matrix.

ii) Determine γ from <T> and Eq.(5.4)

iii) Determine: $\alpha=\gamma/4\pi$

Advantage:

i) More accurate than methods-(1,4); Works for any arbitrary number of driving ports.

ii) Possible to estimate the error in determining α.

iii) Valid for lossy cavities with overlapping resonances.

iv) Possible to determine α from the normalized scattering matrix eigenvalues.

Disadvantage:

i) Errors in the experimental calibration or imperfect impedance normalization can lead systematic errors due to outlying data points, which give an erroneous value for the estimated <T>. This will affect the determined α.

Fig. B. 5: Procedure, advantages and disadvantages of estimating the cavity loss-parameter from the relation between the dephasing parameter (γ) and <T>.

Method 6:

Estimating the loss-parameter for the data-set from the impedance-based Hauser-Feshbach relation.

Procedure: **[See Chapter 7]**

(i) Determine the Hauser-Feshbach impedance ratio from the measured raw cavity impedance matrix.

(ii) Estimate the value of α from Eq.(7.2)

Advantage:

i) Fast and easy to determine

ii) α can be determined from the raw cavity data - no need to normalize the cavity data using the radiation impedance

Disadvantage:

i) Practically useful only when $\alpha < 1$

Not been experimentally established as yet !

ii) Not applicable to one-port systems

iii) Errors in the experimental calibration can lead to systematic errors due to outlying data points, which give an erroneous value for the estimated variance of impedance matrix elements. This will affect the determined α.

iv) Presence of short-ray orbits in the cavity leads to fluctuations in the Hauser-Feshbach impedance ratio. Thus a statistical average of the impedance ratio as a function of frequency must be included.

Fig. B.6: Procedure, advantages and disadvantages of estimating the cavity loss-parameter from the impedance-based Hauser-Feshbach relation.

Appendix C: Estimating the cavity *Q* from the measured cavity S_{11} data

In order to estimate the value of the cavity loss-parameter α from first principles ($\alpha = \frac{k^2}{\Delta k_n^2 Q}$) [Method-1 of Appendix B], it is necessary to make an estimate of the quality factor of the cavity at a given frequency. Here, $k = 2\pi f / c$ is the wavenumber for the incoming frequency f and Δk_n^2 is the mean-spacing of the adjacent eigenvalues of the Helmholtz operator, $\nabla^2 + k^2$, as predicted by the Weyl Formula **[15]** for the closed system. In my dissertation, I make use of the loaded cavity quality factor (Q), which accounts for all internal dielectric losses and cavity-ohmic losses as well as dissipation through the coupled ports (see chapter 2). For a cavity driven by two ports, Q can be determined from the transmitted power-vs-frequency curve ($|S_{21}(f)|^2$), which is a maximum at the resonant frequency (see Fig. C.1 (a)). The quantity Q is then the ratio of the resonant frequency to the 3-dB bandwidth of the resonance curve **[87]** and represents the ratio of stored energy to power dissipated per cycle in the cavity. Methods to determine the *Q* of data like that shown in Fig. C.1(a) are discussed in **[93]**.

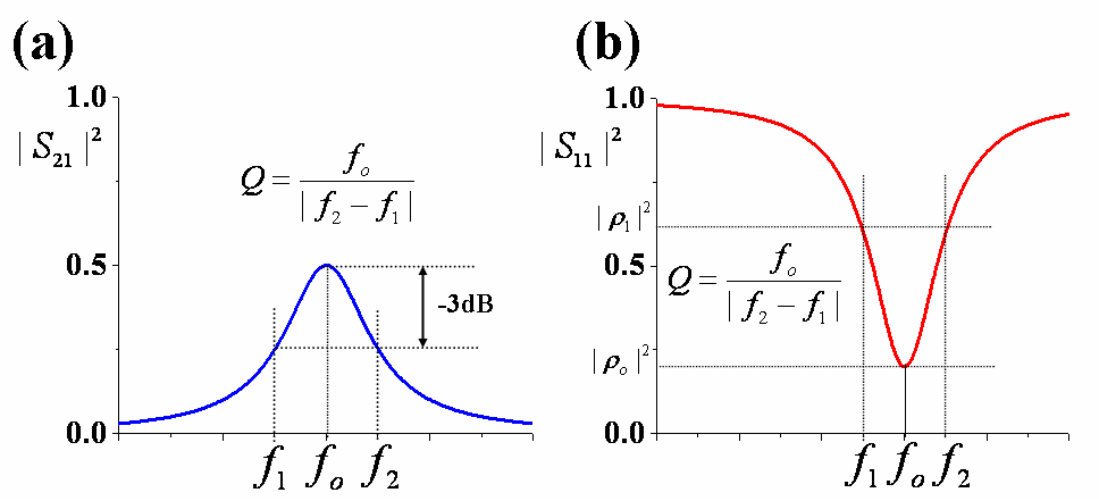

Fig. C.1: (a) Schematic showing the typical nature of a cavity resonance (blue curve) when measured from the transmitted power-vs-frequency $|S_{21}(f)|^2$ curve. The cavity resonance manifests itself as a maximum in the measured $|S_{21}(f)|^2$. (b) Schematic showing the typical nature of a cavity resonance (red curve) when measured from the reflected power-vs-frequency $|S_{11}(f)|^2$ curve. The cavity resonance manifests itself as a minimum in the measured $|S_{11}(f)|^2$.

To estimate the loaded cavity Q at a given frequency, for a cavity driven by a single port, the procedure is more elaborate **[94]** since the degree of coupling (β) between the port and the cavity has to be taken into account. The frequency-dependent coupling coefficient β is defined as the ratio of the power dissipated through the port to the power dissipated within the cavity-resonator due to dielectric and ohmic losses. The port is said to be "critically-coupled" if $\beta = 1$. In a one-port reflected-power measurement ($|S_{11}(f)|^2$), a cavity-resonance manifests itself as a minimum in the reflected power-vs-frequency curve (see Fig. C.1(b)).

For a cavity coupled to a single port and if $\beta < 1$ ("under-coupled"), the numerical value of β can be determined using

$$\beta = \frac{1 - |\rho_o|}{1 + |\rho_o|}, \tag{C.1}$$

where $|\rho_o|$ is the value of $|S_{11}(f)|$ at resonance. If $\beta > 1$ ("over-coupled"), the inverse of Eq.(C.1) is used to determine the value of β. A quick check to estimate if the cavity is under-coupled or over-coupled to the port over a given frequency range is to look at the measured cavity S_{11} on a polar chart $\{\mathrm{Re}[S_{11}], \mathrm{Im}[S_{11}]\}$ (also known as a "Smith chart"). The cavity resonances will then appear as circles (known as Q-circles). The Q-circle for an over-coupled cavity will encircle the origin of the Smith chart, while the Q-circle for an under-coupled cavity will not. From the nature of the blue trace in Fig. 4.15, it is evident that the cavity is strictly under-coupled to the port at all frequencies from 6 to 12 GHz.

After estimating the value of β, the value of the reflection coefficient (ρ_1) corresponding to the width of the resonance curve can be estimated as,

$$|\rho_1|^2 = \frac{1 + \beta^2}{(1 + \beta)^2}. \tag{C.2}$$

By defining f_o to be that frequency at which the reflection coefficient equals $|\rho_o|$, and f_1 , f_2 as the two frequencies around f_o at which the reflection coefficient equals $|\rho_1|^2$, the loaded quality factor Q is defined as ,

$$Q = \frac{f_o}{|f_2 - f_1|}. \tag{C.3}$$

The unloaded quality factor (Q_{ul}) is then defined as,

$$Q_{ul} = (1+\beta)Q\,. \tag{C.4}$$

I adopt the procedure outlined above to estimate the loaded quality factor of the cavity when driven by a single port. The red curve in Fig. C.2 shows one measurement of $|S_{11}(f)|^2$ of the Loss-Case 0 quarter bow-tie cavity, explained in section 3.1, for one configuration of the perturbers. The cavity resonances show up as minima in the measured $|S_{11}(f)|^2$. The data represented by the red curve constitutes a single-rendition of the measured cavity S_{11} data and constitutes a subset of the one-hundred renditions that makes up the ensemble cavity S_{11} data-set used in Fig. 4.4 (stars). The estimated loaded quality factor for two typical resonances along with the corresponding values of the parameters $(\beta, |\rho_o|^2, |\rho_1|^2, f_o, f_1, f_2)$ for each resonance is indicated in Fig. C.2. By employing the prescription outlined above and by analyzing other renditions of the measured cavity S_{11} data, I estimate that the mean value of the loaded quality factor for the cavity to be about ~ 300 over the frequency range of 7.2 to 8.4 GHz. This yields an α-value of about 0.8 for the data set represented by the stars in Fig. 4.4 Note that my estimate of the loaded quality factor is approximate due to the presence of over-lapping resonances observed in the measured cavity reflection coefficient. The presence of over-lapping resonances can potentially lead to under-estimating the cavity quality factor. More elaborate procedures and algorithms to accurately estimate the quality factor in the presence of such over-lapping resonances is outlined in **[95, 96, 97, 98]**.

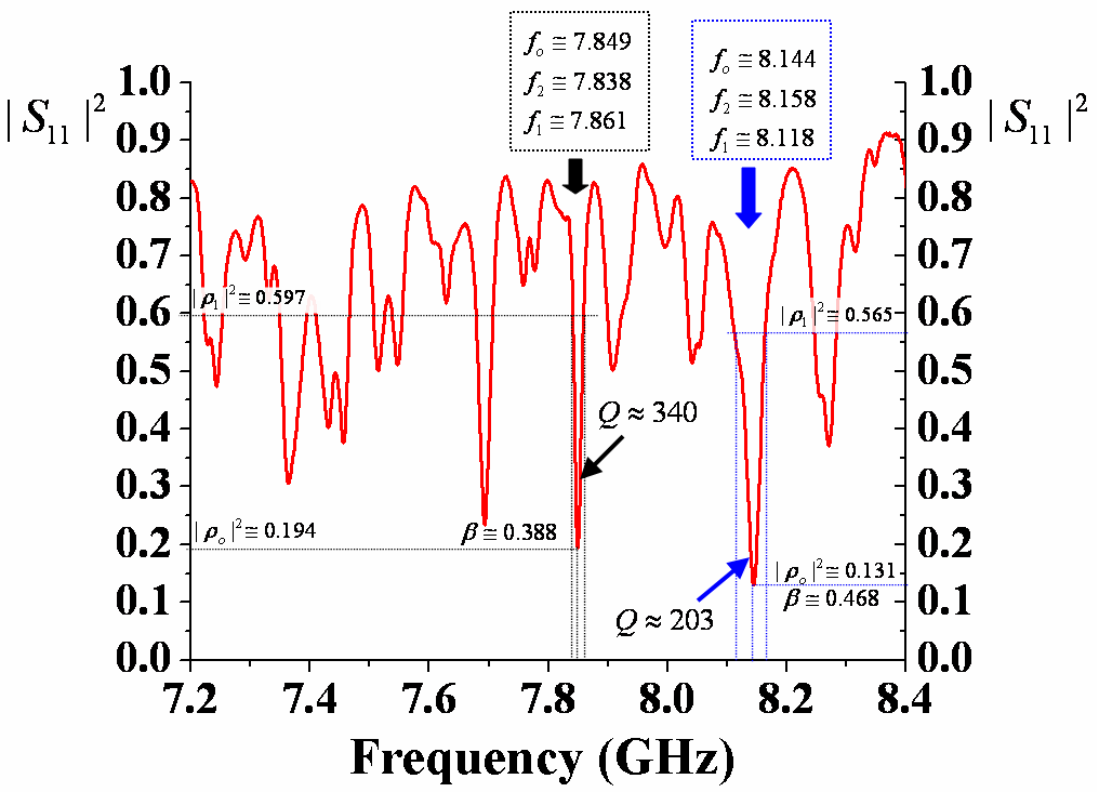

Fig. C.2: The nature of the cavity (see section 3.1) $|S_{11}|^2$ as a function of frequency, for one possible orientation of the perturbers, is shown as the red curve. The cavity resonances show up as minima in the measured $|S_{11}|^2$. The values of the parameters $\beta, |\rho_o|^2, |\rho_1|^2, f_o, f_1, f_2$ for two resonances (referenced by the black and blue dashed-grid lines) yield values of the loaded cavity-Q to be about 340 and 203 respectively. The presence of over-lapping resonances is clearly visible. By examining several such resonances, I estimate the average cavity-Q to be about 300 for this frequency range of 7.2GHz to 8.4GHz.

Appendix D: Derivation of the relation between the dephasing parameter (γ) and the cavity loss-parameter (α)

The relation between the dephasing parameter (γ) in the ballistic quantum dot to the loss-parameter (α) in the microwave cavity can be derived from the exact correspondence between the stationary Schrödinger equation for a two-dimensional quantum billiard and the classical wave-equation for a quasi-two-dimensional microwave cavity of the same shape. This correspondence translates into the mathematical equivalence between the continuity equation for the probability density in the quantum system and the Poynting theorem for the electromagnetic cavity.

From Ref.**[99]**, the relation between the probability density and the current density in the quantum billiard for an imaginary source potential from the "voltage probe" model of Ref.**[59]** is given by,

$$\frac{\partial |\psi|^2}{\partial t} + \vec{\nabla} \cdot \vec{j} = -\frac{2V_I}{\hbar} |\psi|^2, \tag{D.1}$$

where, the term ψ represents the quantum-mechanical wave-function of the particle in the quantum billiard and $\vec{j} = \frac{-j\hbar}{2m}(\psi \nabla \psi^* - \psi^* \nabla \psi)$ is the current density ($j = \sqrt{-1}$). The imaginary potential term is given by $V_I = \frac{\gamma \Delta}{4\pi}$ **[59]**, with Δ being the characteristic eigen-energy spacing in the quantum billiard.

Now for the microwave cavity filled with a linear dissipative dielectric medium of dielectric constant ε, the Poynting theorem gives,

$$\frac{\partial U}{\partial t} + \vec{\nabla} \cdot \vec{S} = -\omega \, \mathrm{Im}(\varepsilon) |E|^2, \tag{D.2}$$

where, the quantity U represents the electromagnetic energy density and plays a role analogous to the probability density in Eq.(D.1). While the quantity $\vec{S}$ represents the energy flow out of the system and is analogous to the current density in Eq.(D.1).

By directly comparing Eq.(D.1) and Eq.(D.2), and under the assumption that the voltage-probe model describing spatially uniform dephasing is equivalent to the imaginary potential model describing spatially uniform cavity losses **[59]**, we get

$$\frac{2V_I}{\hbar} \Leftrightarrow \frac{\omega}{Q}, \tag{D.3}$$

where the dielectric losses in the microwave cavity are related to the cavity quality factor through, $Q \approx \frac{1}{\mathrm{Im}[\varepsilon]}$.

Substituting $V_I = \frac{\gamma\Delta}{4\pi}$ in Eq.(D.3) we get,

$$\frac{2}{\hbar}\frac{\gamma\Delta}{4\pi}\left(\frac{1}{\Delta/\hbar}\right) = \frac{\omega}{Q\Delta\omega}, \tag{D.4}$$

where the LHS and RHS of Eq.(D.4) has been normalized by the respective characteristic energy(frequency) spacing to yield dimensionless quantities.

By reducing the RHS of Eq.(D.4) as follows,

$$\frac{\omega}{Q\Delta\omega} = 2\frac{k}{2Q\Delta k} = 2\frac{k^2}{2Qk\Delta k} = 2\frac{k^2}{Q\Delta k^2}, \tag{D.5}$$

and substituting back in Eq.(D.4), we get $\gamma = 4\pi\alpha$, with $\alpha = k^2/(\Delta k^2 Q)$.

Bibliography

[1] S. Glasstone, "The Effects of Nuclear Weapons", (US Dept. of Defense and Energy Research and Development Administration, Edited 1962, Revised February 1964).

[2] "Dawn of the E-bomb", IEEE Spectrum, Nov. 2003.

[3] Carlo Kopp, "The Electromagnetic Bomb- A Weapon of Electrical Mass Destruction", infoWARcon 5 Conference Proceedings, NCSA, Arlington VA USA, 3-31.

[4] S. M. Sze, "Physics of Semiconductor Devices", (2nd Edition, John Wiley and Sons, Inc. 1981).

[5] Clayton R. Paul, "Introduction to Electromagnetic Compatibility", (John Wiley and Sons,Inc. 2006).

[6] J. -P. Parmantier, Computing and Control Engineering Journal, **9**, 52 (1998).

[7] R. Holland and R. St. John, "Statistical Electromagnetics", (Taylor and Francis, London, 1999), and references therein.

[8] P. Corona, G. Larmiral, and E. Paolini, IEEE Trans. EMC, **22**, 2 (1980).

[9] R. H. Price, H. T. Davis, and E. P. Wenaas, Phys. Rev. E., **48**, 4716 (1993).

[10] D. Hill, IEEE Trans. EMC, **36**, 294 (1994).

[11] D. Hill, IEEE Trans. EMC, **40**, 209 (1998).

[12] L. Cappetta, M. Feo, V. Fiumara, V. Pierro and I. M. Pinto, IEEE Trans. EMC, **40**, 185 (1998).

[13] H.- J. Stöckmann, "Quantum Chaos", (Cambridge University Press, Cambridge 1999), and references therein.

[14] E. P. Wigner, Ann. Math. **53**, 36 (1951); **62**, 548 (1955); **65**, 203 (1957); **67**, 325 (1958).

[15] E. Ott, "Chaos in Dynamical Systems",(Cambridge University Press 1993).

[16] P. So, Ph.D Dissertation, University of Maryland (1995). (also see Ref. [22]).

[17] O. Bohigas, M. J. Giannoni and C. Schmidt, Phys. Rev. Lett. **52**, 1 (1984).

[18] S. W. McDonald and A. N. Kaufman, Phys. Rev. Lett. **42**, 1182 (1979); Phys. Rev. A. **37**, 3067 (1988).

[19] R. L. Weaver, J. Acoust. Soc. Am. **85**, 1005 (1989).

[20] C. Ellegaard, T. Guhr, K. Lindemann, H. Q. Lorensen, J. Nygård, and M. Oxborrow, Phys. Rev. Lett. **75**, 1546 (1995).

[21] L. L. A. Adams, B. W. Lang, and A. M. Goldman, Phys. Rev. Lett. **95**, 146804 (2005).

[22] P. So, S. M. Anlage, E. Ott, and R. N. Oerter, Phys. Rev. Lett. **74**, 2662 (1995).

[23] M. L. Mehta, "Random Matrices", (Academic Press, San Diego, 1991).

[24] F. Haake, "Quantum Signatures of Chaos" (Springer-Verlag, Berlin 1991).

[25] X. Zheng, T. M. Antonsen and E. Ott, Electromagnetics **26**, 3 (2006).

[26] X. Zheng, T. M. Antonsen and E. Ott, Electromagnetics **26**, 37 (2006).

[27] Y. Alhassid, Rev. Mod. Phys. **72**, 895 (2000).

[28] R. U. Haq, A. Pandey and O. Bohigas, Phys. Rev. Lett. **48**, 1086 (1982).

[29] L. Ericson, Ann. Phys. **23**, 390 (1963).

[30] C. W. J. Beenakker, Rev. Mod. Phys. **69**, 731 (1997).

[31] D. Agassi, H. A. Weidenmuller, and G. Mantzouranis, Phys. Rep. **22**, 145 (1975).

[32] P. A. Mello, P. Pereyra and T. H. Seligman, Ann. Phys. **161**, 254 (1985).

[33] P. W. Brouwer, Phys. Rev. B. **51**, 16878 (1995).

[34] D. V. Savin, Y. V. Fyodorov, and H. –J. Sommers, Phys. Rev. E **63**, 035202 (2001).

[35] R.A.Mendez-Sanchez, U. Kuhl, M. Barth, C.H. Kewenkopf and H.-J. Stöckmann, Phys. Rev. Lett. **91**, 174102 (2003).

[36] U. Kuhl, M. Martinez-Mares, R. A. Mendez-Sanchez, and H. –J. Stöckmann, Phys. Rev. Lett. **94**, 144101 (2005).

[37] J. B. French, P. A Mello, and A. Pandey, Phys. Lett. **80B**, 17 (1978).

[38] A. Pandey, Ann. Phys. (N.Y) **119,** 170 (1979).

[39] H. Schanze, H.-J Stöckmann, M. Martinez-Mares, C.H. Lewenkopf, Phys. Rev. E **71**, 016223 (2005).

[40] E. P. Wigner and L. Eisenbud, Phys. Rev. **72**, 29 (1947).

[41] S-H Chung, A. Gokirmak, D-H Wu, J. S. A. Bridgewater, E. Ott, T. M. Antonsen, and S. M. Anlage, Phys. Rev. Lett. **85**, 2482 (2000).

[42] E. Ott, Phys. Fluids **22**, 2246 (1979).

[43] M. V. Berry, " Chaotic Behavior of Deterministic Systems. *Les Houches* Summer School 1981" (North-Holland, 1983).

[44] J. D. Jackson, "Classical Electrodynamics", (3rd Edition, John Wiley and Sons, Inc. 1993).

[45] S. Hemmady, X. Zheng, T. M. Antonsen. E. Ott and S. M. Anlage, Phys. Rev. Lett. **94**, 014102 (2005).

[46] S. Hemmady, X. Zheng, T. M. Antonsen. E. Ott and S. M. Anlage, Phys. Rev. E. **71**, 056215 (2005).

[47] Y. V. Fyodorov and D. V. Savin, JETP Lett., **80**, 725 (2004).

[48] D. V. Savin and H. –J. Sommers, Phys. Rev. E., **69**, 035201 (2004).

[49] (a) L. K. Warne, K. S. H. Lee, H. G. Hudson, W. A. Johnson, R. E. Jorgenson and S. L. Stronach, IEEE Trans. Antennas and Prop., **51**, 978 (2003). (b) L.K. Warne, W.A. Johnson, R. E. Jorgenson, Sandia Report SAND2005-1505.

[50] X. Zheng, Ph.D Dissertation, University of Maryland (2005).

[51] C. E. Porter, "Statistical Theory of Spectra: Fluctuations", (Academic Press-New York, 1965).

[52] H. –J. Stöckmann and J. Stein, Phys. Rev. Lett., **64**, 2215 (1990).

[53] E. Doron, U. Smilansky, and A. Frenkel, Phys. Rev. Lett., **65**, 3072 (1990).

[54] A. Gokirmak, D. –H. Wu, J. S. A. Bridgewater and S. M. Anlage, Rev. Sci. Instrum., **69**, 3410 (1998).

[55] D. –H. Wu, J. S. A. Bridgewater, A. Gokirmak, and S. M. Anlage, Phys. Rev. Lett. **81**, 2890 (1998).

[56] J. Barthélemy, O. Legrand, and F. Mortessagne, Phys. Rev. E., **71**, 016205 (2005).

[57] M. Barth, U. Kuhl, and H. –J. Stöckmann, Phys. Rev. Lett. **82**, 2026 (1999).

[58] S. Hemmady, X. Zheng, T. M. Antonsen. E. Ott and S. M. Anlage, Acta Physica Polonica A, **109**, 65 (2006).

[59] P. W. Brouwer and C. W. J. Beenakker, Phys. Rev. B., **55**, 4695 (1997).

[60] Y. V. Fyodorov, D. V. Savin and H. –J. Sommers, J. Phys. A., **38**, 10731 (2005).

[61] C. A. Balanis, "Advanced Engineering Electromagnetics", (John Wiley and Sons, Inc. 1989).

[62] S. Hemmady, X. Zheng, J. Hart, T.M. Antonsen , E. Ott and S.M. Anlage, Phys. Rev. E. **74**, 036213 (2006)..

[63] A.G Huibers, S.R. Patel and C.M. Marcus, Phys. Rev. Lett. **81**, 1917 (1998).

[64] S. Hemmady, J. Hart, X. Zheng, T.M. Antonsen , E. Ott and S.M. Anlage, accepted by Phys. Rev. B. (in press), cond-mat/0606650.

[65] M. Büttiker, Phys. Rev. B **33**, 3020 (1986).

[66] C. H. Lewenkopf and A. Müller, Phys. Rev. A **45**, 2635 (1992).

[67] H. U. Baranger and P. A. Mello, Phys. Rev. B **51**, 4703 (1995).

[68] C. M. Marcus, R. M. Westervelt, P. F. Hopkins and A. C. Gossard, Phys. Rev. B. **48**, 2460 (1993).

[69] K. B. Efetov, Phys. Rev. Lett. **74**, 2299 (1995).

[70] E. McCann and I.V. Lerner, J. Phys. Cond. Matt. **8**, 6719 (1996).

[71] M. R. Zirnbauer, Nucl. Phys. A **560**, 95 (1993).

[72] E. Doron, U. Smilansky and A. Frenkel, Physica D **50**, 367 (1991).

[73] M. Martínez-Mares and P. A. Mello, Phys., Rev. E **72**, 026224 (2005).

[74] B.L. Altshuler and B. D. Simons, "Mesoscopic Quantum Physics", edited by E. Akkermans, G. Montambaux, J.-L. Pichard and J. Zinn-Justin. Elsevier, Amsterdam (1995).

[75] P. Mohanty and R. A. Webb, Phys. Rev. Lett. **88**, 146601 (2002).

[76] N. Agraït, A. L. Yeyati and J. M. Ruitenbeek, Phys. Rep. **377**, 81 (2003); and references therein.

[77] E. Joos, *et al.*, "Decoherence and the Appearance of a Classical World in Quantum Theory", Springer (December 1, 1996).

[78] H. -D. Gräf, H. L. Harney, H. Lengeler, C. H. Lewenkopf, C. Rangacharyulu, A. Richter, P. Schardt, and H. A. Weidenmüller, Phys. Rev. Lett. **69**, 1296 (1992).

[79] A. Kudrolli, S. Sridhar, A. Pandey, and R. Ramaswamy, Phys. Rev. E., **49**, R11 (1994).

[80] M. Vraničar, M. Barth, G. Veble, M. Robnik, and H. –J. Stöckmann, J. Phys. A: Math. Gen. **35**, 4929 (2002).

[81] X. Zheng, S. Hemmady, T. M. Antonsen, S. M. Anlage, and E. Ott, Phys. Rev. E., **73**, 046208 (2006).

[82] C. Fiachetti and B. Michielsen, Electron. Lett. **39**, 1713 (2003).

[83] W. Hauser and H. Feshbach, Phys. Rev. **87**, 366 (1952).

[84] W. A. Friedman and P. A. Mello, Ann. Phys., **161**, 276 (1985).

[85] C. A. Balanis, "Antenna Theory: Analysis and Design", (3rd Edition, John Wiley and Sons, Inc. 2005).

[86] P. Bhatria, Inder Bahl, R. Garg, and A. Ittipiboon, " Microstrip Antenna Design Handbook", (Artech House antennas and propagation library, 2001).

[87] D. Pozar, " Microwave Engineering", (3rd Edition, John Wiley and Sons, Inc. 2005).

[88] J. Barthélemy, O. Legrand, and F. Mortessagne, Europhys. Lett. **70**, 162 (2005).

[89] D. V. Savin, O. Legrand, and F. Mortessagne, cond-mat/0607810.

[90] P. Mello and N. Kumar, "Quantum Transport in Mesoscopic Systems: Complexity and Statistical Fluctuations", (Oxford University Press, 2004).

[91] E. J. Heller, Phys. Rev. Lett., **53**, 1515 (1984).

[92] T. M. Antonsen, E. Ott, Q. Chen, and R. N. Oerter, Phys. Rev. E., **51**, 111 (1995).

[93] P. J. Petersan and S. M. Anlage, J. Appl. Phys. **84**, 3392 (1998).

[94] D. E. Steinhauer, Ph.D Dissertation, University of Maryland (2000).

[95] W. Cassing, M. Stingl and A. Weiguny, Phys. Rev. C., **26**, 22 (1982).

[96] K. Grosh, E. G. Williams, J. Acoust. Soc. Am. **93**, 836 (1993).

[97] H. Alt, P. von Brentano, H. –D Gräf, R. –D. Herzberg, M. Philipp, A. Richter and P. Schardt, Nuc. Phys. A **560**, 293 (1993).

[98] H. Alt, P. von Brentano, H. –D Gräf, R. Hofferbert, M. Philipp, H. Rehfeld, A. Richter and P. Schardt, Phys. Lett. B. **366**, 7 (1996).

[99] L. D. Landau and E. M. Lifshitz, "Quantum Mechanics (Non-relativistic Theory)", Butterworth-Heinemann, Vol. 3, 3rd Edition, (1981).